Matrix-Mediated Interactions between Particulate Inclusions in Linearly Elastic and Viscoelastic Environments

Inaugural dissertation

for the attainment of the title of doctor
in the Faculty of Mathematics and Natural Sciences
at the Heinrich Heine University Düsseldorf

presented by

Mate Puljiz
from Sindelfingen

Düsseldorf, January 2019

from the Institute for Theoretical Physics II: Soft Matter
at the Heinrich Heine University Düsseldorf

Published by permission of the
Faculty of Mathematics and Natural Sciences at
Heinrich Heine University Düsseldorf

Supervisor: Priv.-Doz. Dr. Andreas M. Menzel

Co-supervisor: Prof. Dr. Hartmut Löwen

Date of the oral examination: 27.03.2019

Abstract

A theoretical description of the interactions between finite-sized particles in linearly elastic or viscoelastic media is presented. Analogously to the famous Stokes flow around a rigid sphere in low-Reynolds-number hydrodynamics, the displacement field around a rigid spherical inclusion that is embedded in a continuous elastic environment can be analytically expressed in the framework of linear elasticity theory. The embedding medium is considered as isotropic, homogeneous, and infinitely extended. On this basis, ensembles of many spherical inclusions are addressed that are rigidly translated and rotated by external forces and torques, respectively. The external force and torque acting on each particle is transmitted to the surrounding medium and affects the other particles through the embedding material via local material distortions, leading to mediated interactions between the individual particles. Resulting effective interactions can formally be summarized by (mathematical) *displaceability* and *rotateability* matrices in analogy to the case of hydrodynamic mobility matrices describing interactions through incompressible fluid environments. These mathematical expressions are determined via expansions in the inverse interparticle separation distances. Here, the interaction matrices were calculated up to (including) sixth inverse interparticle separation distance for a possibly compressible elastic medium. In the limit of incompressibility, the hydrodynamic mobility matrices are formally recovered.

The theory was employed to quantify the experimentally observed interactions between rigid paramagnetic particles embedded in soft polymeric gels. When exposed to an external magnetic field, magnetic moments were induced in the particles. This resulted in magnetic interaction forces that displaced the particles from their initial equilibrium positions. Using the theory, the elastic shear moduli of the embedding polymeric gels, which were inaccessible to direct measurement, were extracted for several experimental samples. Very good agreement was found for the theoretically predicted and the measured particle displacements.

In a further experiment, a reversible collapse of two paramagnetic particles into

contact, starting from an initially well-separated state, was observed, if the (non-saturating) external field magnitude was large enough. Although the overall process is highly nonlinear, both with respect to the elastic and the magnetic effects, the theory could accurately determine the necessary field strength to initiate the collapse and furthermore qualitatively predict a hysteretic behavior for a magnetization-and-demagnetization cycle of the two-particle system.

Finally, a dynamic theory for particulate inclusions in linearly viscoelastic environments is presented. Viscoelastic materials possess both viscous and elastic properties. The theory used to describe the viscoelastic media can be derived from a general continuum approach based on classical conservation laws and symmetry arguments. In analogy to what has been described above, the interactions between rigid inclusions in the viscoelastic media were characterized theoretically and evaluated for basic example situations. For instance, the behavior of active self-propelled microswimmers is briefly addressed in such viscoelastic surroundings.

Affidavit

I declare under oath that I have compiled my dissertation independently and without any undue assistance by third parties under consideration of the "Principles for the Safeguarding of Good Scientific Practice at Heinrich Heine University Düsseldorf".

Düsseldorf, _____   _____

Preface

This dissertation is the result of my work at the Institute for Theoretical Physics II: Soft Matter, Heinrich Heine University Düsseldorf since April 2016 under the supervision of Priv.-Doz. Dr. Andreas M. Menzel. During this time, I have contributed to the following five publications:

- Publication I
  M. Puljiz, S. Huang, G. K. Auernhammer, and A. M. Menzel, *Forces on rigid inclusions in elastic media and resulting matrix-mediated interactions*, Phys. Rev. Lett., **117**, 238003 (2016), Editors' Suggestion.

- Publication II
  M. Puljiz and A. M. Menzel, *Forces and torques on rigid inclusions in an elastic environment: resulting matrix-mediated interactions, displacements, and rotations*, Phys. Rev. E, **95**, 053002 (2017).

- Publication III
  M. Puljiz, S. Huang, K. A. Kalina, J. Nowak, S. Odenbach, M. Kästner, G. K. Auernhammer, and A. M. Menzel, *Reversible magnetomechanical collapse: virtual touching and detachment of rigid inclusions in a soft elastic matrix*, Soft Matter, **14**, 6809 (2018), including inside front cover.

- Publication IV
  M. Puljiz and A. M. Menzel, *Memory-based mediated interactions between rigid particulate inclusions in viscoelastic environments*, Phys. Rev. E, **99**, 012601 (2019).

- Publication V
  M. Puljiz and A. M. Menzel, *Displacement field around a rigid sphere in a compressible elastic environment, corresponding higher-order Faxén relations, as well as higher-order displaceability and rotateability matrices*, arXiv:1901.06303 [cond-mat.soft] (2019).

Acknowledgments

I would like to express my sincere gratitude and appreciation to my supervisor Priv.-Doz. Dr. Andreas Menzel. First, for encouraging me to start my doctorate. Then, for his constant friendly support and assistance as well as for outstanding professional guidance throughout, which in this combination certainly cannot be taken for granted. Under his supervision, I have learned to understand physics from a different and richer angle.

Moreover, I thank Prof. Dr. Hartmut Löwen for providing a comfortable and efficient working environment at the Institute for Theoretical Physics II: Soft Matter at the Heinrich Heine University Düsseldorf as well as for many stimulating scientific discussions during the seminar talks.

Special thanks goes to our co-authors in two publications, Dr. Shilin Huang and Dr. Günter K. Auernhammer, for provision of experimental data, enriching collaboration, and their persistent first-rate work. Furthermore, I thank Karl A. Kalina and Prof. Dr.-Ing. habil. Markus Kästner for efficient and fruitful cooperation.

I thank Prof. Dr. Stefan Odenbach for his strong effort in establishing and coordinating the priority program SPP 1681, within the framework of which my work was supported by the Deutsche Forschungsgemeinschaft.

Furthermore, I owe gratitude to our system administrator Joachim Wenk for help in many respects as well as to our always kind secretary Claudia Stader. I thank all my former colleagues at the Institute for Theoretical Physics II: Soft Matter for their cooperation, mutual assistance, and many pleasant conversations, and especially Giorgio Pessot, Peet Cremer, Christian Hoell, Soudeh Jahanshahi, Christian Scholz, and Segun Goh.

Finally, I thank my family for constant support and encouragement.

x

Contents

Contents

1 Introduction

1.1 Motivation

The question that at the very start initiated this thesis can be summarized as follows: two spherical particles are embedded at a given distance in a continuous elastic environment; how are they displaced with respect to each other, if exposed to external forces? Answers to this question and related ones were found and evaluated by considering example systems within the field of *soft matter* physics.

Soft matter physics addresses materials that exhibit strong responses to comparatively weak forces [1]. This fact is owed to the size of the building blocks of these materials, which are large enough to neglect quantum effects and typically small enough so that thermal fluctuations remain important [2]. One of the subbranches of soft matter physics deals with colloidal suspensions [1]. These are defined as mixtures consisting of small particles, typically $\sim 10\text{nm}\text{--}10\mu\text{m}$, that are dispersed in a medium, e.g., a liquid or a gel.

More precisely, the class of materials addressed by the initial question are soft elastic composite materials, specifically magnetic elastomers and gels [3–6]. In that case, the dispersion medium is represented by a polymeric network. Polymers are macromolecules that, in the simplest case, are given by long chains of repeated small segments, the so-called monomers [1]. The polymer chains exhibit entropic elasticity [7], which means that they prefer curled over stretched chain configurations. Thus, if a polymer is stretched by an external load, it tends to resume a curled shape after the load is removed. A polymeric network is constituted by many such macromolecules. If the polymer molecules are chemically crosslinked, an overall elastic behavior can be the result. In a polymeric gel, the polymer network is additionally swollen by a solvent (liquid), which is trapped in the mesh of the polymeric material. The extent of elasticity can be controlled, for instance, by the degree of chemical crosslinking between individual polymeric chains. On the scales considered here, the elastic dispersion medium can be regarded as continuous [6].

If magnetizable or magnetic colloidal particles are embedded in the elastic dispersion medium, then they can be addressed by external magnetic fields [3, 8]. For instance, we consider a colloidal particle carrying a magnetic moment. Exposed to an external magnetic field gradient, in general a force will be induced that displaces the particle [8]. Since the particle is embedded in an elastic environment, the local material will be reversibly distorted by the particle displacements. Let us now place a second magnetic particle into the vicinity of the first particle. Then, the second particle is necessarily affected by the deformation field created by the first particle. Moreover, since the second particle is also subject to the external field, it will likewise, in general, distort the local surrounding material, which in turn affects the first particle. Thus, a mutual *interaction* occurs between the two particles, mediated by the embedding elastic material [6].

The study of such magneto-elastic composite materials constitutes a broad interdisciplinary research field, involving physics [4, 6], chemistry [9, 10], biology and biophysics [11–13], medicine [14–16], and engineering sciences [17–19]. Depending on the considered length scales, these materials exhibit various characteristic effects. For instance, they allow for the tuning of their macroscopic shape (magnetostriction) [3, 20, 21] and mechanical properties like stiffness by external magnetic fields [4, 22, 23]. This makes them attractive for technological applications, e.g., as soft actuators, sensors, artificial muscles, or tunable dampers [24–29]. Moreover, research is being conducted to combine the properties of nematic liquid crystals and magnetic gels [30, 31]. Biological cells and tissue containing magnetic particles can likewise be classified as magnetic gels. There, drug delivery via field-responsive magnetic colloidal particles and hyperthermal cancer treatment are of medical interest [14–16]. On the mesoscopic scale, interesting magneto-mechanical coupling effects in magnetic gels have been observed [32], involving long chain-like aggregates of magnetic particles that buckled characteristically under a perpendicular external magnetic field due to an interplay of magnetic forces on the particles and the resistance of the embedding elastic medium to deformation. Moreover, theoretical investigations of uniaxial magnetic gels revealed a superelastic behavior [33, 34], i.e., pronounced nonlinear stress-strain behavior.

Many different tools are available to investigate the properties of such systems theoretically. For instance, in a simplified picture, the elastic medium can be modeled by a network of harmonic springs, whereas the magnetic component is represented by point-like or spherical particles with magnetic dipole moments [22, 32, 35–38].

2

This allows, for example, to effectively handle large particle numbers as well as to study relaxational dynamics and dynamic material properties [37, 38]. Alternatively, the colloidal particles and embedding medium can be described by finite-element simulations and related methods [33, 34, 39–43], allowing for the spatially resolved quantification of deformation fields. Often, it is sufficient to assume point dipoles for the magnetic particles [22, 38]. However, in some cases, the internal magnetization of the magnetic particles needs to be resolved, which can likewise be addressed by finite-element simulations [42]. Some studies explicitly resolve the microscopic details of the embedding medium by modeling coarse-grained polymer chains in a discretized way [36, 44, 45]. Statistical methods can provide further insight into particle distributions for a better understanding of macroscopic properties [46]. Furthermore, magnetic gels can be addressed by density functional theory [47]. The broad picture is finally given by macroscopic theories that are derived from conservation laws and symmetry considerations [48, 49]. Such symmetry-based descriptions involve many undetermined macroscopic material parameters that eventually must be functions of the micro- and mesoscopic details. Combining the efforts of micro-, meso-, and macroscopic theory and simulation, connecting these different length scales from the micro- via the meso- to the macroscale is desirable to achieve a more complete understanding [36, 50].

Here, we concentrate on the mesoscopic point of view. That is, the finite size of the colloidal particles is still resolved, whereas the embedding material appears homogeneous and continuous [6]. (According to the definition of the term "mesoscopic" when compared to the term "macroscopic" given in Ref. [6], a macroscopic theory in this context does not resolve the individual magnetic particles but instead includes their effect via a continuous magnetization field, while a mesoscopic theory resolves them individually. Here, we stick to the latter concept.)

The focal point of this thesis lies on interactions between rigid particulate inclusions mediated by the surrounding environment. A real quantitative analysis of such mediated interactions requires to correctly resolve the three-dimensional distortional fields that the particles may induce in the medium upon displacements or rotations. If the considered composite material is predominantly elastic, then the theory of elasticity [51] is used for this purpose. Especially in the regime of small deformations, closed-form expressions can be derived.

We will here first approach the initially stated problem analytically in the framework of linear elasticity theory, with the ambition to describe real experimental samples quantitatively. Later, we extend the theory to dynamic situations. This is

3

motivated by the fact that many composite systems composed of colloidal particles in polymeric solutions do not only exhibit elastic but also viscous properties, i.e., they combine features characteristic for solids and liquids [52]. The term *viscoelastic* has been introduced to refer to this kind of behavior. In formulating a dynamic theory to quantify the behavior of particulate inclusions in linearly viscoelastic materials, our mesoscopic approach is considerably widened, extending, inter alia, also to the description of the behavior of active self-propelled microswimmers [53, 54].

Since the background of this dissertation thesis is theoretic, we first include in Sec. 1.2 some brief remarks on the used notation. Afterwards, we provide a brief introduction to linear elasticity theory in Sec. 1.3. There, all concepts, quantities, and formulae necessary for the understanding of the theoretical parts of our publications are defined or derived. We then address our actual theoretical work in the framework of this thesis and finally briefly summarize our results. A few words concerning our theoretical analysis of experimental sample systems follow in Sec. 1.4. Furthermore, in Sec. 1.5 our dynamic theory for linearly viscoelastic materials is summarized. Part 2 attaches the already peer-reviewed publications (I to IV) together with a statement on the respective contributions of the author to each work. Furthermore, a link to the published preprint version of our last work (V) is included. Finally, we end by some concluding words in Part 3.

1.2 Remarks on notation

Two kinds of mathematical notations are used interchangeably throughout this introduction and the papers, namely the index notation and the vector notation. Vectors and tensors are written in bold in vector notation. In addition to that, tensors of rank two are marked by an underscore, tensors of rank three by two underscores, and so on, for instance, $\underline{\mathbf{G}}$ and $\underline{\underline{\mathbf{M}}}$. All considered vector fields are three-dimensional. The individual components along the different coordinate axes are addressed by index notation: r_i is the ith component of $\mathbf{r}$ with $i \in \{x, y, z\}$ in Cartesian coordinates. Likewise, the components of the tensors $\underline{\mathbf{G}}$ and $\underline{\underline{\mathbf{M}}}$ are given by G_{ij} and M_{ijk} ($j, k \in \{x, y, z\}$). Coordinate indices are always shifted to the subscript. The Euclidian norm (magnitude) of a vector $\mathbf{r}$ is denoted by the scalar $r := |\mathbf{r}|$. Moreover, unit vectors are marked by a hat, e.g., $\hat{\mathbf{r}} := \mathbf{r}/r$ and $\hat{r}_i$ in vector and index notation, respectively. Vectors and tensors can be labeled to refer to different particles, for example, $\mathbf{r}_i$ for the ith particle. Then, $r_{i,j}$ here denotes the jth component of the

$\mathbf{r}_i$-vector (and not the derivative with respect to the jth coordinate as in some other works).

The identity tensor is in vector notation written as $\hat{\underline{\mathbf{I}}}$. Its components are expressed via the Kronecker-delta symbol

$$\delta_{ij} := \begin{cases} 1, & \text{for } i = j, \\ 0, & \text{else.} \end{cases} \tag{1.1}$$

Furthermore, the frequently used Levi-Civita symbol is defined as

$$\epsilon_{ijk} := \begin{cases} 1, & \text{if } (i, j, k) \text{ is an even permutation of } (x, y, z), \\ -1, & \text{if } (i, j, k) \text{ is an odd permutation of } (x, y, z), \\ 0, & \text{else.} \end{cases} \tag{1.2}$$

The Einstein summation convention, i.e., summation over repeated indices, is applied. In vector notation, polyadics are expressed without multiplication sign, e.g., $r_i r_j$ is the ij-component of the dyadic $\mathbf{rr}$. Contractions over two indices are in vector notation marked by a center dot, contractions over four indices by two vertical dots, and so on, for example, $\mathbf{r} \cdot \nabla = r_i \nabla_i$ and $\mathbf{rr} : \nabla\nabla = r_k r_l \nabla_l \nabla_k$.

1.3 Linear elasticity theory

In the following, a brief introduction to the linear theory of elasticity is given. This overview roughly follows Ref. [51], though paying more attention to the aspects that are important in this thesis while neglecting issues less relevant here. Linear elasticity theory is a continuum theory and is built upon symmetry considerations and the axiomatic conservation laws of classical physics. It describes small reversible deformations of solids. These deformations can be caused, e.g., by the gravitational field or by an applied stress. In a composite material, the sources of local interior deformations can also stem from particulate inclusions embedded into the material that are displaced and rotated by external forces and torques, respectively [4,6]. The basic problem of inclusions in an elastic material has been addressed previously [55–61]. Our goal here is to quantify the interactions between rigid inclusions of finite size mediated by the embedding elastic medium, if external forces and torques act on these inclusions.

Elastic materials can in general exhibit various anisotropies [51]. Here, we focus on the simplest but in many cases well applicable case of an isotropic and homogeneous medium. Moreover, we concentrate on the bulk of the material and therefore assume the medium to be for this purpose infinitely extended throughout. We start by first considering a simple elastic solid without any inclusions or other inhomogeneities.

1.3.1 Displacement, strain, and compressibility

In elastostatics, two states of a given elastic solid are distinguished: the undeformed or ground state and the deformed state. Let $\mathbf{r}$ be the position of a material point of the medium in the undeformed state and $\mathbf{r}'$ its position in the deformed state. Then, we can define the displacement

$$\mathbf{u} := \mathbf{r}' - \mathbf{r}. \tag{1.3}$$

More precisely, $\mathbf{u}$ is a field, i.e., $\mathbf{u} = \mathbf{u}(\mathbf{r})$, that describes the displacements at all positions $\mathbf{r}$. In the following sections, we omit the argument of all field quantities for simplicity of notation. Let us now consider two neighboring material points separated by the infinitesimal distance vectors $\mathrm{d}\mathbf{r}$ and $\mathrm{d}\mathbf{r}'$ in the ground state and in the deformed state, respectively. Then, according to Eq. (1.3), we can write

$$\mathrm{d}\mathbf{r}' = \mathrm{d}\mathbf{r} + \mathrm{d}\mathbf{u}, \tag{1.4}$$

with $\mathrm{d}\mathbf{u}$ the infinitesimal difference between the respective displacements of the two material points. Their distance in the deformed state is thus described by the magnitude $\mathrm{d}r'$, or equivalently,

$$\mathrm{d}r_i'^2 = \mathrm{d}r_i^2 + 2\mathrm{d}r_i\mathrm{d}u_i + \mathrm{d}u_i^2. \tag{1.5}$$

Inserting the identity $\mathrm{d}u_i = (\nabla_j u_i)\mathrm{d}r_j$, we find

$$\mathrm{d}r_i'^2 = (\delta_{ij} + 2\varepsilon_{ij})\mathrm{d}r_i\mathrm{d}r_j, \tag{1.6}$$

with

$$\varepsilon_{ij} := \frac{1}{2}\left[\nabla_i u_j + \nabla_j u_i + (\nabla_i u_l)(\nabla_j u_l)\right]. \tag{1.7}$$

If infinitesimal deformations are considered, Eq. (1.7) can be linearized with respect to the gradient of **u** to obtain

$$\varepsilon_{ij} = \frac{1}{2} \left[\nabla_i u_j + \nabla_j u_i \right], \tag{1.8}$$

which we call *strain tensor* in the following. The strain tensor is a tensor of rank two and, being symmetric, possesses six independent and real components. It describes the deformation of an elastic material. Deformations result if any two points of the material are displaced relatively with respect to each other. We can distinguish two kinds of displacements, for which no deformation occurs, namely uniform translations and rotations. Uniform translations are described by constant displacements and thus drop out when calculating the gradients in $\underline{\varepsilon}$. These gradients quantify the relative displacements between neighboring material points. Moreover, the symmetry of the strain tensor automatically guarantees that uniform rotations of the form $\mathbf{u} = \mathbf{\Omega} \times \mathbf{r}$ (with $\mathbf{\Omega}$ constant) do not contribute to $\underline{\varepsilon}$.

Let us now consider the volume elements $\mathrm{d}^3 r$ and $\mathrm{d}^3 r'$ in the undeformed ground state and in the deformed state, respectively. $\mathbf{r}$ and $\mathbf{r}'$ are related by the transformation $\mathbf{r}' = \mathbf{r} + \mathbf{u}$, see Eq. (1.3). The volume elements are then linked to each other by the corresponding Jacobian determinant,

$$\mathrm{d}^3 r' = \left(\det \frac{\partial \mathbf{r}'}{\partial \mathbf{r}} \right) \mathrm{d}^3 r. \tag{1.9}$$

Thus, to linear order in deformation gradients the expression

$$\frac{\mathrm{d}^3 r'}{\mathrm{d}^3 r} \approx 1 + \varepsilon_{xx} + \varepsilon_{yy} + \varepsilon_{zz} \tag{1.10}$$

is obtained. Obviously, for $\varepsilon_{ii} = \varepsilon_{xx} + \varepsilon_{yy} + \varepsilon_{zz} = \nabla \cdot \mathbf{u} = 0$, the volume is conserved. If this is generally the case, the elastic medium is called *incompressible*. Otherwise, a finite ε_{ii} describes a change in volume, which implies a compressible medium. Thus, the compressibility of a given elastic medium is a fundamental material property that can be quantified by an intrinsic *material parameter*. In order to introduce such a parameter, we consider a situation, in which the elastic material undergoes a uniaxial extension along the x-axis. In general, this is accompanied by a finite strain in the transversal yz-plane. Since we assume an isotropic medium, $\varepsilon_{yy} = \varepsilon_{zz}$ due to symmetry and linearity. As a measure of the compressibility, we define the

(dimensionless) *Poisson ratio*

$$\nu := -\frac{\varepsilon_{yy}}{\varepsilon_{xx}} = -\frac{\varepsilon_{zz}}{\varepsilon_{xx}}. \tag{1.11}$$

Then, Eq. (1.10) can be rewritten in the form

$$\frac{\mathrm{d}^3 r'}{\mathrm{d}^3 r} = 1 + \varepsilon_{xx}(1 - 2\nu). \tag{1.12}$$

Ideal incompressibility is thus described by $\nu = 1/2$, for which the material is contracted in the transversal plane antagonistically to uniaxial extension along the x-axis so that the volume is conserved. For $\nu = 0$, the material can be stretched uniaxially without affecting the transversal plane. $\nu < 0$ corresponds to transversal thickening if the material is stretched along one direction. The converse applies for uniaxial compression. We will return to the physical parameter range of ν for an isotropic and homogeneous material in Sec. 1.3.3.

1.3.2 Stress tensor and static equilibrium

In order to generate a situation of finite strain $\underline{\varepsilon}$, external forces must be applied to the elastic material. By Newton's third law, these forces induce internal counterforces in the elastic material, resulting in a final steady state of deformation. We can understand this balanced deformed state by considering the forces that any two adjacent regions in the elastic medium exert mutually onto each other. In a continuous environment, forces between two regions are transmitted across their (imaginary) contact surface. Let us, for instance, consider a plane that divides the medium perpendicular to a uniaxially applied tensile load. The pulling force on the plane in one direction must then be balanced by a force on the same plane but in the opposite direction, otherwise the material would be ripped into two pieces at the dividing plane. Thinking further, this must be true for any plane of any orientation. The final deformed state is thus a static state of equilibrium, in which the imposed forces are balanced by the resistance of the material. These surface forces at each point and along every orientation can be represented by one single field quantity in the form of a second rank tensor, which we call the *stress tensor* $\underline{\sigma} = \underline{\sigma}(\mathbf{r})$. Let $\mathrm{d}S$ be the area of a surface element somewhere in the infinitely extended medium with the outward normal vector $\hat{\mathbf{n}}$. The components of the forces that act from the outside on the surface element, i.e., from the direction to which $\hat{\mathbf{n}}$ points, can then be described in

the form $\sigma_{ij}\hat{n}_j\mathrm{d}S$. By definition, σ_{ij} has the units of pressure. Uniform compression of a given volume element from all sides by convention corresponds to $\sigma_{ij} = -p\delta_{ij}$ and uniform extension to $\sigma_{ij} = p\delta_{ij}$, with $p > 0$ the pressure.

Let us now consider a given volume V in the elastic solid that is enclosed by the surface ∂V. In addition to the surface forces described by the stress tensor, also forces per volume element can be applied to the elastic material, which can be described in terms of a bulk force density $\mathbf{f}_b = \mathbf{f}_b(\mathbf{r})$. The static equilibrium condition then directly follows from the conservation of momentum and reads

$$\int_{\partial V} \mathrm{d}S \; \sigma_{ij}\hat{n}_j + \int_V \mathrm{d}V \; f_{b,i} = 0, \tag{1.13}$$

or, using Gauss's divergence theorem,

$$\int_V \mathrm{d}V \; [\nabla_j\sigma_{ij} + f_{b,i}] = 0. \tag{1.14}$$

Since the choice of V is arbitrary, the equilibrium condition must also hold locally, i.e.,

$$\nabla_j\sigma_{ij} + f_{b,i} = 0. \tag{1.15}$$

Angular momentum must be conserved as well, i.e., the total torque must vanish in equilibrium. We may express the torque density as $\epsilon_{ilk}r_l f_{b,k}$ for the bulk force density and $\epsilon_{ilk}r_l\sigma_{kj}\hat{n}_j$ for the surface force density, with $\mathbf{r}$ the distance vector measured from an arbitrary point. Then,

$$\int_{\partial V} \mathrm{d}S \; \epsilon_{ilk}r_l\sigma_{kj}\hat{n}_j + \int_V \mathrm{d}V \; \epsilon_{ilk}r_l f_{b,k} = 0, \tag{1.16}$$

or, using Gauss's theorem and simplifying,

$$\int_V \mathrm{d}V \; \left\{\epsilon_{ilk}r_l[\nabla_j\sigma_{kj} + f_{b,k}] + \epsilon_{ijk}\sigma_{kj}\right\} = 0. \tag{1.17}$$

Again, this must hold true for any V. Moreover, using Eq. (1.15), the term in the square brackets vanishes and we obtain $\epsilon_{ijk}\sigma_{kj} = 0$. From this it follows that $\sigma_{ij} = \sigma_{ji}$, i.e., the stress tensor is symmetric.

Many situations can be described completely by an applied stress without bulk forces. External forces are then introduced in the form of boundary conditions for the stress tensor, so that $\nabla_j\sigma_{ij} = 0$ is satisfied inside the material. As an example, a

homogeneous uniaxial compressive/tensile stress along the x-axis is given by setting $\sigma_{xx} = \text{const} \neq 0$ and all other stress components to zero. This results in a finite strain ε_{ij} in the material. Consequently, stress and strain are related to each other. To obtain the stress-strain relation, the elastic energy (density) must be derived.

1.3.3 Elastic energy and stress-strain relation

In a closed system, the first law of thermodynamics for a reversible process reads [51]

$$\mathrm{d}U = T\mathrm{d}S - p\mathrm{d}V \tag{1.18}$$

for infinitesimal changes. Here, $\mathrm{d}U$ is the change in internal energy and $T\mathrm{d}S$ the absorbed heat. The last term, $p\mathrm{d}V$, represents a small increment in the work per volume element performed by the system, with p the isotropic pressure and $\mathrm{d}V$ the infinitesimal change in volume. It can be rewritten in terms of the elastic quantities that have been introduced in the previous sections. Uniform compression from all sides then corresponds to $\sigma_{ij} = -p\delta_{ij}$, whereas the relative change in volume is described by ε_{ii}, see Eq. (1.10). Thus, $d\varepsilon_{ii}$ here is related to $\mathrm{d}V$. Taken together, $\sigma_{ij}\mathrm{d}\varepsilon_{ij} = -p\mathrm{d}\varepsilon_{ii}$. Switching to internal energy density u and entropy density s, as well as defining the free energy density $f = u - Ts$ and $\mathrm{d}(Ts) = T\mathrm{d}s + s\mathrm{d}T$, we have thus motivated its infinitesimal change of the form

$$\mathrm{d}f = -s\mathrm{d}T + \sigma_{ij}\mathrm{d}\varepsilon_{ij}. \tag{1.19}$$

At constant temperature, the stress tensor therefore takes the form

$$\sigma_{ij} = \left(\frac{\partial f}{\partial \varepsilon_{ij}}\right)_T. \tag{1.20}$$

(An explicit derivation proceeds by the method of virtual work resulting from virtual displacements.)

This brings us to the stress-strain relation. Obviously, the elastic energy density must be a function of the strain ε_{ij}. In a series expansion of f, there cannot be any linear term in ε_{ij}, otherwise Eq. (1.20) would yield a constant stress σ_{ij} even for $\varepsilon_{ij} = 0$. Hence, f is to lowest possible order quadratic in ε_{ij}, and thus $\sigma_{ij} \sim \varepsilon_{ij}$. At this point, we *assume* that σ_{ij} is a linear function of ε_{ij} for small deformations. Second-rank tensors can be mapped linearly onto each other via tensors of rank four.

The linear stress-strain relation may therefore be expressed as

$$\sigma_{ij} = C_{ijkl}\varepsilon_{kl}. \tag{1.21}$$

Equation (1.21) is also referred to as the generalized Hooke's law. Inserting Eq. (1.21) into Eq. (1.20), we arrive at

$$f = \frac{1}{2}C_{ijkl}\varepsilon_{ij}\varepsilon_{kl}, \tag{1.22}$$

discarding a constant contribution.

C_{ijkl} is referred to as the stiffness or elasticity tensor and has units of pressure. It describes the resistance of the material to strains. Since every of its four indices refers to three distinct coordinates, it possesses $3^4 = 81$ components, each of which representing a material parameter. However, the number of *independent* components is reduced to only 21 due to several inherent symmetries in Eq. (1.22), which we now examine step-by-step. First, the symmetry of the strain tensor, i.e., $\varepsilon_{ij} = \varepsilon_{ji}$ and $\varepsilon_{kl} = \varepsilon_{lk}$, implies that C_{ijkl} is separately symmetric with respect to $i \leftrightarrow j$ and $k \leftrightarrow l$. That is, each of the two pairs, (ij) and (kl), produces 6 independent components, which in total leads to $6^2 = 36$ independent components. We can thus understand the stiffness tensor as a 6×6-matrix, which is in fact the equivalent Voigt notation [62]. As a next step, Eq. (1.22) requires that the pairs $(ij) \leftrightarrow (kl)$ are interchangeable as well. Hence, in Voigt notation this means that the 6×6-matrix is symmetric. Thus, of the 36 components only 6 diagonal and 15 off-diagonal elements remain independent, in total $6 + 15 = 21$. This is the case for a fully anisotropic elastic material. Summarizing, the symmetries read

$$C_{ijkl} = C_{jikl} = C_{ijlk} = C_{jilk} = C_{klij} = C_{lkij} = C_{klji} = C_{lkji}. \tag{1.23}$$

Here, we restrict ourselves to isotropic materials. In an isotropic solid, there are no preferred axes. For instance, all planes in the (infinitely extended) material are planes of symmetry. Technically, this means that the stiffness tensor can be decomposed into identity matrices. For a fourth-rank tensor, this implies a linear combination of terms $\sim \delta_{ij}\delta_{kl}$. Since there are exactly three possible permutations of $\delta_{ij}\delta_{kl}$, we may write the stiffness tensor as $C_{ijkl} = \lambda\delta_{ij}\delta_{kl} + \mu\delta_{ik}\delta_{jl} + c_3\delta_{il}\delta_{jk}$, with the material parameters λ, μ, and c_3. However, from the symmetry $i \leftrightarrow j$ or $k \leftrightarrow l$, it immediately follows

that $\mu = c_3$. Therefore,

$$C_{ijkl} = \lambda \delta_{ij}\delta_{kl} + \mu(\delta_{ik}\delta_{jl} + \delta_{il}\delta_{jk}). \qquad (1.24)$$

In other words, the elastic properties of an isotropic material are uniquely specified by a set of two material parameters. Substituting this result into Eq. (1.22), we obtain for the free energy density

$$f = \frac{1}{2}\lambda\varepsilon_{ii}^2 + \mu\varepsilon_{ij}\varepsilon_{ij}. \qquad (1.25)$$

Moreover, the linear stress-strain relation in Eq. (1.21) can now be expressed via

$$\sigma_{ij} = \lambda\delta_{ij}\varepsilon_{ll} + 2\mu\varepsilon_{ij}, \qquad (1.26)$$

with its inverse reading

$$\varepsilon_{ij} = -\frac{\lambda}{2\mu(2\mu + 3\lambda)}\delta_{ij}\sigma_{ll} + \frac{1}{2\mu}\sigma_{ij}. \qquad (1.27)$$

λ and μ are referred to as Lamé parameters. From Eq. (1.25), it becomes clear that λ is connected to the compressibility of the material, because it only contributes to the energy if ε_{ii} is finite, i.e., if the volume changes at least locally. In order to separate this compressive part from the remaining part, we define $\lambda := K - \frac{2}{3}\mu$. Then, the trace of Eq. (1.26) becomes $\sigma_{ii} = 3K\varepsilon_{ii}$. The parameter K must therefore be positive in a real material. It quantifies the resistance of the material to compression or dilation, i.e., to volume changes, and is referred to as bulk modulus. Next, for $i \neq j$, Eq. (1.26) simplifies to $\sigma_{ij} = 2\mu\varepsilon_{ij}$. The off-diagonal elements of $\underline{\sigma}$ and $\underline{\varepsilon}$ describe remaining shear stresses and strains, respectively. Therefore, the parameter $\mu > 0$ is often referred to as *shear modulus*. It quantifies the resistance of the medium to shear deformations.

In the following, we describe the material solely by the Poisson ratio and the shear modulus and thus need to express λ via ν and μ. To find the corresponding relation, we now consider a uniaxial stress that is applied along the x-axis so that, of all stress components only σ_{xx} is nonzero. From Eq. (1.27), we find the diagonal strain

components

$$\varepsilon_{xx} \quad = \quad \frac{1}{2\mu}\left(1 - \frac{\lambda}{2\mu + 3\lambda}\right)\sigma_{xx}, \tag{1.28}$$

$$\varepsilon_{yy} = \varepsilon_{zz} \quad = \quad -\frac{\lambda}{2\mu(2\mu + 3\lambda)}\sigma_{xx}. \tag{1.29}$$

Using the definition of the Poisson ratio in Eq. (1.11), we therefore obtain

$$\nu = -\frac{\varepsilon_{yy}}{\varepsilon_{xx}} = \frac{\lambda}{2(\mu + \lambda)} = \frac{3K - 2\mu}{2(3K + \mu)}, \tag{1.30}$$

and thus,

$$\lambda = \frac{2\mu\nu}{1 - 2\nu}. \tag{1.31}$$

For $K \gg \mu$, we find from Eq. (1.30) that $\nu \to 1/2$, which corresponds to the limit of incompressibility as mentioned in Sec. 1.3.1. For $\mu \gg K > 0$, we obtain $\nu \to -1$. Thus, the Poisson ratio can assume values $-1 < \nu < 1/2$ for an isotropic linearly elastic material. ($\nu = 1/2$ corresponds to ideal incompressibility.)

Finally, with Eqs. (1.8), (1.26), and (1.31), we may express the stress as a function of the displacement, the shear modulus, and the Poisson ratio as

$$\sigma_{ij} = \frac{2\mu\nu}{1 - 2\nu}\delta_{ij}\nabla \cdot \mathbf{u} + \mu[\nabla_i u_j + \nabla_j u_i]. \tag{1.32}$$

1.3.4 Navier-Cauchy equations

For an isotropic and infinitely extended medium, the static equilibrium condition in Eq. (1.15) can now be reformulated in terms of the material displacements, using the field $\mathbf{u}$. Moreover, we assume that the elastic medium is homogeneous, i.e., that the elastic parameters ν and μ are constant everywhere. Then,

$$\nabla_j\sigma_{ij} = C_{ijkl}\nabla_j\varepsilon_{kl} = \mu\nabla^2 u_i + \frac{\mu}{1 - 2\nu}\nabla_i\nabla \cdot \mathbf{u}. \tag{1.33}$$

Inserting Eq. (1.33) into Eq. (1.15), and from now on explicitly including the spatial arguments for clarity, we obtain the Navier-Cauchy equations [63],

$$\nabla^2\mathbf{u}(\mathbf{r}) + \frac{1}{1 - 2\nu}\nabla\nabla \cdot \mathbf{u}(\mathbf{r}) = -\frac{1}{\mu}\mathbf{f}_b(\mathbf{r}). \tag{1.34}$$

This representation of the equilibrium condition is of importance because it directly relates the imposed force densities to the local material displacements via the material parameters that determine the elastic properties of the medium. The bulk force density $\mathbf{f}_b(\mathbf{r})$ can, for instance, represent the gravitational field that distorts an elastic solid. Or, it can, e.g., describe an external force acting onto a particulate inclusion and transmitted to the embedding medium. In the experimental systems that are described theoretically later, the displacements of individual particles in the medium represent the decisive measured quantities.

If the considered material is incompressible, i.e., for the limiting case of $\nu = 1/2$, see Sec. 1.3.1, the equations for the displacement field read

$$\nabla \cdot \mathbf{u}(\mathbf{r}) = 0, \tag{1.35}$$

$$\mu \nabla^2 \mathbf{u}(\mathbf{r}) = -\mathbf{f}_b(\mathbf{r}). \tag{1.36}$$

The Navier-Cauchy equations for an incompressible material will become important in the context of our theory for linearly viscoelastic media.

1.3.5 Green's function and particulate inclusions

As stated at the beginning of Sec. 1.3, our goal is to describe the interactions between finite-sized particles in the medium that are displaced and rotated by external forces and torques, respectively. To proceed along these lines, let us first consider one single particle that is embedded in the isotropic, infinitely extended, and homogeneous medium. If this particle is displaced by an external force, it distorts its elastic environment, depending on the geometrical shape of the particle. These distortions created by the displaced particle can be measured at a distance $|\mathbf{r} - \mathbf{r}_0|$ from the particle center, located at $\mathbf{r}_0$. Let us for convenience put $\mathbf{r}_0$ to the origin. Then, we can expect the deformations to decay with increasing distance r from the origin. If r is sufficiently large, every finite-sized particle will appear to be *point-like*, i.e., with increasing distance, the created displacement field will more and more loose the characteristic features that are related to the shape of the displaced particle. (This fact will become important later when we investigate the interactions between finite-sized particles at distances of the order of magnitude of the particle diameters.) Technically, the created displacement far-field is equivalent to that created by a point force

attacking at the origin. We may thus express the bulk force density in Eq. (1.34) by

$$\mathbf{f}_b(\mathbf{r}) = \delta(\mathbf{r})\mathbf{F}, \tag{1.37}$$

with $\mathbf{F}$ quantifying the external force that acts on a point-like particle at the origin and $\delta(\mathbf{r})$ denoting the Dirac delta function. The displacement field $\mathbf{u}(\mathbf{r})$ that solves Eq. (1.34) with Eq. (1.37) inserted can then be expressed in terms of a Green's function,

$$\mathbf{u}(\mathbf{r}) = \underline{\mathbf{G}}(\mathbf{r}) \cdot \mathbf{F}, \tag{1.38}$$

as a consequence of the linearity of the Navier-Cauchy equations. The Green's function $\underline{\mathbf{G}}(\mathbf{r})$ is necessarily a tensor of rank two because the created displacement field may not only vary with the distance r but also with the orientation $\hat{\mathbf{r}}$. A detailed derivation of $\underline{\mathbf{G}}(\mathbf{r})$ is given, e.g., in Appendix A of Publication II. The solution reads [51]

$$\underline{\mathbf{G}}(\mathbf{r}) = \frac{1}{16\pi(1-\nu)\mu r}\left[(3-4\nu)\underline{\hat{\mathbf{I}}} + \hat{\mathbf{r}}\hat{\mathbf{r}}\right]. \tag{1.39}$$

The two material parameters ν and μ have been introduced in Secs. 1.3.1 and 1.3.3, respectively. In general, the Poisson ratio ν describes the compressibility of the material and here also affects the orientation of the field lines. The shear modulus μ quantifies the further resistance to the imposed deformations. Overall, the induced displacement field described by Eqs. (1.38) and (1.39) decays as $1/r$ in magnitude. In Fig. 1.1, the corresponding field lines are plotted for $\nu = 1/2$.

The linearity of Eq. (1.34) allows us to superimpose the displacement fields created by arbitrarily distributed point forces in the medium. We express the result in integral form as

$$\mathbf{u}(\mathbf{r}) = \int_{\mathbb{R}^3} \mathrm{d}^3r' \, \underline{\mathbf{G}}(\mathbf{r} - \mathbf{r}') \cdot \mathbf{f}_b(\mathbf{r}'). \tag{1.40}$$

Here, a possibly continuous distribution of point forces is described by the bulk force density $\mathbf{f}_b(\mathbf{r}')$. This enables us to distribute the point forces on the closed surface ∂V of an imaginary particle of finite size, which is here, for convenience, centered at the origin. Then, $\mathbf{f}_b(\mathbf{r}')$ turns into a surface force density $\mathbf{f}(\mathbf{r})'$ and the volume integral over $\mathbb{R}^3$ becomes an integral over the particle surface ∂V,

$$\mathbf{u}(\mathbf{r}) = \int_{\partial V} \mathrm{d}^2r' \, \underline{\mathbf{G}}(\mathbf{r} - \mathbf{r}') \cdot \mathbf{f}(\mathbf{r}'). \tag{1.41}$$

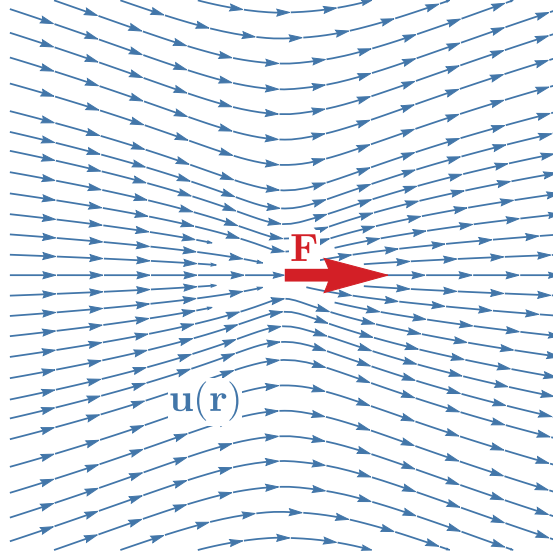In this representation, the material of the particle is thus not distinguished from

Figure 1.1: (a) The displacement field $\mathbf{u}(\mathbf{r})$ created by a point force $\mathbf{F}$ for $\nu = 1/2$, see Eqs. (1.38) and (1.39). (This plot was prepared using Mathematica [64].)

the surrounding elastic environment. Instead, we are dealing with an imaginary particle shell that is displaced according to a continuous force distribution over its surface. This concept of a displaced particle shell is perfectly sufficient to describe the measurable displacement field $\mathbf{u}(\mathbf{r})$ *outside* a finite-sized particle, see also Fig. 1.2. In the following, we always assume that the medium sticks to the particle surface under no-slip conditions.

The kind of particle that we intend to describe is rigid. That means that, irrespectively of the displacements or rotations it undergoes, its geometrical shape always remains unchanged. This situation represents a reasonable approximation for real elastic composite materials, in which the shear modulus inside the particulate inclusions is several orders of magnitude larger than in the enclosing material. In our formalism, the rigidity of the (imaginary) particle *surface* is enforced by a boundary condition, namely

$$\mathbf{u}(\mathbf{r} \in \partial V) = \mathbf{U} + \mathbf{\Omega} \times \mathbf{r}, \tag{1.42}$$

with $\mathbf{U}$ and $\mathbf{\Omega}$ the rigid net displacement and rotation of the particle, respectively. On the right-hand side of Eq. (1.41), the only quantity that can ensure this boundary condition is the surface force density $\mathbf{f}(\mathbf{r}')$. [Another necessary boundary condition, $\mathbf{u}(r \to \infty) = \mathbf{0}$, is automatically satisfied due to the form of $\underline{\mathbf{G}}(\mathbf{r})$, see Eq. (1.39).]
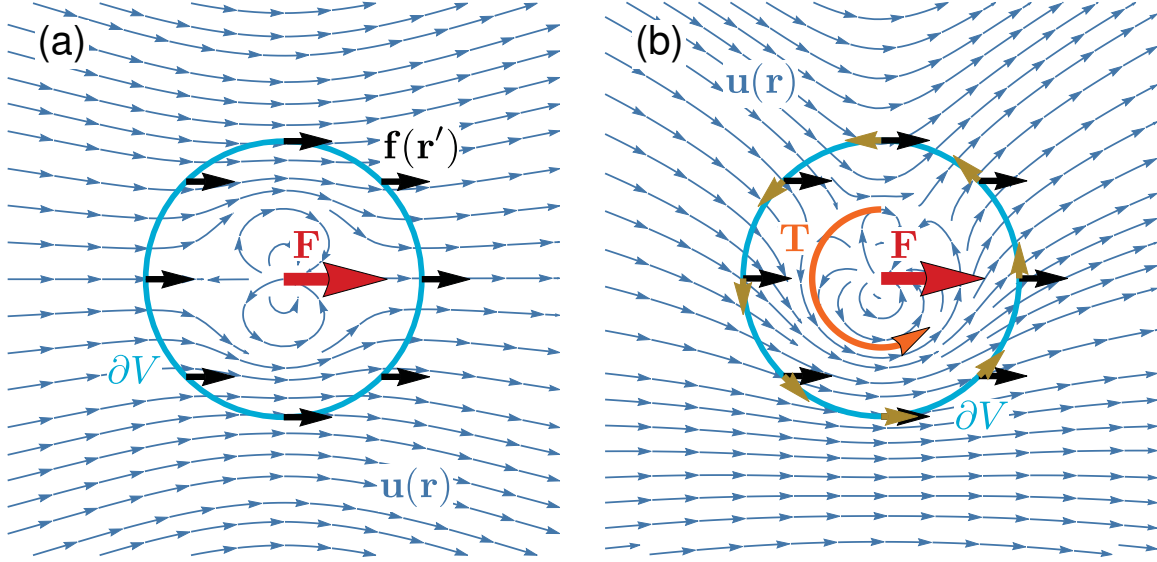
Figure 1.2: (a) Illustration of the displacement field $\mathbf{u}(\mathbf{r})$ created by a continuous distribution of point forces (at some positions indicated by small black arrows) on a spherical surface ∂V according to Eqs. (1.41) and (1.42). The point forces are described by the surface force density $\mathbf{f}(\mathbf{r}')$ (with $\mathbf{r}' \in \partial V$). Here, $\mathbf{f}(\mathbf{r}')$ is constant and thus leads to a rigid displacement of the whole spherical shell. From the outside, the created displacement field is the same as if it were produced by a solid rigid sphere of no-slip surface condition that is uniformly displaced by a constant force $\mathbf{F}$. Clearly, in the vicinity of the spherical shell, effects related to the finite size of the sphere become important, whereas the far field resembles that induced by a point particle, see also Fig. 1.1. (b) The same as in panel (a), but now the force density additionally contains an antisymmetrical contribution (indicated by small ocher arrows), resulting in the superposition of a rigid displacement and rigid rotation of the spherical shell. From the outside, this is equivalent to the effect of a solid rigid sphere that is displaced and rotated by a constant force $\mathbf{F}$ and a constant torque $\mathbf{T}$, respectively. A derivation of the formulae used for panels (a) and (b) is provided in Publication V. (This plot was prepared using Mathematica [64].)

Equation (1.41) may be expanded in $\mathbf{r}'$ as [59]

$$u_i(\mathbf{r}) = \left[F_j - D_{jk}\nabla_k + \frac{1}{2!}M_{jkl}\nabla_k\nabla_l - \frac{1}{3!}N_{jklm}\nabla_k\nabla_l\nabla_m + \ldots \right] G_{ij}(\mathbf{r}), \qquad (1.43)$$

with ! denoting the factorial, and F_j, D_{jk}, M_{jkl}, N_{jklm}, ... constant expansion tensors containing the integral over polyadics of $\mathbf{r}'$ and the force density $\mathbf{f}(\mathbf{r}')$, see also Publication II and Publication V. At larger distances from the particle, the first term of the expansion becomes dominant. This far-field limit is identical to the situation of a point-like particle in the center as given by Eq. (1.38), see also Fig. 1.1. The closer we get to the particle, the more the displacement field is characterized by the specific shape of the particle, see Fig. 1.2. This information is contained in the mentioned expansion tensors beyond $\mathbf{F}$. Equation (1.43) is also called the multipole expansion of the displacement field. It is an important tool that simplifies many calculations and is used (directly or indirectly) throughout all our publications summarized later in this thesis.

So far, a rigid finite-sized particle has been considered that is displaced and/or rotated by an external net force and/or torque, thus creating a characteristic displacement field $\mathbf{u}(\mathbf{r})$ in the medium as specified by Eqs. (1.41) and (1.42). In the complementary situation, there are no external forces and torques acting directly on the sphere. The particle may now be displaced or rotated by a given (arbitrary) deformation field $\mathbf{u}_0(\mathbf{r})$ resulting in the medium from the influence of some other force. $\mathbf{u}_0(\mathbf{r})$ can, e.g., stem from a macroscopic strain applied to the material or a localized disturbance somewhere outside of ∂V. Then, to obtain the displacement and rotation of the particle shell, $\mathbf{u}_0(\mathbf{r} \in \partial V)$ needs to be evaluated. This will in general imply a deformation of the shape. Therefore, if the particle is assumed to be rigid, corrections to the surrounding displacement field will emerge. The effects of these rigidity-induced corrections to the displacement field are described by the higher-order expansion tensors in Eq. (1.43), see Publication II and Publication V. Summarizing, we may thus generalize the boundary condition for a rigid particle from Eq. (1.42) to

$$\mathbf{u}(\mathbf{r}) + \mathbf{u}_0(\mathbf{r}) = \mathbf{U} + \mathbf{\Omega} \times \mathbf{r}, \qquad (1.44)$$

with $\mathbf{r} \in \partial V$, where on the left-hand side the expression in Eq. (1.43) is inserted.

1.3.6 Interacting rigid spherical inclusions

If the surface ∂V of the rigid particle is spherical, the integral in Eq. (1.41) can be calculated analytically [59]. Using the expansion of the displacement field in Eq. (1.43), an explicit approach is presented in Publication V, which we have not found, for instance, in Refs. [59, 65]. From Eq. (1.44) it is possible to calculate the general form of the expansion tensors in Eq. (1.43) as linear functionals of the imposed deformation $\mathbf{u}_0(\mathbf{r})$. These tensors can be referred to as higher-order Faxén laws, following the nomenclature of a similar formalism in low-Reynolds-number hydrodynamics [66–69]. In Publication II and Publication V, we have explicitly calculated the expansion tensors of a rigid sphere, see Eq. (1.43), up to the fourth rank.

Finally, using these results, we can now describe a system consisting of many spherical particles that are distributed at finite distances from each other in an elastic environment. Then, the elastic material serves as a medium of interaction via deformation between the individual spheres. Let us first consider a two-particle system. If sphere i is displaced by an external force $\mathbf{F}_i$, the medium gets distorted and the other sphere j therefore in general experiences a displacement and rotation. However, the rigidity of the sphere j requires the deformation field not to deform its surface in accordance with Eq. (1.44). In turn, this results in a correction to the displacement field of sphere i when compared to the situation in which sphere j is absent. This correction can be understood as an (instantaneous) reflection of the displacement field generated by sphere i due to the rigidity of sphere j. With the same argument, this correction results in another reflection when hitting, after reflection, sphere i, and so on. The associated description in terms of the so-called method of reflections is described in detail in Publication II. As it turns out, the resulting net displacement $\mathbf{U}_i$ and rotation $\mathbf{\Omega}_i$ of the ith sphere can be approximated by an expansion in the inverse interparticle center-to-center distance r_{ij} between the two spheres in the initial, undeformed state. Likewise, external torques $\mathbf{T}_i$ can be included. Generalizing the approach to an N-particle system, we can express $\mathbf{U}_i$ and $\mathbf{\Omega}_i$ as

$$\mathbf{U}_i = \sum_{j=1}^{N} \left[\underline{\mathbf{M}}_{ij}^{\mathrm{tt}} \cdot \mathbf{F}_j + \underline{\mathbf{M}}_{ij}^{\mathrm{tr}} \cdot \mathbf{T}_j \right], \tag{1.45}$$

$$\mathbf{\Omega}_i = \sum_{j=1}^{N} \left[\underline{\mathbf{M}}_{ij}^{\mathrm{rt}} \cdot \mathbf{F}_j + \underline{\mathbf{M}}_{ij}^{\mathrm{rr}} \cdot \mathbf{T}_j \right]. \tag{1.46}$$

Here, all elastic interactions have been summarized in the mathematical matrices $\underline{\mathbf{M}}_{ij}^{\mathrm{tt}}$,

$\underline{\mathbf{M}}_{ij}^{\mathrm{tr}}$, $\underline{\mathbf{M}}_{ij}^{\mathrm{rt}}$, and $\underline{\mathbf{M}}_{ij}^{\mathrm{rr}}$, which we have termed *displaceability* and *rotateability* matrices. In Publication II and Publication V, we have calculated these matrices up to fourth and sixth orders in the inverse interparticle distances, respectively. We used them successfully to describe results from measurements on experimental example configurations in gel-like environments with initial center-to-center interparticle distances of about two to three particle diameters in Publication I and of about 3.5 particle radii in Publication III. In Publication III, we have connected our displaceability matrices to a simplified elastic spring model. Moreover, the limits of our linearly elastic approach have been investigated in Publication III as well. A brief overview is presented in the next section.

1.4 Description of interactions between magnetic particles in soft elastic gels

In Publication I and Publication III, the theory was employed to perform a quantitative analysis of experimental data. The experiments were conducted using paramagnetic nickel particles that were embedded in a soft polymeric gel. Details concerning the experimental set-ups are provided in the mentioned papers.

In the theoretical analysis, the elastic material was assumed to be homogeneous and incompressible, hence we set $\nu = 1/2$. Moreover, the carefully selected paramagnetic particles to good approximation were rigid, spherical, and of equal size within each system. Due to their comparatively large size, their thermal fluctuations were neglected. The center-to-center distance in the initial undeformed state between each two particles amounted to two to three particle diameters in Publication I (in the system considered in the supplemental material of Publication I, the distances were larger) and to about 3.5 radii in Publication III. The particles were located far from any boundaries of the respective experimental samples. Compared to the dimensions of the experimental samples, the particle diameters were small, thus justifying the assumption of an infinitely extended embedding medium. Besides homogeneity, also isotropy of the medium was assumed.

By means of a locally homogeneous external magnetic field, magnetic moments were induced in the paramagnetic particles, resulting in magnetic interaction forces. These forces caused measurable particle displacements and thus local distortions of the elastic material. When the external magnetic field was switched off, the particles lost their magnetization and returned to their initial positions, i.e., the displacements

were fully reversible within the experimental resolution. The magnetization of the magnetic particles as a function of the applied external field was determined from an experimental magnetization curve that is plotted in Publication III, thus allowing for the quantitative determination of the magnetic moments and interparticle forces. Finally, as a consequence of the way the experimental samples were prepared (described in Publication I and Publication III), it was impossible to directly measure in a macrorheological experiment the shear moduli for the elastic medium surrounding the magnetic particles in the different samples. Thus, our theoretical approach was employed to extract these moduli by fitting the theoretical curves for the particle displacements to the experimentally measured ones.

Throughout all our publications referred to in this thesis, the magnetic moments of spherical inclusions were approximated by point dipoles, corresponding to the lowest-order term in an underlying multipole expansion [70]. The finite extension of the magnetic material was thus not resolved. For the interparticle distances considered here, this assumption appears to be justified, as long as the interparticle distances after the induced displacements remain large enough compared to the particle dimensions. In Publication I, strong external magnetic fields were applied, resulting in virtual magnetic saturation. That is, the magnetization and hence the magnetic moment of a magnetizable particle cannot be increased any further by exposing it to stronger fields. In our context, the presence of other localized magnetic moments, i.e., the dipole moments of the other particles, did therefore not change the magnitude of the magnetic moment of any considered particle. Moreover, all dipole moments were assumed to be oriented by the dominant external magnetic field, i.e., the moments of the particles were constant in magnitude and fixed in orientation. Furthermore, since the considered particles were assumed to be identical, the same applies to their magnetic moments. We thus denote the orientation of the dipole moment of any particle by $\hat{\mathbf{m}}$ and its magnitude by m. The magnetic force on the ith particle ($i = 1, \ldots, N$) is then given by [70]

$$\mathbf{F}_i = -\frac{3\mu_0 m^2}{4\pi} \sum_{\substack{j=1 \\ j \neq i}}^{N} \frac{5\hat{\mathbf{r}}_{ij}(\hat{\mathbf{m}} \cdot \hat{\mathbf{r}}_{ij})^2 - \hat{\mathbf{r}}_{ij} - 2\hat{\mathbf{m}}(\hat{\mathbf{m}} \cdot \hat{\mathbf{r}}_{ij})}{r_{ij}^4}, \tag{1.47}$$

with μ_0 the vacuum permeability, $\mathbf{r}_{ij} = \mathbf{r}_i - \mathbf{r}_j$, and $\mathbf{r}_i$ the position of the ith dipole (and thus the center of the ith sphere). Obviously, the magnetic interaction forces exhibit a dependence on the interparticle distances r_{ij} and will therefore in general
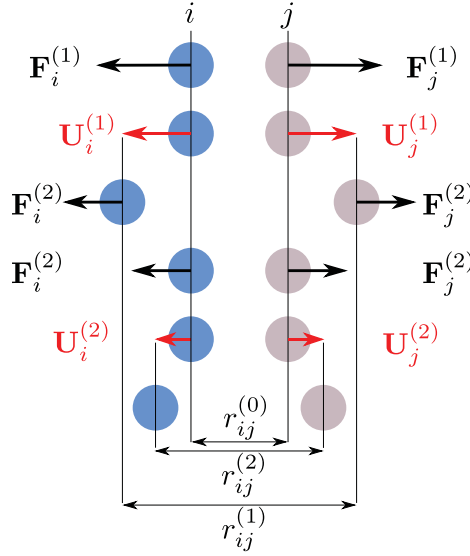
Figure 1.3: A sketch illustrating the numerical scheme to determine the magnetic dipole forces and displacements for two spherical particles in an elastic environment. From top to bottom, the individual steps are depicted. In the first step (top line), the magnetic forces $\mathbf{F}_i^{(1)}$ and $\mathbf{F}_j^{(1)}$ on particles i and j, respectively, are calculated from the initial distance $r_{ij}^{(0)}$. Using the displaceability matrix $\underline{\mathbf{M}}_{ij}^{\text{tt}}$ in Eq. (1.45), the particle displacements $\mathbf{U}_i^{(1)}$ and $\mathbf{U}_j^{(1)}$ are obtained (second line), resulting in a new interparticle distance $r_{ij}^{(1)}$ (third line). In the next step, $r_{ij}^{(1)}$ is used to compute the magnetic forces $\mathbf{F}_i^{(2)}$ and $\mathbf{F}_j^{(2)}$ (third line). $\mathbf{F}_i^{(2)}$ and $\mathbf{F}_j^{(2)}$ are then reinserted into Eq. (1.45) (fourth and fifth line) to calculate the new distance $r_{ij}^{(2)}$ (bottom line), and so on. (To evaluate $\underline{\mathbf{M}}_{ij}^{\text{tt}}$, which depends on the particle configuration as well, always the initial distance $r_{ij}^{(0)}$ is used, otherwise elastic memory would not be conserved.)

change during particle displacements. The actual forces in the steady deformed state that are balanced by the elastic restoring forces are therefore determined by the final interparticle distances *after* displacement. To determine the resulting displacements and magnetic forces in the theoretical description, a numerical loop was employed, which is illustrated in Fig. 1.3 for a two-particle system. This scheme proved to converge quickly for the particle configurations considered in Publication I and Publication III. With this necessary refinement, we found very good agreement between the experimentally measured and theoretically calculated particle displacements for three different sample configurations in Publication I and for one additional in the related supplemental material.

In Publication III, a configuration of two identical particles is considered, labeled by 1 and 2, that were exposed to a non-saturating external magnetic field. The induced magnetic moments were oriented parallel to the center-to-center distance r_{12}, resulting in attractive forces $\mathbf{F}_1 = -\mathbf{F}_2$ between them due to symmetry. Stepwise increasing the external magnetic field, the particles approached each other more and more with every increment. The measured displacements in this regime could still to good approximation be described by linear elasticity theory. At some point, however, the particles suddenly snapped into contact. After the field was switched off, they returned to their initial positions in the undeformed state, i.e., the process was fully reversible within the experimental resolution. These final displacements towards contact amounted in total to more than one radius, which is thus well beyond the range of linear elasticity theory. Hence, this experiment presented an ideal test configuration for the limits of our linearly elastic approach. Moreover, since the external magnetic field did not yield magnetic saturation of the particles, Eq. (1.47) alone did not provide an adequate description of the magnetic dipole-dipole forces. Instead, the particles mutually magnetized each other in a nonlinear procedure and they did so even more the closer they approached. The technical details for a corresponding iterative description in terms of point dipoles are given in Publication III.

While the dipolar approximation is justified at larger particle separation distances, it loses its justification when the particles strongly approach each other. The magnetization then becomes quite inhomogeneous across the volume of each sphere. For a more accurate description of both the nonlinear elastic processes as well as the spatially resolved internal magnetization of the spheres, detailed finite-element (FE) simulations were performed. This allowed for a direct comparison between the different approaches as well as to the experimental results.

Altogether, we found a very good agreement between the different approaches in the well-separated state before the collapse into the state of virtual touching of the two particles. The exact field magnitude at which the spheres snapped into contact could not be determined experimentally. However, our theoretically obtained value was confirmed to good approximation by the FE simulations.

An additional interesting effect predicted theoretically and from the simulations could not yet be confirmed experimentally due to technical limitations. Once the particles are in the collapsed state, their mutual magnetization is strong enough to withstand the elastic restoring forces, even if the external magnetic field is reduced in magnitude to some degree below the magnitude at which the collapse occurred.

Thus, magnetization and subsequent demagnetization of the sample reveals hysteretic behavior. Finally, the symmetry of this specific configuration with respect to one axis allowed us to map our quantitative theory onto reduced dipole-spring models. In these models, the two point dipoles are connected by harmonic springs to each other and to their environment. The spring constants could then be determined by inverting the displaceability matrices. As an advantage of this picture, the elastic energy of the system can be expressed in a very simple way. Using the resulting forms of the total energy of the system, a further analysis of the mentioned hysteretic behavior was performed.

In the analysis of the experimental systems mentioned above, we concentrated on particle displacements. To illustrate the effects of additional rotational couplings as well, see Eqs. (1.45) and (1.46), exemplary situations involving external torques $\mathbf{T}_i$ ($i = 1, 2, \ldots, N$) as well were presented in Publication II and Publication V. If a magnetizable particle is magnetically anisotropic, it will in general rotate when exposed to an external magnetic field in order to align its magnetic moment with the external field. The simplest case is given by uniaxial magnetic anisotropy. Then, the magnetically generated torques $\mathbf{T}_i$ can frequently be modeled using the idealized Stoner-Wohlfarth picture [10, 71]. Different effects of the possible compressibility of the surrounding medium on the displacements and rotations of interacting magnetic spheres are demonstrated in Publication V.

More specifically, in Publication II, the displaceability and rotateability matrices were calculated up to (including) fourth order in the inverse interparticle distances. In Publication V, we extended these results up to (including) sixth order, allowing for a better quantitative description of particle interactions at small distances. Concerning the rotational behavior of the spheres, it is noteworthy that the Poisson ratio ν enters the $\underline{\mathbf{M}}_{ij}^{\mathrm{tr}}$-, $\underline{\mathbf{M}}_{ij}^{\mathrm{rt}}$-, and $\underline{\mathbf{M}}_{ij}^{\mathrm{rr}}$-matrices in Eqs. (1.45) and (1.46) only beyond the fourth order. Moreover, "reflections" of torque-induced displacement fields to the corresponding initiators also start beyond the fourth order. Furthermore, it was found that the overall effect of the compressibility of the medium on the individual particle displacements $\mathbf{U}_i$ and rotations $\mathbf{\Omega}_i$ in Eq. (1.46) can be split into two separate effects. First, in a compressible medium, i.e., for $\nu < 1/2$, already the displacement of an isolated sphere due to an external force is larger when compared to the same situation in an incompressible medium. If two or more particles are considered, the distance-dependent magnetic dipole forces $\mathbf{F}_i$ (calculated from the end distances, see above) can due to the larger displacements of the individual spheres in total lead to

significantly altered particle displacements. Then, the mutual interactions via the embedding medium also have a stronger impact on $\mathbf{U}_i$ and $\mathbf{\Omega}_i$ (described by the $\underline{\mathbf{M}}_{ij}^{\mathrm{tt}}$- and $\underline{\mathbf{M}}_{ij}^{\mathrm{rt}}$-matrices in Eqs. (1.45) and (1.46)). Second, the compressibility of the medium enters the $\underline{\mathbf{M}}_{ij}^{\mathrm{tr}}$-, $\underline{\mathbf{M}}_{ij}^{\mathrm{rt}}$- and $\underline{\mathbf{M}}_{ij}^{\mathrm{rr}}$-matrices directly at the fifth or sixth order.

In our examples, we have found that, if two nearby rigid magnetic particles are simultaneously displaced and rotated by magnetic forces and torques, respectively, the direct magnetic torque $\mathbf{T}_i$, even if weak (yielding particle rotations $|\mathbf{\Omega}_i| \lesssim 5°$), clearly dominates the rotational behavior of the ith sphere, whereas the higher-order contributions resulting from particle interactions are masked by these large direct contributions. However, the situation is different, if torques act only on some of the spheres and no direct forces are imposed (e.g., in a two-particle system, in which one particle is subject to an externally imposed torque but the other is not). Then, the higher-order contributions become increasingly relevant for center-to-center distances of less than about three particle radii [72]. Overall, the effect of the higher-order contributions in Publication V becomes particularly noticeable, if the medium is (nearly) incompressible, i.e., for $\nu \to 1/2$, which often is the case for polymeric gels [72], see also Publication I and Publication III.

1.5 Dynamics of particulate inclusions in linearly viscoelastic media

Finally, we briefly introduce a dynamic theory of linearly viscoelastic media containing particulate inclusions as presented in Publication IV, building on the results of our previous works. A viscoelastic material exhibits both viscous and elastic properties. So far, we have discussed interacting finite-sized particulate inclusions in the framework of linear elasticity theory. There, material deformations are described in terms of the displacement field $\mathbf{u}(\mathbf{r})$. Moreover, the properties of the isotropic, homogeneous, and infinitely extended elastic medium are uniquely determined by two material parameters, for instance, the shear modulus μ and the Poisson ratio ν, see Sec. 1.3.3. There exists an analogue to low-Reynolds-number or creeping flow hydrodynamics, where the interactions of colloidal particles in an isotropic, homogeneous, and unbounded viscous fluid are described for incompressible fluid flow [69, 73, 74].

In hydrodynamics, the fluid flow is described by a velocity field $\mathbf{v} = \mathbf{v}(\mathbf{r}, t)$ defined at every point $\mathbf{r}$ and time t [75]. Moreover, we introduce the mass density field $\rho = \rho(\mathbf{r}, t)$. The amount of fluid mass per time that flows through the surface element

dS oriented by the (outward) normal vector $\hat{\mathbf{n}}$ is then given by $\rho\mathbf{v} \cdot \hat{\mathbf{n}}\mathrm{d}S$, where for better readability, arguments $\mathbf{r}$ and t are not written explicitly any longer. Let us next consider a volume V that is fixed in space and enclosed by the surface ∂V. In this case, the conservation of mass can be written in the form [75]

$$\frac{\mathrm{d}}{\mathrm{d}t} \int_V \mathrm{d}V \; \rho = - \int_{\partial V} \mathrm{d}S \; \rho\mathbf{v} \cdot \hat{\mathbf{n}}, \tag{1.48}$$

i.e., an increase in the total mass in V is equal to the net mass influx into V through the enclosing surface ∂V (hence the negative sign as $\hat{\mathbf{n}}$ is pointing outward), and vice versa for a decrease in the total mass in V. The surface integral on the right-hand side can be transformed into a volume integral using Gauss's theorem. Moreover, since V is arbitrary, this equation must also hold locally, i.e.,

$$\frac{\partial \rho}{\partial t} + \nabla \cdot (\rho\mathbf{v}) = 0. \tag{1.49}$$

Equation (1.49) is referred to as the *continuity equation.*

As a measure of relative motion, we introduce the (linear) rate-of-strain tensor

$$\varepsilon_{ij}^h = \frac{1}{2}[\nabla_i v_j + \nabla_j v_i] \tag{1.50}$$

in analogy to the elastic strain tensor, see Eq. (1.8). Relative motion of nearby fluid elements results in friction. The forces that adjacent regions of the fluid exert onto each other due to friction can therefore be expressed by a viscous stress tensor σ_{ij}^h in analogy to the elastic case, see Sec. 1.3.2. The viscous stress and rate of strain can be linearly related to each other via a material tensor similar to Eq. (1.21). Assuming isotropy, only two parameters determine the behavior of the medium, see also Sec. 1.3.3. Then,

$$\sigma_{ij}^h = \left(\zeta - \frac{2}{3}\eta\right) \delta_{ij}\varepsilon_{ll}^h + 2\eta\varepsilon_{ij}^h, \tag{1.51}$$

with ζ being a constant that is related to the rate of change of the local volume, and η often referred to as *shear viscosity.* σ_{ij}^h has the units of pressure. ζ and η play a role analogous to the elastic bulk modulus K and shear modulus μ, respectively.

Even if $\mathbf{v} = \mathbf{0}$, there still exists a hydrostatic pressure field p in the fluid [75], which obviously is not directly included by the first term on the right-hand side of Eq. (1.51). In general, the pressure can contribute to fluid flows, if it varies in space. Therefore, we take into account the additional force that is exerted by the surrounding fluid onto

an enclosed volume V via its surface ∂V,

$$-\int_{\partial V} \mathrm{d}S\, \hat{\mathbf{n}}p = -\int_V \mathrm{d}V\, \nabla p. \tag{1.52}$$

Locally, this is equivalent to a force density $-\nabla p$.

Here, we restrict ourselves to creeping-flow hydrodynamics, for which the dynamics is overdamped and time derivatives of the momentum of the fluid elements can be neglected. In analogy to Eq. (1.15), the local balance of all force densities reads

$$-\nabla_i p + \nabla_j \sigma_{ij}^h + f_{b,i} = 0, \tag{1.53}$$

with $\mathbf{f}_b$ an additional bulk force density (e.g., due to gravity). Moreover, we assume an incompressible and homogeneous fluid. For an incompressible fluid, the mass density ρ is constant as well and Eq. (1.49) simplifies to

$$\nabla \cdot \mathbf{v} = 0. \tag{1.54}$$

Then, the only remaining material parameter is η. (More precisely, Eq. (1.54) also holds for volume-preserving *flows*, for which the fluid does not necessarily need to be incompressible. However, for typical liquids [75] as well as for many aqueous polymer solutions [53, 54] and polymeric gels, see Publication I and Publication III, incompressibility of the medium itself is often a reasonable assumption. Volume-preserving flow requires that the mass density of any moving material element remains constant, whereas strict incompressibility means that ρ is constant everywhere and at all times, no matter which influences the material is exposed to. Formally, there is no difference for the continuity equation. We will assume incompressibility also for the elastic contribution to the description of a viscoelastic material, see below.) Inserting Eqs. (1.50), (1.51), and (1.54) into Eq. (1.53), we obtain the Stokes equations [75, 76],

$$\eta \nabla^2 \mathbf{v}(\mathbf{r}, t) = \nabla p(\mathbf{r}, t) - \mathbf{f}_b(\mathbf{r}, t), \tag{1.55}$$

where we now have written out again the arguments $\mathbf{r}$ and t for clarity in what follows. Obviously, Eqs. (1.54) and (1.55) are direct formal equivalents to Eqs. (1.35) and (1.36), respectively.

In Publication IV, Eqs. (1.36) and (1.55) are combined into one single equation describing an infinitely extended, isotropic, homogeneous, and incompressible linearly

viscoelastic material,

$$\mu\nabla^2\mathbf{u}(\mathbf{r},t) + \eta\nabla^2\mathbf{v}(\mathbf{r},t) = \nabla p(\mathbf{r},t) - \mathbf{f}_b(\mathbf{r},t), \tag{1.56}$$

now introducing the time t to the displacement field. Here, $\mathbf{v}(\mathbf{r},t)$ quantifies the actual material transport, whereas $\mathbf{u}(\mathbf{r},t)$ describes at time t to which position a given material element at position $\mathbf{r}$ would tend to relax back, when all external loads are removed. $\mathbf{u}(\mathbf{r},t)$ is therefore connected to the memory of the individual material elements in the continuous environment. Since viscoelasticity implies partial loss of memory, there must be a corresponding loss or decay term in the memory field. A simple linear choice reads

$$\dot{\mathbf{u}}(\mathbf{r},t) = \mathbf{v}(\mathbf{r},t) - \gamma\mathbf{u}(\mathbf{r},t), \tag{1.57}$$

with γ denoting the *relaxation rate* of the medium.

For a purely elastic material, the relaxation time $1/\gamma$ approaches infinity. In this case, Eq. (1.57) reduces to $\dot{\mathbf{u}}(\mathbf{r},t) = \mathbf{v}(\mathbf{r},t)$, thus describing the reversible dynamics of a solid. Contrary, in a purely viscous fluid environment, there is basically no memory. Hence, the relaxation time $1/\gamma$ is infinitesimally small, so that the velocity field at a certain time t is not directly affected by the velocity fields at earlier times. A finite but nonzero γ marks the intermediate viscoelastic regime.

In Publication IV, we demonstrated that the correct limits of both linear elasticity and low-Reynolds-number hydrodynamics can be recovered from Eqs. (1.56) and (1.57) in these limits. These equations constitute our continuum theory of linearly viscoelastic media, together with the incompressibility conditions $\nabla \cdot \mathbf{u}(\mathbf{r},t) = 0$ and $\nabla \cdot \mathbf{v}(\mathbf{r},t) = 0$. As is shown in Appendix A of Publication IV, this set of equations is not arbitrary but can be derived from a general continuum approach [52]. Moreover, we addressed the corresponding Kramers-Kronig relations, see Appendix C in Publication IV.

In analogy to what was summarized in Sec. 1.3.5, the displacement field induced in the viscoelastic medium by a concentrated point force impact $\mathbf{F}$ that attacks the medium at position $\mathbf{r}_0$ and time t_0 can be expressed in terms of a Green's function,

$$\mathbf{u}(\mathbf{r},t) = \underline{\mathbf{G}}(\mathbf{r} - \mathbf{r}_0, t - t_0) \cdot \mathbf{F}. \tag{1.58}$$

As a direct consequence, the dynamic behavior of embedded particulate inclusions

and interactions between them via the viscoelastic medium can be described in a way similar to Secs. 1.3.5 and 1.3.6, however, generally not in closed form because of time dependencies. In Publication IV, some selected examples illustrate the dynamics of such particles in viscoelastic surroundings. First, a rigid sphere is considered that is dragged during a certain time interval by a constant external force. Thereafter, the force is switched off. The characteristic relaxational dynamics of the dragged sphere in the elastic and hydrodynamic limits as well as in the intermediate viscoelastic regime are illustratively demonstrated. Next, matrix-mediated interactions between two spherical paramagnetic particles when magnetized from a certain time on by an external magnetic field are evaluated, again for different degrees of viscoelastic memory. After the magnetic field is switched off, the particles relax into their corresponding equilibrium positions, which depend on the memory of the viscoelastic medium. In this case, we have, for instance, found that the paths of the individual particles during the states of magnetization and subsequent relaxation can be different, depending on the initial spatial particle configuration. Finally, we briefly touched the field of self-propelled active microswimmers in a viscoelastic environment, based on a recently derived minimal swimmer model for low-Reynolds-number hydrodynamics [77]. In this model, two species of self-propelled swimmers are distinguished, namely pusher- and puller-like swimmers [77]. Both propel by setting the surrounding fluid into motion. While pushers proceed by pushing out fluid into opposite directions along one axis, pullers draw it inward by inducing inverted flow fields. In a purely hydrodynamic environment, these pushers and pullers have the same steady-state swimming speed. We have found that in a viscoelastic environment with a finite relaxation rate γ this is not the case. A quantitative description thereof as well as an illustrative explanation is given in Publication IV.

2 Publications

Publication I

Forces on rigid inclusions in elastic media and resulting matrix-mediated interactions

Author's contributions

All authors contributed to the work. My contribution to this work partially overlaps with earlier results from my master thesis. There, the displaceability matrices up to (including) fourth order in inverse interparticle distance had already been calculated. It had also already been applied to preliminary experimental data in the master thesis. However, for this publication, new experimental data were used and our theoretical analysis was improved considerably. The part of my work in this publication attributable to the present dissertation involves a detailed error analysis, the numerical implementation of a refined method for calculating the induced forces, as well as fitting the theoretical displacement curves to the experimental data and determining the local shear moduli in the experimental samples. I estimate my overall contribution to this publication attributable to the framework of the present dissertation to approximately 40%.

Copyright and license notice

ℭ

Forces on Rigid Inclusions in Elastic Media and Resulting Matrix-Mediated Interactions

Mate Puljiz,[1,*] Shilin Huang,[2,†] Günter K. Auernhammer,[2,‡] and Andreas M. Menzel[1,§]

[1]*Institut für Theoretische Physik II: Weiche Materie, Heinrich-Heine-Universität Düsseldorf, D-40225 Düsseldorf, Germany*
[2]*Max Planck Institute for Polymer Research, Ackermannweg 10, 55128 Mainz, Germany*

To describe many-particle systems suspended in incompressible low-Reynolds-number *fluids*, effective hydrodynamic interactions can be introduced. Here, we consider particles embedded in *elastic* media. The effective elastic interactions between spherical particles are calculated analytically, inspired by the approach in the fluid case. Our experiments on interacting magnetic particles confirm the theory. In view of the huge success of the method in hydrodynamics, we similarly expect many future applications in the elastic case, e.g., for elastic composite materials.

Hydrodynamics determines our daily life. Examples are given by the flow of air into our lungs [1], drinking of beverages and digestive processes [2], technical applications such as microfluidic devices [3], or shape optimization of planes, vehicles, ships, and propellers [4]. All these processes are described by the Navier-Stokes equations [5] or variants thereof. This set of equations typically poses significant challenges during solution due to a convective nonlinearity reflecting inertial effects. Basically, turbulence is driven by the inertial term. It often renders analytical solutions impossible.

The situation changes for small dimensions and velocities or high viscosity. Then, the relative strength of inertial effects, measured by the Reynolds number, is low. The nonlinearity can be neglected. A Green's function in terms of the so-called Oseen matrix is then available, which formally solves the problem analytically [6,7]. In this way, semidilute colloidal suspensions, i.e., the dispersion of nano- to micrometer-sized particles in a fluid [7,8], or microswimmer suspensions [9] are described effectively. The explicit role of the fluid is eliminated and replaced by effective hydrodynamic interactions between the suspended particles [6,7].

Despite the success of this theoretical approach for colloidal suspensions, hardly any investigations consider a surrounding elastic solid instead of a suspending fluid. This is surprising, since, as we show below, the formalism can be adapted straightforwardly to linearly elastic matrices and is confirmed by our experiments. Our approach will, for instance, facilitate describing the response of elastic composite materials to external stimuli. Such materials consist of more or less rigid inclusions embedded in an elastic matrix. They are of growing technological interest and may serve, e.g., as soft actuators or sound attenuation devices [10].

In previous theoretical studies, the physics of one single rigid or deformable inclusion was addressed [11,12], also under acoustic irradiation [13]. For more than a single

inclusion, mainly the so-called load problem was analyzed theoretically for a pair of rigid inclusions: One prescribes displacements of two rigid inclusions in an elastic matrix and then determines the forces necessary to achieve these given displacements [14].

Here, we take the converse point of view, based on the cause-and-effect chain in our experiments: External forces are imposed onto the inclusions, or mutual forces between the inclusions are induced, for example, to actuate the material or to tune its properties. In response to the forces, the inclusions are displaced. Since they cannot penetrate through the surrounding elastic matrix, they transmit the forces to the matrix and distort it. Such distortions lead to mutual long-ranged interactions between the inclusions, in analogy to hydrodynamic interactions in colloidal suspensions [6,7,15].

We present a basic derivation of analytical expressions for these interactions from the underlying elasticity equations. Then, we verify the theory by experiments on rigid paramagnetic particles embedded in soft elastic matrices. Mutual particle interactions are induced by an external magnetic field. As we demonstrate, theory and experiment are in good agreement and also allow for microrheological measurements [16].

For simplicity, we assume a homogeneous, isotropic, infinitely extended elastic matrix and low-amplitude deformations. Applying a bulk force density $\mathbf{f}_b(\mathbf{r})$ to the matrix, its equilibrated state satisfies the linear elastostatic Navier-Cauchy equations [17]:

$$\nabla^2 \mathbf{u}(\mathbf{r}) + \frac{1}{1-2\nu}\nabla\nabla\cdot\mathbf{u}(\mathbf{r}) = -\frac{1}{\mu}\mathbf{f}_b(\mathbf{r}). \qquad (1)$$

This is the elastic analogue to the linearized Stokes equation in low-Reynolds-number hydrodynamics [7]. Instead of velocities, $\mathbf{u}(\mathbf{r})$ here denotes the displacement field, describing the reversible relocations of the volume elements from their initial positions during deformations. μ is the shear modulus of the matrix and ν its Poisson ratio, connected to its compressibility [18]. We consider an incompressible matrix, i.e., $\nabla\cdot\mathbf{u}(\mathbf{r}) = 0$ along with
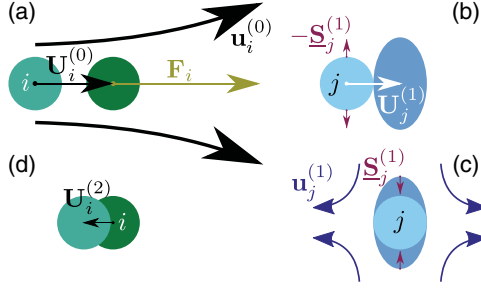
FIG. 1. Illustration of the reflection of a displacement field $\mathbf{u}_i^{(0)}$ induced by (a) the force $\mathbf{F}_i$ that displaces particle i by $\mathbf{U}_i^{(0)}$. (b) Because of $\mathbf{u}_i^{(0)}$, particle j gets displaced by $\mathbf{U}_j^{(1)}$ and would be distorted as described by a stresslet $-\underline{\mathbf{S}}_j^{(1)}$ (rotations $\mathbf{\Omega}_j^{(1)}$ not depicted for simplicity). (c) However, particle j is rigid and resists deformation, expressed by a counteracting stresslet $\underline{\mathbf{S}}_j^{(1)}$, which results in a displacement field $\mathbf{u}_j^{(1)}$. (d) The reflected $\mathbf{u}_i^{(0)}$, i.e., $\mathbf{u}_j^{(1)}$, displaces particle i by $\mathbf{U}_i^{(2)}$.

$\nu = 0.5$. Yet, in contrast to the hydrodynamic case, also compressible elastic systems are readily addressed, and we present the corresponding expressions in the Supplemental Material [19].

Importantly, for a point force density $\mathbf{f}_b(\mathbf{r}) = \mathbf{F}\delta(\mathbf{r})$ acting on the matrix, the resulting deformation field can be calculated analytically from Eq. (1) via Fourier transform as $\mathbf{u}(\mathbf{r}) = \underline{\mathbf{G}}(\mathbf{r}) \cdot \mathbf{F}$. Here,

$$\underline{\mathbf{G}}(\mathbf{r}) = \frac{1}{8\pi\mu}\left(\frac{1}{r}\hat{\underline{\mathbf{I}}} + \frac{\mathbf{rr}}{r^3}\right) \qquad (2)$$

is the corresponding Green's function [18], $\hat{\underline{\mathbf{I}}}$ is the identity matrix, $r = |\mathbf{r}|$, and the underscore marks second-rank tensors and matrices. Still, it is practically impossible to explicitly solve Eq. (1) analytically in the presence of several rigid embedded particles of finite size. An iterative procedure resolves this problem; see Fig. 1.

We consider N rigid spherical particles of radius a, with no-slip boundary conditions on their surfaces. First we address only the ith particle at position $\mathbf{r}_i$, subject to an external force $\mathbf{F}_i$. The embedded particle transmits this force to the surrounding matrix and induces a displacement field

$$\mathbf{u}_i^{(0)}(\mathbf{r}) = \left(1 + \frac{a^2}{6}\nabla^2\right)\underline{\mathbf{G}}(\mathbf{r} - \mathbf{r}_i) \cdot \mathbf{F}_i. \qquad (3)$$

This field is the elastic analogue of hydrodynamic Stokes flow [6,7], for elastic media. Inserting Eq. (2) reproduces a corresponding expression in Ref. [12]. Equation (3) is confirmed as it satisfies Eq. (1), shows the correct limit $\mathbf{u}_i^{(0)}(\mathbf{r}) = \underline{\mathbf{G}}(\mathbf{r} - \mathbf{r}_i) \cdot \mathbf{F}_i$ for $|\mathbf{r} - \mathbf{r}_i| > a$ when $a \to 0$, and for $|\mathbf{r} - \mathbf{r}_i| = a$ is constant on the particle surface. Thus, Eq. (3) for $|\mathbf{r} - \mathbf{r}_i| = a$ reveals the rigid displacement

$$\mathbf{U}_i^{(0)} = \mathbf{u}_i^{(0)}(|\mathbf{r} - \mathbf{r}_i| = a) = \frac{1}{6\pi\mu a}\mathbf{F}_i \qquad (4)$$

of the ith particle in response to $\mathbf{F}_i$ in accord with the no-slip conditions at $|\mathbf{r} - \mathbf{r}_i| = a$.

To find the effective elastic interactions between particles i and j ($j \neq i$), we take the induced displacement field $\mathbf{u}_i^{(0)}(\mathbf{r})$ as given. We need to determine how particle j reacts to the imposed field $\mathbf{u}_i^{(0)}(\mathbf{r})$. In general, particle j can be rigidly translated by a displacement vector $\mathbf{U}_j^{(1)}$ and rigidly rotated by a rotation vector $\mathbf{\Omega}_j^{(1)}$. Taking into account the no-slip conditions on the surface ∂V_j of the jth particle, the equality

$$\mathbf{U}_j^{(1)} + \mathbf{\Omega}_j^{(1)} \times (\mathbf{r} - \mathbf{r}_j)$$
$$= \mathbf{u}_i^{(0)}(\mathbf{r}) + \int_{\partial V_j} \underline{\mathbf{G}}(\mathbf{r} - \mathbf{r}') \cdot \mathbf{f}(\mathbf{r}')dS' \qquad (5)$$

must hold for all $\mathbf{r} \in \partial V_j$. That is, the rigid displacement of each point on the surface shell of particle j (lhs) must equal the displacement field in the matrix at the same point (rhs). The latter is given by the imposed displacement field, here $\mathbf{u}_i^{(0)}(\mathbf{r})$, plus the deformation that the particle surface itself induces in the matrix, i.e., the integral term. Also an externally imposed global displacement field could be included (on the rhs). $\mathbf{f}(\mathbf{r}')$ describes the surface force density exerted by the surface of particle j onto the matrix.

Such an embedded particle will translate and rotate as dictated by the surrounding matrix. We obtain the expression for $\mathbf{U}_j^{(1)}$ by integrating Eq. (5) over ∂V_j. Similarly, for $\mathbf{\Omega}_j^{(1)}$, Eq. (5) is multiplied dyadically by $\mathbf{r} - \mathbf{r}_j$, and after integration over ∂V_j the antisymmetric part is extracted. To perform the calculation, $\mathbf{u}_i^{(0)}(\mathbf{r})$ is Taylor expanded around $\mathbf{r}_j$. Moreover, we use that Eq. (1) for $\mathbf{r} \notin \partial V_i$ leads to $\nabla^4 \mathbf{u}_i^{(0)}(\mathbf{r}) = \mathbf{0}$ and $\nabla \times \nabla^2 \mathbf{u}_i^{(0)}(\mathbf{r}) = \mathbf{0}$. The last term in Eq. (5) vanishes at this stage, as no total net external force or torque is applied to particle j at the present step of iteration. In the end, we recover the elastic analogues of the hydrodynamic [6,7,20] Faxén laws:

$$\mathbf{U}_j^{(1)} = \left(1 + \frac{a^2}{6}\nabla^2\right)\mathbf{u}_i^{(0)}(\mathbf{r})\bigg|_{\mathbf{r}=\mathbf{r}_j}, \qquad (6)$$

$$\mathbf{\Omega}_j^{(1)} = \frac{1}{2}\nabla \times \mathbf{u}_i^{(0)}(\mathbf{r})\bigg|_{\mathbf{r}=\mathbf{r}_j}. \qquad (7)$$

This is how particle j is translated and rotated in the field $\mathbf{u}_i^{(0)}(\mathbf{r})$ induced by particle i. Yet, elastic retroaction occurs between the particles, as described in the following.

The force densities $\mathbf{f}(\mathbf{r}')$ in Eq. (5) that the particles exert on their environment in general will not vanish identically. Since the particles are rigid, they resist any deformation that

$u_i^{(0)}(\mathbf{r})$ would imply. Thus, they exert counteracting stresses onto the deformed matrix. The stresslet exerted by particle j onto the matrix can be denoted as $\underline{\mathbf{S}}_j = \int_{\partial V_j} dS'(\{\mathbf{f}(\mathbf{r}')\mathbf{r}' + [\mathbf{f}(\mathbf{r}')\mathbf{r}']^T\}/2 - \hat{\underline{\mathbf{I}}}[\mathbf{f}(\mathbf{r}') \cdot \mathbf{r}']/3)$, where $[\bullet]^T$ marks the transpose. In our case, we can directly calculate from Eq. (5) the stresslet $\underline{\mathbf{S}}_j^{(1)}$ that particle j exerts onto the matrix when it resists to the deformation described by $u_i^{(0)}(\mathbf{r})$. To find the expression for $\underline{\mathbf{S}}_j^{(1)}$, one proceeds in the same way as described above for $\mathbf{\Omega}_j^{(1)}$ but eventually extracts the symmetric part. The latter contains the definition of $\underline{\mathbf{S}}_j^{(1)}$. We obtain

$$\underline{\mathbf{S}}_j^{(1)} = \frac{10\pi\mu a^3}{-3}\left(1 + \frac{a^2}{10}\nabla^2\right)\{\nabla u_i^{(0)}(\mathbf{r}) + [\nabla u_i^{(0)}(\mathbf{r})]^T\}\bigg|_{\mathbf{r}_j}. \tag{8}$$

This stresslet leads to additional distortions of the matrix (see Fig. 1) described by a displacement field $u_j^{(1)}(\mathbf{r})$ that overlays $u_i^{(0)}(\mathbf{r})$. We find $u_j^{(1)}(\mathbf{r})$ from the general expression $u_j(\mathbf{r}) = \int_{\partial V_j} dS'\underline{\mathbf{G}}(\mathbf{r} - \mathbf{r}') \cdot \mathbf{f}(\mathbf{r}')$ by Taylor expanding the Green's function in $\mathbf{r}'$ around $\mathbf{r}' = \mathbf{r}_j$. The definition of $\underline{\mathbf{S}}_j$ shows up as the symmetric part of the second-order term of the series, similarly to the hydrodynamic case [6,20], leading to

$$u_j^{(1)}(\mathbf{r}) = -(\underline{\mathbf{S}}_j^{(1)} \cdot \nabla) \cdot \underline{\mathbf{G}}(\mathbf{r} - \mathbf{r}_j). \tag{9}$$

This expression completes our first step of iteration. In the second step, it is particle i that is exposed to the field $u_j^{(1)}(\mathbf{r})$. Correspondingly, we find its reaction from Eqs. (6)–(9) by replacing $(u_i^{(0)}, \mathbf{U}_j^{(1)}, \mathbf{\Omega}_j^{(1)}, \underline{\mathbf{S}}_j^{(1)}, u_j^{(1)}, \mathbf{r}_j)$ with $(u_j^{(1)}, \mathbf{U}_i^{(2)}, \mathbf{\Omega}_i^{(2)}, \underline{\mathbf{S}}_i^{(2)}, u_i^{(2)}, \mathbf{r}_i)$. Particle i now feels the consequences of its self-generated field $u_i^{(0)}(\mathbf{r})$ *reflected* by particle j in the form of $u_j^{(1)}(\mathbf{r})$. Therefore, the procedure was termed *method of reflections* in hydrodynamics [6,7]. The displacement $\mathbf{U}_i^{(2)}$ in Fig. 1 results from this reflection. We have not found in the hydrodynamic derivation [7] the above reasoning of explicitly imposing on the matrix environment the rigidity-induced stress.

In principle, this refinement of the deformation field via back-and-forth reflections between the two particles can be continued, leading to increasingly higher-order corrections in a/r_{ij}, where $r_{ij} = |\mathbf{r}_i - \mathbf{r}_j|$. For our example systems below, these iterations converge quickly [see Fig. 3(c)], so that it is sufficient to consider contributions up to (including) the order of r_{ij}^{-4}.

Because of the linearity of Eq. (1), we can sum up the particle displacements obtained from the different steps of iteration. Moreover, we can consider external forces $\mathbf{F}_i$ on *all* particles and calculate the resulting net displacements $\mathbf{U}_i$ due to the mutual elastic interactions ($i = 1, \ldots, N$).

These contributions superimpose. In analogy to the hydrodynamic [7] mobility matrix, we express the result by an elastic *displaceability matrix* $\underline{\mathbf{M}}$:

$$\begin{pmatrix} \mathbf{U}_1 \\ \vdots \\ \mathbf{U}_N \end{pmatrix} = \begin{pmatrix} \underline{\mathbf{M}}_{11} & \cdots & \underline{\mathbf{M}}_{1N} \\ \vdots & \vdots & \vdots \\ \underline{\mathbf{M}}_{N1} & \cdots & \underline{\mathbf{M}}_{NN} \end{pmatrix} \cdot \begin{pmatrix} \mathbf{F}_1 \\ \vdots \\ \mathbf{F}_N \end{pmatrix}. \tag{10}$$

Limiting ourselves to contributions up to (including) the order of r_{ij}^{-4}, we find

$$\underline{\mathbf{M}}_{i=j} = M_0\left[\hat{\underline{\mathbf{I}}} - \sum_{\substack{k=1 \\ k \neq i}}^{N} \frac{15}{4}\left(\frac{a}{r_{ik}}\right)^4 \hat{\mathbf{r}}_{ik}\hat{\mathbf{r}}_{ik}\right], \tag{11}$$

$$\underline{\mathbf{M}}_{i \neq j} = M_0 \frac{3}{4}\frac{a}{r_{ij}}\left[(\hat{\underline{\mathbf{I}}} + \hat{\mathbf{r}}_{ij}\hat{\mathbf{r}}_{ij}) + 2\left(\frac{a}{r_{ij}}\right)^2\left(\frac{1}{3}\hat{\underline{\mathbf{I}}} - \hat{\mathbf{r}}_{ij}\hat{\mathbf{r}}_{ij}\right)\right]$$
$$+ \underline{\mathbf{M}}_{i \neq j}^{(3)}, \tag{12}$$

where $M_0 = 1/6\pi\mu a$ and $\hat{\mathbf{r}}_{ij} = \mathbf{r}_{ij}/r_{ij}$ ($i, j = 1, 2, \ldots, N$).

In Eq. (11), $\hat{\underline{\mathbf{I}}}$ represents the immediate displacement of particle i due to the force $\mathbf{F}_i$ ($\mathbf{U}_i^{(0)}$ in Fig. 1). The second term $\sim r_{ik}^{-4}$ describes the rigidity-induced reflection from another particle ($\mathbf{U}_i^{(2)}$ in Fig. 1). It *counteracts* $\mathbf{U}_i^{(0)}$ or vanishes for $\mathbf{F}_i \perp \hat{\mathbf{r}}_{ik}$.

In Eq. (12), $\hat{\underline{\mathbf{I}}} + \hat{\mathbf{r}}_{ij}\hat{\mathbf{r}}_{ij}$ expresses the consequence of the force $\mathbf{F}_j$ acting on particle j: Particle i is relocated in the induced displacement field ($\mathbf{U}_j^{(1)}$ in Fig. 1, for $i \leftrightarrow j$). The term $\sim r_{ij}^{-3}$ corrects this displacement field due to the finite size of particle j, in analogy to the Rodne-Prager formula in the fluid case [7]. $\underline{\mathbf{M}}_{i \neq j}^{(3)}$ describes additional three-body interactions $\sim r_{ij}^{-4}$ calculated in full analogy to the above procedure for the two-body interaction:

$$\underline{\mathbf{M}}_{i \neq j}^{(3)} = M_0 \frac{15}{8}\sum_{\substack{k=1 \\ k \neq i,j}}^{N}\left(\frac{a}{r_{ik}}\right)^2\left(\frac{a}{r_{jk}}\right)^2[1 - 3(\hat{\mathbf{r}}_{ik} \cdot \hat{\mathbf{r}}_{jk})^2]\hat{\mathbf{r}}_{ik}\hat{\mathbf{r}}_{jk}. \tag{13}$$

That is, the deformation field induced by a force on a first particle j spreads to a second particle k, from where it is reflected towards the third particle i. The angular dependence allows for configuration-dependent attractive, repulsive, or bypass contributions; see Fig. 2.

Equations (10)–(13) represent the central theoretical result. Up to (including) order r_{ij}^{-4} it is exact, higher-body interactions for $N > 3$ do not enter (see Ref. [19] for $N = 4$). To confirm and illustrate the merit of the theory, we performed experiments on small groups of paramagnetic particles embedded in a soft elastic gel matrix. Applying an external magnetic field induced mutual magnetic forces between the particles. Rotating the magnetic field tuned these forces. The resulting relative displacements of the particles were tracked by optical microscopy.
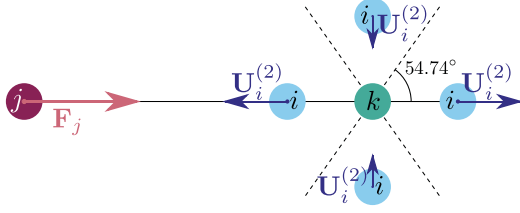
FIG. 2. Illustration of example three-body contributions in Eq. (13). The force $\mathbf{F}_j$ on particle j induces a displacement field that is reflected from particle k due to its rigidity. Depending on its position, particle i is effectively attracted or repelled by particle j (strongest under coaxial alignment), pulled towards particle k (bypass), or not affected at all (dashed lines).

We used paramagnetic nickel (Ni) particles obtained from Alfa Aesar ($-100 + 325$ mesh, purity 99.8%). The magnetic hysteresis curves (measured by a vibrating sample magnetometer, Lake Shore 7407) showed a low remanence of ~ 7.5 kA/m, a low coercive field of ~ 2.4 mT, and a volume magnetization of 291 ± 17 kA/m under an external magnetic field of ~ 216 mT. We carefully selected Ni particles of similar sizes (deviation less than 2% within each group) and a roundness $\gtrsim 0.91$ (measured by image analysis [21]). These particles were embedded in the middle plane of a soft elastic polydimethylsiloxane-based [22] gel; see Fig. 3(a). First, a bottom gel layer with a thickness of 3.3 mm and a diameter of 24 mm was prepared in a plastic mold. Second, after sufficient stiffening (~ 0.5 h), the Ni particles were carefully deposited on its top around the center. Third, a top gel layer with the same composition and size as the bottom layer was added. To ensure good connection between the two layers, at least 7 days of cross-linking were allowed.

Using a 32-magnet Halbach array to generate a homogeneous magnetic field [22], we applied ~ 216 mT to the embedded Ni particles, which is close to saturation. Starting from the initial direction, the magnetic field was rotated clockwise for $180°$ in 18 steps within the plane containing the Ni particles. Their center-of-mass positions were tracked by a CCD camera (MATRIX VISION mvBlueCOUGAR-S) with the zoom macro lens (Navitar Zoom 7000) mounted above the samples and subsequent image analysis [21].

We measured the changes in particle distance Δr_{ij} ($i \neq j$) for a two- and three-particle system (see Figs. 3 and 4, respectively), when rotating the external magnetic field. Forces $\mathbf{F}_i$ on the particles result from mutual magnetic interactions. Because of substantial particle separations, we approximate the induced magnetic moments as point dipoles [23]. Thus, we find [24]

$$\mathbf{F}_i = -\frac{3\mu_0 m^2}{4\pi} \sum_{\substack{j=1 \\ j \neq i}}^{N} \frac{5\hat{\mathbf{r}}_{ij}(\hat{\mathbf{m}} \cdot \hat{\mathbf{r}}_{ij})^2 - \hat{\mathbf{r}}_{ij} - 2\hat{\mathbf{m}}(\hat{\mathbf{m}} \cdot \hat{\mathbf{r}}_{ij})}{r_{ij}^4}, \quad (14)$$
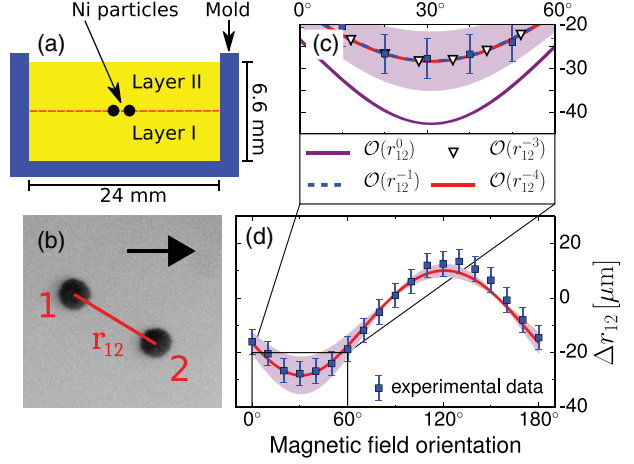

FIG. 3. (a) Schematic of the samples. After fabrication of the bottom gel layer (I), the paramagnetic nickel (Ni) particles are placed into the center plane (dashed line), before the top layer (II) is added. The enclosing plastic molds are open to the top for optical investigation. (b) Snapshot of a system of two Ni particles (diameters 150.6 ± 1.9 μm) embedded in a soft elastic gel, here for a vanishing external magnetic field. (c),(d) Change in distance Δr_{12} between the two particles when applying an external magnetic field along different directions in the particle plane via clockwise rotation. The horizontal arrow in (b) defines the angle of $0°$. Data points in (d) were measured experimentally. The line is calculated from the theory, where shaded areas arise from uncertainties in the experimental input values. An elastic modulus of $\mu = 83.0 \pm 14.3$ Pa is extracted. The enlargement in (c) highlights the rapid convergence of the theory.

with μ_0 the vacuum permeability and $\mathbf{m} = m\hat{\mathbf{m}}$ the induced magnetic moments, considered identical for all particles in the close-to-saturating homogeneous external magnetic field. Using as input parameters the experimentally
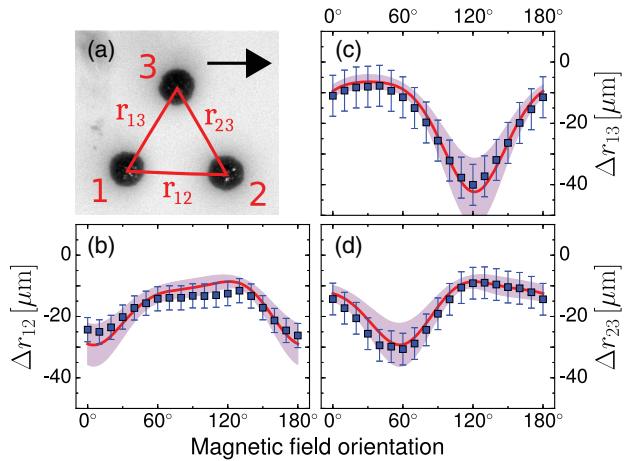

FIG. 4. The same as in Figs. 3(b) and 3(d), now for a three-particle system. (a) The snapshot was taken for a vanishing external magnetic field (particle diameters 208.5 ± 2.3 μm). (b)–(d) Changes Δr_{ij} in all three distances ($i, j = 1, 2, 3, i \neq j$). The elastic modulus is $\mu = 76.3 \pm 11.7$ Pa.

determined particle positions, sizes, and magnetization, we extracted the elastic shear modulus and calculated all changes Δr_{ij} from Eqs. (10)–(14). The magnetic forces $\mathbf{F}_i$ after displacement are determined iteratively. Perfect agreement between the theory and experiment in Figs. 3 and 4 supports the significance of the theoretical approach and highlights its potential for microrheological measurement of the shear modulus.

In summary, we considered rigid spherical particles displaced against a surrounding elastic matrix by externally induced forces. We derived analytical expressions to calculate the resulting particle displacements. Mutual interactions due to induced matrix deformations are effectively included. This renders the procedure a promising tool to describe the behavior of elastic composite materials [25]. Our experiments on paramagnetic particles in a soft elastic gel matrix and subject to tunable magnetic interactions confirm the potential of the theory.

Upon dynamic extension, a prospective application concerns macroscopic rheology [26] or nano- and microrheology [16] where the matrix properties are tested by external agitation of embedded probe particles. Also, biological and medical questions are addressable in this way, for instance, cytoskeletal properties [16,27]. An extension of the theory to include imposed torques on the particles, e.g., due to magnetic anisotropy, is straightforward and will be presented in the near future.

* puljiz@thphy.uni-duesseldorf.de
† huangs@mpip-mainz.mpg.de
‡ auhammer@mpip-mainz.mpg.de
§ menzel@thphy.uni-duesseldorf.de

[1] Z. Zhang and C. Kleinstreuer, Phys. Fluids **14**, 862 (2002).

[2] Y. Meng, M. A. Rao, and A. K. Datta, Food Bioprod. Process. **83**, 297 (2005); M. J. Ferrua and R. P. Singh, J. Food. Sci. **75**, R151 (2010).

[3] T. M. Squires and S. R. Quake, Rev. Mod. Phys. **77**, 977 (2005).

[4] Q. R. Wald, Prog. Aerosp. Sci. **42**, 85 (2006); E. F. Campana, D. Peri, Y. Tahara, and F. Stern, Comput. Methods Appl. Mech. Eng. **196**, 634 (2006); L. Müller, W. Heinze, D. Kožulović, M. Hepperle, and R. Radespiel, J. Aircr. **51**, 249 (2014).

[5] C. L. M. H. Navier, Mém. Acad. Sci. Inst. France **6**, 389 (1822); G. G. Stokes, Trans. Cambridge Philos. Soc. **8**, 287 (1845).

[6] S. Kim and S. J. Karrila, *Microhydrodynamics: Principles and Selected Applications* (Butterworth-Heinemann, Boston, 1991).

[7] J. K. G. Dhont, *An Introduction to Dynamics of Colloids* (Elsevier, Amsterdam, 1996).

[8] B. U. Felderhof, Physica (Amsterdam) **89A**, 373 (1977); D. L. Ermak and J. A. McCammon, J. Chem. Phys. **69**, 1352 (1978); L. Durlofsky, J. F. Brady, and G. Bossis, J. Fluid Mech. **180**, 21 (1987); K. Zahn, J. M. Méndez-Alcaraz, and G. Maret, Phys. Rev. Lett. **79**, 175 (1997); J.-C. Meiners and S. R. Quake, Phys. Rev. Lett. **82**, 2211 (1999); J. K. G. Dhont, J. Chem. Phys. **120**, 1642 (2004); M. Rex and H. Löwen, Eur. Phys. J. E **26**, 143 (2008).

[9] C. M. Pooley, G. P. Alexander, and J. M. Yeomans, Phys. Rev. Lett. **99**, 228103 (2007); A. Baskaran and M. C. Marchetti, Proc. Natl. Acad. Sci. U.S.A. **106**, 15567 (2009); A. M. Menzel, A. Saha, C. Hoell, and H. Löwen, J. Chem. Phys. **144**, 024115 (2016); E. Lauga and T. R. Powers, Rep. Prog. Phys. **72**, 096601 (2009); K. Drescher, R. E. Goldstein, N. Michel, M. Polin, and I. Tuval, Phys. Rev. Lett. **105**, 168101 (2010); K. Drescher, J. Dunkel, L. H. Cisneros, S. Ganguly, and R. E. Goldstein, Proc. Natl. Acad. Sci. U.S.A. **108**, 10940 (2011); W. F. Paxton, K. C. Kistler, C. C. Olmeda, A. Sen, S. K. St. Angelo, Y. Cao, T. E. Mallouk, P. E. Lammert, and V. H. Crespi, J. Am. Chem. Soc. **126**, 13424 (2004).

[10] Y. An and M. T. Shaw, Smart Mater. Struct. **12**, 157 (2003); R. Fuhrer, E. K. Athanassiou, N. A. Luechinger, and W. J. Stark, Small **5**, 383 (2009); H. Böse, R. Rabindranath, and J. Ehrlich, J. Intell. Mater. Syst. Struct. **23**, 989 (2012); W. Cheng, J. Wang, U. Jonas, G. Fytas, and N. Stefanou, Nat. Mater. **5**, 830 (2006); T. Still, G. Gantzounis, D. Kiefer, G. Hellmann, R. Sainidou, G. Fytas, and N. Stefanou, Phys. Rev. Lett. **106**, 175505 (2011); J. Baumgartl, M. Zvyagolskaya, and C. Bechinger, Phys. Rev. Lett. **99**, 205503 (2007); **100**, 219903(E) (2008).

[11] J. D. Eshelby, Proc. R. Soc. A **241**, 376 (1957); **252**, 561 (1959); L. J. Walpole, Proc. R. Soc. A **433**, 179 (1991); **434**, 571 (1991); Q. J. Mech. Appl. Math. **58**, 129 (2005).

[12] N. Phan-Thien, J. Elast. **32**, 243 (1993).

[13] H. L. Oestreicher, J. Acoust. Soc. Am. **23**, 707 (1951); A. N. Norris, J. Acoust. Soc. Am. **119**, 2062 (2006); **123**, 99 (2008).

[14] N. Phan-Thien and S. Kim, ZAMP **45**, 177 (1994); J. Elast. **37**, 93 (1995).

[15] H. Tanaka and T. Araki, Phys. Rev. Lett. **85**, 1338 (2000).

[16] F. Ziemann, J. Rädler, and E. Sackmann, Biophys. J. **66**, 2210 (1994); A. R. Bausch, W. Möller, and E. Sackmann, Biophys. J. **76**, 573 (1999); T. A. Waigh, Rep. Prog. Phys. **68**, 685 (2005); C. Wilhelm, Phys. Rev. Lett. **101**, 028101 (2008).

[17] A.-L. Cauchy, *Exercices de Mathématiques* (Bure frères, Paris, 1828), Vol. 3, pp. 160–187.

[18] L. D. Landau and E. M. Lifshitz, *Theory of Elasticity* (Elsevier, Oxford, 1986).

[19] See Supplemental Material at http://link.aps.org/supplemental/10.1103/PhysRevLett.117.238003 for the corresponding expressions in a compressible elastic matrix and for an analysis of experiments on a four-particle system.

[20] G. K. Batchelor and J. T. Green, J. Fluid Mech. **56**, 375 (1972).

[21] http://imagej.nih.gov/ij/.

[22] S. Huang, G. Pessot, P. Cremer, R. Weeber, C. Holm, J. Nowak, S. Odenbach, A. M. Menzel, and G. K. Auernhammer, Soft Matter **12**, 228 (2016).

[23] S. H. L. Klapp, J. Phys. Condens. Matter **17**, R525 (2005); A. M. Biller, O. V. Stolbov, and Y. L. Raikher, Phys. Rev. E **92**, 023202 (2015).

[24] J. D. Jackson, *Classical Electrodynamics* (Wiley, New York, 1999).

[25] P. Ilg, Soft Matter **9**, 3465 (2013); S. Odenbach, Arch. Appl. Mech. **86**, 269 (2016); A. M. Menzel, Phys. Rev. E **94**, 023003 (2016).

[26] M. M. Denn and J. F. Morris, Annu. Rev. Chem. Biomol. Eng. **5**, 203 (2014).

[27] D. Mizuno, C. Tardin, C. F. Schmidt, and F. C. MacKintosh, Science **315**, 370 (2007).

Supplemental material to
"Forces on rigid inclusions in elastic media and resulting matrix-mediated interactions"

Mate Puljiz,[1, *] Shilin Huang,[2, †] Günter K. Auernhammer,[2, ‡] and Andreas M. Menzel[1, §]

[1] *Institut für Theoretische Physik II: Weiche Materie,*
Heinrich-Heine-Universität Düsseldorf, D-40225 Düsseldorf, Germany
[2] *Max Planck Institute for Polymer Research, Ackermannweg 10, 55128 Mainz, Germany*
(Dated: September 23, 2016)

As stressed in the main text, the derivation of the displaceability matrix can likewise be performed for *compressible* systems. Following the same steps of derivation as in the main text, we present below the corresponding expressions for completeness. Apart from that, we add further experimental results and comparison with the theory for a four-particle system, in complete analogy to our presentation for the three-particle system in the main text.

Expressions for a compressible elastic matrix

For clarity and to facilitate the comparison with the hydrodynamic fluid case, we have presented in the main text the expressions for an *incompressible* elastic system. That is, the system tends to locally preserve the volume of all its volume elements during any type of elastic deformation. However, and in contrast to the hydrodynamic fluid case [1–3], for elastic matrices it is straightforward to allow for *compressibility* in the derivation. This extended derivation proceeds in direct analogy to the one presented in the main text. Corresponding expressions are presented in the following using the same equation numbering as in the main text.

We again assume a homogeneous and isotropic elastic matrix of infinite extension. Once more, we start from the linear elastostatic Navier-Cauchy equations [4],

$$\nabla^2 \mathbf{u}(\mathbf{r}) + \frac{1}{1-2\nu}\nabla\nabla\cdot\mathbf{u}(\mathbf{r}) = -\frac{1}{\mu}\mathbf{f}_b(\mathbf{r}). \qquad (1)$$

As in the main text, $\mathbf{u}(\mathbf{r})$ denotes the displacement field, μ the shear modulus of the matrix [5], ν the Poisson ratio [5], and $\mathbf{f}_b(\mathbf{r})$ the bulk force density. Now, we do not restrict our analysis to incompressible materials that locally adhere to $\nabla\cdot\mathbf{u}(\mathbf{r})=0$, and we do not assign a specific value to ν.

The resulting Green's function for a point force density $\mathbf{f}_b(\mathbf{r}) = \mathbf{F}\delta(\mathbf{r})$ then reads [5]

$$\underline{\mathbf{G}}(\mathbf{r}) = \frac{1}{16\pi(1-\nu)\mu}\left[\frac{3-4\nu}{r}\hat{\underline{\mathbf{I}}} + \frac{\mathbf{r}\mathbf{r}}{r^3}\right]. \qquad (2)$$

Using this expression, if an external force $\mathbf{F}_i$ is acting on a rigid spherical particle i of radius a embedded in the matrix with no-slip boundary conditions on its surface, a displacement field

$$\mathbf{u}_i^{(0)}(\mathbf{r}) = \left(1 + \frac{a^2}{6}\nabla^2\right)\underline{\mathbf{G}}(\mathbf{r}-\mathbf{r}_i)\cdot\mathbf{F}_i \qquad (3)$$

is induced. Eq. (3) has the same form as in the main text, but $\underline{\mathbf{G}}$ is different, see Eq. (2). Again, the validity

of Eq. (3) is confirmed as it satisfies Eq. (1), shows the correct limit $\mathbf{u}_i^{(0)}(\mathbf{r}) = \underline{\mathbf{G}}(\mathbf{r}-\mathbf{r}_i)\cdot\mathbf{F}_i$ for $|\mathbf{r}-\mathbf{r}_i| > a$ when $a \to 0$, and for $|\mathbf{r}-\mathbf{r}_i| = a$ is constant on the particle surface. For $|\mathbf{r}-\mathbf{r}_i| = a$, it reveals the rigid displacement

$$\mathbf{U}_i^{(0)} = \mathbf{u}_i^{(0)}(|\mathbf{r}-\mathbf{r}_i| = a) = \frac{5-6\nu}{24\pi(1-\nu)\mu a}\mathbf{F}_i \qquad (4)$$

of the ith particle in response to $\mathbf{F}_i$.

The no-slip condition under our assumptions applies on the surface ∂V_j of a particle j also for compressible matrices. Thus Eq. (5) in the main text preserves its shape, i.e.

$$\mathbf{U}_j^{(1)} + \mathbf{\Omega}_j^{(1)}\times(\mathbf{r}-\mathbf{r}_j) = \mathbf{u}_i^{(0)}(\mathbf{r}) + \int_{\partial V_j}\underline{\mathbf{G}}(\mathbf{r}-\mathbf{r}')\cdot\mathbf{f}(\mathbf{r}')\mathrm{d}S',$$
$$(5)$$

where $\mathbf{U}_j^{(1)}$ denotes the translation of particle j, $\mathbf{\Omega}_j^{(1)}$ is its rotation, the displacement field $\mathbf{u}_i^{(0)}(\mathbf{r})$ is induced by particle i, and $\mathbf{f}(\mathbf{r}')$ denotes the surface force density that particle j exerts on the surrounding matrix. The derivation of expressions for $\mathbf{U}_j^{(1)}$ and $\mathbf{\Omega}_j^{(1)}$ in the form of the Faxén laws follows the same strategy as described in the main text and leads to

$$\mathbf{U}_j^{(1)} = \left(1 + \frac{a^2}{6}\nabla^2\right)\mathbf{u}_i^{(0)}(\mathbf{r})\bigg|_{\mathbf{r}=\mathbf{r}_j}, \qquad (6)$$

$$\mathbf{\Omega}_j^{(1)} = \frac{1}{2}\nabla\times\mathbf{u}_i^{(0)}(\mathbf{r})\bigg|_{\mathbf{r}=\mathbf{r}_j}. \qquad (7)$$

Also the stresslet $\underline{\mathbf{S}}_j$ exerted by particle j onto the matrix is derived in analogy to what is described in the main text. In general, for compressible systems, this stresslet is given by the expression $\underline{\mathbf{S}}_j = \int_{\partial V_j}\mathrm{d}S'[\mathbf{f}(\mathbf{r}')\mathbf{r}' + (\mathbf{f}(\mathbf{r}')\mathbf{r}')^T]/2$. This expression slightly differs from the one introduced below Eq. (7) in the main text for incompressible systems. There, a trace-free definition was used to exclude compressions and dilations of the matrix, which needs to be the case for volume-conserving systems. It can be seen from the main text that the difference in definitions plays no actual role for our derivation. The reason is Eq. (9), where the extra term $\sim \hat{\underline{\mathbf{I}}}$

in the incompressible case only leads to a contribution $\sim \nabla \cdot \underline{\mathbf{G}}$. Yet, $\nabla \cdot \underline{\mathbf{G}}$ vanishes in the incompressible case. Therefore, following the same strategy as described in the main text, we obtain

$$\underline{\mathbf{S}}_j^{(1)} = -\frac{4\pi(1-\nu)\mu a^3}{4-5\nu}\left(1+\frac{a^2}{10}\nabla^2\right)\left[\frac{1}{1-2\nu}\underline{\hat{\mathbf{I}}}\nabla\cdot\mathbf{u}_i^{(0)}(\mathbf{r})\right.$$
$$\left.+\frac{5}{2}\left(\nabla\mathbf{u}_i^{(0)}(\mathbf{r})+\left(\nabla\mathbf{u}_i^{(0)}(\mathbf{r})\right)^T\right)\right]\Bigg|_{\mathbf{r}=\mathbf{r}_j}. \tag{8}$$

Likewise, the displacement field $\mathbf{u}_j^{(1)}(\mathbf{r})$ resulting from the rigidity of particle j and its resistance to deformation, expressed by the stresslet $\underline{\mathbf{S}}_j^{(1)}$, is calculated as described in the main text. Eq. (8) here contains a term $\sim 1/(1-2\nu)$, which would diverge for $\nu \to 0.5$. However, it gets canceled by a counter-factor $\sim (1-2\nu)$ in the calculation. More precisely, upon inserting Eq. (3) into Eq. (8), the expression $\nabla \cdot \underline{\mathbf{G}}$ appears; straightforward calculation of $\nabla \cdot \underline{\mathbf{G}}$ via Eq. (2) leads to a factor $\sim (1-2\nu)$. In the end, $\mathbf{u}_j^{(1)}(\mathbf{r})$ has the same form as Eq. (9) in the main text,

$$\mathbf{u}_j^{(1)}(\mathbf{r}) = -\left(\underline{\mathbf{S}}_j^{(1)}\cdot\nabla\right)\cdot\underline{\mathbf{G}}(\mathbf{r}-\mathbf{r}_j). \tag{9}$$

In the next step, again, the reaction of particle i in response to the field $\mathbf{u}_j^{(1)}(\mathbf{r})$ is obtained from Eqs. (6)–(9) by replacing $(\mathbf{u}_i^{(0)}, \mathbf{U}_j^{(1)}, \mathbf{\Omega}_j^{(1)}, \underline{\mathbf{S}}_j^{(1)}, \mathbf{u}_j^{(1)})$ with $(\mathbf{u}_j^{(1)}, \mathbf{U}_i^{(2)}, \mathbf{\Omega}_i^{(2)}, \underline{\mathbf{S}}_i^{(2)}, \mathbf{u}_j^{(2)})$.

Summing up the contributions from the different steps of iteration and considering all N particles simultaneously leads to an expression in the form of an elastic displaceability matrix $\underline{\mathbf{M}}$ as given in the main text:

$$\begin{pmatrix}\mathbf{U}_1 \\ \vdots \\ \mathbf{U}_N\end{pmatrix} = \begin{pmatrix}\underline{\mathbf{M}}_{11} & \cdots & \underline{\mathbf{M}}_{1N} \\ \vdots & \vdots & \vdots \\ \underline{\mathbf{M}}_{N1} & \cdots & \underline{\mathbf{M}}_{NN}\end{pmatrix}\cdot\begin{pmatrix}\mathbf{F}_1 \\ \vdots \\ \mathbf{F}_N\end{pmatrix}. \tag{10}$$

Limiting ourselves to contributions up to (including) order r_{ij}^{-4}, we find for a *compressible* system the more general expressions

$$\underline{\mathbf{M}}_{i=j} = M_0\Bigg\{\underline{\hat{\mathbf{I}}} - \sum_{\substack{k=1\\k\neq i}}^N \frac{3}{4(4-5\nu)(5-6\nu)}\left(\frac{a}{r_{ik}}\right)^4$$
$$\left[\left(37-44\nu+10(1-2\nu)^2\right)\hat{\mathbf{r}}_{ik}\hat{\mathbf{r}}_{ik}\right.$$
$$\left.+5(1-2\nu)^2\left(\underline{\hat{\mathbf{I}}}-\hat{\mathbf{r}}_{ik}\hat{\mathbf{r}}_{ik}\right)\right]\Bigg\}, \tag{11}$$

$$\underline{\mathbf{M}}_{i\neq j} = M_0\frac{3}{2(5-6\nu)}\frac{a}{r_{ij}}\left[\left(4(1-\nu)-\frac{4}{3}\left(\frac{a}{r_{ij}}\right)^2\right)\hat{\mathbf{r}}_{ij}\hat{\mathbf{r}}_{ij}\right.$$
$$\left.+\left(3-4\nu+\frac{2}{3}\left(\frac{a}{r_{ij}}\right)^2\right)\left(\underline{\hat{\mathbf{I}}}-\hat{\mathbf{r}}_{ij}\hat{\mathbf{r}}_{ij}\right)\right]+\underline{\mathbf{M}}_{i\neq j}^{(3)}, \tag{12}$$

where $M_0 = (5-6\nu)/24\pi(1-\nu)\mu a$ and $\hat{\mathbf{r}}_{ij} = \mathbf{r}_{ij}/r_{ij}$ $(i,j = 1, 2, ..., N)$. Here, the three-body interactions con-

tribute as given by $\underline{\mathbf{M}}_{i\neq j}^{(3)}$ in the form

$$\underline{\mathbf{M}}_{i\neq j}^{(3)} = M_0\frac{3}{8(4-5\nu)(5-6\nu)}\sum_{\substack{k=1\\k\neq i,j}}^N\left(\frac{a}{r_{ik}}\right)^2\left(\frac{a}{r_{jk}}\right)^2$$
$$\left[-10(1-2\nu)\left((1-2\nu)\left((\hat{\mathbf{r}}_{ik}\cdot\hat{\mathbf{r}}_{jk})\underline{\hat{\mathbf{I}}}+\hat{\mathbf{r}}_{jk}\hat{\mathbf{r}}_{ik}\right)\right.\right.$$
$$\left.+3(\hat{\mathbf{r}}_{ik}\cdot\hat{\mathbf{r}}_{jk})(\hat{\mathbf{r}}_{ik}\hat{\mathbf{r}}_{ik}+\hat{\mathbf{r}}_{jk}\hat{\mathbf{r}}_{jk})-\hat{\mathbf{r}}_{ik}\hat{\mathbf{r}}_{jk}\right)$$
$$\left.+3\left(7-4\nu-15(\hat{\mathbf{r}}_{ik}\cdot\hat{\mathbf{r}}_{jk})^2\right)\hat{\mathbf{r}}_{ik}\hat{\mathbf{r}}_{jk}\right]. \tag{13}$$

The corresponding expressions for *incompressible* systems in the main text readily follow from Eqs. (10)–(13) by setting the Poisson ratio $\nu = 0.5$. Here, we derived and listed the more general expressions for *compressible* elastic matrices.

Four-particle system

In addition to the two- and three-particle samples described in the main text, we also generated and analyzed four-particle systems. Their preparation, experimental analysis, and the corresponding comparison with the theory are in complete analogy to the three-particle system described in the main text. We recall that our theoretical description in the main text *up to the investigated order* (including r_{ij}^{-4}) is exact for arbitrary particle numbers. No higher-body interactions appear to this order. Therefore, Eqs. (10)–(14) in the main text also apply to systems of particle numbers $N > 3$ up to (including) order r_{ij}^{-4}, i.e. if the particle separations are not significantly reduced.

Thus, our four-particle results predominantly provide a supplement to the results presented in the main text. Our experimental and theoretical results for the four-particle system are depicted in Fig. A. One could continue to further increasing particle numbers in the same way.

[*] puljiz@thphy.uni-duesseldorf.de
[†] huangs@mpip-mainz.mpg.de
[‡] auhammer@mpip-mainz.mpg.de
[§] menzel@thphy.uni-duesseldorf.de
[1] G. K. Batchelor and J. T. Green, J. Fluid Mech. **56**, 375 (1972).
[2] S. Kim and S. J. Karrila, *Microhydrodynamics: principles and applications* (Butterworth-Heinemann, Boston, 1991).
[3] J. K. G. Dhont, *Introduction to dynamics of colloids* (Elsevier, Amsterdam, 1996).
[4] A.-L. Cauchy, *Exercices de mathématiques*, Vol. 3 (Bure frères, Paris, 1828) pp. 160–187.
[5] L. D. Landau and E. M. Lifshitz, *Theory of Elasticity* (Elsevier, Oxford, 1986).
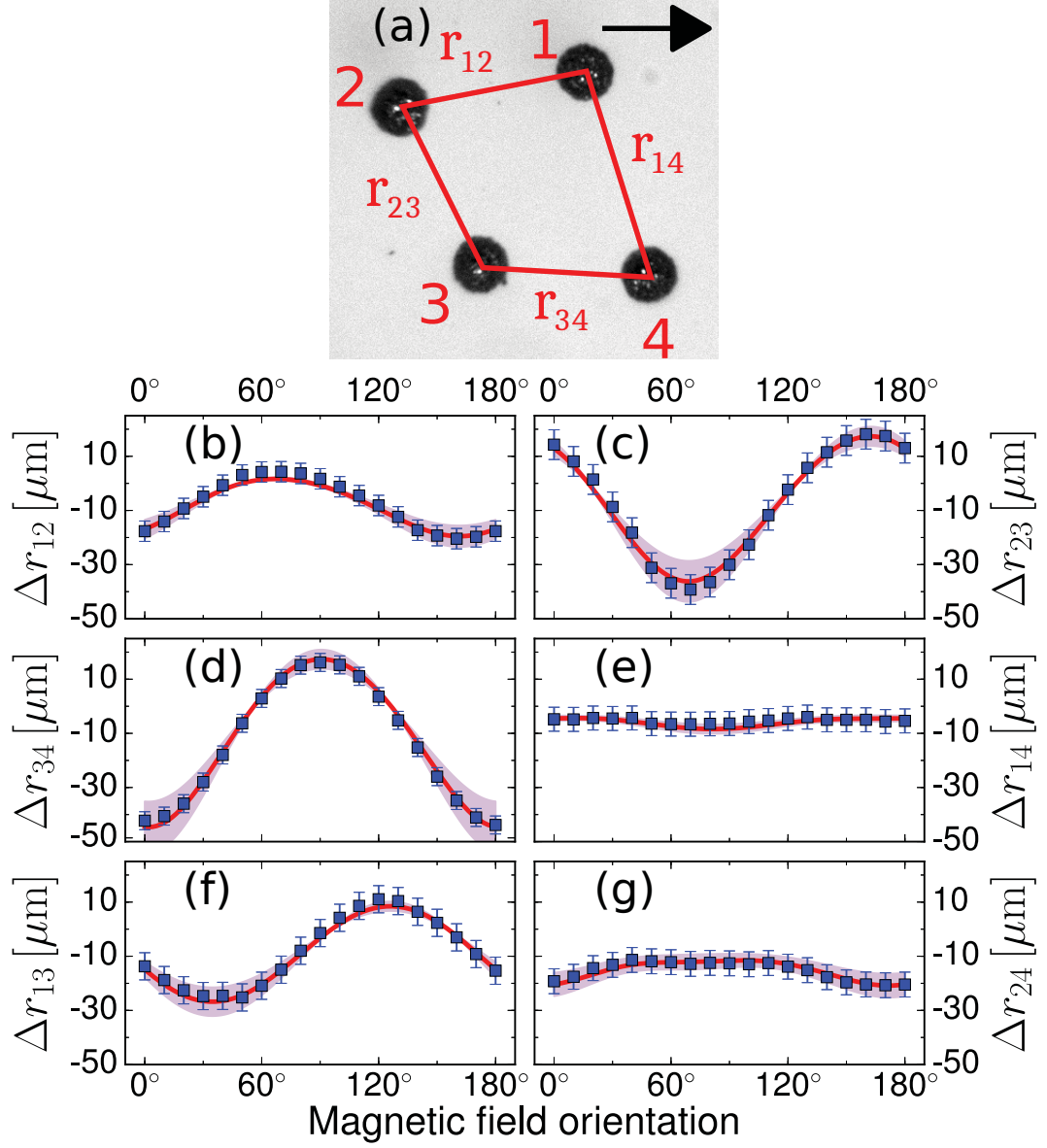
FIG. A. Same as in Figs. 3 and 4 in the main text, here for a four-particle system. (a) The snapshot was taken for vanishing external magnetic field (particle diameters 204.4±2.2 μm). (b–g) Changes Δr_{ij} in all six distances ($i, j = 1, 2, 3, 4$, $i \neq j$). Good agreement between theory (red line) and experiments (blue squares) is observed, and the modulus of the gel matrix for this system is obtained as 85.7±12.6 Pa.

Publication II

Forces and torques on rigid inclusions in an elastic environment: resulting matrix-mediated interactions, displacements, and rotations

Author's contributions

Both authors contributed to this work. My contribution to this publication partially overlaps with earlier results from my master thesis. There, the displaceability and rotateability matrices up to (including) fourth order had already been calculated. The investigation of the additional rotational couplings in exemplary studies belongs to this dissertation. I estimate my overall contribution attributable to the framework of this dissertation to approximately 20%.

Forces and torques on rigid inclusions in an elastic environment: Resulting matrix-mediated interactions, displacements, and rotations

Mate Puljiz[*] and Andreas M. Menzel[†]

Institut für Theoretische Physik II: Weiche Materie, Heinrich-Heine-Universität Düsseldorf, D-40225 Düsseldorf, Germany

Embedding rigid inclusions into elastic matrix materials is a procedure of high practical relevance, for instance, for the fabrication of elastic composite materials. We theoretically analyze the following situation. Rigid spherical inclusions are enclosed by a homogeneous elastic medium under stick boundary conditions. Forces and torques are directly imposed from outside onto the inclusions or are externally induced between them. The inclusions respond to these forces and torques by translations and rotations against the surrounding elastic matrix. This leads to elastic matrix deformations, and in turn results in mutual long-ranged matrix-mediated interactions between the inclusions. Adapting a well-known approach from low-Reynolds-number hydrodynamics, we explicitly calculate the *displacements and rotations* of the inclusions from the externally imposed or induced *forces and torques*. Analytical expressions are presented as a function of the inclusion configuration in terms of *displaceability and rotateability* matrices. The role of the elastic environment is implicitly included in these relations. That is, the resulting expressions allow a calculation of the induced displacements and rotations directly from the inclusion configuration, without having to explicitly determine the deformations of the elastic environment. In contrast to the hydrodynamic case, compressibility of the surrounding medium is readily taken into account. We present the complete derivation based on the underlying equations of linear elasticity theory. In the future, the method will, for example, be helpful to characterize the behavior of externally tunable elastic composite materials, to accelerate numerical approaches, as well as to improve the quantitative interpretation of microrheological results.

DOI: 10.1103/PhysRevE.95.053002

I. INTRODUCTION

It is safe to say that elastic composite materials are of huge technological importance. This statement is backed by the fact that concrete, the most abundant manmade material on Earth [1], is frequently composed of a cement matrix supported by more rigid particulate inclusions [1–5]. Understanding the mutual interactions between the inclusions as well as between the inclusions and the matrix is crucial to understanding the overall material performance.

While hardened concrete is a relatively rigid substance, polymeric gel matrices or biological tissue can provide softer elastic environments. Then, larger-scale displacements and rotations of embedded inclusions can be observed when forces and/or torques are externally imposed or induced. Magnetic microrheology observes the displacements of probe particles caused by externally applied magnetic field gradients [6–9]. For instance, the mechanical response of the cytoskeleton [6–10] was analyzed in this way. Similarly, the rotational motion of magnetic rods under externally imposed magnetic torques can be used for microrheological purposes [11–13]. The same is true for tracking the relative displacements between particles that respond to mutual magnetic forces induced between them [14].

Thinking of rigid inclusions embedded in a soft elastic polymeric gel matrix, artificial soft actuators represent a natural type of application [15–18]. Different approaches are possible. On the one hand, a net external force or torque can be imposed onto the inclusions. For example, magnetic

particles are drawn toward external field gradients [19], while anisotropic particles may experience a torque under an external electric or magnetic field [20–23]. In these cases, the externally imposed forces or torques are transmitted by the inclusions to the embedding matrix and lead to overall deformations. On the other hand, genuinely electrostrictive or magnetostrictive effects can be exploited when external electric or magnetic fields induce mutual attractions and repulsions between the embedded inclusions and, in total, lead to macroscopic deformations [24–26]. In addition to that, the overall mechanical properties can be tuned from outside by external fields in such materials. This allows, during application, reversibly adjusting from outside the elastic properties to a current need. Examples are the magnitudes of the elastic moduli [15,27–33], nonlinear stress-strain behavior [23,34], or dynamic properties [35–39], allowing, for instance, for the construction of tunable soft damping devices [40–42].

In all these situations, for a theoretical characterization and quantitative description of the material behavior, it is necessary to determine the induced displacements and rotations of the rigid inclusions. This is a many-body problem. The inclusions are enclosed by the elastic matrix and transmit the forces and torques to their embedding environment. As a consequence, the matrix gets deformed. The other inclusions are exposed to these induced deformations of their environment. As a consequence, they are additionally displaced and rotated. Moreover, the inclusions are rigid and resist deformations that would result from the induced matrix deformations. This resistance leads to further stresses on the embedding matrix and in turn to additional *matrix-mediated interactions* between the inclusions.

One can address this problem using simplified representations of the surrounding matrix, e.g., in elastic-spring [43]

---

[*]puljiz@thphy.uni-duesseldorf.de
[†]menzel@thphy.uni-duesseldorf.de

or elastic-rod [44,45] models. Alternatively, one can directly perform complete finite-element simulations [46–49] or apply related schemes of simulation [23,34] to explicitly cover the matrix behavior.

Here, for rigid spherical particles embedded with stick boundary conditions in the elastic matrix, we explicitly solve the problem analytically. Following the above cause-and-effect principle, we start from the forces and torques acting on the embedded particles. We then calculate the resulting coupled displacements and rotations of all particles, including the described matrix-mediated interactions between them. Our analytical results are given in terms of *displaceability and rotateability matrices* that, when multiplied with the forces and torques, lead to the caused displacements and rotations. These expressions solely depend on the configuration of the inclusions and *implicitly contain the role of the elastic environment*. As a strong benefit, the deformations of the elastic environment do not need to be calculated explicitly anymore. Therefore, in the future, one can directly calculate analytically the resulting displacements and rotations of the inclusions, without needing to resolve the induced elastic matrix deformations any longer. (To avoid confusion, we note that the term "matrix" is used both for the elastic environment as well as for the mathematical representation of second-rank tensors.)

Our approach is based on the fact that for the static linear elasticity equations a Green's function is available [50]. We then adapt a method from low-Reynolds-number hydrodynamics, called the *method of reflections* [51,52]. There, hydrodynamic interactions, i.e., fluid flows induced by suspended particles, play the role of the matrix-mediated interactions in our case. In hydrodynamics, the approach turned out to be extremely successful in characterizing the behavior of suspensions of colloidal particles [53–60], i.e., nano- to micrometer-sized objects, and of self-propelled microswimmers [61–64]. We expect similar benefits for the characterization of elastic composite materials in the future. In contrast to the hydrodynamic case, *compressible* elastic matrices are readily described as well.

Technically, the method corresponds to an iterative procedure in orders of the inverse separation distance between the rigid inclusions. We here proceed to the fourth order in this inverse distance, but in principle one can proceed to arbitrary order. Parts of our results were presented before (for instance, the elastic Faxén laws [65,66], see below, the derivation of which we here, however, present by explicit calculation in analogy to the hydrodynamic procedure in Refs. [52] and [67]). Mostly, in the very few previous approaches on this subject, the displacements were used as a starting point, and expressions for the forces and torques necessary to achieve these displacements were then derived [65,68]. Here, we follow the converse route, i.e., the forces and torques are used as known input, and we then calculate the resulting displacements and rotations. This is in agreement with the cause-and-effect chain that usually applies in experiments. Our presentation has two main purposes. First, we provide more explicitly the steps of derivation outlined already in Ref. [14] for the displaceability matrix. Second, we amend this procedure by the rotational component, so that now also the influence of imposed torques and the couplings between translational and rotational degrees of freedom are included.

We start in Sec. II with a brief overview on the underlying equations of linear elasticity theory, including the corresponding Green's solution. In Sec. III, we review the multipole expansion (a Taylor expansion) of the Green's solution around the center of a rigid inclusion. Subsequently, the calculation of the displacement field around a finite-sized sphere subject to an external force or torque is explicitly described in Secs. IV and V, respectively. In Sec. VI, the derivation of the translational and rotational Faxén laws of elasticity is presented explicitly; these expressions describe how a single spherical inclusion is displaced and rotated in a given, imposed matrix deformation. The Faxén laws enable us in Secs. VII–IX to calculate the mutual matrix-mediated interactions between spherical inclusions in elastic media. They contribute to the *displaceability and rotateability matrices* defined in Sec. VII, which allow to directly calculate from given *forces and torques* on all inclusions their coupled *displacements and rotations*. We explicitly calculate the components of these matrices to fourth order in inverse inclusion separation distance. For this purpose, we first restrict ourselves to two-sphere interactions in Sec. VIII and after that include three-sphere interactions in Sec. IX. Parts of our results are briefly illustrated by considering simplified and idealized example situations in Sec. X. Brief conclusions and a short outlook follow in Sec. XI, while several technical details are added in the Appendices to render the presentation fully self-contained.

II. GREEN'S FUNCTION IN LINEAR ELASTICITY THEORY

Throughout, we consider an isotropic, homogeneous, and infinitely extended elastic matrix. Displacements of the volume elements of the elastic matrix are described by the displacement field $\mathbf{u}(\mathbf{r})$. We consider a point force $\mathbf{F}$ acting on the matrix at position $\mathbf{r}_0$. If the deformations are restricted to the linear regime, then $\mathbf{u}(\mathbf{r})$ obeys the Navier-Cauchy equations [69] of linear elasticity theory,

$$\nabla^2\mathbf{u}(\mathbf{r}) + \frac{1}{1-2\nu}\nabla\nabla\cdot\mathbf{u}(\mathbf{r}) = -\frac{1}{\mu}\mathbf{F}\delta(\mathbf{r}-\mathbf{r}_0), \quad (1)$$

with ν the Poisson ratio connected to the matrix compressibility, μ the shear modulus, and $\delta(\mathbf{r})$ the Dirac delta function.

At positions different from $\mathbf{r}_0$, three relations arise from Eq. (1) that will prove to be useful in subsequent sections. First, taking the divergence of Eq. (1), we obtain (for $\mathbf{r} \neq \mathbf{r}_0$)

$$\nabla^2\nabla\cdot\mathbf{u} = 0. \quad (2)$$

Second, working on Eq. (1) with ∇^2 therefore leads to

$$\nabla^4\mathbf{u} = \mathbf{0}, \quad (3)$$

which is referred to as biharmonic equation. The third relation is obtained by taking the curl of Eq. (1), resulting in

$$\nabla \times \nabla^2\mathbf{u} = \mathbf{0}. \quad (4)$$

The general solution of Eq. (1) can be expressed by a Green's function,

$$\mathbf{u}(\mathbf{r}) = \underline{G}(\mathbf{r},\mathbf{r}_0)\cdot\mathbf{F}, \quad (5)$$

with $\underline{\mathbf{G}}(\mathbf{r},\mathbf{r}_0)$ a tensor of rank 2 (we mark second-rank tensors and matrices by an underscore). Due to the homogeneity and isotropy of the material, $\underline{\mathbf{G}}(\mathbf{r},\mathbf{r}_0)$ is a function of the vector $\mathbf{r} - \mathbf{r}_0$ only. For completeness, we briefly reproduce its derivation (see, e.g., Ref. [70]).

The generalized Hooke's law [50] of linear elasticity theory reads

$$\sigma_{kp} = \lambda_{kpim} u_{im}, \qquad (6)$$

with σ_{kp} and u_{im} the components of the stress and strain tensor, respectively. λ_{kpim} summarizes the elastic coefficients, and the Einstein summation rule is applied. For isotropic materials, the tensor of elastic coefficients takes the form [50]

$$\lambda_{kpim} = \lambda \delta_{kp} \delta_{im} + \mu(\delta_{ki}\delta_{pm} + \delta_{km}\delta_{pi}), \qquad (7)$$

with

$$\lambda = \frac{2\mu\nu}{1 - 2\nu}, \qquad (8)$$

whereas the linearized strain tensor [50] reads

$$u_{im} = \tfrac{1}{2}(\nabla_i u_m + \nabla_m u_i). \qquad (9)$$

We assume an arbitrary simply connected volume V of the elastic material. The only force acting on this material is our point force $\mathbf{F}$ at position $\mathbf{r}_0$. In equilibrium, this point force is balanced by the forces resulting from the surface stress:

$$\int_{\partial V} dS_p \sigma_{kp} + F_k = 0. \qquad (10)$$

Using the Gaussian divergence theorem, the surface integral can be converted into a volume integral. Therefore, inserting Eqs. (5), (6), and (9) yields the expression

$$\int_V dV[\lambda_{kpim}\nabla_m\nabla_p G_{ij}(\mathbf{r} - \mathbf{r}_0) + \delta_{jk}\delta(\mathbf{r} - \mathbf{r}_0)]F_j = 0. \quad (11)$$

Since the above equation must hold true for any arbitrary volume and point of attack $\mathbf{r}_0$, the Green's function $G_{ij}(\mathbf{r} - \mathbf{r}_0)$ must satisfy the equilibrium condition

$$\lambda_{kpim}\nabla_m\nabla_p G_{ij}(\mathbf{r} - \mathbf{r}_0) + \delta_{jk}\delta(\mathbf{r} - \mathbf{r}_0) = 0. \qquad (12)$$

This equation can be solved by Fourier forth and back transformation, see Appendix A, resulting in

$$\underline{\mathbf{G}}(\mathbf{r}) = \frac{1}{16\pi(1-\nu)\mu}\left[\frac{3 - 4\nu}{r}\hat{\underline{\mathbf{I}}} + \frac{\mathbf{rr}}{r^3}\right], \qquad (13)$$

with $\hat{\underline{\mathbf{I}}}$ the identity matrix and $\mathbf{rr}$ a dyadic product. A graphical representation of Eqs. (5) and (13) is given in Fig. 1. For incompressible materials (in the regime of linear elasticity), ν takes the value $1/2$. In this case, the Green's function in Eq. (13) has the same form as the Oseen tensor in low-Reynolds-number hydrodynamics [51,52,71], where the hydrodynamic viscosity takes the place of μ. In general, $\underline{\mathbf{G}}(\mathbf{r})$ used in Eq. (5) solves Eq. (1) .

III. MULTIPOLE EXPANSION

Using the elastic Green's function $\underline{\mathbf{G}}(\mathbf{r})$, we can express the matrix displacement field $\mathbf{u}(\mathbf{r})$ generated by an arbitrarily
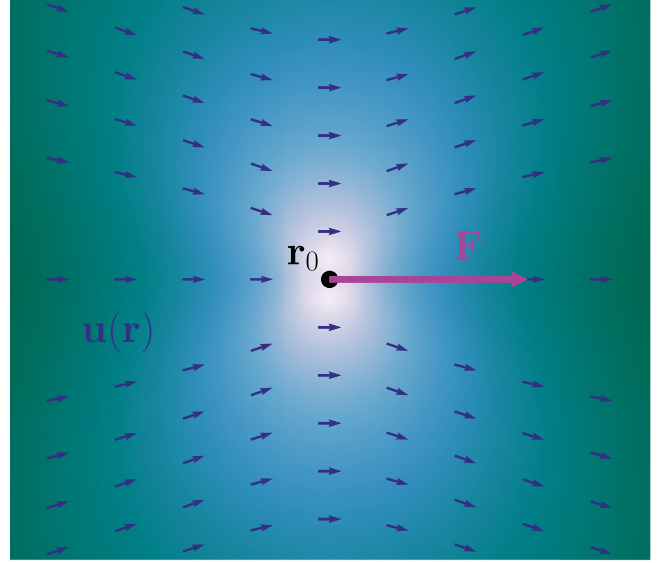

FIG. 1. Illustration of the displacement field $\mathbf{u}(\mathbf{r})$ generated by a point force $\mathbf{F}$ acting on the matrix at position $\mathbf{r}_0$. The displacement field is obtained from Eq. (5) via the elastic Green's function in Eq. (13). Small arrows, for visibility rescaled to identical length, indicate the direction of the displacement field, whereas the background color represents the local magnitude of $\mathbf{u}(\mathbf{r})$ on a logarithmic scale. The brighter the color, the higher the magnitude of $\mathbf{u}(\mathbf{r})$.

shaped embedded rigid particle centered at the origin as

$$\mathbf{u}(\mathbf{r}) = \int_{\partial V} dS' \underline{\mathbf{G}}(\mathbf{r} - \mathbf{r}') \cdot \mathbf{f}(\mathbf{r}'). \qquad (14)$$

Here, $\mathbf{r}'$ is located on the particle surface ∂V and $\mathbf{f}(\mathbf{r}')$ is the force per unit area exerted by the rigid particle onto the matrix. This equation expresses a superposition of displacement fields generated by point forces on the particle surface. A similar situation arises in electrostatics, where a localized continuous charge distribution can be expressed as a superposition of point charges, each of which contributing to the overall electric potential. Moreover, similarly to the electrostatic potential of point charges, in Eq. (13) we have $\underline{\mathbf{G}}(\mathbf{r}) \sim r^{-1}$. Therefore, it is possible to perform a multipole expansion of the Green's function. This is well-known for low-Reynolds-number hydrodynamics [51] and has previously been adapted to elastostatics [72]. We follow the procedure as described for the hydrodynamic case in Ref. [51].

In the far field, one has $|\mathbf{r}| \gg |\mathbf{r}'|$ in Eq. (14). The Taylor series of $\underline{\mathbf{G}}(\mathbf{r} - \mathbf{r}')$ in $\mathbf{r}'$ around $\mathbf{r}' = \mathbf{0}$ reads

$$G_{ij}(\mathbf{r} - \mathbf{r}') = \sum_{n=0}^{\infty} \frac{(-1)^n}{n!}(\mathbf{r}' \cdot \nabla)^n G_{ij}(\mathbf{r}). \qquad (15)$$

Inserting Eq. (15) into Eq. (14), we obtain the components of the displacement field as

$$\begin{aligned} u_i(\mathbf{r}) &= \sum_{n=0}^{\infty} \frac{(-1)^n}{n!}\int_{\partial V} dS' f_j(\mathbf{r}')(\mathbf{r}' \cdot \nabla)^n G_{ij}(\mathbf{r}) \\ &= G_{ij}(\mathbf{r})F_j - \frac{\partial G_{ij}(\mathbf{r})}{\partial r_k}D_{jk} + ..., \end{aligned} \qquad (16)$$

with

$$F_j = \int_{\partial V} dS' f_j(\mathbf{r'}), \quad D_{jk} = \int_{\partial V} dS' f_j(\mathbf{r'}) r_k'. \quad (17)$$

Here, $\mathbf{F}$ can be identified as the total force that the particle exerts on the matrix. The $\underline{\mathbf{D}}$-tensor can be split into an antisymmetric and a symmetric part,

$$D_{jk} = T_{jk} + S_{jk}, \quad (18)$$

with

$$T_{jk} = \frac{1}{2} \int_{\partial V} dS' [f_j(\mathbf{r'}) r_k' - f_k(\mathbf{r'}) r_j'], \quad (19)$$

$$S_{jk} = \frac{1}{2} \int_{\partial V} dS' [f_j(\mathbf{r'}) r_k' + f_k(\mathbf{r'}) r_j']. \quad (20)$$

The symmetric tensor S_{jk} is called stresslet. Furthermore, we set the components of the torque $\mathbf{T}$ that the particle exerts on the matrix to

$$T_i := \epsilon_{ijk} \int_{\partial V} dS' r_j' f_k(\mathbf{r'}) = -\epsilon_{ijk} T_{jk}, \quad (21)$$

with ϵ_{ijk} the Levi-Civita symbol. Therefore, we can express the corresponding part in Eq. (16) through

$$T_{jk} \frac{\partial G_{ij}}{\partial r_k} = -\frac{1}{2} \epsilon_{jkl} T_l \frac{\partial G_{ij}}{\partial r_k} = \frac{1}{2} (\mathbf{T} \times \nabla)_j G_{ij}. \quad (22)$$

In sum, we obtain the following expression for the first terms of the multipole expansion,

$$\mathbf{u}(\mathbf{r}) = \underline{\mathbf{G}}(\mathbf{r}) \cdot \mathbf{F} - \left(\frac{1}{2} \mathbf{T} \times \nabla + \underline{\mathbf{S}} \cdot \nabla \right) \cdot \underline{\mathbf{G}}(\mathbf{r}), \quad (23)$$

which corresponds to the displacement field around a rigid particle in far-field approximation.

IV. DISPLACEMENT FIELD INDUCED BY A UNIFORMLY TRANSLATED RIGID SPHERICAL INCLUSION

To facilitate our analytical approach, we now confine ourselves to rigid spherical particles embedded in the elastic matrix. The center of such a sphere of volume V is located at position $\mathbf{r}_0$ and a is its radius. If an external force $\mathbf{F}$ uniformly translates the sphere, it creates a displacement field in the surrounding matrix. Assuming that the elastic matrix sticks to the surface ∂V of the sphere and that the displacement field vanishes at infinity, the boundary conditions for $\mathbf{u}(\mathbf{r})$ follow as

$$\mathbf{u}(\mathbf{r} \in \partial V) = \mathbf{U}, \quad \mathbf{u}(|\mathbf{r}| \to \infty) = \mathbf{0}. \quad (24)$$

Here $\mathbf{U}$ is the translation of the sphere caused by the external force, which due to the particle rigidity simultaneously applies for all its surface points.

The resulting displacement field can be expressed in terms of the elastic Green's function $\underline{\mathbf{G}}(\mathbf{r} - \mathbf{r}_0)$; see Eq. (14). The integral in Eq. (14), summing over all the contributions from the point forces on the particle surface at positions $\mathbf{r'} \in \partial V$, can for a sphere be calculated explicitly, see Ref. [52] for the case of low-Reynolds-number hydrodynamics. However, this is a lengthy calculation, and we follow the elegant approach outlined in Refs. [51] and [72].

Due to the linearity of the Navier-Cauchy equations Eq. (1), there is only one unique solution satisfying the prescribed boundary conditions. Assuming $\mathbf{F} \sim \mathbf{U}$ in the linear regime, an ansatz $\mathbf{u}(\mathbf{r}) \sim \underline{\mathbf{G}}(\mathbf{r} - \mathbf{r}_0) \cdot \mathbf{F} \sim \underline{\mathbf{G}}(\mathbf{r} - \mathbf{r}_0) \cdot \mathbf{U}$ appears plausible. Moreover, since on ∂V the displacement field $\mathbf{u}(\mathbf{r}) \sim \underline{\mathbf{G}}(\mathbf{r} - \mathbf{r}_0) \cdot \mathbf{U}$ must satisfy Eq. (24), on ∂V the overall multiplicand of $\mathbf{U}$ in this expression must be proportional to $\hat{\underline{\mathbf{I}}}$. This is accomplished by an additional differential operator acting on $\underline{\mathbf{G}}(\mathbf{r} - \mathbf{r}_0)$,

$$\left(1 + \frac{a^2}{6} \nabla^2 \right) \underline{\mathbf{G}}(\mathbf{r} - \mathbf{r}_0) \bigg|_{|\mathbf{r} - \mathbf{r}_0| = a} = \frac{5 - 6\nu}{24\pi(1 - \nu)\mu a} \hat{\underline{\mathbf{I}}}. \quad (25)$$

Altogether,

$$\mathbf{u}(\mathbf{r}) = \frac{24\pi(1 - \nu)\mu a}{5 - 6\nu} \left(1 + \frac{a^2}{6} \nabla^2 \right) \underline{\mathbf{G}}(\mathbf{r} - \mathbf{r}_0) \cdot \mathbf{U} \quad (26)$$

satisfies the boundary conditions Eq. (24) as well as Eq. (1) and thus, due to the uniqueness of the solution, is the desired result.

For $a \to 0$ and $|\mathbf{r} - \mathbf{r}_0| > a$, the contribution $\frac{a^2}{6} \nabla^2$ becomes negligible and we must reproduce Eq. (5). In this way, we find

$$\mathbf{F} = \frac{24\pi(1 - \nu)\mu a}{5 - 6\nu} \mathbf{U} \quad (27)$$

or, equivalently,

$$\mathbf{u}(\mathbf{r} \in \partial V) = \mathbf{U} = \frac{5 - 6\nu}{24\pi(1 - \nu)\mu a} \mathbf{F}. \quad (28)$$

As a consequence, we may rewrite Eq. (26) as

$$\mathbf{u}(\mathbf{r}) = \left(1 + \frac{a^2}{6} \nabla^2 \right) \underline{\mathbf{G}}(\mathbf{r} - \mathbf{r}_0) \cdot \mathbf{F}. \quad (29)$$

This is the elastic analogue to the hydrodynamic Stokes flow [52].

Since, as we just argued, the solution in Eq. (29) is exact, we can for a spherical particle insert it into Eq. (14) to find for $|\mathbf{r} - \mathbf{r}_0| \geqslant a$ the relation

$$\int_{\partial V} \underline{\mathbf{G}}(\mathbf{r} - \mathbf{r'}) \cdot \mathbf{f}(\mathbf{r'}) dS' = \left(1 + \frac{a^2}{6} \nabla^2 \right) \underline{\mathbf{G}}(\mathbf{r} - \mathbf{r}_0) \cdot \mathbf{F}, \quad (30)$$

which we will need later.

V. DISPLACEMENT FIELD INDUCED BY A UNIFORMLY ROTATED RIGID SPHERICAL INCLUSION

In a similar way, we can ask for the displacement field generated in an elastic matrix by a uniformly rotated rigid spherical inclusion at position $\mathbf{r}_0$. For this purpose, we consider an external torque $\mathbf{T}$ acting on the inclusion (see Refs. [51] and [52] for the low-Reynolds-number hydrodynamic and Ref. [72] for the elastic case). The rotation of the particle is quantified by the absolute (static) rotation vector $\mathbf{\Omega}$. Then the boundary conditions on the surface ∂V of the particle and at infinity read

$$\mathbf{u}(\mathbf{r} \in \partial V) = \mathbf{\Omega} \times (\mathbf{r} - \mathbf{r}_0), \quad \mathbf{u}(|\mathbf{r}| \to \infty) = \mathbf{0}. \quad (31)$$

Inserting the displacement field

$$\mathbf{u}(\mathbf{r}) = \left(\frac{a}{|\mathbf{r} - \mathbf{r}_0|} \right)^3 \mathbf{\Omega} \times (\mathbf{r} - \mathbf{r}_0) \quad (32)$$

into these boundary conditions as well as into Eq. (1) confirms that it is the unique solution of the problem. As will be shown in Sec. VI, see Eq. (53), the torque that is externally imposed on the inclusion is related to the rotation vector $\boldsymbol{\Omega}$ via

$$\mathbf{T} = 8\pi\mu a^3 \boldsymbol{\Omega}, \tag{33}$$

with a the radius of the sphere.

VI. FAXÉN'S LAWS

In low-Reynolds-number hydrodynamics, Faxén's laws describe how a spherical particle is translated, rotated, and which stresses act onto it in an imposed fluid flow [51,52,67]. The fluid is typically considered as incompressible.

Due to the similarities of the underlying equations, the procedure can be transferred to the elastic case. That is, we now consider an (externally) imposed deformation of our elastic matrix as described by a displacement field $\mathbf{u}(\mathbf{r})$. We then calculate how a rigid spherical particle embedded in the elastic matrix and exposed to this displacement field is translated, rotated, and which stresses act onto it. A possible *compressibility* of the elastic matrix is readily included. Such elastic Faxén laws have been outlined before [65,66]. Here, we present an explicit derivation by direct calculation. We adapt the hydrodynamic approach in Refs. [52] and [67] by transferring it to the elastic case.

We consider a rigid spherical inclusion of radius a embedded in the elastic matrix at position $\mathbf{r}_0$. In addition to the displacement field imposed onto the matrix, the embedded particle may still be subject to external forces or torques. Moreover, its rigidity resists the imposed matrix deformations. Therefore, its surface elements exert additional forces onto the matrix, summarized again by the surface force density $\mathbf{f}(\mathbf{r}')$ with $\mathbf{r}' \in \partial V$ and ∂V the surface of the particle. The additional displacement field resulting from $\mathbf{f}(\mathbf{r}')$ is calculated according to Eq. (14). Due to the linearity of Eq. (1), the different contributions to the overall displacement field simply superimpose. Describing again translations and rotations of the sphere by a translation vector $\mathbf{U}$ and a (static) rotation vector $\boldsymbol{\Omega}$, respectively, we obtain in total for the surface points $\mathbf{r} \in \partial V$ the stick boundary condition,

$$U_i + [\boldsymbol{\Omega} \times (\mathbf{r} - \mathbf{r}_0)]_i = \int_{\partial V} G_{ij}(\mathbf{r} - \mathbf{r}')f_j(\mathbf{r}')dS' + u_i(\mathbf{r}). \tag{34}$$

On the left-hand side of this equation, we find the displacements of the surface points of the sphere by the rigid translation $\mathbf{U}$ and the rigid rotation $\boldsymbol{\Omega}$. For each point $\mathbf{r} \in \partial V$, these displacements must be identical to the displacements of the matrix stuck to the sphere surface. The total matrix displacement on the surface is given on the right-hand side. There, the first term, i.e., the integral, includes all contributions to the matrix displacements due to the surface force density $\mathbf{f}(\mathbf{r}')$ exerted by the particle onto the matrix. The second term, i.e., $\mathbf{u}(\mathbf{r})$, corresponds to the (externally) imposed deformation field. At this point, one may be concerned with the validity of the equation, as the Green's function $\underline{\mathbf{G}}$ was derived for an infinitely extended matrix. This seems to contradict the presence of a finite-sized rigid embedded sphere. However, for our calculation it is irrelevant whether we consider the sphere

to be rigid inside, or whether it is filled with deformable elastic matrix material as well. The only important point is that the surface shell, which may be considered as infinitely thin, is rigidly translated and rotated as one rigid object.

Integration of both sides of Eq. (34) over ∂V gives

$$4\pi a^2 U_i = \int_{\partial V} \int_{\partial V} G_{ij}(\mathbf{r} - \mathbf{r}')f_j(\mathbf{r}')dS'dS + \int_{\partial V} u_i(\mathbf{r})dS. \tag{35}$$

Using Eq. (30), the first term on the right-hand side can be connected to the displacement of the sphere due to an external force $\mathbf{F}$. On ∂V, the resulting expression is further simplified using Eqs. (28) and (29).

For the evaluation of the second term on the right-hand side, we insert the Taylor expansion of $u_i(\mathbf{r})$ around the particle center at $\mathbf{r} = \mathbf{r}_0$,

$$u_i(\mathbf{r}) = u_i(\mathbf{r}_0) + (\mathbf{r} - \mathbf{r}_0)_j [\nabla_j u_i(\mathbf{r})]_{\mathbf{r}=\mathbf{r}_0}$$
$$+ \frac{1}{2}(\mathbf{r} - \mathbf{r}_0)_j(\mathbf{r} - \mathbf{r}_0)_k [\nabla_j \nabla_k u_i(\mathbf{r})]_{\mathbf{r}=\mathbf{r}_0}$$
$$+ \frac{1}{3!}(\mathbf{r}-\mathbf{r}_0)_j(\mathbf{r}-\mathbf{r}_0)_k(\mathbf{r}-\mathbf{r}_0)_l [\nabla_j \nabla_k \nabla_l u_i(\mathbf{r})]_{\mathbf{r}=\mathbf{r}_0} + \dots \tag{36}$$

Since there are no body forces generating the imposed field $\mathbf{u}(\mathbf{r})$ at $\mathbf{r} = \mathbf{r}_0$, Eq. (3) must hold, i.e., $\nabla^4 \mathbf{u}(\mathbf{r} = \mathbf{r}_0) = \mathbf{0}$. Thus, under the integral, terms of fourth and higher even order in ∇ must vanish due to isotropy. Furthermore, all odd terms in $(\mathbf{r} - \mathbf{r}_0)$ of the Taylor series must vanish during integration due to symmetry. Taking this into account, the second term on the right-hand side of Eq. (35) can be evaluated as

$$\int_{\partial V} u_i(\mathbf{r})\, dS = 4\pi a^2 u_i(\mathbf{r}_0)$$
$$+ \frac{1}{2} \int_{\partial V} (\mathbf{r} - \mathbf{r}_0)_j(\mathbf{r} - \mathbf{r}_0)_k [\nabla_j \nabla_k u_i(\mathbf{r})]_{\mathbf{r}=\mathbf{r}_0} dS$$
$$= 4\pi a^2 \left(1 + \frac{a^2}{6}\nabla^2\right)u_i(\mathbf{r})\bigg|_{\mathbf{r}=\mathbf{r}_0}. \tag{37}$$

Here, in the step to the last line, we have used that

$$\int_{\partial V} r_j r_k\, dS = \frac{4\pi a^4}{3}\delta_{jk}. \tag{38}$$

Collecting all results, Eq. (35) leads to

$$\mathbf{U} = \frac{5 - 6\nu}{24\pi(1 - \nu)\mu a}\mathbf{F} + \left(1 + \frac{a^2}{6}\nabla^2\right)\mathbf{u}(\mathbf{r})\bigg|_{\mathbf{r}=\mathbf{r}_0}. \tag{39}$$

In this expression, the first contribution to the rigid translation is caused by the external force $\mathbf{F}$, see our previous result in Eq. (28). The second contribution is due to the imposed matrix displacement field $\mathbf{u}(\mathbf{r})$. As we can see, the sphere is not simply advected by the imposed displacement. Due to its finite size, the additional contribution $\frac{a^2}{6}\nabla^2$ arises.

In the absence of an external force on the sphere, i.e., for $\mathbf{F} = \mathbf{0}$, we obtain what is referred to as Faxén's first law in hydrodynamics [67]:

$$\mathbf{U}^{\text{Faxén}} = \left(1 + \frac{a^2}{6}\nabla^2\right)\mathbf{u}(\mathbf{r})\bigg|_{\mathbf{r}=\mathbf{r}_0}. \tag{40}$$

This relation describes the rigid translation of a rigid sphere in an imposed deformation of the surrounding matrix.

To obtain corresponding expressions for the rotation vector and for the stresslet, we multiply both sides of Eq. (34) with $(\mathbf{r} - \mathbf{r}_0)_k$ and integrate over ∂V,

$$
\int_{\partial V} (\mathbf{r} - \mathbf{r}_0)_k [\mathbf{\Omega} \times (\mathbf{r} - \mathbf{r}_0)]_i \, dS
$$
$$
= \int_{\partial V} \int_{\partial V} (\mathbf{r} - \mathbf{r}_0)_k \, G_{ij}(\mathbf{r} - \mathbf{r}') f_j(\mathbf{r}') \, dS dS'
$$
$$
+ \int_{\partial V} (\mathbf{r} - \mathbf{r}_0)_k u_i(\mathbf{r}) \, dS. \tag{41}
$$

The integral on the left-hand side is easily evaluated using Eq. (38) and reads

$$
\frac{4\pi a^4}{3} \epsilon_{ilk} \Omega_l. \tag{42}
$$

In order to calculate the inner integral of the first term on the right-hand side, we substitute $\mathbf{r}'' = \mathbf{r} - \mathbf{r}_0$ and express

the integral in terms of the Fourier transform of the Green's function,

$$
\int_{\partial V} G_{ij}(\mathbf{r} - \mathbf{r}') (\mathbf{r} - \mathbf{r}_0)_k \, dS
$$
$$
= \int_{\partial V} G_{ij}(\mathbf{r}'' - \mathbf{r}' + \mathbf{r}_0) r_k'' \, dS''
$$
$$
= \frac{1}{(2\pi)^3} \int_{\partial V} dS'' \int d^3 k \, \tilde{G}_{ij}(\mathbf{k}) r_k'' e^{i\mathbf{k}\cdot(\mathbf{r}'' - \mathbf{r}' + \mathbf{r}_0)}. \tag{43}
$$

Now the integral with respect to $\mathbf{r}''$ can be evaluated as

$$
\int_{\partial V} dS'' e^{i\mathbf{k}\cdot\mathbf{r}''} r_k'' = -i \nabla_{\mathbf{k},k} \int_{\partial V} dS'' e^{i\mathbf{k}\cdot\mathbf{r}''}
$$
$$
= -4\pi i a^2 \hat{k}_k \frac{d}{dk} \frac{\sin(ka)}{ka}. \tag{44}
$$

The integral $\int d^3 k$ in Eq. (43) can be split into $\int dS(\hat{\mathbf{k}}) \int_0^\infty k^2 dk$. Inserting Eq. (A3), Eq. (43) becomes

$$
\frac{2\pi^2 \mu}{a^2} \int_{\partial V} G_{ij}(\mathbf{r} - \mathbf{r}') (\mathbf{r} - \mathbf{r}_0)_k \, dS
$$
$$
= -i \int_{\partial V} dS(\hat{\mathbf{k}}) \left[\delta_{ij} - \frac{1}{2(1-\nu)} \hat{k}_i \hat{k}_j \right] \hat{k}_k \int_0^\infty dk \, e^{ik\hat{\mathbf{k}}\cdot(\mathbf{r}_0 - \mathbf{r}')} \frac{d}{dk} \frac{\sin(ka)}{ka}
$$
$$
= -i \int_{\partial V} dS(\hat{\mathbf{k}}) \left[\delta_{ij} - \frac{1}{2(1-\nu)} \hat{k}_i \hat{k}_j \right] \hat{k}_k \left[\frac{\sin(ka)}{ka} e^{ik\hat{\mathbf{k}}\cdot(\mathbf{r}_0 - \mathbf{r}')} \Big|_0^\infty - i\hat{k}_l (\mathbf{r}_0 - \mathbf{r}')_l \int_0^\infty dk \, \frac{\sin(ka)}{ka} e^{ik\hat{\mathbf{k}}\cdot(\mathbf{r}_0 - \mathbf{r}')} \right]
$$
$$
= \int_{\partial V} dS(\hat{\mathbf{k}}) \left[\delta_{ij} - \frac{1}{2(1-\nu)} \hat{k}_i \hat{k}_j \right] \hat{k}_k \hat{k}_l (\mathbf{r}' - \mathbf{r}_0)_l \int_0^\infty dk \, \frac{\sin(ka)}{ka} e^{ik\hat{\mathbf{k}}\cdot(\mathbf{r}_0 - \mathbf{r}')}. \tag{45}
$$

In the last line, the imaginary part is odd in $\hat{\mathbf{k}}$ and therefore vanishes upon integration. The remaining real part is an even function in both $\hat{\mathbf{k}}$ and k, so that, under the $\int dS(\hat{\mathbf{k}})$ integral, we may rewrite the $\int dk$ integral as

$$
\frac{1}{2} \int_{-\infty}^\infty dk \, \frac{\sin(ka)}{ka} e^{ik\hat{\mathbf{k}}\cdot(\mathbf{r}_0 - \mathbf{r}')} = \begin{cases} \frac{\pi}{2a}, & \text{for } -1 < \frac{\hat{\mathbf{k}}\cdot(\mathbf{r}' - \mathbf{r}_0)}{a} < 1, \\ 0, & \text{otherwise}; \end{cases} \tag{46}
$$

see Appendix B. We obtain

$$
\int_{\partial V} G_{ij}(\mathbf{r} - \mathbf{r}') (\mathbf{r} - \mathbf{r}_0)_k \, dS = \frac{a}{4\pi\mu} (\mathbf{r}' - \mathbf{r}_0)_l \int_{\Delta S} dS(\hat{\mathbf{k}}) \left(\delta_{ij} - \frac{1}{2(1-\nu)} \hat{k}_i \hat{k}_j \right) \hat{k}_k \hat{k}_l, \tag{47}
$$

where the surface of integration ΔS is given by

$$
\Delta S = \left\{ \hat{\mathbf{k}} \, \middle| \, -1 < \frac{\hat{\mathbf{k}} \cdot (\mathbf{r}' - \mathbf{r}_0)}{a} < 1 \right\}. \tag{48}
$$

Since $\mathbf{r}'$ is located on the surface of the inclusion, i.e., $|\mathbf{r}' - \mathbf{r}_0| = a$, ΔS corresponds to the surface of the unit sphere. Using Eq. (38) (for $\hat{\mathbf{k}}$ instead of $\mathbf{r}$) and

$$
\int_{\Delta S} \hat{k}_i \hat{k}_j \hat{k}_k \hat{k}_l \, dS(\hat{\mathbf{k}}) = \frac{4\pi}{15} (\delta_{ij}\delta_{kl} + \delta_{ik}\delta_{jl} + \delta_{il}\delta_{jk}) \tag{49}
$$

finally leads to

$$
\int_{\partial V} (\mathbf{r} - \mathbf{r}_0)_k G_{ij}(\mathbf{r} - \mathbf{r}') f_j(\mathbf{r}') \, dS = \frac{a}{15\mu} \left\{ 5(\mathbf{r}' - \mathbf{r}_0)_k f_i - \frac{1}{2(1-\nu)} [(\mathbf{r}' - \mathbf{r}_0)_k f_i + (\mathbf{r}' - \mathbf{r}_0)_i f_k + (\mathbf{r}' - \mathbf{r}_0)_l f_l \delta_{ik}] \right\}. \tag{50}
$$

The second term on the right-hand side of Eq. (41) can be evaluated by inserting the Taylor expansion of $\mathbf{u}(\mathbf{r})$ from Eq. (36),

$$
\int_{\partial V} (\mathbf{r} - \mathbf{r}_0)_k u_i(\mathbf{r}) \, dS = \int_{\partial V} (\mathbf{r} - \mathbf{r}_0)_k (\mathbf{r} - \mathbf{r}_0)_j [\nabla_j u_i(\mathbf{r})]_{\mathbf{r}=\mathbf{r}_0} dS
$$

$$
+ \frac{1}{6} \int_{\partial V} (\mathbf{r} - \mathbf{r}_0)_k (\mathbf{r} - \mathbf{r}_0)_j (\mathbf{r} - \mathbf{r}_0)_l (\mathbf{r} - \mathbf{r}_0)_m [\nabla_j \nabla_l \nabla_m u_i(\mathbf{r})]_{\mathbf{r}=\mathbf{r}_0} dS
$$

$$
= \frac{4\pi a^4}{3} \left(1 + \frac{a^2}{10} \nabla^2\right) \nabla_k u_i(\mathbf{r}) \Big|_{\mathbf{r}=\mathbf{r}_0}, \tag{51}
$$

where again we have used Eqs. (38) and (49) [for $(\mathbf{r} - \mathbf{r}_0)$ instead of $\hat{\mathbf{k}}$ in the latter]. The other terms in the expansion again vanish due to isotropy and symmetry upon integration.

Altogether, combining Eqs. (41), (42), (50), and (51), we find

$$
\frac{4\pi a^4}{3} \epsilon_{ilk} \Omega_l = \frac{a}{15\mu} \int_{\partial V} dS' \left\{ 5(\mathbf{r}' - \mathbf{r}_0)_k f_i - \frac{1}{2(1-\nu)} [(\mathbf{r}' - \mathbf{r}_0)_k f_i + (\mathbf{r}' - \mathbf{r}_0)_i f_k + (\mathbf{r}' - \mathbf{r}_0)_l f_l \delta_{ik}] \right\}
$$

$$
+ \frac{4\pi a^4}{3} \left(1 + \frac{a^2}{10} \nabla^2\right) \nabla_k u_i(\mathbf{r}) \Big|_{\mathbf{r}=\mathbf{r}_0}. \tag{52}
$$

This tensor equation can be split into a symmetric and an antisymmetric part. First, we calculate the antisymmetric part by multiplying Eq. (52) by ϵ_{ijk}. Since there are no body forces generating the imposed field $\mathbf{u}(\mathbf{r})$ at $\mathbf{r} = \mathbf{r}_0$, Eq. (4) most hold for the last term, i.e., $\nabla \times \nabla^2 \mathbf{u}(\mathbf{r} = \mathbf{r}_0) = \mathbf{0}$. Therefore, the $\frac{a^2}{10} \nabla^2$-term in Eq. (52) vanishes. Using the definition of the torque from Eq. (21), we obtain

$$
\mathbf{\Omega} = \frac{1}{8\pi \mu a^3} \mathbf{T} + \frac{1}{2} \nabla \times \mathbf{u}(\mathbf{r}) \Big|_{\mathbf{r}=\mathbf{r}_0}. \tag{53}
$$

$\mathbf{T}$ corresponds to an external torque acting onto the sphere, which is transmitted by the sphere onto the surrounding matrix (with the reference point of the torque at the center of the sphere).

Similarly to the previous case of rigid translations, in the absence of an external torque acting on the sphere, i.e., for $\mathbf{T} = \mathbf{0}$, we obtain a relation referred to as Faxén's second law in hydrodynamics [67]:

$$
\mathbf{\Omega}^{\text{Faxén}} = \frac{1}{2} \nabla \times \mathbf{u}(\mathbf{r}) \Big|_{\mathbf{r}=\mathbf{r}_0}. \tag{54}
$$

This relation quantifies the (static) rigid rotation of a rigid sphere in an imposed deformation of the surrounding matrix.

Finally, we calculate the symmetric part of Eq. (52). The $\mathbf{\Omega}$-term vanishes because of its antisymmetry. Thus, we find

$$
0 = \frac{a}{15\mu} \frac{1}{2(1-\nu)} \int_{\partial V} dS' \left\{ (4 - 5\nu) \left[(\mathbf{r}' - \mathbf{r}_0)_i f_k + (\mathbf{r}' - \mathbf{r}_0)_k f_i \right] - (\mathbf{r}' - \mathbf{r}_0)_j f_j \delta_{ik} \right\}
$$

$$
+ \frac{4\pi a^4}{3} \left(1 + \frac{a^2}{10} \nabla^2\right) \frac{1}{2} [\nabla_i u_k(\mathbf{r}) + \nabla_k u_i(\mathbf{r})] \Big|_{\mathbf{r}=\mathbf{r}_0}
$$

$$
=: \frac{1}{2}(A_{ik} + A_{ki}). \tag{55}
$$

To obtain an expression solely for the stresslet as defined in Eq. (20), we add a vanishing trace term

$$
\frac{1}{5(1-2\nu)} A_{jj} \delta_{ik} = \frac{a}{15\mu} \frac{1}{2(1-\nu)} \int_{\partial V} dS' (\mathbf{r}' - \mathbf{r}_0)_j f_j \delta_{ik} + \frac{4\pi a^4}{15} \left(1 + \frac{a^2}{10} \nabla^2\right) \frac{1}{1-2\nu} \nabla_j u_j(\mathbf{r}) \delta_{ik} \Big|_{\mathbf{r}=\mathbf{r}_0}, \tag{56}
$$

leading to

$$
0 = \frac{1}{2}(A_{ik} + A_{ki}) + \frac{1}{5(1-2\nu)} A_{jj} \delta_{ik}. \tag{57}
$$

Then, the definition of S_{ik} appears in Eq. (57). Solving for S_{ik}, we find the stresslet as

$$
\underline{\mathbf{S}} = -\frac{4\pi(1-\nu)\mu a^3}{4 - 5\nu} \left(1 + \frac{a^2}{10} \nabla^2\right) \left(\frac{1}{1-2\nu} \hat{\mathbf{I}} \nabla \cdot \mathbf{u}(\mathbf{r}) + \frac{5}{2} \{\nabla \mathbf{u}(\mathbf{r}) + [\nabla \mathbf{u}(\mathbf{r})]^T\}\right) \Big|_{\mathbf{r}=\mathbf{r}_0}, \tag{58}
$$

where the superscript $(\bullet)^T$ marks the transpose.

Equation (58) expresses the stress that a rigid spherical inclusion exerts onto the surrounding matrix in the imposed displacement field $\mathbf{u}(\mathbf{r})$ of the matrix. The matrix deformation is imposed from elsewhere, that is, not by the spherical inclusion itself. However, the inclusion due to its rigidity resists this deformation. This resistance leads to the described stresslet.

Vice versa, the stresslet that the matrix exerts onto the particle is given by

$$\underline{\mathbf{S}}^{\text{Faxén}} = -\underline{\mathbf{S}}, \tag{59}$$

which together with Eq. (58) may be referred to as Faxén's third law and was derived by Batchelor in the hydrodynamic case [67].

VII. DISPLACEABILITY AND ROTATEABILITY MATRIX

Now we have all the ingredients to consider the coupled displacements and rotations of N spherical inclusions embedded in the infinitely extended homogeneous elastic medium. For simplicity, we consider identical spheres of radius a, labeled by $1,...,N$.

We here adhere to the following cause-and-effect chain. Each spherical inclusion j is subject to an external force $\mathbf{F}_j$ and an external torque $\mathbf{T}_j$, $j = 1,...,N$. As a consequence of these forces and torques, the inclusions are displaced and rotated by rigid translation vectors $\mathbf{U}_i$ and rigid rotation vectors $\boldsymbol{\Omega}_i$, respectively, $i = 1,...,N$. Moreover, the spheres transmit the forces and torques to the surrounding elastic medium, causing additional deformations in their environment. Other inclusions are exposed to these induced deformations and counteract due to their rigidity. This leads to further distortions, acting back on all other rigid spheres that likewise resist induced deformations, resulting in mutually coupled particle translations and rotations. In the following, we derive analytical expressions for these translations and rotations, using the external forces and torques as an input.

In formal analogy to the hydrodynamic mobility matrices [52,73], we can define *elastic displaceability and rotateability matrices*. Given the external (quasi)static forces $\mathbf{F}_j$ and (quasi)static torques $\mathbf{T}_j$, $j = 1,...,N$, applied to the spherical inclusions, these matrices directly express the caused displacements $\mathbf{U}_i$ and rotations $\boldsymbol{\Omega}_i$ in the resulting situation of new (quasi)static equilibrium, $i = 1,...,N$:

$$\begin{pmatrix} \mathbf{U}_1 \\ \vdots \\ \mathbf{U}_N \\ \boldsymbol{\Omega}_1 \\ \vdots \\ \boldsymbol{\Omega}_N \end{pmatrix} = \begin{pmatrix} \underline{\mathbf{M}}_{11}^{\text{tt}} & \cdots & \underline{\mathbf{M}}_{1N}^{\text{tt}} & \underline{\mathbf{M}}_{11}^{\text{tr}} & \cdots & \underline{\mathbf{M}}_{1N}^{\text{tr}} \\ \vdots & \ddots & \vdots & \vdots & \ddots & \vdots \\ \underline{\mathbf{M}}_{N1}^{\text{tt}} & \cdots & \underline{\mathbf{M}}_{NN}^{\text{tt}} & \underline{\mathbf{M}}_{N1}^{\text{tr}} & \cdots & \underline{\mathbf{M}}_{NN}^{\text{tr}} \\ \underline{\mathbf{M}}_{11}^{\text{rt}} & \cdots & \underline{\mathbf{M}}_{1N}^{\text{rt}} & \underline{\mathbf{M}}_{11}^{\text{rr}} & \cdots & \underline{\mathbf{M}}_{1N}^{\text{rr}} \\ \vdots & \ddots & \vdots & \vdots & \ddots & \vdots \\ \underline{\mathbf{M}}_{N1}^{\text{rt}} & \cdots & \underline{\mathbf{M}}_{NN}^{\text{rt}} & \underline{\mathbf{M}}_{N1}^{\text{rr}} & \cdots & \underline{\mathbf{M}}_{NN}^{\text{rr}} \end{pmatrix} \cdot \begin{pmatrix} \mathbf{F}_1 \\ \vdots \\ \mathbf{F}_N \\ \mathbf{T}_1 \\ \vdots \\ \mathbf{T}_N \end{pmatrix}. \tag{60}$$

Here, the submatrices $\underline{\mathbf{M}}_{ij}^{\text{tt}}$ express how the particles are translated due to the forces acting on all the particles

(translation–translation coupling, $i,j = 1,...,N$). Their components have been derived already in a previous work [14]. The submatrices $\underline{\mathbf{M}}_{ij}^{\text{tr}}$ include contributions to the translations due to the torques acting on the inclusions (translation–rotation coupling). Similarly, the submatrices $\underline{\mathbf{M}}_{ij}^{\text{rt}}$ determine how forces acting on the particles lead to their rotations (rotation–translation coupling). The cause of rotations by torques is given by the submatrices $\underline{\mathbf{M}}_{ij}^{\text{rr}}$ (rotation–rotation coupling).

We stress that the role of the surrounding elastic medium is implicitly contained in these matrices. Their components will solely depend on the configuration of the rigid inclusions. Therefore, they significantly facilitate the problem of calculating the coupled displacements and rotations described above. It is not necessary any longer to explicitly calculate the displacement field $\mathbf{u}(\mathbf{r})$ of the surrounding medium once the expressions for these matrices have been derived.

Below, we shall explicitly perform this derivation for the components $\underline{\mathbf{M}}_{ij}^{\text{tt}}$, $\underline{\mathbf{M}}_{ij}^{\text{tr}}$, $\underline{\mathbf{M}}_{ij}^{\text{rt}}$, and $\underline{\mathbf{M}}_{ij}^{\text{rr}}$ as an expansion in the inverse separation distance of the inclusions. Here, we proceed up to (including) fourth order. This comprises pairwise interactions mediated by the surrounding elastic medium, see Sec. VIII, and three-body interactions, see Sec. IX.

VIII. TWO-BODY INTERACTIONS

In the following, we start from the forces and torques acting on the inclusions, which as a consequence leads to the coupled particle translations and rotations. Our approach adapts the *method of reflections* from the hydrodynamic literature as presented in Ref. [52]. In addition to that, we here explicitly include the role of imposed torques as for instance exerted by external magnetic fields on magnetically anisotropic inclusions. Moreover, we take into account the rigidity of the inclusions directly via the stresslets that follow from their resistance to deformations [51,67].

The initial forces and torques acting on the inclusions are either imposed externally, or they are induced between the inclusions from outside. These are *not* the forces and torques exerted by the elastic matrix onto the inclusions. For clarity, we consider the influence of the imposed or induced forces and torques separately in two steps. Due to the linearity of the governing equations, the results of these two steps can in the end simply be added/superimposed.

A. Forces imposed on or induced between the inclusions

In the following, we consider two rigid spherical inclusions i and j, both of radius a. They are located at positions $\mathbf{r}_i$ and $\mathbf{r}_j$, respectively. The forces $\mathbf{F}_i$ and $\mathbf{F}_j$ are externally applied to the spheres i and j, respectively, or induced between them. As indicated before, we will proceed below by an expansion in the inverse separation distance between the two spheres.

To zeroth order, the spheres are thus effectively considered to be infinitely far away from each other. Consequently, the interactions between the two spheres via the surrounding elastic matrix do not enter. The actual translations of the spheres, $\mathbf{U}_i^{(0)}$ and $\mathbf{U}_j^{(0)}$, respectively, are then given by the
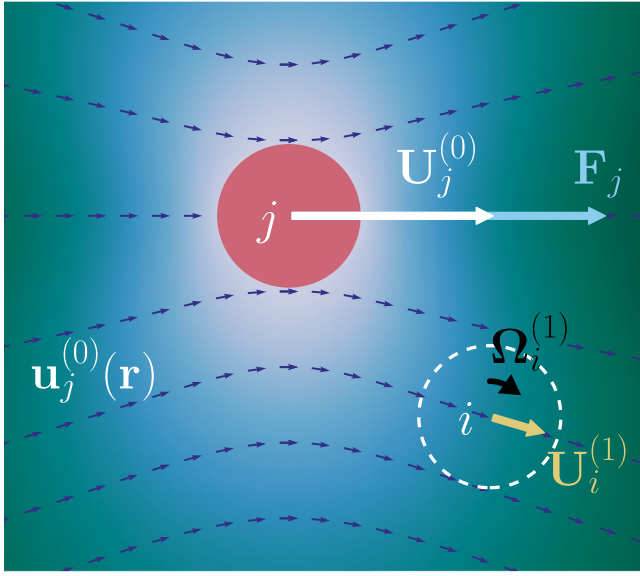
FIG. 2. Illustration of the immediate effect that the displacement of sphere j has on the translation and rotation of another sphere i. A force $\mathbf{F}_j$ is externally imposed on sphere j. As a consequence, sphere j gets rigidly translated as given by $\mathbf{U}_j^{(0)}$; see Eq. (62). Moreover, the surrounding matrix is distorted, as described by the displacement field $\mathbf{u}_j^{(0)}(\mathbf{r})$; see Eq. (64). The local directions of $\mathbf{u}_j^{(0)}(\mathbf{r})$ are indicated by the small arrows that, for visibility, are rescaled to identical length. We indicated the local magnitude of $\mathbf{u}_j^{(0)}(\mathbf{r})$ by background color, where brighter color represents higher magnitude and the color values follow an arc-tangent scale. Sphere i is exposed to the induced displacement field $\mathbf{u}_j^{(0)}(\mathbf{r})$ and therefore gets translated as denoted by $\mathbf{U}_i^{(1)}$ and rotated as denoted by $\mathbf{\Omega}_i^{(1)}$. These quantities can be calculated from $\mathbf{u}_j^{(0)}(\mathbf{r})$ via Eqs. (65) and (66), respectively, leading to Eqs. (72) and (73). Overall, in this way we obtain the corresponding contributions to the *displaceability and rotateability matrices* $\underline{\mathbf{M}}_{i=j}^{\mathrm{tt}}$, $\underline{\mathbf{M}}_{i\neq j}^{\mathrm{tt}}$, $\underline{\mathbf{M}}_{i=j}^{\mathrm{rt}}$, and $\underline{\mathbf{M}}_{i\neq j}^{\mathrm{rt}}$ in Eqs. (78), (79), (81), and (82), respectively, up to inverse quartic order in the particle distances.

solution for isolated spherical inclusions, see Eq. (28), and read

$$\mathbf{U}_i^{(0)} = \mathbf{u}_i^{(0)}(\mathbf{r} \in \partial V_i) = \frac{5 - 6\nu}{24\pi(1-\nu)\mu a}\mathbf{F}_i, \qquad (61)$$

$$\mathbf{U}_j^{(0)} = \mathbf{u}_j^{(0)}(\mathbf{r} \in \partial V_j) = \frac{5 - 6\nu}{24\pi(1-\nu)\mu a}\mathbf{F}_j. \qquad (62)$$

Furthermore, to zeroth order, the induced displacement field of the elastic matrix around each sphere i and j has been calculated in Eq. (29), i.e.,

$$\mathbf{u}_i^{(0)}(\mathbf{r}) = \left(1 + \frac{a^2}{6}\nabla^2\right)\underline{\mathbf{G}}(\mathbf{r} - \mathbf{r}_i) \cdot \mathbf{F}_i, \qquad (63)$$

$$\mathbf{u}_j^{(0)}(\mathbf{r}) = \left(1 + \frac{a^2}{6}\nabla^2\right)\underline{\mathbf{G}}(\mathbf{r} - \mathbf{r}_j) \cdot \mathbf{F}_j. \qquad (64)$$

In Fig. 2, $\mathbf{u}_j^{(0)}(\mathbf{r})$ is indicated by the small arrows.

Next, we take into account the mutual interactions between the two spheres mediated by the surrounding elastic matrix. For example, we consider particle i that is embedded in the elastic matrix. Thus it is exposed to the displacement field

$\mathbf{u}_j^{(0)}(\mathbf{r})$ that results from the force $\mathbf{F}_j$ acting on sphere j. An additional translation $\mathbf{U}_i^{(1)}$ and rotation $\mathbf{\Omega}_i^{(1)}$ of sphere i are induced in this way, which we can calculate from the Faxén relations, Eqs. (40) and (54). They read

$$\mathbf{U}_i^{(1)} = \left.\left(1 + \frac{a^2}{6}\nabla^2\right)\mathbf{u}_j^{(0)}(\mathbf{r})\right|_{\mathbf{r}=\mathbf{r}_i}, \qquad (65)$$

$$\mathbf{\Omega}_i^{(1)} = \left.\frac{1}{2}\nabla \times \mathbf{u}_j^{(0)}(\mathbf{r})\right|_{\mathbf{r}=\mathbf{r}_i}. \qquad (66)$$

That is, $\mathbf{u}_j^{(0)}(\mathbf{r})$ now plays the role of the imposed matrix displacement field $\mathbf{u}(\mathbf{r})$ in Eqs. (40) and (54).

In general, the displacement field $\mathbf{u}_j^{(0)}(\mathbf{r})$ would tend to deform sphere i. In other words, a stress is exerted on particle i. Yet, because of its rigidity, sphere i resists this deformation. As a consequence, the overall displacement field induced by sphere j, i.e., $\mathbf{u}_j^{(0)}(\mathbf{r})$, is disturbed via the presence of sphere i. We can find this disturbance from the stress that the rigid sphere i itself exerts back onto the matrix. The corresponding stresslet follows from Eq. (58) and here takes the form

$$\underline{\mathbf{S}}_i^{(1)} = -\frac{4\pi(1-\nu)\mu a^3}{4 - 5\nu}\left(1 + \frac{a^2}{10}\nabla^2\right)\left(\frac{1}{1-2\nu}\hat{\mathbf{I}}\nabla \cdot \mathbf{u}_j^{(0)}(\mathbf{r})\right.$$
$$\left.\left. + \frac{5}{2}\left\{\nabla\mathbf{u}_j^{(0)}(\mathbf{r}) + \left[\nabla\mathbf{u}_j^{(0)}(\mathbf{r})\right]^T\right\}\right)\right|_{\mathbf{r}=\mathbf{r}_i}. \qquad (67)$$

Analogous expressions for sphere j are obtained by swapping the indices $i \leftrightarrow j$ in Eqs. (65)–(67).

We now proceed to improve our solution by iteration. For this purpose, we calculate the mentioned disturbances $\mathbf{u}_i^{(1)}(\mathbf{r})$ and $\mathbf{u}_j^{(1)}(\mathbf{r})$ that the stresslets $\underline{\mathbf{S}}_i^{(1)}$ and $\underline{\mathbf{S}}_j^{(1)}$ cause in the matrix, respectively. We find corresponding expressions from Eq. (23):

$$\mathbf{u}_i^{(1)}(\mathbf{r}) = -(\underline{\mathbf{S}}_i^{(1)} \cdot \nabla) \cdot \underline{\mathbf{G}}(\mathbf{r} - \mathbf{r}_i), \qquad (68)$$

$$\mathbf{u}_j^{(1)}(\mathbf{r}) = -(\underline{\mathbf{S}}_j^{(1)} \cdot \nabla) \cdot \underline{\mathbf{G}}(\mathbf{r} - \mathbf{r}_j). \qquad (69)$$

We should remark that Eq. (23) also contains the forces imposed on the inclusions. However, at this stage of iteration, they do not contribute. The direct influence of the forces has already been determined in Eqs. (61)–(64). The spheres simply follow the resulting induced displacement fields, without any additional extra net force or torque resistance, see Eqs. (65) and (66). Their only resistance is due to their rigidity as described above, which now enters Eqs. (68) and (69) in the form of the stresslets. Due to the linearity of the Navier-Cauchy equations, Eq. (1), the disturbances in Eqs. (68) and (69) can in the end simply be added/superimposed to the displacement fields in Eqs. (63) and (64).

In the next step, each sphere is now additionally exposed to one of these rigidity-induced displacement fields $\mathbf{u}_i^{(1)}(\mathbf{r})$ and $\mathbf{u}_j^{(1)}(\mathbf{r})$ created by the other sphere. This leads to yet another contribution to the translation ($\mathbf{U}_i^{(2)}$ and $\mathbf{U}_j^{(2)}$) and rotation ($\mathbf{\Omega}_i^{(2)}$ and $\mathbf{\Omega}_j^{(2)}$) of each sphere. Again, we can calculate these contributions from the Faxén laws, see Eqs. (40) and (54), now taking $\mathbf{u}_j^{(1)}(\mathbf{r})$ and $\mathbf{u}_i^{(1)}(\mathbf{r})$ as the imposed displacement fields,
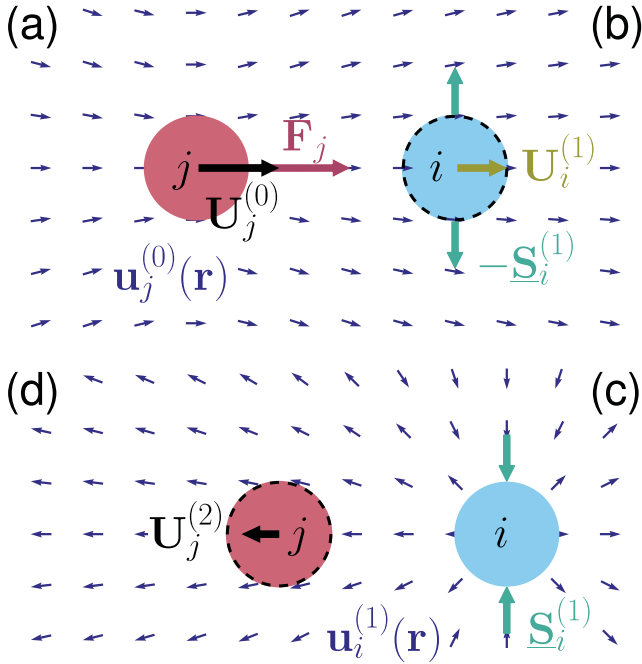
FIG. 3. Illustration of the rigidity-based *reflection* of an induced displacement field by another sphere. (a) As in Fig. 2, an externally imposed force $\mathbf{F}_j$ acts onto the spherical particle j. This directly results in the particle translation $\mathbf{U}_j^{(0)}$ and in the displacement field $\mathbf{u}_j^{(0)}(\mathbf{r})$ in the surrounding elastic matrix; see Eqs. (62), (64), and Fig. 2. The small arrows indicate the local direction of the induced displacement fields. (b) Particle i is exposed to the displacement field $\mathbf{u}_j^{(0)}(\mathbf{r})$ and is therefore translated by $\mathbf{U}_i^{(1)}$; see Eq. (65). Rotations are not considered here for simplicity. Simultaneously, the displacement field tends to deform particle i as given by the stresslet $-\underline{\mathbf{S}}_i^{(1)}$; see Eqs. (58) and (59). (c) However, the rigid particle i resists deformation and imposes the stresslet $\underline{\mathbf{S}}_i^{(1)}$ onto the surrounding elastic matrix; see Eq. (67). $\underline{\mathbf{S}}_i^{(1)}$ induces yet another displacement field $\mathbf{u}_i^{(1)}(\mathbf{r})$ in the elastic environment, see Eq. (68), which overlays the initial field $\mathbf{u}_j^{(0)}(\mathbf{r})$. In this way, the initial field $\mathbf{u}_j^{(0)}(\mathbf{r})$ gets partially *reflected* by the rigid particle i, leading to $\mathbf{u}_i^{(1)}(\mathbf{r})$. (d) Now, particle j is exposed to $\mathbf{u}_i^{(1)}(\mathbf{r})$. Its initial translation $\mathbf{U}_j^{(0)}$ thus gets corrected by a translation $\mathbf{U}_j^{(2)}$; see Eq. (75) after swapping indices i and j. Altogether, this leads to the quartic contribution in the inverse particle separation distance to the *displaceability matrices* $\underline{\mathbf{M}}_{i=j}^{tt}$ in Eq. (78), after switching $i \leftrightarrow j$. In analogy, we may consider, instead of the initial particle j, a different, third particle exposed to the reflected field. Following the same scheme and calculating its induced translation, we obtain the *three-body interaction* included by the contribution $\underline{\mathbf{M}}_{i \neq j}^{tt(3)}$ in Eq. (104). (For the latter purpose, the first, second, and third particle are referred to as j, k, and i, respectively.)

respectively:

$$\mathbf{U}_i^{(2)} = \left(1 + \frac{a^2}{6}\nabla^2\right)\mathbf{u}_j^{(1)}(\mathbf{r})\Big|_{\mathbf{r}=\mathbf{r}_i}, \qquad (70)$$

$$\mathbf{\Omega}_i^{(2)} = \frac{1}{2}\nabla \times \mathbf{u}_j^{(1)}(\mathbf{r})\Big|_{\mathbf{r}=\mathbf{r}_i}, \qquad (71)$$

with $\mathbf{U}_j^{(2)}$ and $\mathbf{\Omega}_j^{(2)}$ obtained by swapping the indices $i \leftrightarrow j$. The overall situation resulting in the displacement $\mathbf{U}_j^{(2)}$ is illustrated in Fig. 3 and has already been considered in Ref. [14].

Altogether, one can say that parts of the displacement fields $\mathbf{u}_i^{(0)}(\mathbf{r})$ and $\mathbf{u}_j^{(0)}(\mathbf{r})$, initially generated by the first sphere, are *reflected* by the respectively other sphere in the form of $\mathbf{u}_j^{(1)}(\mathbf{r})$ and $\mathbf{u}_i^{(1)}(\mathbf{r})$. This is due to the rigidity of the spheres. Then these fields are felt again by the corresponding first sphere.

In principle, one can continue this iteration by considering further reflections. Also the first sphere is rigid and will resist deformations in the reflected field, etc. We can use the same formulae summarized above to continue this iteration. Accordingly, this approach was called *method of reflections* in the hydrodynamic literature [52]. Overall, it turns out that this iterative procedure corresponds to an expansion in the inverse particle separation distance r_{ij}^{-1}, with $r_{ij} = |\mathbf{r}_i - \mathbf{r}_j|$. Here, we proceed up to (including) the fourth order r_{ij}^{-4}. Then, counting factors r_{ij}^{-1} and gradients shows that we may stop at the presented stage.

To find the resulting explicit analytical expressions for the matrix-mediated particle interactions, let us now explicitly calculate the contributions in Eqs. (65), (66), (70), and (71). From Eqs. (13), (64), and (65), using Eq. (3), we find for the first correction of the translation of sphere i

$$\mathbf{U}_i^{(1)} = \left(1 + \frac{a^2}{3}\nabla^2\right)\underline{\mathbf{G}}(\mathbf{r} - \mathbf{r}_j) \cdot \mathbf{F}_j\Big|_{\mathbf{r}=\mathbf{r}_i}$$

$$= \frac{1}{16\pi(1-\nu)\mu}\frac{1}{r_{ij}}\left\{\left[4(1-\nu) - \frac{4}{3}\left(\frac{a}{r_{ij}}\right)^2\right]\hat{\mathbf{r}}_{ij}\hat{\mathbf{r}}_{ij}\right.$$

$$\left. + \left[3 - 4\nu + \frac{2}{3}\left(\frac{a}{r_{ij}}\right)^2\right](\hat{\underline{\mathbf{I}}} - \hat{\mathbf{r}}_{ij}\hat{\mathbf{r}}_{ij})\right\} \cdot \mathbf{F}_j, \qquad (72)$$

with $\hat{\mathbf{r}}_{ij} = (\mathbf{r}_i - \mathbf{r}_j)/r_{ij}$ the unit vector pointing from sphere j to sphere i; see Fig. 2. Similarly, using Eqs. (13), (64), (66), and $\nabla \times \nabla^2 \underline{\mathbf{G}}(\mathbf{r}) = \underline{\mathbf{0}}$, which follows from Eq. (4), we find for the corresponding rotation of sphere i

$$\mathbf{\Omega}_i^{(1)} = \frac{1}{2}\nabla \times \left(1 + \frac{a^2}{6}\nabla^2\right)\underline{\mathbf{G}}(\mathbf{r} - \mathbf{r}_j) \cdot \mathbf{F}_j\Big|_{\mathbf{r}=\mathbf{r}_i}$$

$$= -\frac{1}{8\pi\mu r_{ij}^2}\hat{\mathbf{r}}_{ij} \times \mathbf{F}_j; \qquad (73)$$

see Fig. 2.

To determine $\mathbf{U}_i^{(2)}$ and $\mathbf{\Omega}_i^{(2)}$, we first have to calculate the stresslet induced by sphere j and acting onto the matrix as given by Eq. (67) with switched indices $i \leftrightarrow j$,

$$\underline{\mathbf{S}}_j^{(1)} = \frac{1}{4(4-5\nu)}\frac{a^3}{r_{ij}^2}[5(1-2\nu)(\mathbf{F}_i\hat{\mathbf{r}}_{ij} + \hat{\mathbf{r}}_{ij}\mathbf{F}_i)$$

$$- 3\hat{\underline{\mathbf{I}}}\hat{\mathbf{r}}_{ij} \cdot \mathbf{F}_i + 15\hat{\mathbf{r}}_{ij}\hat{\mathbf{r}}_{ij}\hat{\mathbf{r}}_{ij} \cdot \mathbf{F}_i] + O(r_{ij}^{-4}). \quad (74)$$

It is sufficient to calculate $\underline{\mathbf{S}}_j^{(1)}$ to this order because $\nabla\underline{\mathbf{G}}(\mathbf{r} - \mathbf{r}_j)$ in Eq. (69) is already of order r_{ij}^{-2} at $\mathbf{r} = \mathbf{r}_i$. The additional translation of sphere i induced by the stresslet $\underline{\mathbf{S}}_j^{(1)}$ can now be calculated from Eqs. (69) and (70). To our desired order, we

may omit the $\frac{a^2}{6}\nabla^2$ term and obtain

$$\mathbf{U}_i^{(2)} = -\frac{1}{32\pi(1-\nu)(4-5\nu)\mu}\frac{a^3}{r_{ij}^4}[5(1-2\nu)^2(\hat{\underline{\mathbf{I}}}+\hat{\mathbf{r}}_{ij}\hat{\mathbf{r}}_{ij})$$
$$+ (37-44\nu)\hat{\mathbf{r}}_{ij}\hat{\mathbf{r}}_{ij}]\cdot\mathbf{F}_i. \tag{75}$$

This expression for $\mathbf{U}_i^{(2)}$ corresponds to the lowest-order correction to the displacement of sphere i resulting from a reflection of the displacement field $\mathbf{u}_i^{(0)}(\mathbf{r})$ from sphere j. As for the contribution to the rotation $\boldsymbol{\Omega}_i^{(2)}$ of sphere i, since $\mathbf{u}_j^{(1)}(\mathbf{r}_i)$ in Eq. (69) is already of order r_{ij}^{-4}, Eq. (71) would yield an expression of higher order $O(r_{ij}^{-5})$.

As indicated above, to obtain the next-order contributions, we would have to calculate the stresslet $\underline{\mathbf{S}}_i^{(2)}$ that results from

the rigidity-caused resistance of sphere i in the displacement field $\mathbf{u}_i^{(1)}(\mathbf{r})$. This can be achieved again via Eq. (67) by switching the indices $(^{(0)},^{(1)}) \to (^{(1)},^{(2)})$. In analogy, the resulting additional displacement field $\mathbf{u}_i^{(2)}(\mathbf{r})$ follows via Eq. (68) by replacing $^{(1)} \to {}^{(2)}$, and the additional contribution $\mathbf{U}_j^{(3)}$ to the translation of sphere j via Eq. (70) by $(^{(1)},^{(2)},i,j) \to (^{(2)},^{(3)},j,i)$. Also the $O(r_{ij}^{-4})$ terms in Eq. (74) then need to be taken into account, and the rotations $\boldsymbol{\Omega}_i^{(2)}$ contribute as well. This scheme can basically be continued up to an arbitrary iteration level.

Up to (including) order r_{ij}^{-4}, the total translation of sphere i is given by $\mathbf{U}_i = \mathbf{U}_i^{(0)} + \mathbf{U}_i^{(1)} + \mathbf{U}_i^{(2)}$ and reads

$$\mathbf{U}_i = \left\{\frac{5-6\nu}{24\pi(1-\nu)\mu a}\hat{\underline{\mathbf{I}}} - \frac{1}{32\pi(1-\nu)(4-5\nu)\mu}\frac{a^3}{r_{ij}^4}\left[\left(37-44\nu+10(1-2\nu)^2\right)\hat{\mathbf{r}}_{ij}\hat{\mathbf{r}}_{ij} + 5(1-2\nu)^2(\hat{\underline{\mathbf{I}}}-\hat{\mathbf{r}}_{ij}\hat{\mathbf{r}}_{ij})\right]\right\}\cdot\mathbf{F}_i$$
$$+ \frac{1}{16\pi(1-\nu)\mu}\frac{1}{r_{ij}}\left\{\left[4(1-\nu)-\frac{4}{3}\left(\frac{a}{r_{ij}}\right)^2\right]\hat{\mathbf{r}}_{ij}\hat{\mathbf{r}}_{ij} + \left[3-4\nu+\frac{2}{3}\left(\frac{a}{r_{ij}}\right)^2\right](\hat{\underline{\mathbf{I}}}-\hat{\mathbf{r}}_{ij}\hat{\mathbf{r}}_{ij})\right\}\cdot\mathbf{F}_j. \tag{76}$$

Similarly, the total rotation of sphere i accurate up to (including) order r_{ij}^{-4} is given by

$$\boldsymbol{\Omega}_i = -\frac{1}{8\pi\mu r_{ij}^2}\hat{\mathbf{r}}_{ij}\times\mathbf{F}_j. \tag{77}$$

So far, we have only considered two particles i and j. However, since the governing Navier-Cauchy equations Eq. (1) are linear, we can linearly superimpose the influence of additional inclusions. That is, we simply add contributions of identical form to the right-hand sides of Eqs. (76) and (77) caused by each additional particle j.

Up to (including) order r_{ij}^{-4}, the individual terms on the right-hand side of Eq. (76) then identify the components of the displaceability matrices $\underline{\mathbf{M}}_{ij}^{\mathrm{tt}}$ in Eq. (60) resulting from one- and two-body interactions [14] as illustrated in Figs. 2 and 3:

$$\underline{\mathbf{M}}_{i=j}^{\mathrm{tt}} = M_0^{\mathrm{t}}\left\{\hat{\underline{\mathbf{I}}} - \sum_{\substack{k=1\\k\neq i}}^{N}\frac{3}{4(4-5\nu)(5-6\nu)}\left(\frac{a}{r_{ik}}\right)^4\left[\left(37-44\nu+10(1-2\nu)^2\right)\hat{\mathbf{r}}_{ik}\hat{\mathbf{r}}_{ik} + 5(1-2\nu)^2(\hat{\underline{\mathbf{I}}}-\hat{\mathbf{r}}_{ik}\hat{\mathbf{r}}_{ik})\right]\right\}, \tag{78}$$

$$\underline{\mathbf{M}}_{i\neq j}^{\mathrm{tt}} = M_0^{\mathrm{t}}\frac{3}{2(5-6\nu)}\frac{a}{r_{ij}}\left\{\left[4(1-\nu)-\frac{4}{3}\left(\frac{a}{r_{ij}}\right)^2\right]\hat{\mathbf{r}}_{ij}\hat{\mathbf{r}}_{ij} + \left[3-4\nu+\frac{2}{3}\left(\frac{a}{r_{ij}}\right)^2\right](\hat{\underline{\mathbf{I}}}-\hat{\mathbf{r}}_{ij}\hat{\mathbf{r}}_{ij})\right\} + \underline{\mathbf{M}}_{i\neq j}^{\mathrm{tt}(3)}, \tag{79}$$

with $i,j \in \{1,2,...,N\}$ and

$$M_0^{\mathrm{t}} = \frac{5-6\nu}{24\pi(1-\nu)\mu a}. \tag{80}$$

The contribution $\underline{\mathbf{M}}_{i\neq j}^{\mathrm{tt}(3)}$ represents three-body interactions and will be separately derived in Sec. IX.

Furthermore, from Eq. (77) we find for the components of the rotateability matrices $\underline{\mathbf{M}}_{ij}^{\mathrm{rt}}$ up to (including) order r_{ij}^{-4}

$$\underline{\mathbf{M}}_{i=j}^{\mathrm{rt}} = \underline{\mathbf{0}}, \tag{81}$$

$$\underline{\mathbf{M}}_{i\neq j}^{\mathrm{rt}} = -M_0^{\mathrm{r}}\frac{\hat{\mathbf{r}}_{ij}}{r_{ij}^2}\times, \tag{82}$$

see Fig. 2, with

$$M_0^{\mathrm{r}} = \frac{1}{8\pi\mu}. \tag{83}$$

B. Torques externally imposed on or induced between the inclusions

Instead of forces $\mathbf{F}_i$ and $\mathbf{F}_j$, let us now consider torques $\mathbf{T}_i$ and $\mathbf{T}_j$ externally imposed on or induced between two rigid spherical inclusions i and j. The treatment of this situation follows the same lines, therefore we will be significantly briefer here.

To zeroth order, where matrix-mediated interactions between the two spheres are ignored, the torques cause rotations $\boldsymbol{\Omega}_i^{(0)}$ and $\boldsymbol{\Omega}_j^{(0)}$ of the particles, respectively, which follow via Eq. (33) as

$$\boldsymbol{\Omega}_i^{(0)} = \frac{1}{8\pi\mu a^3}\mathbf{T}_i, \tag{84}$$

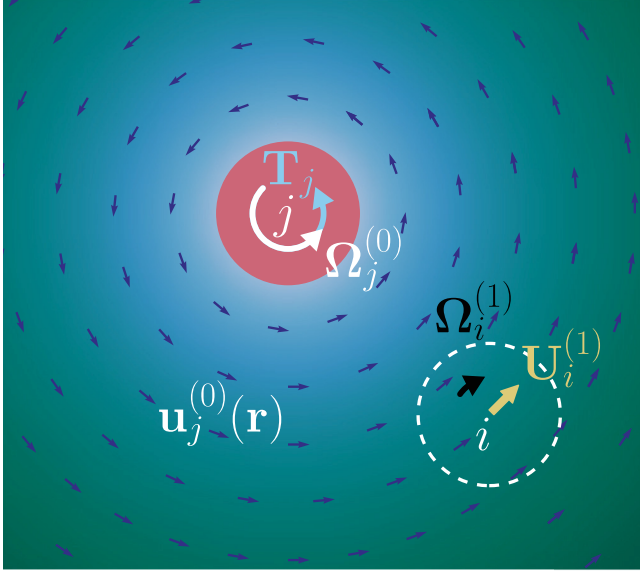FIG. 4. Illustration of the immediate effect that the rotation of sphere j has on the translation and rotation of another sphere i. A torque $\mathbf{T}_j$ is externally imposed onto sphere j that, as a consequence, gets rigidly rotated by $\boldsymbol{\Omega}_j^{(0)}$; see Eq. (85). Moreover, the surrounding matrix is distorted, as described by the displacement field $\mathbf{u}_j^{(0)}(\mathbf{r})$; see Eq. (87). The local directions of $\mathbf{u}_j^{(0)}(\mathbf{r})$ are marked by the small normalized arrows. We indicated the local magnitude of $\mathbf{u}_j^{(0)}(\mathbf{r})$ by the background color, where brighter color represents higher magnitude and the color values follow an arc-tangent scale. Sphere i is exposed to the induced displacement field $\mathbf{u}_j^{(0)}(\mathbf{r})$ and therefore gets translated by $\mathbf{U}_i^{(1)}$ and rotated by $\boldsymbol{\Omega}_i^{(1)}$, see Eqs. (88) and (89), respectively. Explicit results are given in Eqs. (92) and (93). Overall, in this way we obtain the corresponding contributions to the *displaceability and rotateability matrices* $\underline{\mathbf{M}}_{i=j}^{\mathrm{tr}}$, $\underline{\mathbf{M}}_{i\neq j}^{\mathrm{tr}}$, $\underline{\mathbf{M}}_{i=j}^{\mathrm{rr}}$, and $\underline{\mathbf{M}}_{i\neq j}^{\mathrm{rr}}$ in Eqs. (94)–(97), respectively, up to inverse quartic order in the particle distances.

$$\boldsymbol{\Omega}_j^{(0)} = \frac{1}{8\pi\mu a^3}\mathbf{T}_j. \qquad (85)$$

Due to the stick boundary conditions, the rotated spheres drag the surrounding matrix along and therefore generate displacement fields as given by Eq. (32),

$$\mathbf{u}_i^{(0)}(\mathbf{r}) = \left(\frac{a}{|\mathbf{r}-\mathbf{r}_i|}\right)^3 \boldsymbol{\Omega}_i^{(0)} \times (\mathbf{r}-\mathbf{r}_i), \qquad (86)$$

$$\mathbf{u}_j^{(0)}(\mathbf{r}) = \left(\frac{a}{|\mathbf{r}-\mathbf{r}_j|}\right)^3 \boldsymbol{\Omega}_j^{(0)} \times (\mathbf{r}-\mathbf{r}_j); \qquad (87)$$

see Fig. 4.

Similarly to the case of translated spheres, the displacement field $\mathbf{u}_j^{(0)}(\mathbf{r})$ resulting from the rotation of sphere j affects the total displacement and rotation of sphere i. Moreover, due to its rigidity, additional stresses occur when sphere i resists deformations that would be induced by the displacement field $\mathbf{u}_j^{(0)}(\mathbf{r})$. The induced translation $\mathbf{U}_i^{(1)}$, additional rotation $\boldsymbol{\Omega}_i^{(1)}$, and rigidity-based stresslet $\underline{\mathbf{S}}_i^{(1)}$ exerted by sphere i can be calculated using Eqs. (40), (54), and (58), respectively. There,

$\mathbf{u}_j^{(0)}(\mathbf{r})$ is inserted as the imposed displacement field. We find

$$\mathbf{U}_i^{(1)} = \left.\left(1 + \frac{a^2}{6}\nabla^2\right)\mathbf{u}_j^{(0)}(\mathbf{r})\right|_{\mathbf{r}=\mathbf{r}_i}, \qquad (88)$$

$$\boldsymbol{\Omega}_i^{(1)} = \left.\frac{1}{2}\boldsymbol{\nabla}\times\mathbf{u}_j^{(0)}(\mathbf{r})\right|_{\mathbf{r}=\mathbf{r}_i}, \qquad (89)$$

$$\underline{\mathbf{S}}_i^{(1)} = -\frac{4\pi(1-\nu)\mu a^3}{4-5\nu}\left(1+\frac{a^2}{10}\nabla^2\right)\left(\frac{1}{1-2\nu}\hat{\underline{\mathbf{I}}}\boldsymbol{\nabla}\cdot\mathbf{u}_j^{(0)}(\mathbf{r})\right.$$
$$\left.+\frac{5}{2}\left\{\boldsymbol{\nabla}\mathbf{u}_j^{(0)}(\mathbf{r})+\left[\boldsymbol{\nabla}\mathbf{u}_j^{(0)}(\mathbf{r})\right]^T\right\}\right)\Bigg|_{\mathbf{r}=\mathbf{r}_i}. \qquad (90)$$

Analogously to Eq. (68), the displacement field resulting from the rigidity-based resistance of sphere i against deformation is given by

$$\mathbf{u}_i^{(1)}(\mathbf{r}) = -\left(\underline{\mathbf{S}}_i^{(1)}\cdot\boldsymbol{\nabla}\right)\cdot\underline{\mathbf{G}}(\mathbf{r}-\mathbf{r}_i). \qquad (91)$$

Since the stresslet $\underline{\mathbf{S}}_i^{(1)}$ here yields an expression of order r_{ij}^{-3}, $\mathbf{u}_i^{(1)}(\mathbf{r}_j)$ is already of order r_{ij}^{-5}. Therefore, we can stop our iteration at this point, confining ourselves to contributions up to (including) order r_{ij}^{-4}. Again, all corresponding expressions for sphere j are obtained by simply switching all indices $i \leftrightarrow j$.

To derive explicit analytical expressions, we insert Eqs. (85) and (87) into Eqs. (88) and (89). We obtain

$$\mathbf{U}_i^{(1)} = -\frac{1}{8\pi\mu r_{ij}^2}\hat{\mathbf{r}}_{ij}\times\mathbf{T}_j, \qquad (92)$$

$$\boldsymbol{\Omega}_i^{(1)} = \frac{1}{16\pi\mu r_{ij}^3}[3\hat{\mathbf{r}}_{ij}\hat{\mathbf{r}}_{ij}-\hat{\underline{\mathbf{I}}}]\cdot\mathbf{T}_j, \qquad (93)$$

as illustrated in Fig. 4. From Eq. (92), we see that an additional translation of sphere i only occurs, if $\hat{\mathbf{r}}_{ij}$ is not (anti)parallel to $\mathbf{T}_j$. Moreover, sphere i is translated in the same direction as the nearest surface point of sphere j. The sense of the additional rotation $\boldsymbol{\Omega}_i^{(1)}$ that only vanishes at infinite particle separation r_{ij} depends on the relative angular configuration according to Eq. (93). For instance, if $\hat{\mathbf{r}}_{ij}\parallel\mathbf{T}_j$, i.e., both spheres and the imposed torque $\mathbf{T}_j$ align along a common axis, then the zero-order rotation $\boldsymbol{\Omega}_j^{(0)}$ and the additional rotation $\boldsymbol{\Omega}_i^{(1)}$ have the same sense. For $\hat{\mathbf{r}}_{ij}\perp\mathbf{T}_j$, i.e., the imposed torque $\mathbf{T}_j$ is perpendicular to the plane that contains both spheres, these two rotations have opposite sense.

Overall, the total translation of sphere i to our desired order is given by $\mathbf{U}_i^{(1)}$ in Eq. (92). The total rotation up to (including) order r_{ij}^{-4} equals $\boldsymbol{\Omega}_j^{(0)}+\boldsymbol{\Omega}_i^{(1)}$; see Eqs. (84) and (93). Therefore, with the same reasoning as in Sec. VIII A, we can read off the components of the corresponding displaceability matrices $\underline{\mathbf{M}}_{ij}^{\mathrm{tr}}$ and rotateability matrices $\underline{\mathbf{M}}_{ij}^{\mathrm{rr}}$ from Eqs. (84), (92), and (93) as

$$\underline{\mathbf{M}}_{i=j}^{\mathrm{tr}} = \mathbf{0}, \qquad (94)$$

$$\underline{\mathbf{M}}_{i\neq j}^{\mathrm{tr}} = -M_0^{\mathrm{r}}\frac{\hat{\mathbf{r}}_{ij}}{r_{ij}^2}\times, \qquad (95)$$

$$\underline{\mathbf{M}}_{i=j}^{\mathrm{rr}} = M_0^{\mathrm{r}}\frac{1}{a^3}\hat{\underline{\mathbf{I}}}, \qquad (96)$$

$$\underline{\mathbf{M}}_{i\neq j}^{\mathrm{rr}} = M_0^{\mathrm{r}}\frac{1}{2r_{ij}^3}[3\hat{\mathbf{r}}_{ij}\hat{\mathbf{r}}_{ij}-\hat{\underline{\mathbf{I}}}], \qquad (97)$$

where M_0^r was introduced in Eq. (83). See also the illustration in Fig. 4. Based on the linearity of the governing Navier-Cauchy equations in Eq. (1), we may sum up the influence of imposed or induced forces in Sec. VIII A and the ones just derived for imposed or induced torques and combine them in an overall matrix equation as given in Eq. (60).

IX. THREE-BODY INTERACTIONS

Following the same strategy as in Sec. VIII, we now derive similar expressions for the three-body interactions. In this way, we determine the components of the matrix $\underline{\mathbf{M}}_{i \neq j}^{\mathrm{tt}(3)}$ in Eq. (79). Again, we adapt the procedure for low-Reynolds-number hydrodynamics presented in Ref. [52].

For this purpose, we now consider three rigid spherical inclusions of radius a, located at positions $\mathbf{r}_i$, $\mathbf{r}_j$, and $\mathbf{r}_k$. They are acted on by externally imposed or induced forces $\mathbf{F}_i$, $\mathbf{F}_j$, and $\mathbf{F}_k$, respectively. To zeroth order, i.e., not taking into account matrix-mediated interactions between the inclusions, sphere i creates a displacement field as given by Eq. (63). Corresponding expressions follow for spheres j and k by switching indices $i \to j$ and $i \to k$, respectively.

In analogy to Eq. (65), we can calculate from the first Faxén law Eq. (40) the translation that sphere i acquires within the linearly superimposed displacement fields $\mathbf{u}_j^{(0)}(\mathbf{r})$ and $\mathbf{u}_k^{(0)}(\mathbf{r})$. Using $\mathbf{u}_j^{(0)}(\mathbf{r}) + \mathbf{u}_k^{(0)}(\mathbf{r})$ as the imposed field on the right-hand side of Eq. (40), we obtain

$$\mathbf{U}_i^{(1)} = \left(1 + \frac{a^2}{6}\nabla^2\right)\left[\mathbf{u}_j^{(0)}(\mathbf{r}) + \mathbf{u}_k^{(0)}(\mathbf{r})\right]\Big|_{\mathbf{r}=\mathbf{r}_i}. \tag{98}$$

Corresponding expressions follow for spheres j and k by switching in this equation $i \leftrightarrow j$ and $i \leftrightarrow k$, respectively.

Again, sphere i resists any deformation that would be implied by the matrix deformations described by $\mathbf{u}_j^{(0)}(\mathbf{r})$ and $\mathbf{u}_k^{(0)}(\mathbf{r})$. The resulting stresslet that sphere i thus exerts onto the matrix can be calculated in analogy to Eq. (67) and using Eq. (58),

$$\underline{\mathbf{S}}_i^{(1)} = -\frac{4\pi(1-\nu)\mu a^3}{4 - 5\nu}\left(1 + \frac{a^2}{10}\nabla^2\right)\left[\frac{1}{1 - 2\nu}\hat{\mathbf{I}}\nabla \cdot \left[\mathbf{u}_j^{(0)}(\mathbf{r}) + \mathbf{u}_k^{(0)}(\mathbf{r})\right]\right.$$
$$\left. + \frac{5}{2}\left(\nabla\left[\mathbf{u}_j^{(0)}(\mathbf{r}) + \mathbf{u}_k^{(0)}(\mathbf{r})\right] + \left\{\nabla\left[\mathbf{u}_j^{(0)}(\mathbf{r}) + \mathbf{u}_k^{(0)}(\mathbf{r})\right]\right\}^T\right)\right]\Big|_{\mathbf{r}=\mathbf{r}_i}. \tag{99}$$

It produces the displacement field

$$\mathbf{u}_i^{(1)}(\mathbf{r}) = -\left(\underline{\mathbf{S}}_i^{(1)} \cdot \nabla\right) \cdot \underline{\mathbf{G}}(\mathbf{r} - \mathbf{r}_i), \tag{100}$$

see Eq. (23), due to the resistance of sphere i to deformations implied by $\mathbf{u}_j^{(0)}(\mathbf{r})$ and $\mathbf{u}_k^{(0)}(\mathbf{r})$. Once more, expressions for spheres j and k are obtained from this equation by replacing $i \to j$ and $i \to k$, respectively.

Next, we use the sum of the resulting displacement fields $\mathbf{u}_j^{(1)}(\mathbf{r}) + \mathbf{u}_k^{(1)}(\mathbf{r})$ as the imposed field on the right-hand side of Faxén's first law, Eq. (40). In this way, we can calculate the additional translation $\mathbf{U}_i^{(2)}$ that sphere i experiences in these rigidity-induced displacement fields,

$$\mathbf{U}_i^{(2)} = \left(1 + \frac{a^2}{6}\nabla^2\right)\left[\mathbf{u}_j^{(1)}(\mathbf{r}) + \mathbf{u}_k^{(1)}(\mathbf{r})\right]\Big|_{\mathbf{r}=\mathbf{r}_i}. \tag{101}$$

At first glance, this expression is of identical shape as Eq. (70) for the two-sphere interaction. The only difference seems to be that here we take into account the two contributions from the two spheres j and k, instead of only one. Indeed, we here recover all contributions that we have already identified in Sec. VIII A. However, there is now more to that.

For simplicity, let us for the moment only consider in Eq. (101) the effect of the displacement field $\mathbf{u}_k^{(1)}(\mathbf{r})$, where the latter according to Eq. (100) is given by

$$\mathbf{u}_k^{(1)}(\mathbf{r}) = -\left(\underline{\mathbf{S}}_k^{(1)} \cdot \nabla\right) \cdot \underline{\mathbf{G}}(\mathbf{r} - \mathbf{r}_k). \tag{102}$$

Here, $\underline{\mathbf{S}}_k^{(1)}$ is the stresslet that sphere k exerts onto the surrounding matrix due to its rigidity. It arises as sphere k opposes to deformations implied by $\mathbf{u}_i^{(0)}(\mathbf{r})$ and $\mathbf{u}_j^{(0)}(\mathbf{r})$. The latter displacement fields directly result from the external forces $\mathbf{F}_i$ and $\mathbf{F}_j$ acting onto spheres i and j, respectively. These two forces lead to two different scenarios.

The first scenario has already been described in Sec. VIII A. A force $\mathbf{F}_i$ acting onto sphere i generates the displacement field $\mathbf{u}_i^{(0)}(\mathbf{r})$. This field is *reflected* by sphere k. Then it acts back onto sphere i in the form of $\mathbf{u}_k^{(1)}(\mathbf{r})$, contributing to $\mathbf{U}_i^{(2)}$ in Eq. (101). We abbreviate this chain of matrix-mediated interactions as $i \leftarrow k \leftarrow i$.

In the second scenario, a force $\mathbf{F}_j$ acting onto a *third* sphere j induces a displacement field $\mathbf{u}_j^{(0)}(\mathbf{r})$. This field is then reflected by sphere k due to its rigidity in the form of $\mathbf{u}_k^{(1)}(\mathbf{r})$. However, in the present three-body configuration, the reflected field also affects sphere i and contributes to its displacement $\mathbf{U}_i^{(2)}$ in Eq. (101). This *three-body interaction* thus defines a further contribution in addition to the pairwise interactions derived in Sec. VIII A. We abbreviate the corresponding chain of matrix-mediated interactions as $i \leftarrow k \leftarrow j$.

Altogether, we find two such three-body interactions contributing to $\mathbf{U}_i^{(2)}$ in Eq. (101) in addition to the pairwise interactions. The first one works as described, $i \leftarrow k \leftarrow j$, and we denote it as $\mathbf{U}_{ikj}^{(2)}$. The second one works via $i \leftarrow j \leftarrow k$, which would then be termed $\mathbf{U}_{ijk}^{(2)}$. Explicit calculation yields

$$
\mathbf{U}_{ikj}^{(2)} = -\left(1 + \frac{a^2}{6}\nabla^2\right)\left(\mathbf{S}_k^{(1)} \cdot \nabla\right) \cdot \underline{\mathbf{G}}(\mathbf{r} - \mathbf{r}_k)\Big|_{\mathbf{r}=\mathbf{r}_i} = \frac{1}{64\pi(1-\nu)(4-5\nu)\mu}\frac{a^3}{r_{ik}^2 r_{jk}^2}(-10(1-2\nu)\{(1-2\nu)[(\hat{\mathbf{r}}_{ik} \cdot \hat{\mathbf{r}}_{jk})\underline{\hat{\mathbf{I}}} + \hat{\mathbf{r}}_{jk}\hat{\mathbf{r}}_{ik}]
$$

$$
+ 3(\hat{\mathbf{r}}_{ik} \cdot \hat{\mathbf{r}}_{jk})(\hat{\mathbf{r}}_{ik}\hat{\mathbf{r}}_{ik} + \hat{\mathbf{r}}_{jk}\hat{\mathbf{r}}_{jk}) - \hat{\mathbf{r}}_{ik}\hat{\mathbf{r}}_{jk}\} + 3[7 - 4\nu - 15(\hat{\mathbf{r}}_{ik} \cdot \hat{\mathbf{r}}_{jk})^2]\hat{\mathbf{r}}_{ik}\hat{\mathbf{r}}_{jk}) \cdot \mathbf{F}_j + O[(r_{ik}, r_{jk})^{-5}]. \tag{103}
$$

$\mathbf{U}_{ijk}^{(2)}$ is readily obtained from this expression by switching indices $j \leftrightarrow k$.

In summary, to our desired order, i.e., up to (including) quartic order in the inverse particle separation distances, two- and three-body interactions contribute to $\mathbf{U}_i^{(2)}$. The latter follow from Eq. (103) for $i \neq j$. For $i = j$, Eq. (103) exactly reproduces the two-body contributions listed already in Eq. (75). Again due to the linearity of the governing elasticity equations Eq. (1), we may simply add the additional contributions $\mathbf{U}_{ijk}^{(2)}$ and $\mathbf{U}_{ikj}^{(2)}$ to our previous explicit analytical expression for the overall displacement of sphere i.

Superimposing all contributions that result for the coupled displacements and rotations of N identical spherical inclusions, we return to our formalism in terms of the displaceability and rotateability matrices in Eq. (60). We can now read off from Eq. (103) the additional *three-body contribution* $\underline{\mathbf{M}}_{i\neq j}^{tt(3)}$ to the *displaceability matrix* in Eq. (79) [14],

$$
\underline{\mathbf{M}}_{i\neq j}^{tt(3)} = M_0^t \frac{3}{8(4-5\nu)(5-6\nu)} \sum_{\substack{k=1 \\ k\neq i,j}}^{N} \left(\frac{a}{r_{ik}}\right)^2 \left(\frac{a}{r_{jk}}\right)^2 (-10(1-2\nu)\{(1-2\nu)[(\hat{\mathbf{r}}_{ik} \cdot \hat{\mathbf{r}}_{jk})\underline{\hat{\mathbf{I}}} + \hat{\mathbf{r}}_{jk}\hat{\mathbf{r}}_{ik}]
$$

$$
+ 3(\hat{\mathbf{r}}_{ik} \cdot \hat{\mathbf{r}}_{jk})(\hat{\mathbf{r}}_{ik}\hat{\mathbf{r}}_{ik} + \hat{\mathbf{r}}_{jk}\hat{\mathbf{r}}_{jk}) - \hat{\mathbf{r}}_{ik}\hat{\mathbf{r}}_{jk}\} + 3[7 - 4\nu - 15(\hat{\mathbf{r}}_{ik} \cdot \hat{\mathbf{r}}_{jk})^2]\hat{\mathbf{r}}_{ik}\hat{\mathbf{r}}_{jk}), \tag{104}
$$

where M_0^t was introduced in Eq. (80). This expression is exact up to (including) order $(r_{ik}, r_{jk})^{-4}$.

It can readily be seen that rotations caused by three-body interactions are of higher order than $(r_{ik}, r_{jk})^{-4}$. The additional rotation $\mathbf{\Omega}_i^{(2)}$ of sphere i due to the reflected displacement fields $\mathbf{u}_j^{(1)}(\mathbf{r})$ and $\mathbf{u}_k^{(1)}(\mathbf{r})$ follows from Faxén's second law Eq. (54) and reads

$$
\mathbf{\Omega}_i^{(2)} = \frac{1}{2}\nabla \times \left[\mathbf{u}_j^{(1)}(\mathbf{r}) + \mathbf{u}_k^{(1)}(\mathbf{r})\right]\Big|_{\mathbf{r}=\mathbf{r}_i}. \tag{105}
$$

This expression is already of order $(r_{ik}, r_{jk})^{-5}$, because both $\mathbf{u}_j^{(1)}(\mathbf{r}_i)$ and $\mathbf{u}_k^{(1)}(\mathbf{r}_i)$ are of order $(r_{ik}, r_{jk})^{-4}$, which is obtained by combining Eqs. (13), (63), (99), (100), and (102). Therefore, to our desired order, we find

$$
\underline{\mathbf{M}}_{i\neq j}^{rt(3)} = \underline{\mathbf{0}}. \tag{106}
$$

Similarly, we do not obtain any three-body contribution to the remaining displaceability and rotateability matrices up to our desired order. Reconsidering the above derivation of $\underline{\mathbf{M}}_{i\neq j}^{tt(3)}$, we find that solely the lowest-order parts of all contributing expressions finally enter Eq. (104). When torques are externally imposed on or induced between the individual spheres, already the resulting zero-order displacement fields are one order higher in the inverse separation distances. This follows by comparing Eqs. (84)–(87) to the case of imposed or induced forces, see Eqs. (13), (63), and (64). Therefore, the reflected displacement fields due to the rigidity of the spherical inclusions, see Eqs. (99) and (100), already yield expressions of order $(r_{ik}, r_{jk})^{-5}$. Thus, we find to our desired order

$$
\underline{\mathbf{M}}_{i\neq j}^{tr(3)} = \underline{\mathbf{0}}, \tag{107}
$$

$$
\underline{\mathbf{M}}_{i\neq j}^{rr(3)} = \underline{\mathbf{0}}. \tag{108}
$$

These results complete our derivation of the displaceability and rotateability matrices up to (including) inverse quartic order in the separation distances between the individual spherical particles.

Naturally, for larger deformations, the more the nonlinearities in the elastic response of the embedding matrix become significant, the less exact our approach will become. In nonlinearly elastic situations, if an exact quantitative evaluation is necessary, simulations are still mandatory. Yet, for a first and quick qualitative scan in the absence of bifurcational behavior, our analytical expressions will in many cases be helpful. Moreover, our approach may still be valuable to significantly speed up corresponding simulations. For this purpose, the configuration calculated from our linearly elastic formalism could be used as an initialization in iterative simulation methods.

X. SOME ILLUSTRATIVE EXAMPLES

Confining ourselves to the sole effect of induced forces between the embedded particles, we have in a previous work determined the resulting coupled translations [14]. For this purpose, we considered an example system of identical spherical paramagnetic particles that were embedded in a planar configuration into a soft elastic polymeric gel matrix. Then, an external magnetic field was applied and rotated within the configurational plane. In this way, magnetic interactions between the particles were induced and tuned by rotating the

field. The elevated amplitude of the magnetic field caused a close-to-saturation magnetization of the particles. Thus, the induced magnetic dipole moments $\mathbf{m} = m\hat{\mathbf{m}}$ ($m = |\mathbf{m}|$) of the particles could be considered identical and aligned along the external magnetic field. Then, the magnetic dipole–dipole force on a particle i is given by [74]

$$\mathbf{F}_i = -\frac{3\mu_0 m^2}{4\pi} \sum_{\substack{j=1 \\ j \neq i}}^{N} \frac{5\hat{\mathbf{r}}_{ij}(\hat{\mathbf{m}} \cdot \hat{\mathbf{r}}_{ij})^2 - \hat{\mathbf{r}}_{ij} - 2\hat{\mathbf{m}}(\hat{\mathbf{m}} \cdot \hat{\mathbf{r}}_{ij})}{r_{ij}^4},$$

(109)

where μ_0 is the magnetic vacuum permeability and N the total number of particles. We then evaluated the coupled translations resulting for the magnetized particles in response to the induced magnetic forces. Based on the magnetic nature of the particles and their size, this pure focus on induced forces and resulting translations was justified.

Here, we consider the effect of additional torques applied to the particles. The translationally and rotationally coupled situation is analyzed. We demonstrate for some minimal example configurations how the additional torques and rotational couplings modify our previous results.

For illustration, we assume the following idealized model situation. Again, we consider identical spherical magnetizable particles with no-slip surface conditions. As before, a strong external magnetic field shall be applied that saturates the magnetization of the particles and always keeps their magnetic moments oriented along the external field. However, the particles shall now be magnetically anisotropic. More precisely, we assume uniaxial magnetic anisotropy. That is, an energetic penalty arises whenever the nonpolar axis $\hat{\mathbf{n}}_i$ of magnetic anisotropy of each particle i is not aligned parallel to the direction $\hat{\mathbf{m}} = \hat{\mathbf{B}}$ of the external magnetic field. Assuming particles of this kind and following the idealized Stoner-Wohlfarth model [75], the energetic penalty for misalignment is expressed as

$$E_{\mathrm{SW}} = K V_{\mathrm{S}}[1 - (\hat{\mathbf{n}}_i \cdot \hat{\mathbf{B}})^2].$$

(110)

In general, V_{S} denotes the volume of each particle and the anisotropy parameter K quantifies the strength of its uniaxial magnetic anisotropy. Its magnitude may vary significantly with the magnetic nature of the particles and their shape. One factor is the type of internal lattice structure in the particles that may cause the magnetic anisotropy [76,77]. Moreover, an elongated, e.g., rod-like shape of the particles may likewise cause magnetic uniaxiality [11,13]. Since here we are considering spherical particles, our uniaxiality must be due to a magnetocrystalline anisotropy axis. Below, we set the rescaled relative strengths of magnetic interactions $m^2\mu_0/\mu a^6 = 22.5 \times 10^3$ and 24.5×10^3 for the considered two- and three-particle systems, respectively, corresponding to the experimental parameters in our previous study [14]. Moreover, we then choose a comparatively low value for the rescaled anisotropy parameter of $K/\mu = 3$ [78]. It leads to an effect that shows up in an illustrative way when comparing to corresponding results in the absence of imposed torques. Using Eq. (110), we can calculate the imposed torque on each particle i resulting from its orientation with respect to the
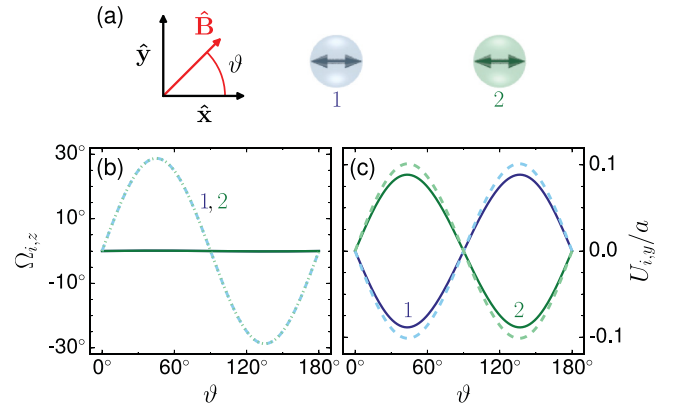

FIG. 5. (a) Schematic illustration of the modified initial spatial configuration of a two-particle system that had been investigated before in Ref. [14] in the absence of induced torques. The double arrows indicate the initial orientations of additional magnetic anisotropy axes. ϑ here is defined as the angle between the unit vector $\hat{\mathbf{x}}$ and the direction $\hat{\mathbf{B}}$ of an external magnetic field (right-handed system). This external magnetic field is initially applied parallel to $\hat{\mathbf{x}}$ and then rotated counterclockwise in the xy plane until $\vartheta = 180°$. Magnetic forces arise between the particles as given by Eq. (109) due to induced magnetic moments $\mathbf{m} \parallel \mathbf{B}$. (b) Plot of the z components of the rotation vectors $\mathbf{\Omega}_i$ of the particles as functions of ϑ. In this configuration, all rotations occur in the xy plane, therefore all other components of $\mathbf{\Omega}_i$ vanish. The continuous line represents the rotations of particles 1 and 2, if induced torques are set to zero. The dashed and dotted lines show the results when the torques are included as they result from Eqs. (110) and (111). The maximum magnitudes of rotation occur around $\vartheta = 45°$ and $135°$, respectively, as expected from the underlying Stoner-Wohlfarth model, with opposite signs beyond $90°$ because the anisotropy axes do not have any preferred direction. (c) The y components of the displacement vectors $\mathbf{U}_i$ without (continuous lines) and with (dashed) inclusion of the torques. The curves are labeled by the particle numbers; see (a). In this setup, the torques amplify the magnitudes of the displacements due to their sense of rotation.

external magnetic field,

$$\mathbf{T}_i = 2K V_{\mathrm{S}}(\hat{\mathbf{n}}_i \cdot \hat{\mathbf{B}}) \hat{\mathbf{n}}_i \times \hat{\mathbf{B}}.$$

(111)

Since the forces $\mathbf{F}_i$ change with altering interparticle distance (during the process of particle displacement), we had implemented an iterative loop to calculate the magnetic forces in the final state [14]. Now, we have extended the approach to include the torques $\mathbf{T}_i$. Their magnitude finally decreases with progressing rotation of the anisotropy axis towards the external magnetic field.

In Figs. 5–9 we display our results for two- and three-particle example configurations. The initial spatial arrangements, distances, and material parameters are the same as in Ref. [14]. In each of Figs. 5–9, a schematic sketch (a) indicates the initial orientation of the magnetic anisotropy axes. The external magnetic field is applied in the indicated xy plane (right-handed coordinate system) and rotated in a counterclockwise way, starting from $\hat{\mathbf{B}} \cdot \hat{\mathbf{x}} = 1$. The plots (b) in each figure illustrate the resulting rotations $\mathbf{\Omega}_i$ as functions of the angle $\vartheta = \arccos(\hat{\mathbf{B}} \cdot \hat{\mathbf{x}})$ of the magnetic field direction. Moreover, the plots (c) show the displacements $\mathbf{U}_i$ in distinct
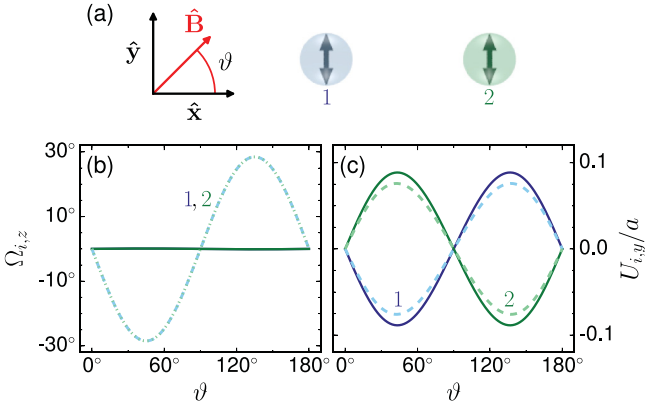
FIG. 6. The same as in Fig. 5, except for the orientations of the anisotropy axes. They are now initially oriented along $\hat{\mathbf{y}}$; see (a). Therefore, the particles are rotated inversely when compared to Fig. 5, as shown by the dashed and dotted lines in (b). Overall, this now leads to an attenuation of the displacements in $\hat{\mathbf{y}}$ direction (c).

directions. Continuous lines represent the results without imposed torques, whereas dashed and/or dotted lines represent the results for the torques $\mathbf{T}_i$ included. For distinction, the curves are labeled by the corresponding particle numbers.

Several different initial configurations of the anisotropy axes were considered in Figs. 5–9. All plotted quantities were calculated via Eqs. (60), (78)–(83), (94)–(97), (104), and (109)–(111). The resulting calculated rotations and their amplifying or dampening effects on the particle displacements can be qualitatively comprehended with the help of simple geometric considerations. For example, in Fig. 5(a) the anisotropy axes of both particles 1 and 2 are initially oriented along the $\hat{\mathbf{x}}$ axis. From Eq. (111) it then follows that the torques $\mathbf{T}_1$ and $\mathbf{T}_2$ (and thus the directly induced rotations) are maximized around $\vartheta = 45°$; see Fig. 5(b). Both particles are therefore rotated in counterclockwise direction, thereby creating displacement fields in the surrounding matrix (see also Fig. 4). As a result of their matrix-mediated interactions, particle 2 is pushed into the $\hat{\mathbf{y}}$ direction due to the torque $\mathbf{T}_1$, whereas particle 1 is pushed into the $(-\hat{\mathbf{y}})$ direction due to $\mathbf{T}_2$, see the dashed lines in comparison to the continuous lines in Fig. 5(c) around $\vartheta = 45°$. Overall, this leads to an amplification of the particle displacements $|U_{i,y}|$ for all ϑ.

In contrast to that, in Fig. 6 the anisotropy axes are initially aligned along the $\hat{\mathbf{y}}$ axis, i.e., perpendicular to the anisotropy axes in Fig. 5. All other parameters remain unchanged. As a consequence, the sense of rotation of both particles is inverted with respect to the previous configuration, see Figs. 5(b) and 6(b). This leads to a mutual damping of the magnitudes $|U_{i,y}|$, see Fig. 6(c), in opposition to the previous situation in Fig. 5(c).

Another example is depicted in Fig. 7, where the anisotropy axis $\hat{\mathbf{n}}_2$ of particle 2 remains the same as in Fig. 5. However, $\hat{\mathbf{n}}_1$ now points out of the xy plane, along the $\hat{\mathbf{z}}$ axis. That is, $\hat{\mathbf{n}}_1$ is always oriented perpendicular to the external magnetic field $\hat{\mathbf{B}}$. From Eq. (111) we find that $\mathbf{T}_1 = \mathbf{0}$ for all ϑ. Thus, there is no directly induced rotation of particle 1 that would modify the overall displacement of particle 2. In contrast to that, the displacement $U_{1,y}$ in Fig. 7(c) remains identical to $U_{1,y}$ in Fig. 5(c).
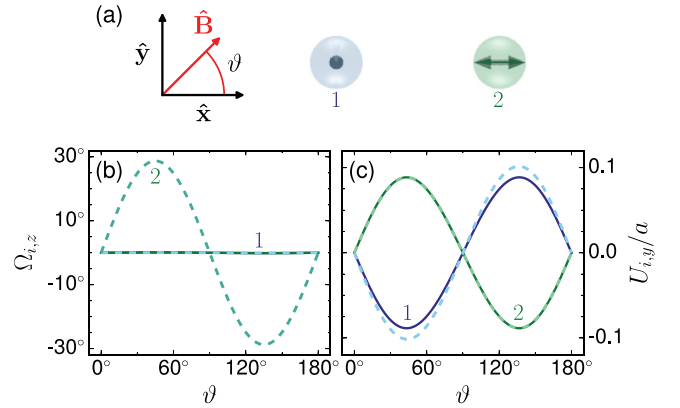

FIG. 7. The same as in Fig. 5, but now the anisotropy axis of particle 1 is along $\hat{\mathbf{z}}$; see (a). (b) Then, the induced torque $\mathbf{T}_1$ vanishes for all ϑ and particle 1 is only weakly rotated due to the rotation–translation coupling in Eq. (82). Therefore, we do not observe a change in the displacements $U_{2,y}$ in (c) when the torques are included.

In Fig. 8(a), the spatial configuration of the three-particle system studied in Ref. [14] is illustrated. Additional anisotropy axes are chosen such that they are rotated by 120° with respect to each other, all of them confined to the xy plane. This is reflected by the resulting phase-shift in the torque-induced rotations, see Fig. 8(b). The displacement $\mathbf{U}_i$ of each particle
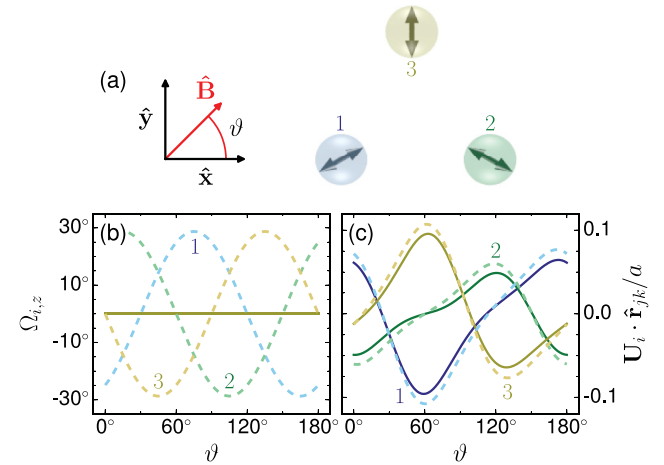

FIG. 8. Similar to Fig. 5 but now for a three-particle system. (a) Schematic illustration of the initial spatial configuration of the three-particle system in Ref. [14] and the orientations of the added initial anisotropy axes. Here, the anisotropy axes $\hat{\mathbf{n}}_i$ are rotated with respect to each other by 120°, with $\hat{\mathbf{n}}_3$ along $\hat{\mathbf{y}}$. (b) Plot of the z components of the rotation vectors $\mathbf{\Omega}_i$. Again, in this configuration all rotations take place in the xy plane. The individual curves are phase-shifted with respect to each other according to the initial shifted orientations of the anisotropy axes. (c) Projection of the displacements $\mathbf{U}_i$ onto the interparticle unit vector $\hat{\mathbf{r}}_{jk}$ set by the respective other particles [with $(i,j,k) \in \{(1,2,3),(2,3,1),(3,1,2)\}$]. The induced torques amplify the magnitudes of displacements in the directions $\hat{\mathbf{r}}_{jk}$ (dashed lines). Due to small deviations of the configuration from a perfect equilateral triangle [14], the curves are not simply phase-shifted with respect to each other.
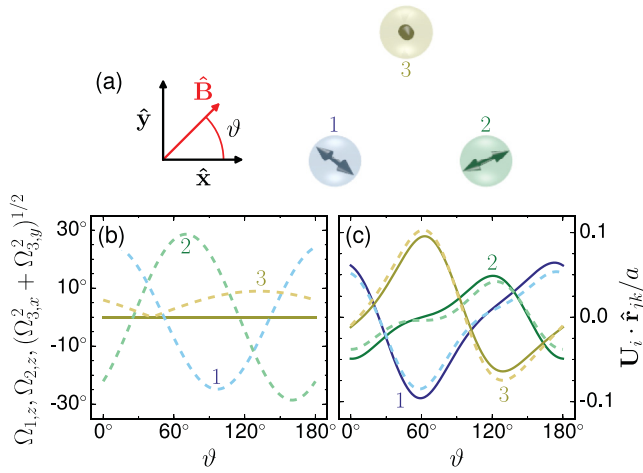
FIG. 9. The same as in Fig. 8, but now the anisotropy axes are oriented "randomly" in all three dimensions as indicated in (a). (b) Here, components of the rotations $\mathbf{\Omega}_i$ are plotted as $\Omega_{1,z}, \Omega_{2,z}, [(\Omega_{3,x})^2 + (\Omega_{3,y})^2]^{1/2}$. Since initially $\hat{\mathbf{n}}_3$ is almost oriented along $\hat{\mathbf{z}}$, the torques $\mathbf{T}_3$ and therefore the rotations $\mathbf{\Omega}_3$ are relatively small compared to those of particles 1 and 2, which have a larger projection onto the xy plane. Moreover, the symmetry of Fig. 8(b) does not exist anymore. (c) Due to the additional torques, the projections $\mathbf{U}_i \cdot \hat{\mathbf{r}}_{jk}$ for particles 1 and 2 are reduced (dashed lines), whereas the result for particle 3 remains qualitatively the same as in Fig. 8. Here, additional displacements out of the xy plane occur (not shown).

i in Fig. 8(c) is projected onto the interparticle unit vector $\hat{\mathbf{r}}_{jk}$ between the two other particles j and k, i.e., $(i,j,k) \in \{(1,2,3),(2,3,1),(3,1,2)\}$. An amplification is observed for all of these displacement components. This can be directly inferred from the sense of the imposed rotation of each particle, see also Fig. 4 and Eq. (92).

Finally, a random initial configuration of the anisotropy axes was chosen in Fig. 9(a) for the same spatial configuration as in Fig. 8(a). In view of the initial setup, we plot in Fig. 9(b) the components $\Omega_{1,z}$, $\Omega_{2,z}$, and $[(\Omega_{3,x})^2 + (\Omega_{3,y})^2]^{1/2}$ of the rotation vectors. Since $\hat{\mathbf{n}}_3$ is nearly oriented along the $\hat{\mathbf{z}}$ axis, the torque $\mathbf{T}_3$ and therefore the overall rotation $\mathbf{\Omega}_3$ is mostly relatively weak when compared to $\mathbf{T}_1$ and $\mathbf{T}_2$; see Fig. 9(b). The orientations of the anisotropy axes of particles 1 and 2 can roughly be compared with those of particles 2 and 1 in Fig. 8(a), respectively, i.e., their roles are approximately inverted. This leads to a mutual reduction of the depicted displacement amplitudes of particles 1 and 2 in Fig. 9(c) when the torques are included. In contrast to that, the depicted displacement of particle 3 remains qualitatively the same as in Fig. 9(c).

In addition to that, we have tested how the modifications above would affect the induced changes in interparticle distances that had been plotted in Ref. [14]. However, the relative deviations from the situations without torques were only of the order $\sim 10^{-2}$.

XI. CONCLUSIONS AND OUTLOOK

In summary, we have presented the derivation of explicit analytical expressions to calculate from given forces and torques acting on rigid spherical inclusions in an elastic matrix their resulting coupled displacements and rotations. The surrounding elastic matrix is assumed to be an infinitely extended, homogeneous, isotropic elastic medium with stick boundary conditions on the inclusion surfaces. Matrix deformations are induced by the forces and torques acting on the inclusions. These deformations lead to mutual, long-ranged, matrix-mediated interactions between the rigid inclusions. The role of such matrix-mediated interactions is implicitly contained in our resulting analytical expressions. Technically, to perform the derivation, the well-known approach in terms of Faxén's theorems and the method of reflections is adapted from the field of low-Reynolds-number hydrodynamics [52]. Throughout, we have included the case of *compressible* elastic environments. We summarize our results in terms of *displaceability and rotateability* matrices that are functions of the given inclusion configuration only. These matrices express how given *forces and torques* on the inclusions lead to their coupled *displacements and rotations*. In the considered static, linearly elastic case of nontouching inclusions, these expressions replace the need for finite-element simulations that explicitly calculate the matrix deformations between the inclusions.

As a next step, more complex inclusion geometries can be addressed. Of particular interest are elongated particles that can more directly be exposed to external torques and are also used for microrheological purposes [11–13]. Theoretically, it should be possible to derive expressions for ellipsoidal inclusions [51,65], but due to the significantly more complicated structure of such expressions they may already be of limited use for practical applications. Long thin rods could be approximated by long chains of spheres [52]. Recent experiments observed a buckling of chains of spherical magnetic particles in soft gel matrices under perpendicular magnetic fields [79]. Possibly, such behavior could likewise be interpreted more quantitatively in terms of our formalism. As in low-Reynolds-number hydrodynamics, more complex inclusion objects should become accessible by the raspberry model, i.e., collections of rigidly connected identical spheres that as an entity represent more complex objects [80–82]. Moreover, similarly to low-Reynolds-number hydrodynamics, the effect of system boundaries should be analyzed [83,84]. Possibly, also hydrodynamic methods to describe more concentrated colloidal suspensions [85,86] could be transferred to the case of elastic environments.

Our results will be helpful in the quantitative interpretation of microrheological experiments [6–13], as already indicated in our previous work [14]. In principle, they should apply to different sorts of elastic matrix environments, as long as the material appears sufficiently homogeneous and isotropic down to the scale of the probe particle. For example, a related picture applies to the modeling of active forces generated by and within biological cells, where particularly the effect of active force dipoles is investigated [87,88]. Another field of application is to further characterize the tunability of composite materials by externally imposed fields [15,27–33]. For example, the change in the linear elastic moduli of magnetorheological elastomers when applying an external magnetic field could be addressed using our formalism. The method could be combined with statistical descriptions that

use a probability distribution to characterize the arrangement of the inclusions in an elastic matrix [89].

One strength is that larger numbers of inclusions can be handled than with simulation methods that explicitly resolve the matrix environment [23,34,46–49], at least to the accuracy given by the expansion in the particle distance and as long as linear elasticity theory is sufficient to describe the resulting matrix deformations to the desired degree of accuracy. Naturally, concerning the latter point, nonlinear elastic effects arising in real materials with increasing amplitude of deformation will first quantitatively affect the results and may, for large degrees of deformation, even lead to qualitative differences in the behavior. Extending such formalisms as the present one to the nonlinear regime is a nontrivial future task and incomparably more involved. Nevertheless, as we have demonstrated, in many cases numerical and experimental

results are still well reproduced. Thus, considering the explicit form of our resulting anlytical expressions and their efficient numerical evaluation, our approach will still be beneficial for analyzing the behavior of real materials. For example, it allows to quickly qualitatively scan the response of a multitude of different possible particle distributions and internal structural realizations in elastic composites. In this way, our approach shall help to quantitatively support the development of tunable composite materials designed for a specific requested purpose.

APPENDIX A

Equation (12) can be solved by Fourier forth and back transformation. The former replaces the nabla operator ∇ by $i\mathbf{k}$ and the Dirac delta function $\delta(\mathbf{r} - \mathbf{r}_0)$ by 1 in Eq. (12),

$$\lambda_{kpim}\hat{k}_m\hat{k}_p k^2 \tilde{G}_{ij}(\mathbf{k}) = \delta_{jk}, \tag{A1}$$

with the unit vector $\hat{\mathbf{k}} = \mathbf{k}/k$ in $\mathbf{k}$-space. Inserting

$$\lambda_{kpim}\hat{k}_m\hat{k}_p = \mu\left[\delta_{ik} + \frac{\lambda + \mu}{\mu}\hat{k}_i\hat{k}_k\right] \tag{A2}$$

via Eq. (7), we can solve for the Green's function in Fourier space:

$$\underline{\tilde{\mathbf{G}}}(\mathbf{k}) = \frac{1}{\mu k^2}\left[\underline{\hat{\mathbf{I}}} - \frac{\lambda + \mu}{\lambda + 2\mu}\hat{\mathbf{k}}\hat{\mathbf{k}}\right] = \frac{1}{\mu k^2}\left[\underline{\hat{\mathbf{I}}} - \frac{1}{2(1-\nu)}\hat{\mathbf{k}}\hat{\mathbf{k}}\right], \tag{A3}$$

with $\underline{\hat{\mathbf{I}}}$ the identity matrix and $\hat{\mathbf{k}}\hat{\mathbf{k}}$ a dyadic product. Next, we transform back to real space,

$$\underline{\mathbf{G}}(\mathbf{r}) = \frac{1}{(2\pi)^3}\int_0^{2\pi} d\varphi \int_0^{\pi} d\vartheta \sin\vartheta \int_0^{\infty} dk\, k^2 e^{i\mathbf{k}\cdot\mathbf{r}}\underline{\tilde{\mathbf{G}}}(\mathbf{k}) = \frac{1}{(2\pi)^3\mu}\int_0^{2\pi} d\varphi \int_0^{\pi} d\vartheta \sin\vartheta \int_0^{\infty} dk\, e^{ikr\cos\vartheta}\left[\underline{\hat{\mathbf{I}}} - \frac{1}{2(1-\nu)}\hat{\mathbf{k}}\hat{\mathbf{k}}\right]. \tag{A4}$$

The Dirac delta function is linked to its Fourier transform via

$$\int_{-\infty}^{\infty} dk\, e^{ikx} = \int_{-\infty}^{\infty} dk[\cos(kx) + i\sin(kx)] = 2\pi\delta(x). \tag{A5}$$

Keeping this in mind, the k-integral in Eq. (A4) is reformulated:

$$\int_0^{\infty} dk\, e^{ikr\cos\vartheta} = \int_0^{\infty} dk\cos(kr\cos\vartheta) + \int_0^{\infty} dk\, i\sin(kr\cos\vartheta) = \frac{1}{2}\int_{-\infty}^{\infty} dk\cos(kr\cos\vartheta) + \int_0^{\infty} dk\, i\sin(kr\cos\vartheta)$$

$$= \frac{1}{2}\int_{-\infty}^{\infty} dk[\cos(kr\cos\vartheta) + i\sin(kr\cos\vartheta)] - \frac{1}{2}\int_{-\infty}^{0} dk\, i\sin(kr\cos\vartheta)$$

$$= \pi\delta(r\cos\vartheta) - \frac{1}{2}\int_{-\infty}^{0} dk\, i\sin(kr\cos\vartheta). \tag{A6}$$

We find that the second term in the last line of the previous expression does not contribute. Upon inserting it into Eq. (A4), it leads to

$$\int_0^{2\pi} d\varphi \int_0^{\pi} d\vartheta \sin\vartheta \int_{-\infty}^{0} dk\sin(kr\cos\vartheta)\left[\hat{\mathbf{I}} - \frac{1}{2(1-\nu)}\hat{\mathbf{k}}\hat{\mathbf{k}}\right]. \tag{A7}$$

Substituting $u = \cos \vartheta$ and $-du = \sin \vartheta \, d\vartheta$, it can easily be seen that the first term in the square brackets leads to an odd function of u and therefore vanishes upon integration over du from $u = 1$ to -1. Calculating for the second term in the square brackets all matrix components $\hat{k}_i \hat{k}_j$ explicitly by inserting the components of $\hat{\mathbf{k}}$, the second term is found to vanish as well.

Thus, for the remainder of Eq. (A4), we obtain

$$\underline{\mathbf{G}}(\mathbf{r}) = \frac{1}{8\pi^2 \mu r} \int_0^{2\pi} d\varphi \int_{-1}^1 du \, \delta(u) \left[\hat{\underline{\mathbf{I}}} - \frac{1}{2(1-\nu)} \hat{\mathbf{k}} \hat{\mathbf{k}} \right] = \frac{1}{8\pi^2 \mu r} \int_0^{2\pi} d\varphi \left[\hat{\underline{\mathbf{I}}} - \frac{1}{2(1-\nu)} \hat{\mathbf{k}} \hat{\mathbf{k}} \right] \bigg|_{\hat{\mathbf{k}} \cdot \mathbf{r} = 0}, \tag{A8}$$

with the condition $\hat{\mathbf{k}} \perp \mathbf{r}$ arising from the delta function. Thus, $\hat{\mathbf{k}}$ can be expressed as

$$\hat{\mathbf{k}} = \hat{\boldsymbol{\alpha}} \cos \varphi + \hat{\boldsymbol{\beta}} \sin \varphi, \tag{A9}$$

with the constant unit vectors $\hat{\boldsymbol{\alpha}}$ and $\hat{\boldsymbol{\beta}}$, $\hat{\boldsymbol{\alpha}} \perp \hat{\boldsymbol{\beta}}$, and $\hat{\boldsymbol{\alpha}} \perp \mathbf{r} \perp \hat{\boldsymbol{\beta}}$. Then, $\hat{\boldsymbol{\alpha}}$, $\hat{\boldsymbol{\beta}}$, and $\hat{\mathbf{r}} = \mathbf{r}/r$ form an orthonormal basis, and we can write

$$\hat{\boldsymbol{\alpha}} \hat{\boldsymbol{\alpha}} + \hat{\boldsymbol{\beta}} \hat{\boldsymbol{\beta}} + \hat{\mathbf{r}} \hat{\mathbf{r}} = \hat{\underline{\mathbf{I}}}. \tag{A10}$$

Inserting Eq. (A9) into Eq. (A8), we evaluate the remaining integral over $d\varphi$ and obtain

$$\underline{\mathbf{G}}(\mathbf{r}) = \frac{1}{8\pi \mu r} \left[2\hat{\underline{\mathbf{I}}} - \frac{1}{2(1-\nu)} (\hat{\boldsymbol{\alpha}} \hat{\boldsymbol{\alpha}} + \hat{\boldsymbol{\beta}} \hat{\boldsymbol{\beta}}) \right] = \frac{1}{8\pi \mu r} \left[2\hat{\underline{\mathbf{I}}} - \frac{1}{2(1-\nu)} (\hat{\underline{\mathbf{I}}} - \hat{\mathbf{r}} \hat{\mathbf{r}}) \right]. \tag{A11}$$

Finally, combining the prefactors of $\hat{\underline{\mathbf{I}}}$ leads to the expression for the elastic Green's function in Eq. (13).

APPENDIX B

Our goal is to evaluate the integral

$$\frac{1}{2} \int_{-\infty}^{\infty} dk \, \frac{\sin(ka)}{ka} e^{ik\hat{\mathbf{k}} \cdot \mathbf{r}} \tag{B1}$$

appearing in Eq. (46). For this purpose, we rewrite the expression by substituting $z = ka$:

$$\frac{1}{2} \int_{-\infty}^{\infty} dk \, \frac{\sin(ka)}{ka} e^{ik\hat{\mathbf{k}} \cdot \mathbf{r}} = \frac{1}{4ia} \int_{-\infty}^{\infty} dz \, \frac{1}{z} \left[e^{iz(1 + \frac{\hat{\mathbf{k}} \cdot \mathbf{r}}{a})} - e^{iz(-1 + \frac{\hat{\mathbf{k}} \cdot \mathbf{r}}{a})} \right]. \tag{B2}$$

The evaluation can be accomplished in a straightforward way by using contour integration in the complex z plane. We start by considering only the first term on the right-hand side and define the function

$$f(z) = \frac{1}{z} e^{iz(1 + \frac{\hat{\mathbf{k}} \cdot \mathbf{r}}{a})}. \tag{B3}$$

Depending on the value of $\hat{\mathbf{k}} \cdot \mathbf{r}/a$, the integration path is amended on a case-by-case basis over a semicircle of infinite radius R in either the upper or the lower complex z half-plane. Starting with $\hat{\mathbf{k}} \cdot \mathbf{r}/a > -1$, the integration path is closed in the upper z half-plane. According to Cauchy's integral theorem, in our case all closed integration paths that do not contain the origin are zero, therefore

$$0 = \oint dz \, f(z) = \lim_{R \to \infty} \left[\int_{-R}^{-\varepsilon} dz \, f(z) - \int_{\mathcal{C}_\varepsilon} dz \, f(z) + \int_{\varepsilon}^{R} dz \, f(z) + \int_{\mathcal{C}_R} dz \, f(z) \right], \tag{B4}$$

with $\mathcal{C}_\varepsilon = \{\varepsilon e^{i\varphi} \,|\, 0 \leqslant \varphi \leqslant \pi\}$ and $\mathcal{C}_R = \{R e^{i\vartheta} \,|\, 0 \leqslant \vartheta \leqslant \pi\}$. The integral over the path $\mathcal{C}_R$ vanishes for $R \to \infty$. Combining these relations with the principal value,

$$\mathcal{P} \int (\ldots) = \lim_{\varepsilon \searrow 0} \left[\int_{-\infty}^{-\varepsilon} (\ldots) + \int_{\varepsilon}^{\infty} (\ldots) \right], \tag{B5}$$

we obtain in this first case

$$\mathcal{P} \int_{-\infty}^{\infty} dz \, f(z) = \lim_{\varepsilon \searrow 0} i \int_0^{\pi} d\varphi \, e^{i\varepsilon e^{i\varphi}(1 + \frac{\hat{\mathbf{k}} \cdot \mathbf{r}}{a})} = i\pi. \tag{B6}$$

Similarly, for $\hat{\mathbf{k}} \cdot \mathbf{r}/a < -1$ we amend the integration path over the semicircle of infinite radius in the lower z half-plane and obtain for the principal value

$$\mathcal{P} \int_{-\infty}^{\infty} dz \, f(z) = -\lim_{\varepsilon \searrow 0} i \int_{\pi}^{2\pi} d\varphi \, e^{i\varepsilon e^{i\varphi}(1 + \frac{\hat{\mathbf{k}} \cdot \mathbf{r}}{a})} = -i\pi. \tag{B7}$$

An analogous procedure for the second term on the right-hand side of Eq. (B2) yields

$$\mathcal{P} \int_{-\infty}^{\infty} dz \, \frac{1}{z} e^{iz(-1+\frac{\hat{\mathbf{k}}\cdot\mathbf{r}}{a})} = \begin{cases} i\pi, & \text{for } \frac{\hat{\mathbf{k}}\cdot\mathbf{r}}{a} > 1, \\ -i\pi, & \text{for } \frac{\hat{\mathbf{k}}\cdot\mathbf{r}}{a} < 1. \end{cases} \tag{B8}$$

Inserting Eqs. (B6)–(B8) into Eq. (B2) finally leads to [52]

$$\frac{1}{2} \int_{-\infty}^{\infty} dk \, \frac{\sin(ka)}{ka} e^{ik\hat{\mathbf{k}}\cdot\mathbf{r}} = \begin{cases} \frac{\pi}{2a}, & \text{for } -1 < \frac{\hat{\mathbf{k}}\cdot\mathbf{r}}{a} < 1, \\ 0, & \text{otherwise.} \end{cases} \tag{B9}$$

[1] K. E. Kurtis, MRS Bull. **40**, 1102 (2015).

[2] G. Li, Y. Zhao, S.-S. Pang, and Y. Li, Cement Concrete Res. **29**, 1455 (1999).

[3] G. Constantinides and F.-J. Ulm, Cement Concrete Res. **34**, 67 (2004).

[4] E. N. Landis and J. E. Bolander, J. Phys. D: Appl. Phys. **42**, 214002 (2009).

[5] V. Mechtcherine, A. Gram, K. Krenzer, J.-H. Schwabe, S. Shyshko, and N. Roussel, Mater. Struct. **47**, 615 (2014).

[6] F. Ziemann, J. Rädler, and E. Sackmann, Biophys. J. **66**, 2210 (1994).

[7] A. R. Bausch, W. Möller, and E. Sackmann, Biophys. J. **76**, 573 (1999).

[8] T. A. Waigh, Rep. Prog. Phys. **68**, 685 (2005).

[9] C. Wilhelm, Phys. Rev. Lett. **101**, 028101 (2008).

[10] D. Mizuno, C. Tardin, C. F. Schmidt, and F. C. MacKintosh, Science **315**, 370 (2007).

[11] P. Bender, A. Günther, A. Tschöpe, and R. Birringer, J. Magn. Magn. Mater. **323**, 2055 (2011).

[12] L. Roeder, P. Bender, A. Tschöpe, R. Birringer, and A. M. Schmidt, J. Polym. Sci., Part B: Polym. Phys. **50**, 1772 (2012).

[13] P. Bender, A. Tschöpe, and R. Birringer, J. Magn. Magn. Mater. **346**, 152 (2013).

[14] M. Puljiz, S. Huang, G. K. Auernhammer, and A. M. Menzel, Phys. Rev. Lett. **117**, 238003 (2016).

[15] Y. An and M. T. Shaw, Smart Mater. Struct. **12**, 157 (2003).

[16] R. Fuhrer, E. K. Athanassiou, N. A. Luechinger, and W. J. Stark, Small **5**, 383 (2009).

[17] H. Böse, R. Rabindranath, and J. Ehrlich, J. Intell. Mater. Syst. Struct. **23**, 989 (2012).

[18] M. Roussel, C. Malhaire, A.-L. Deman, J.-F. Chateaux, L. Petit, L. Seveyrat, J. Galineau, B. Guiffard, C. Seguineau, J.-M. Desmarres, and J. Martegoutte, J. Micromech. Microeng. **24**, 055011 (2014).

[19] M. Zrínyi, L. Barsi, and A. Büki, J. Chem. Phys. **104**, 8750 (1996).

[20] O. V. Stolbov, Y. L. Raikher, and M. Balasoiu, Soft Matter **7**, 8484 (2011).

[21] P. Ilg, Soft Matter **9**, 3465 (2013).

[22] R. Weeber, S. Kantorovich, and C. Holm, J. Chem. Phys. **143**, 154901 (2015).

[23] P. Cremer, H. Löwen, and A. M. Menzel, Phys. Chem. Chem. Phys. **18**, 26670 (2016).

[24] G. Diguet, E. Beaugnon, and J.-Y. Cavaillé, J. Magn. Magn. Mater. **321**, 396 (2009).

[25] K. Wongtimnoi, B. Guiffard, A. Bogner-Van de Moortele, L. Seveyrat, C. Gauthier, and J.-Y. Cavaillé, Combust. Sci. Technol. **71**, 885 (2011).

[26] E. Allahyarov, H. Löwen, and L. Zhu, Phys. Chem. Chem. Phys. **17**, 32479 (2015).

[27] M. R. Jolly, J. D. Carlson, B. C. Muñoz, and T. A. Bullions, J. Intell. Mater. Syst. Struct. **7**, 613 (1996).

[28] L. Gao and X. Zhao, J. Appl. Polym. Sci. **94**, 2517 (2004).

[29] K. Minagawa and K. Koyama, Curr. Org. Chem. **9**, 1643 (2005).

[30] G. Filipcsei, I. Csetneki, A. Szilágyi, and M. Zrínyi, Adv. Polym. Sci. **206**, 137 (2007).

[31] D. Ivaneyko, V. Toshchevikov, M. Saphiannikova, and G. Heinrich, Condens. Matter Phys. **15**, 33601 (2012).

[32] A. M. Menzel, Phys. Rep. **554**, 1 (2015).

[33] S. Odenbach, Arch. Appl. Mech. **86**, 269 (2016).

[34] P. Cremer, H. Löwen, and A. M. Menzel, Appl. Phys. Lett. **107**, 171903 (2015).

[35] E. Jarkova, H. Pleiner, H.-W. Müller, and H. R. Brand, Phys. Rev. E **68**, 041706 (2003).

[36] S. Bohlius, H. R. Brand, and H. Pleiner, Phys. Rev. E **70**, 061411 (2004).

[37] M. Tarama, P. Cremer, D. Y. Borin, S. Odenbach, H. Löwen, and A. M. Menzel, Phys. Rev. E **90**, 042311 (2014).

[38] G. Pessot, H. Löwen, and A. M. Menzel, J. Chem. Phys. **145**, 104904 (2016).

[39] T. I. Volkova, V. Böhm, T. Kaufhold, J. Popp, F. Becker, D. Y. Borin, G. V. Stepanov, and K. Zimmermann, J. Magn. Magn. Mater. **431**, 262 (2017).

[40] H.-X. Deng, X.-L. Gong, and L.-H. Wang, Smart Mater. Struct. **15**, N111 (2006).

[41] T. L. Sun, X. L. Gong, W. Q. Jiang, J. F. Li, Z. B. Xu, and W. H. Li, Polym. Test. **27**, 520 (2008).

[42] W. Li and X. Zhang, Recent Pat. Mech. **1**, 161 (2008).

[43] G. Pessot, P. Cremer, D. Y. Borin, S. Odenbach, H. Löwen, and A. M. Menzel, J. Chem. Phys. **141**, 124904 (2014).

[44] A. M. Biller, O. V. Stolbov, and Y. L. Raikher, J. Appl. Phys. **116**, 114904 (2014).

[45] A. M. Biller, O. V. Stolbov, and Y. L. Raikher, Phys. Rev. E **92**, 023202 (2015).

[46] Y. Han, W. Hong, and H. E. Faidley, Int. J. Solids Struct. **50**, 2281 (2013).

[47] C. Spieler, M. Kästner, J. Goldmann, J. Brummund, and V. Ulbricht, Acta Mech. **224**, 2453 (2013).

[48] A. Attaran, J. Brummund, and T. Wallmersperger, J. Magn. Magn. Mater. **431**, 188 (2017).

[49] P. Metsch, K. A. Kalina, C. Spieler, and M. Kästner, Comput. Mater. Sci. **124**, 364 (2016).

[50] L. D. Landau and E. M. Lifshitz, *Theory of Elasticity* (Elsevier, Oxford, 1986).

[51] S. Kim and S. J. Karrila, *Microhydrodynamics: Principles and Selected Applications* (Butterworth-Heinemann, Boston, 1991).

[52] J. K. G. Dhont, *An Introduction to Dynamics of Colloids* (Elsevier, Amsterdam, 1996).

[53] B. U. Felderhof, Phys. A **89**, 373 (1977).

[54] D. L. Ermak and J. A. McCammon, J. Chem. Phys. **69**, 1352 (1978).

[55] L. Durlofsky, J. F. Brady, and G. Bossis, J. Fluid Mech. **180**, 21 (1987).

[56] K. Zahn, J. M. Méndez-Alcaraz, and G. Maret, Phys. Rev. Lett. **79**, 175 (1997).

[57] J.-C. Meiners and S. R. Quake, Phys. Rev. Lett. **82**, 2211 (1999).

[58] J. K. G. Dhont, J. Chem. Phys. **120**, 1642 (2004).

[59] M. Rex and H. Löwen, Eur. Phys. J. E **26**, 143 (2008).

[60] S. Jäger, H. Stark, and S. H. L. Klapp, J. Phys. Condens. Matter **25**, 195104 (2013).

[61] C. M. Pooley, G. P. Alexander, and J. M. Yeomans, Phys. Rev. Lett. **99**, 228103 (2007).

[62] E. Lauga and T. R. Powers, Rep. Prog. Phys. **72**, 096601 (2009).

[63] A. Baskaran and M. C. Marchetti, Proc. Natl. Acad. Sci. USA **106**, 15567 (2009).

[64] A. M. Menzel, A. Saha, C. Hoell, and H. Löwen, J. Chem. Phys. **144**, 024115 (2016).

[65] S. Kim and N. Phan-Thien, J. Elast. **37**, 93 (1995).

[66] A. N. Norris, J. Acoust. Soc. Am. **123**, 99 (2008).

[67] G. K. Batchelor and J. T. Green, J. Fluid Mech. **56**, 375 (1972).

[68] N. Phan-Thien and S. Kim, ZAMP **45**, 177 (1994).

[69] C. L. M. H. Navier, Mém. Acad. Sci. Inst. France **6**, 389 (1822).

[70] C. Weinberger, W. Cai, and D. Barnett, *Lecture Notes—Elasticity of Microscopic Structures* (Stanford University, Stanford, 2005).

[71] L. D. Landau and E. M. Lifshitz, *Fluid Mechanics* (Elsevier, Oxford, 1987).

[72] N. Phan-Thien, J. Elast. **32**, 243 (1993).

[73] M. Reichert and H. Stark, Phys. Rev. E **69**, 031407 (2004).

[74] J. D. Jackson, *Classical Electrodynamics* (Wiley, New York, 1999).

[75] E. C. Stoner and E. P. Wohlfarth, Philos. Trans. R. Soc. London A **240**, 599 (1948).

[76] Q. Chen and Z. J. Zhang, Appl. Phys. Lett. **73**, 3156 (1998).

[77] L. Roeder, P. Bender, M. Kundt, A. Tschöpe, and A. M. Schmidt, Phys. Chem. Chem. Phys. **17**, 1290 (2015).

[78] R. Skomski, J. Phys. Condens. Matter **15**, R841 (2003).

[79] S. Huang, G. Pessot, P. Cremer, R. Weeber, C. Holm, J. Nowak, S. Odenbach, A. M. Menzel, and G. K. Auernhammer, Soft Matter **12**, 228 (2016).

[80] V. Lobaskin and B. Dünweg, New J. Phys. **6**, 54 (2004).

[81] V. Lobaskin, B. Dünweg, and C. Holm, J. Phys. Condens. Matter **16**, S4063 (2004).

[82] C. Passow, B. ten Hagen, H. Löwen, and J. Wagner, J. Chem. Phys. **143**, 044903 (2015).

[83] T. M. Squires and M. P. Brenner, Phys. Rev. Lett. **85**, 4976 (2000).

[84] Y. W. Kim and R. R. Netz, J. Chem. Phys. **124**, 114709 (2006).

[85] H. Tanaka and T. Araki, Phys. Rev. Lett. **85**, 1338 (2000).

[86] J. F. Morris, Rheol. Acta **48**, 909 (2009).

[87] J. Yuval and S. A. Safran, Phys. Rev. E **87**, 042703 (2013).

[88] O. Cohen and S. A. Safran, Soft Matter **12**, 6088 (2016).

[89] T. Gundermann, P. Cremer, H. Löwen, A. M. Menzel, and S. Odenbach, Smart Mater. Struct. **26**, 045012 (2017).

Publication III

Reversible magnetomechanical collapse: virtual touching and detachment of rigid inclusions in a soft elastic matrix

Reproduced from

Author's contributions

All authors have contributed to this publication. I performed the theoretical analysis and comparison with the experimental data (including measurement error analysis of the experimental data), the theoretical analysis using the dipole-spring model, as well as the completion of the associated inside front cover. I estimate my overall contribution to this work to approximately 60%.

Copyright and license notice

Reversible magnetomechanical collapse: virtual touching and detachment of rigid inclusions in a soft elastic matrix†

Mate Puljiz,[a] Shilin Huang,[b] Karl A. Kalina,[c] Johannes Nowak,[d] Stefan Odenbach,[d] Markus Kästner,[c] Günter K. Auernhammer‡[b] and Andreas M. Menzel [ID] *[a]

Soft elastic composite materials containing particulate rigid inclusions in a soft elastic matrix are candidates for developing soft actuators or tunable damping devices. The possibility to reversibly drive the rigid inclusions within such a composite together to a close-to-touching state by an external stimulus would offer important benefits. Then, a significant tuning of the mechanical properties could be achieved due to the resulting mechanical hardening. For a long time, it has been argued whether a virtual touching of the embedded magnetic particles with subsequent detachment can actually be observed in real materials, and if so, whether the process is reversible. Here, we present experimental results that demonstrate this phenomenon in reality. Our system consists of two paramagnetic nickel particles embedded at finite initial distance in a soft elastic polymeric gel matrix. Magnetization in an external magnetic field tunes the magnetic attraction between the particles and drives the process. We quantify our experimental results by different theoretical tools, *i.e.*, explicit analytical calculations in the framework of linear elasticity theory, a projection onto simplified dipole-spring models, as well as detailed finite-element simulations. From these different approaches, we conclude that in our case the cycle of virtual touching and detachment shows hysteretic behavior due to the mutual magnetization between the paramagnetic particles. Our results are important for the design and construction of reversibly tunable mechanical damping devices. Moreover, our projection on dipole-spring models allows the formal connection of our description to various related systems, *e.g.*, magnetosome filaments in magnetotactic bacteria.

[a] *Institut für Theoretische Physik II: Weiche Materie, Heinrich-Heine-Universität Düsseldorf, 40225 Düsseldorf, Germany. E-mail: menzel@thphy.uni-duesseldorf.de*

[b] *Max Planck Institute for Polymer Research, Ackermannweg 10, 55128 Mainz, Germany*

[c] *Technische Universität Dresden, Institute of Solid Mechanics, 01062 Dresden, Germany*

[d] *Technische Universität Dresden, Institute of Fluid Mechanics, 01062 Dresden, Germany*

† Electronic supplementary information (ESI) available. See DOI: 10.1039/c8sm01051j

‡ Present address: Leibniz Institute for Polymer Research, 01069 Dresden, Germany. E-mail: auernhammer@ipfdd.de

1 Introduction

The fabrication of soft elastic composite materials that consist of rigid particles embedded in a soft elastic environment serves to develop soft actuators,[1–7] tunable dampers and vibration absorbers,[8–11] components of tunable anisotropic electric conductivity,[12] or devices for energy storage.[13–18] For instance, actuation is achieved by exposing composites that contain para- or ferromagnetic particles to an external magnetic field gradient.[2,19,20] In this way, forces are directly imposed onto the embedded particles that are drawn into the field gradient.[21] Indirectly, magnetic or electric moments can be induced on the particles by external magnetic or electric fields. Then, overall distortions result from the induced mutual particle interactions.[22–30]

At the same time, inducing, altering, or reorienting magnetic moments by external magnetic fields affects the overall mechanical properties of the materials due to the modified particle interactions. As a consequence, the static and dynamic elastic moduli are tuned,[2,24,27,31–45] and also the nonlinear stress–strain behavior can be qualitatively affected.[46,47]

In both situations of actuator applications and tuning the mechanical properties it is often desired to achieve a maximum of the externally induced relative displacements between the particles. For inclusions that approach each other during such displacements, the maximum is reached when the particles come into close contact and virtually touch each other. In such a situation, the overall material can significantly harden as the steric interactions between the virtually touching particles now

come into effect and contribute to the overall mechanical stiffness.[44,48] Moreover, as the magnetic interactions strongly increase with reduced distance between the particles, such an approach of the particles can show hysteretic behavior when compared to a subsequent detachment.[43,46,47,49–54] For instance, ref. 51 and 52 address such hysteretic effects by theoretical and simulation approaches in detail for a two-particle model set-up.

Experimentally, observing and tracking externally induced rearrangements of magnetic particles within elastic environments is standard. For example, this concerns active magnetic microrheology,[55–61] or, in fact, quantifying the structural rearrangement within samples of magnetic elastic composite materials.[28,62–64] Recently, in different samples of initially rather isotropically distributed and well separated inclusions, the formation of short chain-like arrangements has been observed experimentally.[34,50,64,65] Still, in the final state of the induced textures in ref. 64, there are gaps between the individual particles. If the particles could be driven basically into contact by further increasing the magnetic interactions between them, a strong increase of the elastic moduli may be observed as indicated above. To really observe such an approach in actual experiments has so far been difficult to conceive. On the one hand, elastic polymeric systems are typically rather incompressible. Yet, the material between the particles would need to be significantly compressed or be squeezed out laterally. On the other hand, the elastic matrix could be ruptured by the particle approach to allow a touching of the particles. However, in this case, the desired reversibility of the whole process, to allow repeated usage in practice, is questioned.

In spite of these legitimate concerns, we have found that the described process is possible and actually observable in experiments. We have embedded two magnetizable nickel particles into a soft elastic polymeric gel matrix. Stepwise increasing the magnetic attraction between the two particles by an external magnetic field, the particles approached until they finally snapped together into close contact. Switching off the magnetic attraction, the particles returned to their initial state. The process appeared reversible, and we were able to start this cycle repeatedly from the beginning.

Reduced minimal models that come into question to describe such situations address rigid spherical magnetic particles of finite size. In such models, some elastic contribution, representing the embedding elastic environment, tries to maintain a preset distance between the two particles. This can be achieved by an elastic spring-like interaction,[18,42,44,48,50,66–69] more refined contributions such as elastic bars and rods,[51,52] or discretized volume elements describing the elastic matrix.[30,46,47,70,71] Apart from that, the elastic restoring forces resulting from deformations of the surrounding elastic environment can also be calculated analytically in the framework of linear elasticity theory.[72–78] Often, the magnetic moments on the particles are represented by magnetic dipoles of permanent magnitude.[22,37,39,42,44,46–48,66,67,79–82] Addressing magnetization of dipolar particles by a non-saturating external magnetic field is possible by including "loop corrections", i.e., an iterative numerical loop that calculates the additional contributions to the dipole moments

resulting from the mutually induced magnetization between the magnetic particles.[18,83] More refined approaches resolve the finite size of the particles and take into account spatial variations of the induced magnetization across the particle interior.[30,39,52,70,84]

Below, we first report our experimental observations in Section 2. We then continue by an analytical description of the situation in terms of linear elasticity theory in Section 3. Despite the strong relative distortions, we find that the experimental results can be described reasonably well by the linearly elastic approach. An effective local elastic modulus for the elastic matrix can be extracted in this way. This allows to map the whole situation to simplified dipole-spring approaches in Section 4. Moreover, we predict significant hysteretic behavior on this basis. After that, we present results from significantly more detailed finite-element (FE) simulations in Section 5. They include nonlinear contributions to the response of the elastic matrix and resolve the magnetization across the inside of the magnetic particles. Particularly, they support the analytical approaches in the still separated state, but imply quantitative corrections close to touching of the particles and for the predicted hysteretic behavior. Several conclusions are given in Section 6.

2 Experimental observations

Our experimental system was generated in a way similar to the one presented in ref. 76. Two nickel particles (purchased from Alfa Aesar $-$ 100 $\pm$ 325 mesh, purity 99.8%) were embedded in the center plane of a polydimethylsiloxane-based soft gel[28] enclosed in a plastic mold (diameter $\sim$24 mm, height $\sim$6 mm). For this purpose, we first filled the sample volume only to half height with the reaction solution and allowed for a first cross-linking (for about 0.5 h). We then placed the particles by hand on top of the surface of this first gel layer with a center-to-center distance of initially $r_{12} = (302.4 \pm 1.9)$ μm as defined in Fig. 1(a). Thereafter, we filled in the top half layer of the gel. To guarantee a good connection between the two gel layers, a cross-linking for at least 7 days at room temperature was allowed. Our samples were prepared close to the percolation threshold of the resulting cross-linked polymer network to achieve a pronounced mechanical softness. As a consequence, small uncontrollable perturbations and fluctuations during preparation lead to measurable deviations in the elastic moduli for different samples. Therefore, our elastic modulus cannot be determined by a measurement on a rheometer, because this requires the preparation of a separate sample in a different compartment. The nickel particles had a diameter of 170 $\pm$ 10 μm. Fig. 2 shows the corresponding magnetization curve determined by a vibrating sample magnetometer, Lake Shore 7407. It indicates a small remanence of $\sim$7.5 kA m^{-1} and a low coercive field of $\sim$2.4 mT. In our experiment, an external magnetic field was applied along the center-to-center vector of the two particles, see Fig. 1(a). This field was generated by a Halbach array of four magnets. To allow for an adjustable magnitude of the field, the magnets in the array could be moved radially in discrete steps from
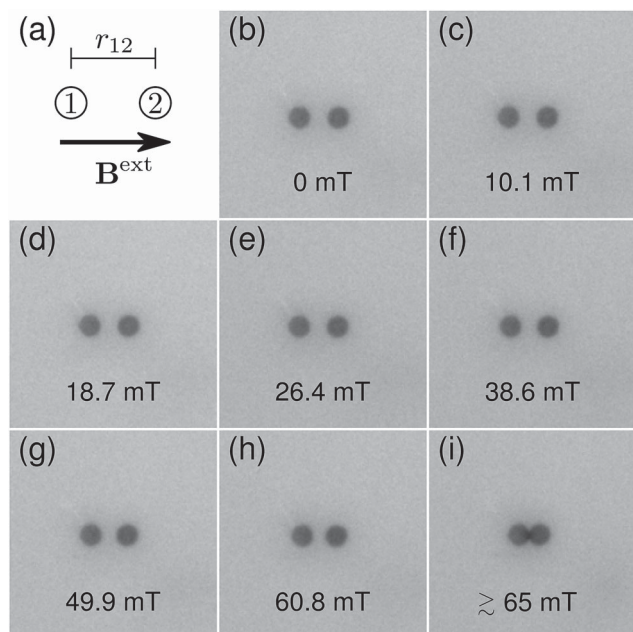
Fig. 1 (a) Schematic illustration of our set-up. Two magnetic nickel particles are embedded in an elastic polymer matrix, separated by a distance r_{12}. An external magnetic field $\mathbf{B}^{ext}$ is applied along the center-to-center vector of the two particles. (b–i) Experimental snapshots for increasing the magnetic field strength as indicated by the given magnitudes. At high enough field strengths (i) the particles come into close contact. This snapping together is reversible, that is, switching off the field, the particles separate again (b).
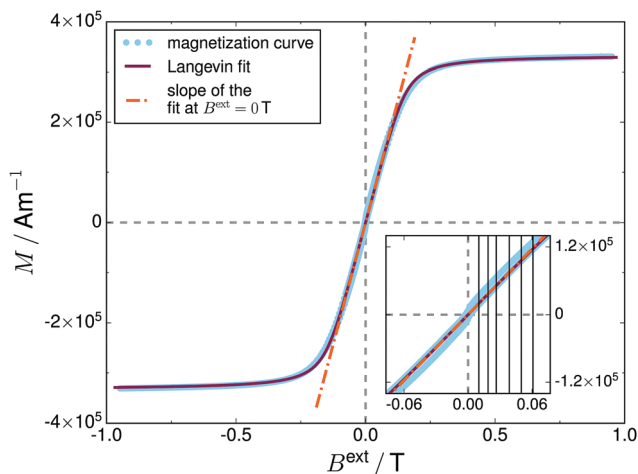
Fig. 2 Bulk magnetization curve $M(B^{ext})$ for the investigated nickel particles. The experimentally measured data curve (bright blue dots) reveals minor remnant magnetization, where a small hysteresis between increasing and decreasing external magnetic field can be identified (see also the inset). A fit of the data points using a Langevin function, see eqn (1), is performed (purple line). Linearizing the function, a slope of the curve at $B^{ext} = 0$ T is found as indicated by the orange dash-dotted line. It leads to a value for the relative permeability of $\mu_r = 14.10 \pm 0.58$. In the inset, the applied field strengths in our two-particle experiment are marked by the vertical lines.

distances of ~ 2 cm to ~ 10 cm from the center of the sample. In this way, the magnetic field strength could be varied in a range from 0 mT to ~ 100 mT. For each used position of the magnets, the magnetic field at the sample center was measured by a Lake Shore Model 425 Gaussmeter with a transverse probe.[28]

In the experiment, the magnetic field was increased in 6 steps from 0 mT to 60.8 mT. After applying the next possible field strength ~ 65.1 mT, the particles reversibly snapped into close contact. To determine the center-to-center distance of the particles, their positions were imaged using a CCD camera (MATRIX VISION mvBlueCOUGAR-S) equipped with a zoom macro lens (Navitar Zoom 7000). The particle tracker module of ImageJ was employed.[85] Due to little variations of the image quality, the uncertainty in the measured particle positions varied slightly during the experiment, but was always below 4% of the particle diameter.

As a result, we observed that the center-to-center distance with increasing magnetic field smoothly decreased up to a field strength ~ 60.8 mT. Fig. 3 contains the measured experimental data points and Fig. 1(b–i) shows the corresponding snapshots. Applying fields of strength ~ 65.1 mT, we observed that the particles snap into close contact, see Fig. 1(i). However, this approach is reversible. Switching off the external magnetic field, the particles separated again and took their initial position, at least within the experimental errors. We also repeated the procedure several times, reversibly observing the snapping at the same magnetic field strength.

An interesting question is whether there is some hysteresis involved in the approach of the particles. Does the separation of the particles, when continuously reducing the strength of the magnetic field, occur at lower field magnitudes than when increasing the magnetic field?

Unfortunately, our experimental set-up does not allow to clarify this question. To alter the field strength, we have to take away the magnets, readjust their holders, and then reinsert the magnets at the new distance from the center of the sample. The reinsertion always corresponds to an increase of the magnetic field amplitude, with an intermediate state of vanishing field. It is therefore up to theoretical approaches and simulations to clarify the question on possible hysteresis in our present set-up when decreasing the magnetic field. The general possibility of either hysteretic or continuous behavior has been theoretically outlined and investigated before.[48,51,52]

3 Description by linear elasticity theory

Consequently, we now compare our experimental results in Fig. 3 with different theoretical approaches. In this way, we can extract from the theories the effective local elastic shear modulus μ that, as described above, could not be measured by a rheometer. Using this result, we will be able to address the question of underlying hysteresis.

We start by a description in the framework of linear elasticity theory.[86] The advantage of this approach is that, assuming a homogeneous, isotropic, and infinitely extended elastic matrix, the situation of two displaced spheres can, in principle, be solved analytically to any desired accuracy. On the downside,

Paper
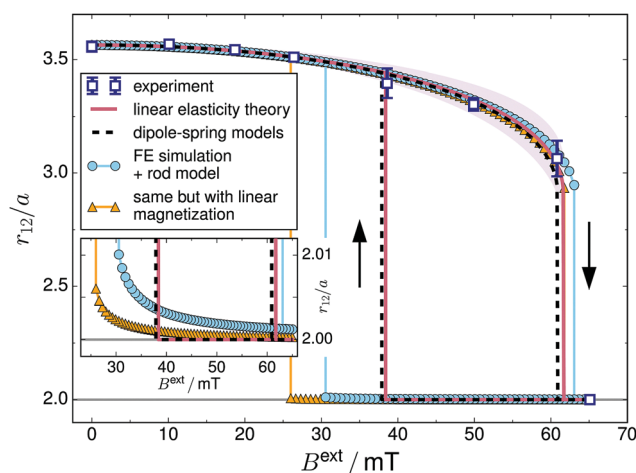
Fig. 3 Interparticle center-to-center distance r_{12} as a function of the magnitude B^{ext} of the externally applied magnetic field. Open squares with error bars mark the experimentally measured distances as a function of the applied magnetic field. The solid (red) curve is obtained analytically from linear elasticity theory and a magnetic dipole model as described in Section 3. Fitting to the experimental data points, we extract a shear modulus of $\mu = 226.0 \pm 2.8$ Pa. The shaded area corresponds to the uncertainty in the theoretical result because of the uncertainties in the fit and the experimental input parameters.[76] A collapse of the separated state is predicted at $B^{ext} \approx 61.7$ mT ($r_{12}/a = 2$ corresponds to a touching state where the particle surfaces are in contact). For decreasing magnetic field strength, the theory indicates pronounced hysteresis and a detachment at $B^{ext} \approx 38.3$ mT. We have mapped the theory to simplified dipole-spring models as described in Section 4, represented by the dashed line. The curve shows good agreement with the results obtained from linear elasticity theory. Apart from that, we performed additional finite-element simulations as detailed in Section 5 and marked by the light blue data points. They include effects of nonlinear elasticity of the polymeric matrix, nonlinear magnetization, and spatially resolved magnetization within the spherical particles. To good approximation, they confirm the field magnitude at which the particles approach. As may have been expected, they reveal an even more pronounced hysteresis relatively to the linearly elastic theory. Additionally, we have included simulation results for linearized magnetization behavior as marked by the (orange) triangles. Moreover, as shown by the inset, the simulations indicate that a finite gap may remain between the particles in the collapsed state.

of course, only a linearly elastic response of the matrix is described. In Fig. 3, the experimental data points before the collapse are confined to relative distance changes $\lesssim 15\%$ between the particle centers, in favor of a linearly elastic characterization of the investigated soft elastic gel matrix. Moreover, we consider the elastic matrix to be incompressible and in the theory take the well-defined limit $\nu \rightarrow 1/2$ for the Poisson ratio. This, likewise, represents a reasonable approximation for the system under investigation.

Our two idealized rigid spherical inclusions, both of radius a and labeled by 1 and 2, are initially centered at positions $\mathbf{r}_1$ and $\mathbf{r}_2$, respectively. If an external magnetic field $\mathbf{H}^{ext}$ is applied from outside, the spheres are magnetized. To present our results, we use the quantity $\mathbf{B}^{ext} = \mu_0 \mathbf{H}^{ext}$, where μ_0 is the magnetic vacuum permeability. For an infinitely extended bulk material, the corresponding magnetization curve is given by Fig. 2.

Assuming magnetic isotropy within our particles, we describe their internal magnetization $\mathbf{M}$ by the Langevin function

$$\mathbf{M} = M^s \left[\coth\left(\alpha |\mathbf{H}^{in}|\right) - \frac{1}{\alpha |\mathbf{H}^{in}|} \right] \frac{\mathbf{H}^{in}}{|\mathbf{H}^{in}|}, \qquad (1)$$

where M^s and $\mathbf{H}^{in}$ denote the magnitude of the saturation magnetization and the magnetic field inside the material, respectively. The parameter α determines the linearized relation between $\mathbf{M}$ and $\mathbf{H}^{in}$ for weak magnetic fields, given by $\mathbf{M} = \alpha M^s \mathbf{H}^{in}/3$. Considering only one spherical particle exposed to a homogeneous external magnetic field $\mathbf{H}^{ext}$, also $\mathbf{M}$ and $\mathbf{H}^{in}$ are homogeneous. Because of the spherical geometry, a demagnetization effect with a demagnetization factor of 1/3 occurs, so that[21]

$$\mathbf{H}^{in} = \mathbf{H}^{ext} - \frac{1}{3}\mathbf{M}. \qquad (2)$$

Fitting eqn (1) to the experimental data given in Fig. 2, we find the values $M^s = (3.333 \pm 0.290) \times 10^5$ A m^{-1} and $\alpha = (1.179 \pm 0.057) \times 10^{-4}$ m A^{-1}, respectively.

The experimentally measured data points displayed in Fig. 3 before the collapse were obtained at $B^{ext} \lesssim 61$ mT, and the collapse of the particles occurred below 65.1 mT. Fig. 2 demonstrates that the overall magnetization curve of the material in this regime can be well approximated by a straight line. We may thus treat the problem within the framework of linear magnetization behavior by[21]

$$\mathbf{M} = (\mu_r - 1)\mathbf{H}^{in}, \qquad (3)$$

with μ_r the relative magnetic permeability.[21] A linearization of eqn (1) for small values of H^{in} leads to $\mu_r = \alpha M^s/3 + 1$, so that in our case $\mu_r = 14.10 \pm 0.58$.

Combining eqn (2) and (3) yields

$$\mathbf{H}^{in} = \frac{3}{\mu_r + 2}\mathbf{H}^{ext}, \qquad \mathbf{M} = 3\frac{\mu_r - 1}{\mu_r + 2}\mathbf{H}^{ext}. \qquad (4)$$

Outside the spherical particle, the induced magnetic field resulting from the internal magnetization coincides with the one of a magnetic point dipole[21]

$$\mathbf{m} = \frac{4\pi}{3}a^3 \mathbf{M}, \qquad (5)$$

located at the center of the sphere.

Since the magnetic particles in the states corresponding to the experimental data points before the collapse are well separated from each other, we maintain this picture also in our situation of two particles. That is, we approximate the magnetic moment of each particle by a point dipole $\mathbf{m}_i$, $i = 1, 2$, located at the particle center. However, the role of $\mathbf{H}^{ext}$ in eqn (4) is now not only played by the external magnetic field itself. Also the field induced by the other dipole contributes at this point. We denote the magnetic field induced at position $\mathbf{r}$ by a dipole $\mathbf{m}_j$ located at $\mathbf{r}_j$ as

$$\mathbf{H}_j^{dip}(\mathbf{r}) = \frac{1}{4\pi}\left(\frac{3(\mathbf{r} - \mathbf{r}_j)\mathbf{m}_j \cdot (\mathbf{r} - \mathbf{r}_j)}{|\mathbf{r} - \mathbf{r}_j|^5} - \frac{\mathbf{m}_j}{|\mathbf{r} - \mathbf{r}_j|^3}\right). \qquad (6)$$

Together, from eqn (4)–(6), we obtain

$$\mathbf{m}_i = 4\pi a^3 \frac{\mu_\mathrm{r} - 1}{\mu_\mathrm{r} + 2}\Big[\mathbf{H}^\mathrm{ext} + \mathbf{H}_j^\mathrm{dip}(\mathbf{r}_i)\Big]. \tag{7}$$

Obviously, eqn (6) and (7) need to be solved by iteration.[18,83] After convergence, the final magnetic moments are obtained for a certain particle configuration. For the dipole configurations resulting for the experimental data points in the separated state in Fig. 3 we have estimated $H^\mathrm{dip}/H^\mathrm{ext} \lesssim 6\%$, which supports our approximation in terms of magnetic dipoles.

Next, we need to determine the magnetic forces resulting from the mutual interaction between the two induced magnetic moments. For our set-up and in the regime of linear magnetization, a corresponding expression for the change in overall magnetic energy when including the magnetic particles into the external magnetic field[21] reads

$$W^\mathrm{mag} = -\frac{1}{2}(\mathbf{m}_1 + \mathbf{m}_2) \cdot \mathbf{B}^\mathrm{ext}. \tag{8}$$

Here, $\mathbf{m}_1$ and $\mathbf{m}_2$ are the magnetic moments obtained from the above iteration and contain the mutual magnetization between the two particles. The magnetic forces on the two particles then are obtained as

$$\mathbf{F}_i = -\nabla_{\mathbf{r}_i} W^\mathrm{mag} \tag{9}$$

for $i = 1, 2$. Our set-up is axially symmetric with respect to the center-to-center direction $\hat{\mathbf{r}}_{ij} = \mathbf{r}_{ij}/r_{ij}$, with $\mathbf{r}_{ij} = \mathbf{r}_i - \mathbf{r}_j$ and $r_{ij} = |\mathbf{r}_{ij}|$. Moreover, it is symmetric with respect to the center position between the two particles that we choose as the origin. Then, we may discretize eqn (9) as

$$\mathbf{F}_i = -\hat{\mathbf{r}}_i \lim_{\varDelta \searrow 0} \frac{W^\mathrm{mag}\big|_{(r_i + \varDelta)\hat{\mathbf{r}}_i} - W^\mathrm{mag}\big|_{(r_i - \varDelta)\hat{\mathbf{r}}_i}}{2\varDelta}, \tag{10}$$

where $i \in \{1,2\}$, $\mathbf{r}_i = r_i\hat{\mathbf{r}}_i$ with $r_i = |\mathbf{r}_i|$, and $\hat{\mathbf{r}}_1 = -\hat{\mathbf{r}}_2 = \hat{\mathbf{r}}_{12}$. In this expression, the $\mathbf{m}_i$ for each modification in position $\varDelta$ need to be reevaluated by the iterative procedure described above.

As the magnetic forces act on the particulate inclusions, the particles are pressed against the surrounding elastic matrix. This leads to matrix deformations and, in turn, to elastic restoring forces on the particles that limit their induced displacements. Moreover, the final displacements $\mathbf{U}_i$ of the particles are elastically coupled to each other through the induced matrix deformations. If one of the particles distorts the environment, the other particle, likewise embedded in the elastic matrix, is displaced together with the induced matrix relocation, and *vice versa*. Recently, we have derived analytical expressions to quantify these coupled particle displacements using no-slip boundary conditions for the matrix on the surfaces of the particles.[76,77] The resulting displacements for our two-particle system in response to the magnetic forces $\mathbf{F}_i$ are given by

$$\mathbf{U}_i = \underline{\mathbf{M}}_{ii} \cdot \mathbf{F}_i + \underline{\mathbf{M}}_{i \neq j} \cdot \mathbf{F}_j, \tag{11}$$

where $(i,j) \in \{(1,2),(2,1)\}$, while $\underline{\mathbf{M}}_{ii}$ and $\underline{\mathbf{M}}_{i \neq j}$ are called displaceability matrices[76,77] (we mark tensors of second rank and

mathematical matrices by an underscore). Here, the corresponding expressions read

$$\underline{\mathbf{M}}_{ii} = M_0 \left[\hat{\underline{\mathbf{I}}} - \frac{15}{4}\left(\frac{a}{r_{ij}^{(0)}}\right)^4 \hat{\mathbf{r}}_{ij}^{(0)}\hat{\mathbf{r}}_{ij}^{(0)} \right], \tag{12}$$

$$\underline{\mathbf{M}}_{i \neq j} = M_0 \frac{3}{4}\frac{a}{r_{ij}^{(0)}} \left[\left(\hat{\underline{\mathbf{I}}} + \hat{\mathbf{r}}_{ij}^{(0)}\hat{\mathbf{r}}_{ij}^{(0)}\right) + 2\left(\frac{a}{r_{ij}^{(0)}}\right)^2\left(\frac{1}{3}\hat{\underline{\mathbf{I}}} - \hat{\mathbf{r}}_{ij}^{(0)}\hat{\mathbf{r}}_{ij}^{(0)}\right) \right], \tag{13}$$

with $M_0 = 1/6\pi\mu a$, $\hat{\underline{\mathbf{I}}}$ the unity matrix, $\hat{\mathbf{r}}_{ij}^{(0)} = \mathbf{r}_{ij}^{(0)}/r_{ij}^{(0)}$, $r_{ij}^{(0)} = |\mathbf{r}_{ij}^{(0)}|$, and the distance vector $\mathbf{r}_{ij}^{(0)} = \mathbf{r}_i^{(0)} - \mathbf{r}_j^{(0)}$ referring to the initial state at $\mathbf{H}^\mathrm{ext} = 0$. These displaceability matrices essentially contain all matrix-mediated elastic interactions between the two spheres mediated by the embedding elastic environment up to (including) order $(a/r_{ij}^{(0)})^4$.

Naturally, the stronger the magnetic forces $\mathbf{F}_i$ on the particles, the larger the particle displacements, see eqn (11). Simultaneously, the magnetic forces $\mathbf{F}_i$ significantly increase with decreasing particle separation. Therefore, another iteration loop is necessary to calculate the final configuration at each magnitude of the external magnetic field.[76–78]

Solving eqn (6)–(13) numerically by iteration as described, we can for a given external magnetic field calculate the resulting interparticle distance. Using a chi-square fit[87] to the experimental data points, we extracted in this way a local shear modulus $\mu = (226.0 \pm 2.8)$ Pa of the elastic matrix and an initial interparticle distance $r_{12}^{(0)} = (303.0 \pm 0.1)$ μm within the experimental error. The resulting theoretical fitting curve for the interparticle distance r_{12}/a as a function of the magnitude B^ext of the external magnetic field is shown in Fig. 3.

At an external magnetic field strength of $B^\mathrm{ext} \approx 61.7$ mT, the linear elastic theory predicts a steep drop. Beyond this point, the magnetic forces become larger than the linearly elastic restoring forces. Since the magnetic forces strongly increase with decreasing interparticle distance, they can grow significantly more strongly than the restoring elastic forces. Therefore, the separated state collapses. The particles are driven towards each other, until their steric volume exclusion hinders penetration when their surfaces virtually get into contact and basically touch each other. Experimentally, the field strength at which the collapse occurs could be located within the interval $B^\mathrm{ext} \in [60.8\ \mathrm{mT},\ 65.1\ \mathrm{mT}]$, in line with the prediction of our theory.

Finally, we address the question of hysteresis within our linearly elastic description. In our situation this would imply that, starting from the collapsed state and subsequently reducing the magnitude of the field, the particles separate at a lower magnetic field strength than the one at which they collapsed. Such a behavior is conceivable in our picture. The magnitude of the restoring elastic forces in the collapsed state is independent of the strength of the external magnetic field. However, the magnitude of the mutual magnetic interaction forces strongly depends on the actual distance between the two particles. It scales approximately with the inverse fourth power of the

particle separation. Therefore, a stronger external magnetic field is necessary to overcome the elastic barrier when the particles are well separated than to maintain the collapsed state when the particles have already approached.

To calculate the value of B^{ext} at which the separation occurs, we thus first determined the magnitude of the restoring elastic force in the collapsed state. This was performed by stepwise increasing an external force that drives the particles together, the magnitude of which not depending on the particle separation. The force at which we reach $r_{12}/a \approx 2$ identifies the strength of the elastic restoring forces. Then, artificially keeping the particles in the collapsed situation, we decreased B^{ext} from a very high value until the attractive magnetic forces just balanced the previously determined elastic restoring forces. From this procedure, we obtained $B^{\text{ext}} \approx 38.3$ mT for the separation of the particles. This detachment is indicated in Fig. 3 and, in this simplified picture, signals pronounced hysteresis.

The interparticle distance at which the collapse starts is not too far away from the last experimental data point, which is still well represented by the theory. Moreover, its magnitude of $r_{12}/a \approx 3$ is still significantly larger than in the collapsed state ($r_{12}/a \approx 2$). Therefore, we expect that our theory, despite its simplifications, particularly the dipolar picture and the restriction to linear elasticity, still captures the point of collapse reasonably well. The situation is different in the collapsed state, when the surfaces of the particles virtually touch each other. In this state, the material between the particles is strongly distorted, and nonlinear elastic effects certainly play a central role. Moreover, the magnetization across the interior of the particles becomes inhomogeneous, which challenges our reduced description in terms of magnetic dipoles. Therefore, in the collapsed state a nonlinear approach and a spatially resolved treatment of the magnetization are necessary to describe the behavior quantitatively correctly, see Section 5. Before we address this issue, however, we demonstrate that a mapping onto significantly reduced models is possible in the present set-up.

4 Mapping onto reduced dipole-spring models

To the given order in the inverse particle separation and within the framework of linear elasticity theory, our approach in Section 3 is exact concerning the treatment of the elastic polymer matrix. In previous approaches, simplified spring-like interactions had been introduced to model the matrix elasticity.[18,42,44,48,50,66–69] We now argue that in the present highly symmetric and simplified set-up the reduction to effective harmonic spring-like interactions is exact within the framework of linear elasticity theory. Moreover, the spring constants can be calculated as a function of the given parameters.

We consider the interparticle unit vector $\hat{\mathbf{r}}_{21} = -\hat{\mathbf{r}}_{12}$ to point along $\mathbf{B}^{\text{ext}}$. Then, by the symmetry of the set-up, all particle displacements, magnetic moments, and magnetic forces are

oriented parallel to $\hat{\mathbf{r}}_{21} \| \mathbf{B}^{\text{ext}}$. Thus, we project all vector quantities by scalar multiplication onto this axis of symmetry. This leads to a scalar formulation of the theory in Section 3 in terms of $U_i = \mathbf{U}_i \cdot \hat{\mathbf{r}}_{21}$, $m_i = \mathbf{m}_i \cdot \hat{\mathbf{r}}_{21}$, and $F_i = \mathbf{F}_i \cdot \hat{\mathbf{r}}_{21}$, $i \in \{1,2\}$. In this way, eqn (11) reduces to

$$\begin{pmatrix} U_1 \\ U_2 \end{pmatrix} = M_0 \begin{pmatrix} 1 - \frac{15}{4}\left(\frac{a}{r_{ij}^{(0)}}\right)^4 & \frac{3}{2}\frac{a}{r_{ij}^{(0)}} - \left(\frac{a}{r_{ij}^{(0)}}\right)^3 \\ \frac{3}{2}\frac{a}{r_{ij}^{(0)}} - \left(\frac{a}{r_{ij}^{(0)}}\right)^3 & 1 - \frac{15}{4}\left(\frac{a}{r_{ij}^{(0)}}\right)^4 \end{pmatrix} \cdot \begin{pmatrix} F_1 \\ F_2 \end{pmatrix}.$$

(14)

4.1 Three-spring model

Illustratively, the matrix term in eqn (14) suggests to introduce three harmonic springs to model the elastic situation, see Fig. 4(a). On the one hand, its diagonal contains the zeroth-order contributions in the particle separation that arise already when one single particle is displaced against the surrounding elastic matrix. The corresponding counteracting force by the surrounding elastic matrix makes us introduce two harmonic springs of constant K_0 that anchor each particle to its ground state position. The coefficient K_0 further contains a fourth-order correction that results from the displacement field induced in the matrix by one particle when this field is "reflected" by the rigidity of the other particle.[76,77] On the other hand, the off-diagonal entries describe the displacements of the particles due to the forces exerted on the respective other particle. These particle interactions are mediated by the elastic matrix. Consequently, we introduce another harmonic spring
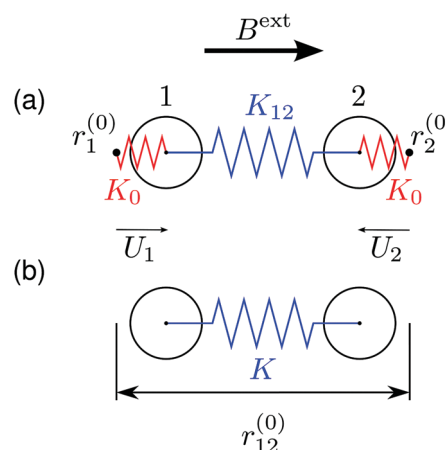

Fig. 4 Two reduced spring models that exploit the symmetry of the set-up (all vector quantities characterizing and affecting the particles are projected onto the symmetry axis along $\mathbf{B}^{\text{ext}}$). (a) Three-spring model. Each particle is anchored by one harmonic spring of spring constant K_0 to its ground-state position (red). Moreover, it is connected to the other particle by one additional harmonic spring of spring constant K_{12} (blue). (b) One-spring model. The three-spring approach can further be reduced to a one-spring model involving only one effective harmonic spring of spring constant K connecting the two particles.

of constant K_{12} coupling the two particles to each other. Together, this spring-model leads to the elastic potential energy

$$W^{\text{el}} = \frac{1}{2}K_0\left(U_1^2 + U_2^2\right) + \frac{1}{2}K_{12}(U_1 - U_2)^2. \quad (15)$$

From this expression, the elastic restoring forces F_i^{el}, $i \in \{1,2\}$, follow as

$$F_i^{\text{el}} = -\frac{\partial}{\partial U_i}W^{\text{el}}. \quad (16)$$

To calculate the spring constants K_0 and K_{12} from our linear elasticity theory, we invert eqn (14) and obtain, up to (including) order $(a/r_{ij}^{(0)})^4$,

$$\binom{F_1}{F_2} = \frac{1}{M_0}\begin{pmatrix} 1+\frac{9}{4}\left(\frac{a}{r_{ij}^{(0)}}\right)^2+\frac{93}{16}\left(\frac{a}{r_{ij}^{(0)}}\right)^4 & -\frac{3}{2}\frac{a}{r_{ij}^{(0)}}-\frac{19}{8}\left(\frac{a}{r_{ij}^{(0)}}\right)^3 \\ -\frac{3}{2}\frac{a}{r_{ij}^{(0)}}-\frac{19}{8}\left(\frac{a}{r_{ij}^{(0)}}\right)^3 & 1+\frac{9}{4}\left(\frac{a}{r_{ij}^{(0)}}\right)^2+\frac{93}{16}\left(\frac{a}{r_{ij}^{(0)}}\right)^4 \end{pmatrix}$$
$$\cdot \binom{U_1}{U_2}. \quad (17)$$

This equation lists the forces F_1 and F_2 that need to be imposed onto the particles to achieve their displacements U_1 and U_2. Corresponding expressions for the forces as functions of the displacements have been derived directly, *i.e.*, without the intermediate inversion, already in ref. 74 and agree with ours to the given order.

In a stationary state, the forces F_1 and F_2 in eqn (17) imposed on the particles need to be equal in magnitude but oppositely oriented to the forces F_1^{el} and F_2^{el} exerted onto the particles by the elastic matrix, respectively. Comparing eqn (16) and (17), we read off the spring constants

$$K_0 = \frac{1}{M_0}\left[1 - \frac{3}{2}\frac{a}{r_{ij}^{(0)}} + \frac{9}{4}\left(\frac{a}{r_{ij}^{(0)}}\right)^2 - \frac{19}{8}\left(\frac{a}{r_{ij}^{(0)}}\right)^3 + \frac{93}{16}\left(\frac{a}{r_{ij}^{(0)}}\right)^4\right], \quad (18)$$

$$K_{12} = \frac{1}{M_0}\left[\frac{3}{2}\frac{a}{r_{ij}^{(0)}} + \frac{19}{8}\left(\frac{a}{r_{ij}^{(0)}}\right)^3\right]. \quad (19)$$

Overall, in this dipole-spring model, the total energy characterizing a certain configuration is given by

$$W^{\text{tot}} = W^{\text{mag}} + W^{\text{el}}. \quad (20)$$

Here, the magnetic contribution follows from eqn (8) and is calculated in the same way as described in Section 3.

To find the state of our system for a given B^{ext}, we minimize W^{tot} using a simple relaxational method.[87] In this way, we can stepwise increase and decrease B^{ext}, inserting as an initial condition after each modification of B^{ext} the previously relaxed state of the system. As a result, we naturally obtain the

hysteresis loop in the particle separation, depicted in Fig. 3 by the dashed line. There, the deviations from the solid line obtained from the calculation using linear elasticity theory in Section 3 can be traced back to our matrix inversion from eqn (14) to eqn (17). As the overall formalism, this inversion is exact only to (including) order $(a/r_{ij}^{(0)})^4$. If, instead, we invert eqn (16), $i \in \{1,2\}$, and obtain the spring constants by comparison with eqn (14), the two curves collapse. Thus the deviations in Fig. 3 between the direct calculation using continuum elasticity theory as in Section 3 and our dipole-spring reduction represent higher-order effects.

4.2 One-spring model

Further exploiting the symmetry of our geometry, it is straightforward to additionally reduce eqn (15) to the situation of one effective spring of constant K connecting the two particles, see Fig. 4(b). Mirror symmetry of the set-up dictates the relations $U_1 = -U_2$, $F_1 = -F_2$, as well as $m_1 = m_2 = m$ for the magnetic moments. Defining $U = U_1 = -U_2$, we obtain

$$W^{\text{el}} = \frac{1}{2}KU^2 \quad (21)$$

with the effective spring constant $K = 2K_0 + 4K_{12}$ and the elastic forces on the two particles given by $\mp\partial W^{\text{el}}/2\partial U$. Naturally, we obtain the same hysteresis loop in Fig. 3 after rewriting the theory into the effective one-spring model in eqn (21). To the given order, it contains the same information as the linearly elastic approach in Section 3, therefore representing an effective reduction of the theory.

Using the total energy of the system W^{tot} in eqn (20) together with the elastic energy of the effective one-spring model in eqn (21), we can readily illustrate the origin of the hysteretic behavior. In spirit, this follows Landau's theory of phase transitions[88] and has previously been discussed for the two-sphere problem including nonlinear elasticity[51,52] and for an infinitely extended chain of magnetic particles under linear elasticity.[48] Here it is directly connected to our experimental results *via* the derivation above. Fig. 5 shows the corresponding shape of the total energy for increasing amplitude of the external magnetic field.

At $B^{\text{ext}} = 0$ mT, the overall energy features one minimum at a distance $r_{12}/a = r_{12}^{(0)}/a \approx 3.57$ as displayed in Fig. 5(a). Starting from $B^{\text{ext}} \gtrsim 37.9$ mT, see Fig. 5(b), a second minimum begins to develop at the distance of close approach $r_{12}/a \approx 2$. That is, the slope of the overall energy $W^{\text{tot}}(r_{12})$ becomes zero at $r_{12}/a \approx 2$ for $B^{\text{ext}} \approx 37.9$ mT. Afterwards, with increasing amplitude B^{ext} of the external field and as depicted in Fig. 5(c), the point of $W^{\text{tot}}(r_{12}) = 0$ shifts to larger interparticle distances r_{12}. In this regime, two local minima in the overall energy coexist over a broader range of external field amplitudes. Only around $B^{\text{ext}} \gtrsim 60.9$ mT, the initial minimum has vanished and the one remaining minimum at $r_{12}/a \approx 2$ represents the collapsed state, see Fig. 5(d).

If thermal fluctuations and external perturbations are negligible, the energetic barrier separating the two minima in the range of magnetic fields 37.9 mT $\lesssim B^{\text{ext}} \lesssim 60.9$ mT cannot be
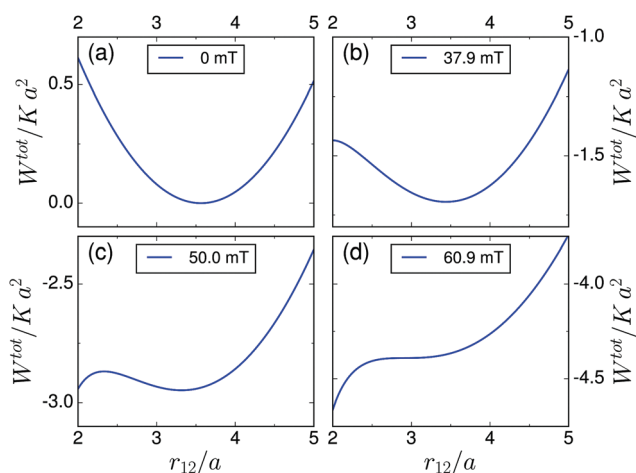
Fig. 5 Total energy W^{tot} for the one-spring dipole–spring model as a function of the interparticle distance r_{12} for increasing amplitude B^{ext} of the external magnetic field. (a) At $B^{ext} = 0$ T, $W^{tot} = W^{el}$ is given by eqn (21), with one minimum at $r_{12}^{(0)}/a \approx 3.57$. (b) Starting from the threshold field $B^{ext} \approx 37.9$ mT, a second local minimum starts to develop at $r_{12}/a \approx 2$, after the slope of the curve $W^{tot}(r_{12})$ has passed through zero at $r_{12}/a \approx 2$. (c) With increasing B^{ext}, the minimum at $r_{12}/a \approx 2$ deepens, whereas the minimum for $r_{12}/a \gtrsim 3$ flattens out. (d) Finally, for $B^{ext} \gtrsim 60.9$ mT, only the minimum at $r_{12}/a \approx 2$ remains. In the absence of thermal fluctuations and external perturbations, the system cannot cross the energetic barrier between the two local minima at intermediate field strengths 37.9 mT $\lesssim B^{ext} \lesssim$ 60.9 mT. Only when one of the two minima vanishes at one of the two threshold strengths, a jump to the other minimum can occur, which explains the hysteresis loop in Fig. 3.

crossed. Then, the state of the system in this regime depends on its history. If the external field is increased and the particles had previously been well separated, the system is trapped in the minimum at $r_{12}/a \gtrsim 3$. Only at the threshold amplitude $B^{ext} \approx 60.9$ mT, where this minimum vanishes, see Fig. 5(d), the particles collapse to the state of $r_{12}/a \approx 2$. *Vice versa*, upon then decreasing the field amplitude, the particles only re-separate at the lower threshold amplitude $B^{ext} \approx 37.8$ mT. There, the minimum at $r_{12}/a \approx 2$ has vanished, see Fig. 5(b). In this way, the hysteresis loop in Fig. 3 can be directly read off from the energy curves in Fig. 5.

What we have achieved above was a reduction of the linearly elastic description to a simple Hookean relation in terms of one single linearly elastic spring. The elastic theory implicitly resolves the spatially inhomogeneous distortions surrounding the magnetic particles, the effect of which is in this way quantitatively contained in the resulting spring constant K. For many practical applications, the decisive question is, which magnetic field amplitude needs to be applied to realize the collapse. This concerns the mentioned tunable dampers[8–11] as well as the search for large magnetostrictive effects to exploit them in soft actuators.[1–7] As Fig. 3 demonstrates, the linearized theory is sufficient to predict this threshold magnetic field strength quantitatively correctly. Conversely, the separation of the particles in such applications will most likely be realized simply by switching off the magnetic field.

5 Results from finite-element simulations

To test our theoretical conclusions and the consequences of our approximations, we performed additional FE simulations, adjusted to the present experimental set-up. They are based on a coupled magneto-mechanical continuum formulation including nonlinear contributions to the magnetic and elastic properties of the magnetic particles and elastic matrix, respectively.[70,89] In addition to the theoretical approaches above, the magnetic field is spatially resolved also within the two particles. In parts, methods developed in an earlier theory and simulation study on the hysteretic two-particle problem are adopted.[51,52] The simulations resolve in more detail the backward path of the hysteresis loop in Fig. 3 of our experimental set-up, which is out of quantitative reach for the linearized theory. From a fundamental material-science point of view concerned with the nonlinear elastic properties of the elastic polymer matrix under strong deformation, this backward path is indeed the more interesting one. Possibly, our experimental set-up can in the farther future with higher resolution provide additional information on the corresponding material properties.

5.1 Continuum approach

We consider a piece of the material described above with density distribution $\rho(\mathbf{r})$, containing the two spherical particles. In the stationary case, the magnetic part of the corresponding coupled continuum formulation is given by the two Maxwell equations

$$\nabla \cdot \mathbf{B}^{in}(\mathbf{r}) = 0 \quad \text{with} \quad \hat{\mathbf{n}}(\mathbf{r}) \cdot [\![\mathbf{B}^{in}(\mathbf{r})]\!] = 0 \text{ on } \mathscr{S}^{d} \qquad (22)$$

and

$$\nabla \times \mathbf{H}^{in}(\mathbf{r}) = \mathbf{0} \quad \text{with} \quad \hat{\mathbf{n}}(\mathbf{r}) \times [\![\mathbf{H}^{in}(\mathbf{r})]\!] = \mathbf{0} \text{ on } \mathscr{S}^{d}. \qquad (23)$$

In these expressions, $\mathbf{B}^{in}(\mathbf{r})$ and $\mathbf{H}^{in}(\mathbf{r})$ denote the local magnetic flux density and magnetic field inside the material, respectively, both in the magnetic particles and in the elastic matrix.[21] They are connected *via* $\mathbf{B}^{in}(\mathbf{r}) = \mu_0(\mathbf{H}^{in}(\mathbf{r}) + \mathbf{M}(\mathbf{r}))$, with $\mathbf{M}(\mathbf{r})$ describing the magnetization field. $\mathscr{S}^{d}$ denotes a surface of discontinuity, here the interface between the particles and the elastic matrix. The brackets $[\![\cdot]\!]$ quantify the jump of the contained quantity across $\mathscr{S}^{d}$, while $\hat{\mathbf{n}}(\mathbf{r})$ corresponds to the unit normal vector on $\mathscr{S}^{d}$.

The magnetic fields cause magnetic coupling terms that enter the mechanical part of the problem, *e.g.*, the magnetic body force density $\mathbf{f}^{mag}(\mathbf{r}) = (\nabla \mathbf{B}^{in}(\mathbf{r}))^{\mathrm{T}} \cdot \mathbf{M}(\mathbf{r})$, with the superscript $^{\mathrm{T}}$ marking the transpose. Since $\mathbf{f}^{mag}(\mathbf{r})$ can be expressed as the divergence of the magnetic stress tensor $\underline{\sigma}^{mag}(\mathbf{r})$, the balance of linear momentum is given by the relation[70,89,90]

$$\nabla \cdot \underline{\sigma}^{tot}(\mathbf{r}) = \mathbf{0} \quad \text{with} \quad \hat{\mathbf{n}}(\mathbf{r}) \cdot [\![\underline{\sigma}^{tot}(\mathbf{r})]\!] = \mathbf{0} \quad \text{on } \mathscr{S}^{d}. \qquad (24)$$

Here, the total stress tensor $\underline{\sigma}^{tot}(\mathbf{r})$ is defined as the sum of the mechanical and the magnetic stress tensors, $\underline{\sigma}^{tot}(\mathbf{r}) = \underline{\sigma}(\mathbf{r}) + \underline{\sigma}^{mag}(\mathbf{r})$. A detailed discussion of the complete magneto-mechanical field equations is given, *e.g.*, in ref. 90 and 91.

The constitutive behavior of the considered particle-matrix system can be described by a specific free-energy density (per mass) Ψ, split into a magnetic and a mechanical part[30,70,84,89,92]

$$\Psi(\underline{\mathbf{F}}(\mathbf{r}),\ \mathbf{H}^{\mathrm{in}}(\mathbf{r})) = \Psi^{\mathrm{mag}}(\mathbf{H}^{\mathrm{in}}(\mathbf{r})) + \Psi^{\mathrm{el}}(\underline{\mathbf{F}}(\mathbf{r})) \tag{25}$$

In this expression, $\underline{\mathbf{F}}(\mathbf{r})$ denotes the deformation gradient tensor. Hence, the constitutive relations

$$\mathbf{M}(\mathbf{r}) = -\frac{\rho(\mathbf{r})}{\mu_0}\frac{\partial\Psi^{\mathrm{mag}}(\mathbf{H}^{\mathrm{in}}(\mathbf{r}))}{\partial\mathbf{H}^{\mathrm{in}}(\mathbf{r})} \tag{26}$$

and

$$\underline{\sigma}(\mathbf{r}) = \rho(\mathbf{r})\underline{\mathbf{F}}(\mathbf{r})\cdot\frac{\partial\Psi^{\mathrm{el}}(\underline{\mathbf{F}}(\mathbf{r}))}{\partial\underline{\mathbf{F}}^{\mathrm{T}}(\mathbf{r})} - \frac{\mu_0}{2}(\mathbf{M}(\mathbf{r})\cdot\mathbf{M}(\mathbf{r}))\hat{\underline{\mathbf{I}}} \tag{27}$$

can be found from the evaluation of the second law of thermodynamics, see, e.g., ref. 91.

Eqn (1) already defines a relation between the magnetization and the magnetic field within the particles, while $\mathbf{M}(\mathbf{r}) = \mathbf{0}$ within the elastic matrix, so that we choose Ψ^{mag} in eqn (26) accordingly. We specify the mechanical part Ψ^{el} in both components, the particles and the elastic matrix, following an elastic Neo–Hookean model.[70,89] Accordingly, $\underline{\sigma}^{\mathrm{mag}}(\mathbf{r})$ is expressed as

$$\underline{\sigma}^{\mathrm{tot}}(\mathbf{r}) = \frac{1}{J(\mathbf{r})}\left[\mu(\mathbf{r})\left(\underline{\mathbf{b}}(\mathbf{r}) - \hat{\underline{\mathbf{I}}}\right) + \frac{\mu(\mathbf{r})\nu(\mathbf{r})}{1 - 2\nu(\mathbf{r})}\left((J(\mathbf{r}))^2 - 1\right)\hat{\underline{\mathbf{I}}}\right]$$
$$+ \mathbf{B}^{\mathrm{in}}(\mathbf{r})\mathbf{H}^{\mathrm{in}}(\mathbf{r}) - \frac{\mu_0}{2}\left(\mathbf{H}^{\mathrm{in}}(\mathbf{r})\cdot\mathbf{H}^{\mathrm{in}}(\mathbf{r})\right)\hat{\underline{\mathbf{I}}}, \tag{28}$$

where $\underline{\mathbf{b}}(\mathbf{r})$ is the left Cauchy–Green deformation tensor, $J(\mathbf{r}) = \det\underline{\mathbf{F}}(\mathbf{r})$ denotes the Jacobi determinant of the deformation gradient tensor, $\mu(\mathbf{r})$ is the local elastic shear modulus, and $\nu(\mathbf{r})$ is the local Poisson ratio. Within the elastic matrix, the material is characterized by the shear modulus μ determined in Section 3 and the Poisson ratio $\nu = 0.49$, corresponding to a nearly incompressible material. Inside the magnetizable nickel particles, we set the parameters of elasticity to $\mu = 80.77$ GPa and $\nu = 0.3$ (which is of the order of magnitude of the values listed, e.g., in ref. 93). The exact numerical values for the nickel particles are not significant because of their much higher mechanical stiffness relatively to the polymeric matrix.

5.2 Numerical solution

In our FE simulations, we address a cuboid region of the system with fixed boundary and dimensions $22a \times 10a \times 10a$. Exploiting the symmetries of the set-up, only one eighth of this region needs to be evaluated explicitly with appropriate boundary conditions. Major challenges result from the underlying bifurcation scenario and the extremely high degrees of deformation of the elastic matrix between the two particles in the virtual touching state. As a consequence, it was not possible to solve the problem in a direct way using the fully coupled FE solution scheme.[70,89] Therefore, we separately calculated the magnitudes F^{mag} of the attractive magnetic force and the magnitude F^{el} of the counteracting mechanical restoring force on each particle for decreasing particle distances. In parts, methods outlined in ref. 51 were utilized when evaluating F^{el}. Afterwards, we identified the states in which these two forces balance each other.

First, for each evaluated magnitude of the external magnetic flux density $\mathbf{B}^{\mathrm{ext}}$, we determined F^{mag} for 22 different particle distances $2.001 \leq r_{12}/a \leq 3.565$. For this purpose, in total 22 different FE meshes were generated. F^{mag} is calculated for each distance by fixing the center positions of the particles. We then determine the necessary mechanical force to keep the particle positions fixed within a coupled magneto-mechanical FE simulation.[30,70,89] The magnitude B^{ext} of the external magnetic field is increased in 100 increments from 0 mT to 65 mT. The obtained values for F^{mag} for each considered magnitude B^{ext} are then interpolated between the evaluated distances r_{12} using cubic splines. Example curves for $B^{\mathrm{ext}} = 13$ mT, 39 mT, and 65 mT are shown in Fig. 6.

Second, to determine F^{el}, the centers of the non-magnetized particles are moved towards each other within another FE simulation that addresses this purely mechanical problem of nonlinear elasticity (see the ESI† for the illustration of three different states of deformation). Yet, it is not possible to directly simulate interparticle distances arbitrarily close to $r_{12}/a \approx 2$ because of the strong distortion of the FE meshes. Consequently, we are not able to directly evaluate the strong local displacement and deformation fields within the elastic matrix in the state of virtual touching. Therefore, a reduced fitting function of sufficient physical significance needs to be employed to extrapolate F^{el} in this regime. We chose the elastic rod model introduced in ref. 51 as a workaround for this purpose. It replaces the action of the elastic matrix by five nonlinearly elastic rods of lengths $l_{0,i}$ and radii $r_{0,i}$ in the undeformed configuration ($i = 1,\ldots,5$).
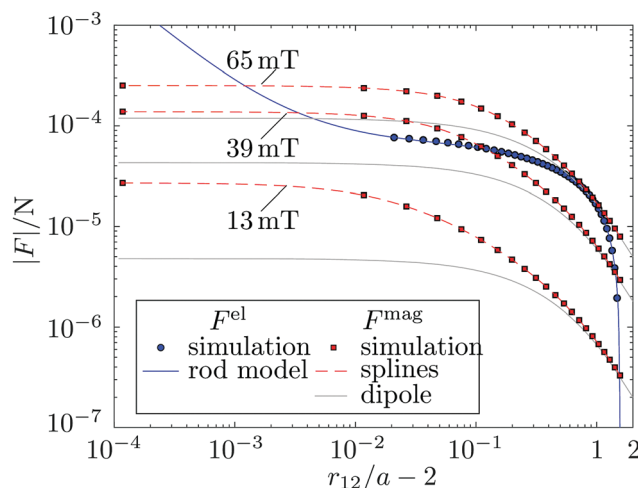
Fig. 6 FE simulation results for the magnitudes F^{mag} and F^{el} of the attractive magnetic and counteracting elastic restoring forces, respectively, at various separation distances r_{12} between the two particles (the values $r_{12}/a - 2$ on the abscissa label the separations of the two closest surface points of the two spheres). Values for F^{mag} are interpolated using cubic splines, and example curves for magnetic field amplitudes $B^{\mathrm{ext}} = 13$ mT, 39 mT, and 65 mT are shown. For comparison, the corresponding forces calculated as in Sections 3 and 4 by the simplified magnetic dipole approach are included as gray lines to demonstrate the agreement in the separated state. Values for the mechanical restoring force F^{el} due to the deformation of the elastic matrix are fitted by an elastic rod model according to eqn (29). Actual distances between the two particles for a given value of B^{ext} are identified from the intersections between the curves for the two different forces.

This rod model allows to calculate F^{el} analytically by quantitatively adjusting it to corresponding FE simulations in the accessible regime and extrapolating the simulation results down to $r_{12}/a \to 2$, as outlined in ref. 51. As a benefit, the constitutive elastic behavior of the rods can be described by the same Neo-Hookean material model that we use for the elastic matrix in the FE simulation. In this framework, F^{el} is given by

$$F^{el} = \sum_{i=1}^{5} \pi r_{0,i}^2 \left[\mu \left(\lambda_{l,i} - \frac{1}{\lambda_{l,i}} \right) + \frac{\beta}{2} \left(\lambda_{l,i} \lambda_{t,i}^4 - \frac{1}{\lambda_{l,i}} \right) \right]$$

$$\text{with} \quad \lambda_{t,i} = -\frac{\mu}{\beta \lambda_{l,i}^2} + \sqrt{\frac{\mu^2}{\beta^2 \lambda_{l,i}^4} + \frac{2\mu}{\beta \lambda_{l,i}^2} + \frac{1}{\lambda_{l,i}^2}}.$$

$$(29)$$

Here, $\lambda_{l,i} = l_i/l_{0,i}$ and $\lambda_{t,i} = r_i/r_{0,i}$ denote the deformation ratios of the rods in the directions parallel (longitudinal) and perpendicular (transversal) to the rod axes, respectively, with l_i and r_i the corresponding rod dimensions in the deformed state. Moreover, $\beta = 2\mu\nu/(1 - 2\nu)$, where μ is the elastic shear modulus and ν is the Poisson ratio of the elastic polymer matrix. This effective rod model is fitted to the FE-simulation results using the radii $r_{0,i}$ as fit parameters, with the corresponding values listed in Table 1.

Fig. 6 displays the results for F^{el} from the FE simulation together with the fitted rod model according to eqn (29). With a maximum error of 3.3%, the model shows acceptable deviations from the FE simulation. Furthermore, for $r_{12}/a \to 2$ it describes the qualitatively expected behavior of a diverging restoring force in response to the high local distortion. Experimental results providing quantitative information on the behavior of the present gel matrix under the very extreme local deformations are not yet available.

Finally, we determine the resulting particle center-to-center distances r_{12} for each considered magnitude B^{ext} of the external magnetic field as a function of the history of the system. To this end, we identify the intersections between the curves for $F^{mag}(r_{12})$ (spline curves) and $F^{el}(r_{12})$ (rod model), see Fig. 6. As the figure also illustrates, there are three qualitatively different situations: (i) only one intersection between $F^{el}(r_{12})$ and $F^{mag}(r_{12})$ close to $r_{12}/a \approx 3.5$, see the case of $B^{ext} = 13$ mT; (ii) three intersections, one located at $r_{12}/a \approx 3.5$, one at $r_{12}/a \approx 2$, and one between these values, see the case of $B^{ext} = 39$ mT; and (iii) only one intersection close to $r_{12}/a \approx 2$, see the case of $B^{ext} = 65$ mT.

Increasing the magnetic field from 0 mT, our evaluations demonstrate that there are states of balanced magnetic and mechanical forces and significant particle separation for center-to-center distances down to $r_{12}/a \approx 2.95$. Initially, this corresponds to the intersection described by case (i), then to the first intersection of case (ii). The intermediate intersection of

case (ii) corresponds to a metastable saddle configuration in the overall energy, see Fig. 5(c). At an external field strength of $B^{ext} \approx 63.05$ mT, the simulation predicts a switch from case (ii) to case (iii). Thus the state of separated particles collapses towards a state of virtual touching of $r_{12}/a \approx 2$. Subsequently decreasing B^{ext}, the system switches from case (iii) back to case (ii). However, the particles now remain in the state of virtual touching of $r_{12}/a \approx 2$ corresponding to the third intersection of case (ii). Only at $B^{ext} \approx 30.55$ mT, the set-up switches back to case (i), which implies that the particles re-separate. Consequently, the FE simulations confirm the scenario of hysteresis predicted qualitatively by the theoretical analysis in Sections 3 and 4. The corresponding simulation results are shown by the filled circles in Fig. 3.

More precisely, the FE simulations provide the following additional and more quantitative insights. As Fig. 3 and the comparison for the magnetic forces in Fig. 6 demonstrate, the theoretical analyses in Sections 3 and 4 describe the system in the non-collapsed state quantitatively correctly in a broad initial interval of increasing amplitude of the magnetic field. Thus, for well-separated spherical particles in an elastic matrix, the theoretical schemes developed in ref. 73, 74 and 76–78 provide an efficient and accurate characterization.

The point of collapse is predicted correctly by the analytical theory to good approximation. Our FE simulations indicate a slightly elevated amplitude of the magnetic field at which the collapse occurs. We thus have repeated the simulations, now following a linearized law of magnetization as in eqn (3) instead of the nonlinear relation of eqn (1). The linearized law allows for an in principle unbounded growth of the magnetization, resulting in stronger magnetic attraction. Consequently, the corresponding simulations predict a slightly earlier collapse of the separated state in quite good agreement with the theoretical results, see the triangles in Fig. 3. However, the situation is more complex than might be expected from this agreement of the data. In the simulations, which resolve the spatial inhomogeneity of the magnetization across the particles, see below, the linearization mainly affects those parts of the particles that are closest to each other and thus are most strongly magnetized. In contrast to that, in our theory the dipoles are concentrated in the more distanced particle centers and are not as severely affected by the linearization.

In the collapsed state, the extrapolation of the simulation curves predict that a complete touching of the particles does not occur. In such a situation, an extreme compression of the elastic material between the particles would be necessary, if the assumed no-slip anchoring of the polymeric matrix on the surfaces of the particles persists. This leads to values of r_{12}/a slightly larger than 2 as stressed by the inset in Fig. 3. Our experimental resolution did not allow us to further clarify this issue on the actual experimental system.

Most importantly, the FE simulations reveal an even more pronounced hysteretic behavior of our experimental system. The magnitude of the external magnetic field for re-separation of the particles is found to be significantly lower than predicted from the theoretical analyses in Sections 3 and 4, see Fig. 3. Particularly, this is due to the approximation in terms of magnetic dipoles located at the particle centers. Our FE simulations reveal that,

Table 1 Parameters of the rod model eqn (29): lengths $l_{0,i}$ and fitted radii $r_{0,i}$ of the five rods

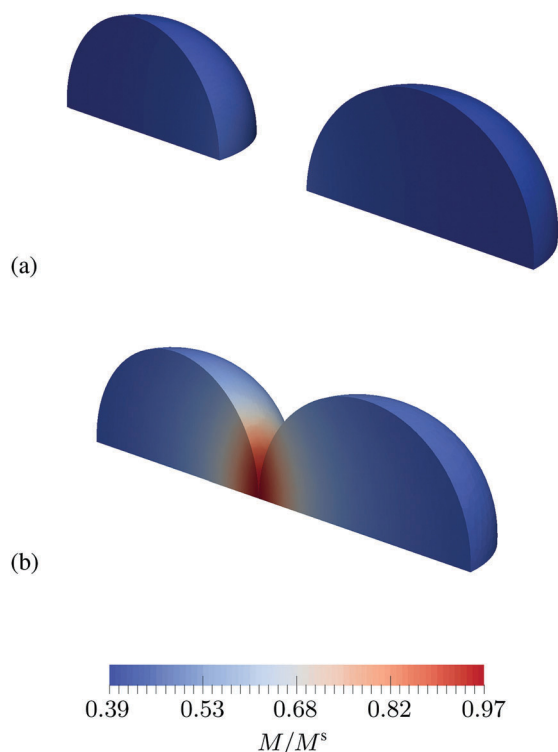| i	1	2	3	4	5
$l_{0,i}$	$r_{12} - 2a$	$r_{12} - a$	$r_{12} - a$	$(20a - r_{12})/2$	$(20a - r_{12})/2$
$r_{0,i}/\mu m$	2.80	72.17	72.17	273.15	273.15

Fig. 7 Color plot of the magnitudes of the spatially resolved magnetization field within the spherical particles (a) for $B^{\text{ext}} = 63.05$ mT shortly before the collapse and (b) for $B^{\text{ext}} = 65.00$ mT after the collapse in the state of virtual touching of the particles.

in the state of virtual touching, the magnetization within the particles is strongly inhomogeneous. Around the virtual contact points of the nearly touching particles, local magnetic field amplitudes of up to 0.66 T are found inside the particles, despite the relatively small value of the maximum external magnetic field amplitude of 65 mT. In this case, a spatial resolution of the magnetization field inside the particles becomes important, together with the nonlinear magnetization behavior according to eqn (1) in the vicinity of the virtual contact points between the particles. The local magnitude of the magnetization within quarters of the particles is illustrated in Fig. 7 for a separated state at $B^{\text{ext}} = 63.05$ mT and a state of virtual touching at $B^{\text{ext}} = 65.00$ mT. Naturally, not bounding the magnetization by using a linearized magnetization law allows for even stronger magnetization in the near-touching parts of the particles. In such a case, corresponding simulation results predict an even more pronounced hysteresis, see the triangles in Fig. 3.

Nevertheless, from Fig. 3 we note that the different ways of description all lead to results that agree well with the experimental data within the experimental error bars. A higher resolution of measurement will allow to further develop and specify the theoretical and numerical tools in the future.

6 Conclusions

In summary, we have experimentally observed the reversible approach and separation of two paramagnetic metallic particles in a soft elastic gel matrix, induced by adjusting the magnitude of an external magnetic field. Above a certain threshold of the magnetic field, the particles collapsed into a virtually touching state. We have theoretically analyzed the behavior of our experimental set-up using a dipolar approximation for the magnetic interactions and linear elasticity theory to describe the distortions of the elastic matrix. This description was further simplified by projecting it onto reduced dipole-spring models. Significant hysteretic behavior was revealed in this way. That is, the collapse into the state of virtual touching occurred at a markedly larger magnetic field than their sudden separation back into a well-distanced state when subsequently decreasing the field amplitude. Finally, we further quantified our experimental observations by additional finite-element simulations adjusted to our experimental set-up. They spatially resolve the magnetic field also inside the magnetic particles and allow for nonlinear elasticity of the elastic environment. Our simulations are in agreement with the experimental observations and to good approximation confirm our theoretical analysis until the collapse into the virtually touching state occurs. However, they predict a more pronounced hysteresis with the separation of the particles occurring at a lower magnetic field amplitude than calculated from the linearized analytical theory.

We expect our results, which explicitly demonstrate the reversible externally induced virtual touching and separation of hard particles in a soft elastic matrix, to be of high practical relevance from an application point of view. A very illustrative example is certainly a switchable damping device. Instead of using only two particles, one may arrange many particles in parallel rows.[26] Then, in the absence of magnetic fields, the material of separated particles is soft under compression along the axis of the rows. When the particles enter a state of virtual touching under magnetic fields, the resulting aggregates significantly harden.[48]

In a broader framework, our investigations are related to various studies in several other areas. Far away from the two particles, the distortion induced in the elastic matrix resembles that of a point-like mechanical force dipole. In such an approximation, for example, the stress exerted by active biological cells on their environment has been addressed.[94] For instance, preferred mutual orientations were explained *via* induced long-ranged elasticity-mediated interactions between the cells.[95,96] Similarly, localized force dipoles and their mutual interactions by distortion of their elastic environment are treated in the theory of defects in crystal structures.[97] In a different framework, the question of whether the separated state of the two magnetic particles is stable, and at which point this state collapses and the particles touch each other, has recently been studied in the context of magnetosome filaments.[98] These elastic elements are found, for instance, in magnetotactic bacteria that detect the magnetic field of the earth for their orientation. Elastic filaments connecting the magnetic particles need to provide sufficient rigidity to avoid the particle collapse.

We believe that our results are important for the future construction of tunable dampers and vibration absorbers, soft actuators, and energy storage devices from elastic composite materials.

Particularly when exploiting the described effects in soft actuation devices, it will be a central concern to reveal aspects of the underlying dynamical processes. Moreover, we here mainly concentrated on magnetically induced effects. Yet, many of the described properties may carry over to the case of electric fields.[18] There, also the question of energy storage will be more prevalent.[13–18] In that case, however, touching of the particles together with the formation of chained structures should be hindered to avoid electric short circuits.

Conflicts of interest

There are no conflicts of interest to declare.

Acknowledgements

References

1 Y. An and M. T. Shaw, *Smart Mater. Struct.*, 2003, **12**, 157.
2 G. Filipcsei, I. Csetneki, A. Szilágyi and M. Zrínyi, *Adv. Polym. Sci.*, 2007, **206**, 137–189.
3 K. Zimmermann, V. A. Naletova, I. Zeidis, V. A. Turkov, E. Kolev, M. V. Lukashevich and G. V. Stepanov, *J. Magn. Magn. Mater.*, 2007, **311**, 450–453.
4 Y. L. Raikher, O. V. Stolbov and G. V. Stepanov, *J. Phys. D: Appl. Phys.*, 2008, **41**, 152002.
5 R. Fuhrer, E. K. Athanassiou, N. A. Luechinger and W. J. Stark, *Small*, 2009, **5**, 383–388.
6 H. Böse, R. Rabindranath and J. Ehrlich, *J. Intell. Mater. Syst. Struct.*, 2012, **23**, 989–994.
7 P. Ilg, *Soft Matter*, 2013, **9**, 3465–3468.
8 H.-x. Deng, X.-l. Gong and L.-h. Wang, *Smart Mater. Struct.*, 2006, **15**, N111.
9 T. L. Sun, X. L. Gong, W. Q. Jiang, J. F. Li, Z. B. Xu and W. H. Li, *Polym. Test.*, 2008, **27**, 520–526.
10 G. J. Liao, X. L. Gong, S. H. Xuan, C. J. Kang and L. H. Zong, *J. Intell. Mater. Syst. Struct.*, 2012, **23**, 25–33.
11 V. S. Molchanov, G. V. Stepanov, V. G. Vasiliev, E. Y. Kramarenko, A. R. Khokhlov, Z.-D. Xu and Y.-Q. Guo, *Macromol. Mater. Eng.*, 2014, **299**, 1116–1125.
12 J. L. Mietta, P. I. Tamborenea and R. M. Negri, *Soft Matter*, 2016, **12**, 6430–6441.
13 J. Y. Li, L. Zhang and S. Ducharme, *Appl. Phys. Lett.*, 2007, **90**, 132901.
14 P. Kim, N. M. Doss, J. P. Tillotson, P. J. Hotchkiss, M.-J. Pan, S. R. Marder, J. Li, J. P. Calame and J. W. Perry, *ACS Nano*, 2009, **3**, 2581–2592.
15 J. Li, S. I. Seok, B. Chu, F. Dogan, Q. Zhang and Q. Wang, *Adv. Mater.*, 2009, **21**, 217–221.
16 Q. Wang and L. Zhu, *J. Polym. Sci., Part B: Polym. Phys.*, 2011, **49**, 1421–1429.
17 L. A. Fredin, Z. Li, M. T. Lanagan, M. A. Ratner and T. J. Marks, *Adv. Funct. Mater.*, 2013, **23**, 3560–3569.
18 E. Allahyarov, H. Löwen and L. Zhu, *Phys. Chem. Chem. Phys.*, 2016, **18**, 19103–19117.
19 M. Zrnyi, L. Barsi and A. Büki, *J. Chem. Phys.*, 1996, **104**, 8750–8756.
20 D. Collin, G. K. Auernhammer, O. Gavat, P. Martinoty and H. R. Brand, *Macromol. Rapid Commun.*, 2003, **24**, 737–741.
21 J. D. Jackson, *Classical Electrodynamics*, Wiley, New York, 1999.
22 G. Diguet, E. Beaugnon and J.-Y. Cavaillé, *J. Magn. Magn. Mater.*, 2009, **321**, 396–401.
23 O. V. Stolbov, Y. L. Raikher and M. Balasoiu, *Soft Matter*, 2011, **7**, 8484–8487.
24 D. Ivaneyko, V. Toshchevikov, M. Saphiannikova and G. Heinrich, *Condens. Matter Phys.*, 2012, **15**, 33601.
25 A. Y. Zubarev, *Soft Matter*, 2013, **9**, 4985–4992.
26 W. Chen, L. Sun, X. Li and D. Wang, *Smart Mater. Struct.*, 2013, **22**, 105012.
27 A. M. Menzel, *Phys. Rep.*, 2015, **554**, 1–45.
28 S. Huang, G. Pessot, P. Cremer, R. Weeber, C. Holm, J. Nowak, S. Odenbach, A. M. Menzel and G. K. Auernhammer, *Soft Matter*, 2016, **12**, 228–237.
29 D. Romeis, V. Toshchevikov and M. Saphiannikova, *Soft Matter*, 2016, **12**, 9364–9376.
30 P. Metsch, K. A. Kalina, C. Spieler and M. Kästner, *Comput. Mater. Sci.*, 2016, **124**, 364–374.
31 M. R. Jolly, J. D. Carlson, B. C. Muñoz and T. A. Bullions, *J. Intell. Mater. Syst. Struct.*, 1996, **7**, 613–622.
32 M. R. Jolly, J. D. Carlson and B. C. Muñoz, *Smart Mater. Struct.*, 1996, **5**, 607.
33 E. Jarkova, H. Pleiner, H.-W. Müller and H. R. Brand, *Phys. Rev. E: Stat., Nonlinear, Soft Matter Phys.*, 2003, **68**, 041706.
34 G. V. Stepanov, S. S. Abramchuk, D. A. Grishin, L. V. Nikitin, E. Y. Kramarenko and A. R. Khokhlov, *Polymer*, 2007, **48**, 488–495.
35 H. Böse and R. Röder, *J. Phys.: Conf. Ser.*, 2009, **149**, 012090.
36 A. V. Chertovich, G. V. Stepanov, E. Y. Kramarenko and A. R. Khokhlov, *Macromol. Mater. Eng.*, 2010, **295**, 336–341.
37 D. S. Wood and P. J. Camp, *Phys. Rev. E: Stat., Nonlinear, Soft Matter Phys.*, 2011, **83**, 011402.
38 B. A. Evans, B. L. Fiser, W. J. Prins, D. J. Rapp, A. R. Shields, D. R. Glass and R. Superfine, *J. Magn. Magn. Mater.*, 2012, **324**, 501–507.
39 Y. Han, W. Hong and L. E. Faidley, *Int. J. Solids Struct.*, 2013, **50**, 2281–2288.
40 D. Y. Borin, G. V. Stepanov and S. Odenbach, *J. Phys.: Conf. Ser.*, 2013, **412**, 012040.
41 N. Chiba, K. Yamamoto, T. Hojo, M. Kawai and T. Mitsumata, *Chem. Lett.*, 2013, **42**, 253–254.
42 G. Pessot, P. Cremer, D. Y. Borin, S. Odenbach, H. Löwen and A. M. Menzel, *J. Chem. Phys.*, 2014, **141**, 015005.

43 V. V. Sorokin, G. V. Stepanov, M. Shamonin, G. J. Monkman, A. R. Khokhlov and E. Y. Kramarenko, *Polymer*, 2015, **76**, 191–202.

44 G. Pessot, H. Löwen and A. M. Menzel, *J. Chem. Phys.*, 2016, **145**, 104904.

45 T. I. Volkova, V. Böhm, T. Kaufhold, J. Popp, F. Becker, D. Y. Borin, G. V. Stepanov and K. Zimmermann, *J. Magn. Magn. Mater.*, 2017, **431**, 262–265.

46 P. Cremer, H. Löwen and A. M. Menzel, *Appl. Phys. Lett.*, 2015, **107**, 171903.

47 P. Cremer, H. Löwen and A. M. Menzel, *Phys. Chem. Chem. Phys.*, 2016, **18**, 26670–26690.

48 M. A. Annunziata, A. M. Menzel and H. Löwen, *J. Chem. Phys.*, 2013, **138**, 204906.

49 P. V. Melenev, V. V. Rusakov and Y. L. Raikher, *J. Magn. Magn. Mater.*, 2006, **300**, e187–e190.

50 G. V. Stepanov, D. Y. Borin, Y. L. Raikher, P. V. Melenev and N. S. Perov, *J. Phys.: Condens. Matter*, 2008, **20**, 204121.

51 A. M. Biller, O. V. Stolbov and Y. L. Raikher, *J. Appl. Phys.*, 2014, **116**, 114904.

52 A. M. Biller, O. V. Stolbov and Y. L. Raikher, *Phys. Rev. E: Stat., Nonlinear, Soft Matter Phys.*, 2015, **92**, 023202.

53 A. Zubarev, D. Chirikov, G. Stepanov and D. Borin, *J. Magn. Magn. Mater.*, 2017, **431**, 120–122.

54 A. M. Biller, O. V. Stolbov and Y. L. Raikher, *J. Phys.: Conf. Ser.*, 2018, **994**, 012001.

55 F. H. C. Crick and A. F. W. Hughes, *Exp. Cell Res.*, 1950, **1**, 37–80.

56 F. Ziemann, J. Rädler and E. Sackmann, *Biophys. J.*, 1994, **66**, 2210–2216.

57 T. A. Waigh, *Rep. Prog. Phys.*, 2005, **68**, 685.

58 C. Wilhelm, *Phys. Rev. Lett.*, 2008, **101**, 028101.

59 L. Roeder, P. Bender, A. Tschöpe, R. Birringer and A. M. Schmidt, *J. Polym. Sci., Part B: Polym. Phys.*, 2012, **50**, 1772–1781.

60 P. Bender, A. Tschöpe and R. Birringer, *J. Magn. Magn. Mater.*, 2013, **346**, 152–160.

61 S. Huang, K. Gawlitza, R. von Klitzing, W. Steffen and G. K. Auernhammer, *Macromolecules*, 2017, **50**, 3680–3689.

62 H.-N. An, J. Groenewold, S. J. Picken and E. Mendes, *Soft Matter*, 2014, **10**, 997–1005.

63 T. Gundermann and S. Odenbach, *Smart Mater. Struct.*, 2014, **23**, 105013.

64 T. Gundermann, P. Cremer, H. Löwen, A. M. Menzel and S. Odenbach, *Smart Mater. Struct.*, 2017, **26**, 045012.

65 M. Schümann, D. Borin, S. Huang, G. Auernhammer, R. Müller and S. Odenbach, *Smart Mater. Struct.*, 2017, **26**, 095018.

66 M. Tarama, P. Cremer, D. Y. Borin, S. Odenbach, H. Löwen and A. M. Menzel, *Phys. Rev. E: Stat., Nonlinear, Soft Matter Phys.*, 2014, **90**, 042311.

67 D. Ivaneyko, V. Toshchevikov and M. Saphiannikova, *Soft Matter*, 2015, **11**, 7627–7638.

68 G. Pessot, M. Schümann, T. Gundermann, S. Odenbach, H. Löwen and A. M. Menzel, *J. Phys.: Condens. Matter*, 2018, **30**, 125101.

69 P. Cremer, M. Heinen, A. M. Menzel and H. Löwen, *J. Phys.: Condens. Matter*, 2017, **29**, 275102.

70 K. A. Kalina, P. Metsch and M. Kästner, *Int. J. Solids Struct.*, 2016, **102**, 286–296.

71 A. Attaran, J. Brummund and T. Wallmersperger, *J. Magn. Magn. Mater.*, 2017, **431**, 188–191.

72 N. Phan-Thien, *J. Elasticity*, 1993, **32**, 243–252.

73 S. Kim and N. Phan-Thien, *J. Elasticity*, 1995, **37**, 93–111.

74 N. Phan-Thien and S. Kim, *ZAMP*, 1994, **45**, 177–201.

75 A. N. Norris, *J. Acoust. Soc. Am.*, 2008, **123**, 99–108.

76 M. Puljiz, S. Huang, G. K. Auernhammer and A. M. Menzel, *Phys. Rev. Lett.*, 2016, **117**, 238003.

77 M. Puljiz and A. M. Menzel, *Phys. Rev. E*, 2017, **95**, 053002.

78 A. M. Menzel, *Soft Matter*, 2017, **13**, 3373–3384.

79 S. H. L. Klapp, *J. Phys.: Condens. Matter*, 2005, **17**, R525.

80 C. Holm and J.-J. Weis, *Curr. Opin. Colloid Interface Sci.*, 2005, **10**, 133–140.

81 A. M. Menzel, *J. Chem. Phys.*, 2014, **141**, 194907.

82 G. Pessot, R. Weeber, C. Holm, H. Löwen and A. M. Menzel, *J. Phys.: Condens. Matter*, 2015, **27**, 325105.

83 A. Zubarev, *Physica A*, 2013, **392**, 4824–4836.

84 D. Romeis, P. Metsch, M. Kästner and M. Saphiannikova, *Phys. Rev. E*, 2017, **95**, 042501.

85 http://imagej.nih.gov/ij/.

86 L. D. Landau and E. M. Lifshitz, *Theory of Elasticity*, Elsevier, Oxford, 1986.

87 W. H. Press, S. A. Teukolsky, W. T. Vetterling and B. P. Flannery, *Numerical Recipes in C*, Cambridge University Press, Cambridge, 1982.

88 L. D. Landau and E. M. Lifshitz, *Statistical Physics*, Butterworth-Heinemann, Oxford, 1980.

89 K. A. Kalina, J. Brummund, P. Metsch, M. Kästner, D. Y. Borin, J. M. Linke and S. Odenbach, *Smart Mater. Struct.*, 2017, **26**, 105019.

90 A. C. Eringen and G. A. Maugin, *Electrodynamics of Continua I: Foundations and Solid Media*, Springer, New York, 1990.

91 S. V. Kankanala and N. Triantafyllidis, *J. Mech. Phys. Solids*, 2004, **52**, 2869–2908.

92 K. Danas, *J. Mech. Phys. Solids*, 2017, **105**, 25–53.

93 H. M. Ledbetter and R. P. Reed, *J. Phys. Chem. Ref. Data*, 1973, **2**, 531–617.

94 U. S. Schwarz and S. A. Safran, *Phys. Rev. Lett.*, 2002, **88**, 048102.

95 I. B. Bischofs, S. A. Safran and U. S. Schwarz, *Phys. Rev. E: Stat., Nonlinear, Soft Matter Phys.*, 2004, **69**, 021911.

96 J. Yuval and S. A. Safran, *Phys. Rev. E*, 2013, **87**, 042703.

97 C. Teodosiu, *The Elastic Field of Point Defects*, Springer Berlin/Heidelberg, 1982.

98 H.-H. Boltz and S. Klumpp, *Eur. Phys. J. E: Soft Matter Biol. Phys.*, 2017, **40**, 86.

Electronic Supplementary Information (ESI)

Reversible magnetomechanical collapse: virtual touching and detachment of rigid inclusions in a soft elastic matrix

Mate Puljiz,[a] Shilin Huang,[b] Karl A. Kalina,[c]
Johannes Nowak,[d] Stefan Odenbach,[d] Markus Kästner,[c]
Günter K. Auernhammer,[b,e] and Andreas M. Menzel[a]

[a] Institut für Theoretische Physik II: Weiche Materie, Heinrich-Heine-Universität Düsseldorf, 40225 Düsseldorf, Germany.
[b] Max Planck Institute for Polymer Research, Ackermannweg 10, 55128 Mainz, Germany.
[c] Technische Universität Dresden, Institute of Solid Mechanics, 01062 Dresden, Germany.
[d] Technische Universität Dresden, Institute of Fluid Mechanics, 01062 Dresden, Germany.
[e] Leibniz Institute for Polymer Research, 01069 Dresden, Germany (present address).

In the figure on the next page, we illustrate the strong local deformation fields occurring between the two approaching particles. There, we show results from direct purely elastic finite-element simulations of the Neo-Hookean model when the two particles of radius a are driven towards each other within the soft elastic matrix, see the main article. The initial center-to-center particle separation was $r_{12}^{(0)}/a \approx 3.57$. All results are obtained directly from the simulations, without extrapolation of the deformations, down to center-to-center particle distances $r_{12}/a \approx 2.1$. (This implies an approach of the surface-to-surface distance down to $a/10$.) More precisely, states for (a) $r_{12}/a \approx 2.9$, (b) $r_{12}/a \approx 2.4$, and (c) $r_{12}/a \approx 2.1$ are displayed.

We depict the components u_1 and u_2 of the local displacement field along the axes x_1 and x_2, respectively. Furthermore, to characterize the degree of compression of the deformed matrix along the corresponding principal axis, the spatial variation of the smallest principal stretch λ_3 is illustrated. The pure stretch of a line element is defined as
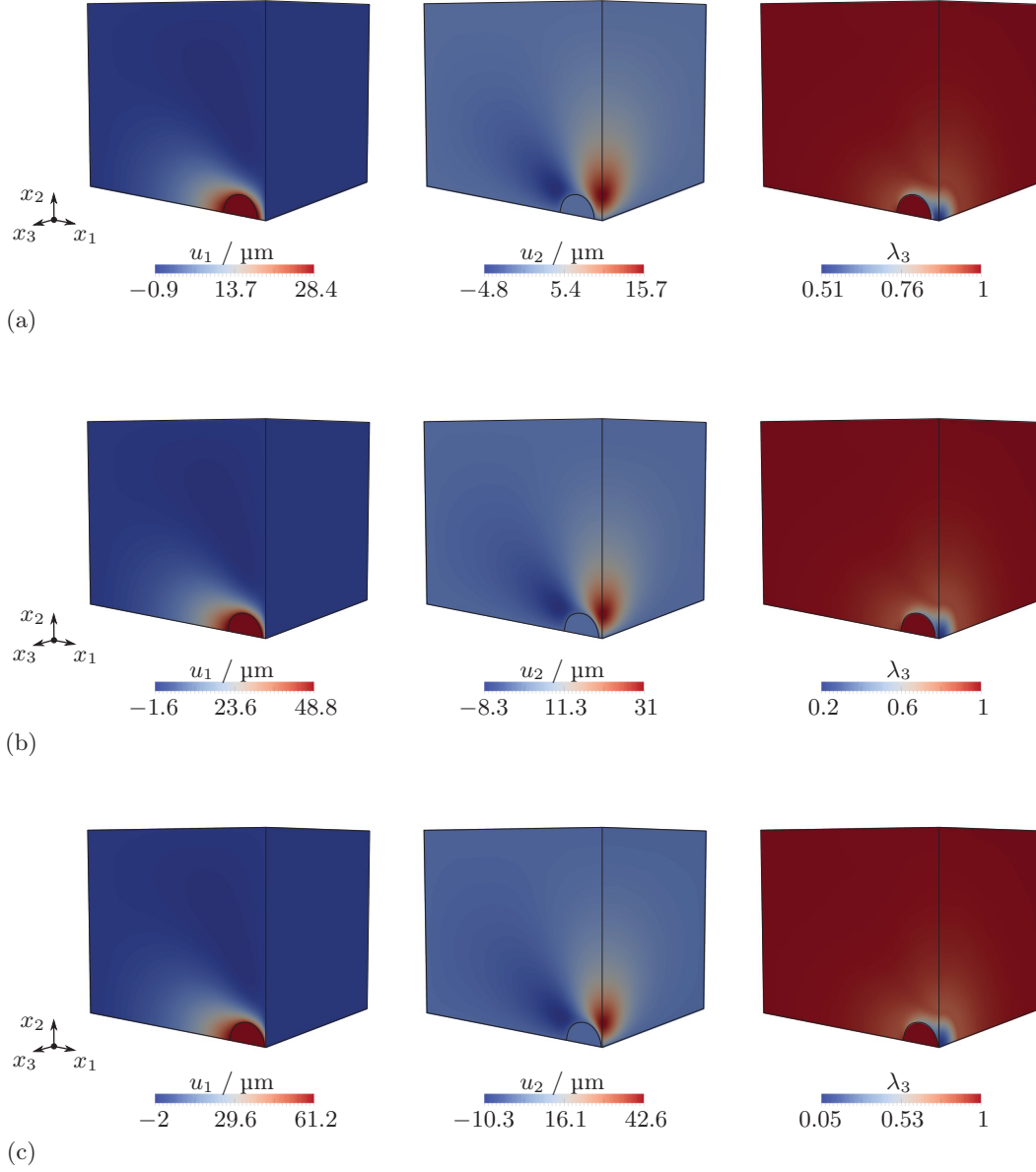
$$\lambda = \frac{ds}{dS} > 0 \,,$$

1

Figure: Results from the mechanical part of the direct finite-element simulations of the elastic Neo-Hookean model in the set-up described in the main article. Components u_1 and u_2 along the axes x_1 and x_2, respectively, of the local displacement field are shown, together with the spatial variation of the smallest principal stretch λ_3 within the polymer matrix. $0 < \lambda_3 < 1$ indicates compression along the corresponding principal axis. From top to bottom, the inter-particle distance decreases as (a) $r_{12}/a \approx 2.9$, (b) $r_{12}/a \approx 2.4$, and (c) $r_{12}/a \approx 2.1$.

where ds and dS denote the infinitesimal length in the deformed and in the undeformed state, respectively. Basically, the quasi-incompressible matrix ($\nu = 0.49$ within the simulation) is squeezed out from between the particles by the particle approach. Between the particles, a region of extreme compression occurs along the corresponding local principal axis of deformation.

Publication IV

Memory-based mediated interactions between rigid particulate inclusions in viscoelastic environments

Reproduced from

Author's contributions

Both authors contributed to this work. A. M. Menzel postulated the theory. I contributed a considerable part to the elaboration of the theory under his supervision, including the derivation of the viscoelastic Green's function, the derivation from a general continuum theory, the theoretical description of spherical inclusions and their interactions via the medium, and the investigation of the relaxational dynamics of particles for different degrees of elastic memory. I performed all numerical evaluations. I estimate my overall contribution to this work to approximately 80%.

Copyright and license notice

Memory-based mediated interactions between rigid particulate inclusions in viscoelastic environments

Mate Puljiz[*] and Andreas M. Menzel[†]

Institut für Theoretische Physik II: Weiche Materie, Heinrich-Heine-Universität Düsseldorf, D-40225 Düsseldorf, Germany

Many practically relevant materials combine properties of viscous fluids and elastic solids to viscoelastic behavior. Our focus is on the induced dynamic behavior of damped finite-sized particulate inclusions in such substances. We explicitly describe history-dependent interactions that emerge between the embedded particles. These interactions are mediated by the viscoelastic surroundings. They result from the flows and distortions of the viscoelastic medium when induced by the rigid inclusions. Both viscoelastic environments of terminal fluidlike flow and of completely reversible damped elastic behavior are covered. For illustration and to highlight the role of the formalism in potential applications, we briefly address the relevant examples of dragging a rigid sphere through a viscoelastic environment together with subsequent relaxation dynamics, the switching dynamics of magnetic fillers in elastic gel matrices, and the swimming behavior of active microswimmers in viscoelastic solutions. The approach provides a basis for more quantitative and extended investigations of these and related systems in the future.

I. INTRODUCTION

To a large extent, real materials do not behave in a purely liquid- or solidlike way. Substances that on long timescales show a fluidlike terminal flow may feature reversible quasielastic deformations under sufficiently short application of external forces. Prominent examples are melts or solutions of entangled polymer molecules [1,2]. Vice versa, the dynamics of materials that do feature reversible elastic deformations on long timescales, like rubbers or soft elastic polymeric gels, may still be damped by internal viscouslike friction [1,2].

Materials combining such viscous and elastic characteristics are termed viscoelastic. Studying their behavior on a mesoscopic particulate length scale becomes important when they contain immersed or embedded rigid inclusions. Especially, this concerns interactions between the embedded particles mediated by the viscoelastic environment. They arise when forces or torques imposed on or actively generated by the particles are transmitted to their surroundings. Recently studied experimental examples comprise microrheological investigations probing the environment of embedded colloidal particles when driving them via external magnetic or optical fields [3–7], switching the magnetic interactions between rigid inclusions in soft elastic gel matrices by external magnetic fields [8–11], or self-driven active microswimmers [12–15] propelling through viscoelastic environments [16–20].

Here we provide a corresponding theoretical framework. Our focus is on systems featuring discrete finite-sized particulate inclusions embedded in a surrounding viscoelastic continuous matrix. We concentrate on the overdamped dynamics

of the embedded particles. The interactions between the embedded particles that are mediated by the viscoelastic environment are covered. Moreover, our approach allows to describe both long-time terminal flow and long-time reversible elastic behavior of the viscoelastic surroundings. Accordingly, the broad range of physical systems mentioned above can be addressed. Later our results will serve to study, e.g., by statistical means, links between the collective behavior of embedded particle ensembles and overall material properties [21–29].

Next, we introduce in Sec. II the continuum description that we use to represent the viscoelastic environment. The linearity of the employed approach allows to derive and use the Green's function associated with a localized force impulse acting within the viscoelastic medium. We proceed in Sec. III by inserting and quantifying the role of finite-sized rigid spherical inclusions in this viscoelastic background. To illustrate in Sec. IV the strength of the approach, we then briefly and qualitatively address its possible application to different examples. This opens the way to a broad range of more detailed and quantitative studies in the future. Some conclusions are listed in Sec. V. Apart from that, we illustrate in Appendix A how the continuum equation characterizing our viscoelastic environment can be obtained from a generalized hydrodynamic approach [30]. Moreover, we include in Appendix B the detailed derivation of the Green's function mentioned above. In Appendix C we demonstrate that this Green's function satisfies the Kramers-Kronig relations as required. A basic example situation considered in Appendix D serves to further illustrate our approach. We show in Appendix E that the formalism used here to address the role of net forces acting on rigid particles embedded in a viscoelastic environment is readily extended to include net torques as well. Finally, Appendix F lists some technical details concerning our numerical discretization scheme.

[*]puljiz@thphy.uni-duesseldorf.de
[†]menzel@thphy.uni-duesseldorf.de

II. BASIC CONTINUUM DESCRIPTION OF THE VISCOELASTIC ENVIRONMENT

To characterize the behavior of the viscoelastic environment, we consider an isotropic and homogeneous viscoelastic continuum on the scale of the mesoscopic inclusions. A simple linearized description will be employed to allow for an effective analytical treatment. First, we recall the limits of purely viscous and purely linearly elastic materials. Incompressible viscous low-Reynolds-number fluid flows are quantified by Stokes's equations [25,31]

$$\eta \nabla^2 \mathbf{v}(\mathbf{r}, t) = \nabla p(\mathbf{r}, t) - \mathbf{f}_b(\mathbf{r}, t), \quad \nabla \cdot \mathbf{v}(\mathbf{r}, t) = 0, \quad (1)$$

with η the dynamic viscosity, $\mathbf{v}(\mathbf{r}, t)$ the flow velocity field, $p(\mathbf{r}, t)$ the pressure field, and $\mathbf{f}_b(\mathbf{r}, t)$ the bulk force density acting on the fluid. Contrariwise, reversible deformations of incompressible linearly elastic solids are quantified by the Navier-Cauchy equations [32]

$$\mu \nabla^2 \mathbf{u}(\mathbf{r}, t) = -\mathbf{f}_b(\mathbf{r}, t), \quad \nabla \cdot \mathbf{u}(\mathbf{r}, t) = 0, \quad (2)$$

with μ the shear modulus, $\mathbf{u}(\mathbf{r}, t)$ the displacement field of the material elements, and $\mathbf{f}_b(\mathbf{r}, t)$ the bulk force density acting on the solid. The assumed incompressibility represents a reasonable approximation in many cases. Namely, this should include (semi)dilute aqueous solutions of polymers [18,33] and classes of swollen polymeric gels [11,34].

For an incompressible, infinitely extended, isotropic, and homogeneous viscoelastic medium, we now combine these balances of force densities, Eqs. (1) and (2), yielding

$$\mu \nabla^2 \mathbf{u}(\mathbf{r}, t) + \eta \nabla^2 \mathbf{v}(\mathbf{r}, t) = \nabla p(\mathbf{r}, t) - \mathbf{f}_b(\mathbf{r}, t). \quad (3)$$

This relation can be confirmed by linearizing a general continuum approach based purely on conservation laws and symmetry arguments [30], constricted to the regime of the overdamped dynamics considered here. See Appendix A for the details. Moreover, in this limit, Eq. (3) likewise follows when combining the dynamic equations of a two-fluid approach that contains frictional coupling between an elastic component and a viscous fluid component [35–37].

Formally, linear elasticity theory does not distinguish whether the coordinates $\mathbf{r}$ refer to the initial (undeformed) or the present (deformed) state of a material [30,38]. Yet, hydrodynamics dictates the latter, Euler point of view [30]. Thus, $\mathbf{u}(\mathbf{r}, t)$ describes the reversible elastic displacements that have taken the material elements *to* the positions $\mathbf{r}$. Or, probably more appropriately in the present context, $\mathbf{u}(\mathbf{r}, t)$ quantifies the *memory* of those positions that the material elements would tend to displace back to from their present positions, if the material is relaxed from its current state.

In a viscoelastic medium, this memory of the initial positions stored in $\mathbf{u}(\mathbf{r}, t)$ may fade away over time. In addition to changes in $\mathbf{u}(\mathbf{r}, t)$ arising from material motion $\mathbf{v}(\mathbf{r}, t)$, we therefore assume a simple relaxation

$$\dot{\mathbf{u}}(\mathbf{r}, t) = \mathbf{v}(\mathbf{r}, t) - \gamma \mathbf{u}(\mathbf{r}, t). \quad (4)$$

The relaxation rate γ sets the "forgetfulness" of the medium, implying complete reversibility for $\gamma = 0$. (This equation is different from the corresponding one in Refs. [35–37], where instead of the relaxational decay a diffusional contribution appears.)

Here, the material parameters were chosen as constants, not depending, for instance, on the length scale of the induced distortions. If the building blocks of the viscoelastic environment are significantly smaller than the inserted rigid particles considered below, this should represent a reasonable approximation in many cases. Then typical distortions induced by the rigid particles in the viscoelastic surroundings will often be observed to vary on a scale of the size of the particles themselves, which thus is significantly more extended than the building blocks of the environment. Colloidal particles in polymeric surroundings can provide a corresponding example.

Eliminating $\mathbf{v}(\mathbf{r}, t)$ from Eqs. (3) and (4), we obtain

$$(\mu + \gamma \eta) \nabla^2 \mathbf{u}(\mathbf{r}, t) + \eta \nabla^2 \dot{\mathbf{u}}(\mathbf{r}, t) = \nabla p(\mathbf{r}, t) - \mathbf{f}_b(\mathbf{r}, t). \quad (5)$$

Due to the linearity in $\mathbf{u}(\mathbf{r}, t)$, the Green's function can be determined. It solves Eq. (5) for a given force impact $\mathbf{F}$ at position $\mathbf{R}_0$ and time t_0, setting $\mathbf{f}_b(\mathbf{r}, t) = \mathbf{F}\delta(\mathbf{r} - \mathbf{R}_0)\delta(t - t_0)$, which involves the corresponding delta functions in both space and time. The procedure is well established, e.g., in low-Reynolds-number hydrodynamics [25,39] or linear elasticity theory [11,40,41]. After transforming to Fourier space, here both in space and time, solving for the displacement field, projecting on transverse modes according to the incompressibility relation in Eq. (2), and transforming back, we obtain

$$\mathbf{u}(\mathbf{r}, t) = \underline{\mathbf{G}}(\mathbf{r} - \mathbf{R}_0, t - t_0) \cdot \mathbf{F}, \quad (6)$$

with $\underline{\mathbf{G}}(\mathbf{r}, t)$ the second-rank tensor

$$\underline{\mathbf{G}}(\mathbf{r}, t) = \frac{1}{8\pi \eta |\mathbf{r}|} [\hat{\underline{\mathbf{I}}} + \hat{\mathbf{r}}\hat{\mathbf{r}}] \Theta(t) e^{-\frac{\mu + \gamma \eta}{\eta} t}. \quad (7)$$

$\hat{\underline{\mathbf{I}}}$ is the identity matrix, $\hat{\mathbf{r}}\hat{\mathbf{r}}$ a dyadic product with $\hat{\mathbf{r}} = \mathbf{r}/|\mathbf{r}|$, and $\Theta(t)$ the Heaviside function. (For readers unfamiliar with this common technique, we reproduce it in Appendix B, together with a remark on the associated Kramers-Kronig relations in Appendix C). We note that $\underline{\mathbf{G}}(\mathbf{r}, t) = \underline{\mathbf{G}}(\mathbf{r})G(t)$, with

$$\underline{\mathbf{G}}(\mathbf{r}) = \frac{1}{8\pi \eta |\mathbf{r}|} [\hat{\underline{\mathbf{I}}} + \hat{\mathbf{r}}\hat{\mathbf{r}}], \quad G(t) = \Theta(t) e^{-\frac{\mu + \gamma \eta}{\eta} t}, \quad (8)$$

where $\underline{\mathbf{G}}(\mathbf{r})$ has the same form as the hydrodynamic Oseen tensor [25]. The viscoelastic displacements resulting from a general force density $\mathbf{f}_b(\mathbf{r}, t)$ are thus obtained as

$$\mathbf{u}(\mathbf{r}, t) = \int_{\mathbb{R}} dt' \, G(t - t') \int_{\mathbb{R}^3} d^3 r' \, \underline{\mathbf{G}}(\mathbf{r} - \mathbf{r}') \cdot \mathbf{f}_b(\mathbf{r}', t'). \quad (9)$$

For illustration, we consider the example trajectory of one material element subject to an interim constant and otherwise vanishing concentrated force density in Appendix D.

III. RIGID SPHERICAL INCLUSIONS

We now turn to rigid spherical particles of radius a embedded in the viscoelastic medium. No-slip conditions prevail on their surfaces. An external force $\mathbf{F}(t)$ exerted on a particle centered at $\mathbf{R}(t)$ is transmitted to the environment, distorting it, and/or setting it into motion. Starting from the Green's function and the formal analogy of $\underline{\mathbf{G}}(\mathbf{r})$ to the hydrodynamic

case [39], we consider the displacement field

$$\mathbf{u}(\mathbf{r}, t) = \int_{\mathbb{R}} dt' \, G(t - t') \left\{ \left[\left(1 + \frac{a^2}{6} \nabla^2 \right) \underline{\mathbf{G}}(\mathbf{s}(t')) \right] \cdot \mathbf{F}(t') \right.$$
$$\left. \times \, \Theta(|\mathbf{s}(t')| - a) + \frac{1}{6\pi \eta a} \mathbf{F}(t') \, \Theta(a - |\mathbf{s}(t')|) \right\},$$
(10)

with $\mathbf{s}(t') := \mathbf{r} - \mathbf{R}(t')$ and a continuous integrand for each $|\mathbf{s}(t')| = a$. This expression solves inside the embedding medium, for $|\mathbf{s}(t)| > a$, the linear Eq. (5) for $\mathbf{f}_b(\mathbf{r}, t) = \mathbf{0}$, together with the pressure field $p(\mathbf{r}, t) = \mathbf{s}(t)/4\pi |\mathbf{s}(t)|^3 \cdot \mathbf{F}(t)$ as in the hydrodynamic case [39]. It satisfies $\nabla \cdot \mathbf{u}(\mathbf{r}, t) = 0$ and the boundary condition $\mathbf{u}(\mathbf{r}, t) \to \mathbf{0}$ for $|\mathbf{s}(t)| \to \infty$ [see Eq. (7)] if all $|\mathbf{R}(t')|$ remain finite. At each instant in time t', the expression in the square brackets is constant on the surface of the sphere ($|\mathbf{s}(t')| = a$), reflecting its rigid displacement and confirmed by explicitly evaluating $(1 + a^2 \nabla^2/6)\underline{\mathbf{G}}(\mathbf{r} - \mathbf{R}(t'))$. Similar relations can be obtained when applying a net torque; see Appendix E. We determine the reaction of the sphere at time t to the contributions generated by itself at earlier times $t' < t$ [see Eq. (10)] via Eqs. (12) and (13) below.

At each point in time t, the no-slip condition on the particle surface $\mathbf{r} \in \partial V$ reads

$$\mathbf{U}(t) + \mathbf{\Omega}(t) \times (\mathbf{r} - \mathbf{R}(t)) = \mathbf{u}(\mathbf{r}, t).$$
(11)

It states that the displacements of the particle surface points, given by its rigid displacement $\mathbf{U}(t)$ and rotation $\mathbf{\Omega}(t)$, must be equal to the displacement $\mathbf{u}(\mathbf{r}, t)$ of the there anchored surrounding medium. Here $\mathbf{u}(\mathbf{r}, t)$ contains the displacements in the medium induced by the particle itself, also at earlier times [see Eq. (10)] and all displacements generated by all other sources. Due to the linearity of Eq. (5), all contributions superimpose.

Equation (11) allows to determine at each time t how a rigid sphere is displaced [$\mathbf{U}(t)$] and rotated [$\mathbf{\Omega}(t)$] in a given displacement field $\mathbf{u}(\mathbf{r}, t)$. The derivation of these so-called Faxén laws follows the same lines as in low-Reynolds-number hydrodynamics [25,39] and linear elasticity theory [11,41–43]. Integrating both sides of Eq. (11) over the surface ∂V of the sphere, the antisymmetric $\mathbf{\Omega}(t)$ term vanishes, and we obtain

$$\mathbf{U}(t) = \frac{1}{4\pi a^2} \int_{\partial V} d^2 |\mathbf{r} - \mathbf{R}(t)| \, \mathbf{u}(\mathbf{r}, t).$$
(12)

Similarly, multiplying Eq. (11) by $(\mathbf{r} - \mathbf{R}(t))$ before the integration, we find

$$\mathbf{\Omega}(t) = \frac{3}{8\pi a^4} \int_{\partial V} d^2 |\mathbf{r} - \mathbf{R}(t)| \, (\mathbf{r} - \mathbf{R}(t)) \times \mathbf{u}(\mathbf{r}, t). \quad (13)$$

These integrals can be evaluated numerically [44]. If $\mathbf{u}(\mathbf{r}, t)$ in Eqs. (12) and (13) is infinitely differentiable, we may expand it in $\mathbf{s}(t) = \mathbf{r} - \mathbf{R}(t)$ as $\mathbf{u}(\mathbf{R}(t) + \mathbf{s}(t), t) = (1 + \mathbf{s}(t) \cdot \nabla + \mathbf{s}(t)\mathbf{s}(t) : \nabla\nabla/2 + \cdots)\mathbf{u}(\mathbf{r}, t)|_{\mathbf{r}=\mathbf{R}(t)}$. Uneven dyadics in $\mathbf{s}(t)$ vanish upon integration $\int_{\partial V} d^2 |\mathbf{s}(t)|$, even dyadics of $\mathbf{s}(t)$ lead to dyadic combinations of $\underline{\mathbf{I}}$, and $\nabla^{(2n)}\mathbf{u}(\mathbf{r}, t) = \mathbf{0} = \nabla \times \nabla^2 \mathbf{u}(\mathbf{r}, t)$ ($n \geqslant 2$ integer), which follows from directly applying these differential operators to the Green's function

in Eq. (7). Then the Faxén relations are again of the form [11,25,39,41–43]

$$\mathbf{U}(t) = \left(1 + \frac{a^2}{6} \nabla^2 \right) \mathbf{u}(\mathbf{r}, t) \bigg|_{\mathbf{r}=\mathbf{R}(t)}, \quad (14)$$

$$\mathbf{\Omega}(t) = \frac{1}{2} \nabla \times \mathbf{u}(\mathbf{r}, t)|_{\mathbf{r}=\mathbf{R}(t)}. \quad (15)$$

Correspondingly, the analog to Eq. (11) links the velocity $\mathbf{V}(t)$ and angular velocity $\mathbf{W}(t)$ of the sphere to the velocity field $\mathbf{v}(\mathbf{r}, t)$ of the environment. Repeating the above steps, we obtain the associated Faxén laws in analogy to Eqs. (12)–(15), simply replacing $\mathbf{U}(t) \to \mathbf{V}(t)$, $\mathbf{\Omega}(t) \to \mathbf{W}(t)$, and $\mathbf{u}(\mathbf{r}, t) \to \mathbf{v}(\mathbf{r}, t)$. These relations are consistent with Eq. (4), $\mathbf{V}(t) = \dot{\mathbf{U}}(t) + \gamma \mathbf{U}(t)$, and $\mathbf{W}(t) = \dot{\mathbf{\Omega}}(t) + \gamma \mathbf{\Omega}(t)$.

We stress the physical importance of the velocity field and the particle velocities. If one is interested in the local material transport within the material, the important quantity is the velocity field $\mathbf{v}(\mathbf{r}, t)$, and not predominantly the *memory* displacement field $\mathbf{u}(\mathbf{r}, t)$. The latter at each instant in time describes towards where the material points would tend to relax, if all forces exerted on the material are switched off. For $\gamma \neq 0$, these in general are not the positions that the material points had started from initially because the memory decays over time. In our case, we consider the transport of the rigid spheres. Their total net translation is given by integration of their velocities $\mathbf{V}(t)$ over their course of motion, and not simply by the value of the current memory variables $\mathbf{U}(t)$.

Accordingly, our picture is closed. From Eq. (10) we calculate $\mathbf{u}(\mathbf{r}, t)$ at each requested position $\mathbf{r}$ and time t, resulting from the forces exerted by the spherical particles on their viscoelastic environment. $\mathbf{v}(\mathbf{r}, t)$ follows via Eq. (4). From the Faxén relations we obtain the velocities $\mathbf{V}(t)$ and angular velocities $\mathbf{W}(t)$ of the particles. Integrating these over time leads to the particle trajectories $\mathbf{R}(t)$ and courses of rotation.

What we neglect in this approach are additional contributions to the displacement field that arise from the resistance of the rigid particles to their deformations under strong local distortion [11]. In the hydrodynamic language, we here stop at the common Rodne-Prager level [25], rendering the results qualitative when our spheres meet areas of stronger distortion. Moreover, our formulas are evaluated numerically. By construction, this involves finite time steps and finite displacements. Technically, to apply in our numerical discretization the force density $\mathbf{f}_b(\mathbf{r}, t)$ in Eq. (5) at the positions where it causes the resulting displacements, we shift back the force centers at each time step according to the memorized displacements to calculate the induced $\mathbf{u}(\mathbf{r}, t)$. This scheme correctly reproduces complete elastic reversibility for $\gamma \to 0$; see Appendix F.

IV. EXAMPLES

To demonstrate the range of the theory and for illustration, we now briefly consider several examples. First, this concerns a single sphere dragged by a net force through a viscoelastic environment. In this context, we also demonstrate that the familiar Green's functions associated with incompressible linearly elastic solids and low-Reynolds-number incompressible fluid flows are reproduced in the corresponding
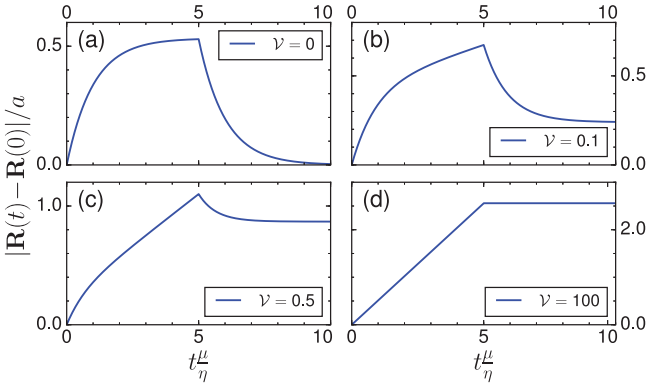
FIG. 1. Overall translation $|\mathbf{R}(t) - \mathbf{R}(0)|$ for a spherical particle of radius a, dragged by a constant force of magnitude $|\mathbf{F}| = 10\mu a^2$ during times $0 \leqslant t \leqslant 5\eta/\mu$. $\mathcal{V} = \gamma\eta/\mu$ sets the memory of the viscoelastic environment and determines the degree of relaxation back to the initial position for $t > 5\eta/\mu$, when the drag force has been switched off again. (a) $\mathcal{V} = 0$ implies fully reversible elasticity, while (b, c) intermediate values of $\mathcal{V}$ imply partial loss of memory and partial reversibility. (d) $\mathcal{V} = 100$ already shows the phenomenology of viscous hydrodynamics ($\mathcal{V} \to \infty$). The ordinates feature different scales, so that the magnitude of maximum translation grows from panel (a) to (d).

limits. Next, the pairwise interactions between magnetizable finite-sized particles are considered. These particles interact both magnetically and via the flows and distortions induced in their viscoelastic surroundings. Afterwards, we touch the topic of self and mutual interactions of active self-propelled microswimmers in viscoelastic media.

A. Dragged rigid sphere

Figure 1 starts with the basic scenario of dragging one spherical particle through a viscoelastic medium by a constant external force, switched on and off at given times. For instance, this situation concerns active magnetic microrheological measurements, where colloidal particles are driven by external magnetic field gradients to probe the viscoelastic environment [3–7].

The description correctly reproduces the limiting cases. To confirm this, we meanwhile measure lengths in particle radii a, bulk force densities in units of μ/a, and time in units of η/μ. Then the whole system behavior is controlled by one remaining dimensionless number appearing in the exponent in Eq. (7) or (8), and particularly as the relaxation parameter in Eq. (4),

$$\mathcal{V} = \frac{\gamma\eta}{\mu}. \qquad (16)$$

Indeed, for $\mathcal{V} \to 0$, complete elastic reversibility is recovered; see Fig. 1(a). Theoretically, this limit follows from switching on a static force density $\mathbf{f}_b(\mathbf{r})$ at $t = t_0$ in Eq. (9) via $\mathbf{f}_b(\mathbf{r}, t) = \mathbf{f}_b(\mathbf{r})\Theta(t - t_0)$. After complete relaxation for $t \to \infty$, we obtain the correct steady-state displacements in an incompressible linearly elastic solid [11,40,41,45]

$$\mathbf{u}(\mathbf{r}, t) = \int_{\mathbb{R}^3} d^3 r' \, \frac{\eta}{\mu} \underline{\mathbf{G}}(\mathbf{r} - \mathbf{r}') \cdot \mathbf{f}_b(\mathbf{r}'). \qquad (17)$$

Conversely, $\mathcal{V} \gg 1$ implies the hydrodynamic limit of negligible memory; see Fig. 1(d). In the theory, we take the time derivative of Eq. (9), insert it as $\dot{\mathbf{u}}(\mathbf{r}, t)$ into Eq. (4), and then take the limit $\mathcal{V} \to \infty$ of vanishing elasticity. This leads to

$$\mathbf{v}(\mathbf{r}, t) = \int_{\mathbb{R}^3} d^3 r' \, \underline{\mathbf{G}}(\mathbf{r} - \mathbf{r}') \cdot \mathbf{f}_b(\mathbf{r}', t), \qquad (18)$$

reproducing the correct Oseen expression of low-Reynolds-number hydrodynamics [25,39]. Intermediate finite values of $\mathcal{V} > 0$ imply viscoelasticity of partially decaying memory, with example cases depicted in Figs. 1(b) and 1(c).

B. Magnetically induced particle interactions

A more specific example of practical relevance is given by magnetic hybrid materials of magnetic or magnetizable colloidal particles embedded in soft polymeric environments [8,15,46,47]. Manipulating the magnetic particle interactions by external magnetic fields allows to reversibly tune from outside the mechanical material stiffness [8,48]. Studying the switching dynamics on the particle scale [10,11,49–51] becomes especially important in applications as soft actuators [8,52–55].

Approximating the magnetic moments of the particles by dipoles [56], we consider for illustration the effect of pairwise interactions between two identical spherical paramagnetic particles, labeled 1 and 2. For simplicity, a strong homogeneous external magnetic field is applied, leading to identical saturated magnetic moments $\mathbf{m}$. The dipolar interaction force on particle i is given by [57]

$$\mathbf{F}_i(t) = \frac{3\mu_0 |\mathbf{m}|^2}{4\pi} \frac{2\hat{\mathbf{m}}(\hat{\mathbf{m}} \cdot \hat{\mathbf{d}}(t)) + \hat{\mathbf{d}}(t) - 5\hat{\mathbf{d}}(t)(\hat{\mathbf{m}} \cdot \hat{\mathbf{d}}(t))^2}{|\mathbf{d}(t)|^4}, \qquad (19)$$

with μ_0 the magnetic vacuum permeability, $\hat{\mathbf{m}} = \mathbf{m}/|\mathbf{m}|$, $\mathbf{d}(t) = \mathbf{R}_i(t) - \mathbf{R}_{j\neq i}(t)$, and $\hat{\mathbf{d}}(t) = \mathbf{d}(t)/|\mathbf{d}(t)|$ ($i, j \in \{1, 2\}$).

In Fig. 2 we consider two such magnetizable spherical particles embedded in different viscoelastic background media. The solid circles indicate the initial positions in the unmagnetized state. Next, the particles are magnetized by a strong external magnetic field in a way that they repel each other. After a longer time of magnetization, the positions in the fully reversible elastic case (a) of $\mathcal{V} = 0$ are set by the balance of magnetic repulsive and counteracting mechanical restoring forces, the latter resulting from the elastic distortion. In the other cases (b) and (c) of $\mathcal{V} \neq 0$, an in principle unbounded withdrawal of the particles from each other is observed with elapsing time. Yet, the speed of withdrawal decreases as the magnetic repulsion drops with increasing mutual particle distance. Dashed circles mark the positions attained when the field is switched off again.

The second row of Fig. 2 then shows the reaction after switching off the induced magnetic repulsion. We depict the positions after sufficient times of relaxation by dotted circles. While complete reversibility is observed for $\mathcal{V} = 0$ in (a), virtually no relaxation takes place for the case of basically absent memory (c). Intermediate amounts of relaxation occur for intermediate strengths of the memory (b).
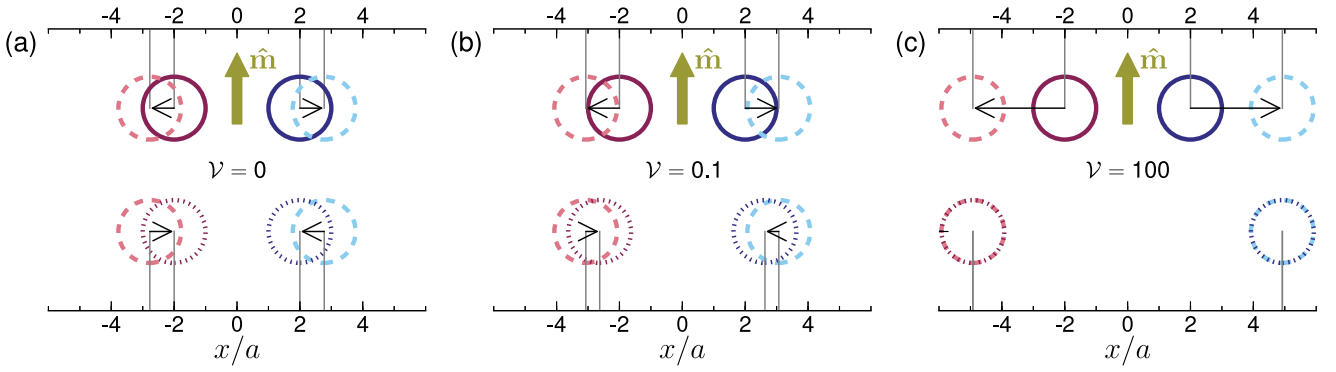
FIG. 2. Two magnetizable spherical particles are exposed to a saturating external magnetic field. Repulsive magnetic dipole moments $\mathbf{m} = 300(\mu a^6/\mu_0)^{1/2}\hat{\mathbf{m}}$ are induced during times $0 \leqslant t \leqslant 10\eta/\mu$ (upper row) and then switched off again (bottom row), for (a) complete elastic reversibility $\mathcal{V} = 0$, (b) $\mathcal{V} = 0.1$, and (c) basically absent memory $\mathcal{V} = 100$. Circles mark the positions at $t = 0$ (solid), $t = 10\eta/\mu$ (dashed), and $t \gg 10\eta/\mu$ (dotted). Black arrows indicate trajectories.

We stress that the depicted dynamical behavior is evaluated by the formalism presented in Sec. III. Accordingly, the mutual interactions mediated between the rigid particles by the viscoelastic environment as well as the finite particle sizes are taken into account to the degree specified above.

Similar situations, but for initially oblique particle separation vectors relatively to the induced magnetization, are shown in Fig. 3. Interestingly, in this case the trajectories of initial motion in the magnetized state and of relaxation after the magnetic field has been switched off do not collapse. This even applies to the fully reversible elastic case in Fig. 3(b), although the spheres there return to their initial positions. The reason can be associated with the nonreciprocity of the induced magnetic forces during the process. On the forward path, the nonvanishing magnetic forces change during the motion because of their positional dependence. However, they are zero throughout the subsequent relaxational return path.
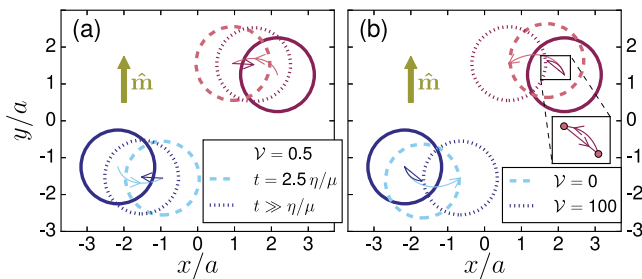

FIG. 3. Same as in Fig. 2, but for an oblique configuration and $\mathbf{m} = 200(\mu a^6/\mu_0)^{1/2}\hat{\mathbf{m}}$. (a) For $\mathcal{V} = 0.5$, $\mathbf{m}$ is induced during times $0 \leqslant t \leqslant 2.5\eta/\mu$. Rearrangements affect the magnetic interactions, while they are constant (zero) for $t > 2.5\eta/\mu$. Significantly different paths of induced rearrangement (brighter arrows) and subsequent relaxation (darker arrows) result. (b) The cases $\mathcal{V} = 0$ (reversibly elastic solid) and $\mathcal{V} = 100$ (nearly memoryless fluid) are shown together for $\mathbf{m}$ induced during $0 \leqslant t \leqslant 1.8\eta/\mu$. For $\mathcal{V} = 0$, the spheres from their intermediate locations at $t = 1.8\eta/\mu$ (dashed circles) relax back to their initial positions (solid circles) as the closed darker trajectories and the inset demonstrate. For $\mathcal{V} = 100$, the spheres first cover longer paths (brighter arrows), but for $t \geqslant 1.8\eta/\mu$ basically remain in their final locations (dotted circles).

C. Active self-propelled microswimmers

Another field of significantly growing interest concerns active self-propelled microswimmers and their mutual hydrodynamic interactions [12–15,58–60]. Increasingly, their behavior in viscoelastic environments is addressed [16–20,61]. We adapt a recently introduced minimal microswimmer model [29,62,63]; see Fig. 4. A spherical swimmer body and two concentrated force centers are arranged along a common axis oriented by the unit vector $\hat{\boldsymbol{\Phi}}(t)$. They form one rigid entity that displaces and rotates as one object. The spherical swimmer body is located at position $\mathbf{R}(t)$, asymmetrically between the two force centers. The latter are separated by a distance L, exert axial but oppositely oriented forces $\pm\mathbf{F}(t) = \pm F(t)\hat{\boldsymbol{\Phi}}(t)$ onto the surrounding medium, thus distorting it and setting it into motion. Pushing the medium outward along the symmetry axis as in Fig. 4(a) identifies a so-called pusher. Inverting the forces and $\hat{\boldsymbol{\Phi}}(t)$ transforms it into a puller. The latter pulls the medium inward along the symmetry axis; see Fig. 4(b). This induced distortion of the surrounding medium leads to a self-induced straight advective transport of an isolated swimmer along $\hat{\boldsymbol{\Phi}}$, if there are no other perturbations. The velocity $\mathbf{V}(t)$ of the swimmer is obtained from the magnitude of the flow field at the location of the swimmer body. That is, $\mathbf{V}(t) = \mathbf{v}(\mathbf{R}(t), t)$, here neglecting the finite extension of the center sphere [62].

First, we address individual, isolated microswimmers in the absence of any perturbations. In this context, we analyze how the steady-state swimming speed of the swimmers in Fig. 4 changes with the rescaled "forgetfulness" of the viscoelastic environment as defined in Eq. (16). For this purpose, the force density

$$\mathbf{f}_b(\mathbf{r}, t) = F\hat{\boldsymbol{\Phi}}(t)\{\delta(\mathbf{r} - (\mathbf{R}(t) \pm bL\hat{\boldsymbol{\Phi}}(t)))$$
$$- \delta(\mathbf{r} - (\mathbf{R}(t) \mp (1-b)L\hat{\boldsymbol{\Phi}}(t)))\} \quad (20)$$

is inserted into Eq. (9) [with $\delta(\mathbf{r})$ the Dirac delta function] and then the velocity field is calculated from Eq. (4). The upper signs in the $\pm$ and $\mp$ operators in Eq. (20) represent the force density generated by a pusher and the lower signs the case of a puller. For the resulting unperturbed straight steady-state motion $\mathbf{V} \parallel \hat{\boldsymbol{\Phi}}$ of the microswimmer considered here, a scalar expression for the swimming speed $V = |\mathbf{V}|$
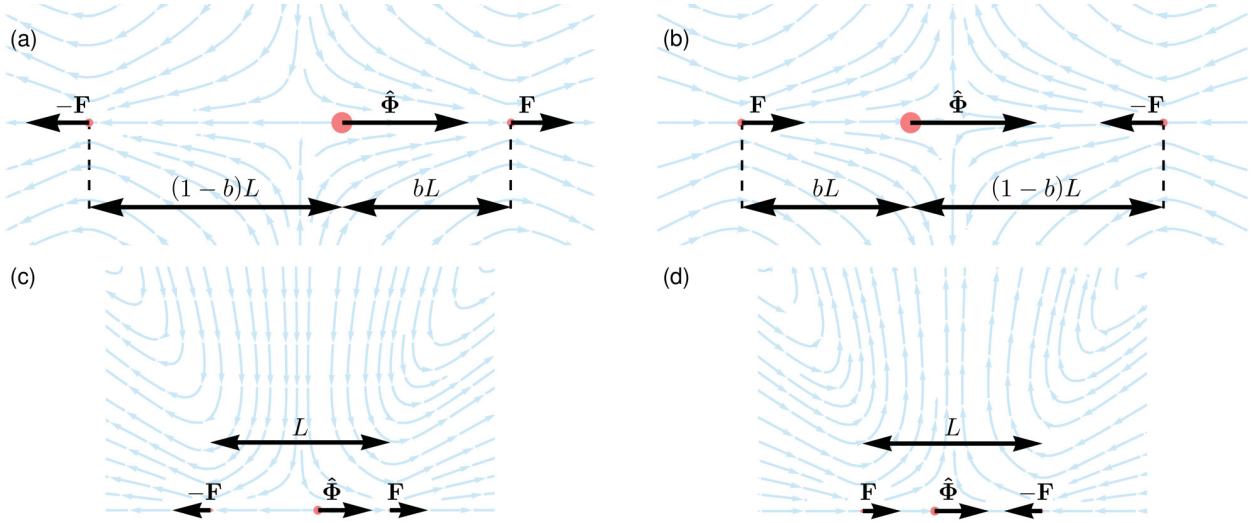
FIG. 4. Illustration of our microswimmer model, adapted from Ref. [62]. Two concentrated force centers, separated by a distance L, exert forces $\pm\mathbf{F} = \pm F(t)\hat{\boldsymbol{\Phi}}(t)$ onto the surrounding medium, set it into motion, and distort it. A sphere representing the swimmer body is asymmetrically placed in between, as determined by the parameter b, and is thus subject to net displacements along $\hat{\boldsymbol{\Phi}}(t)$. The resulting minimal model microswimmer displaces and rotates as one rigid entity. A so-called pusher is shown in panel (a), while inverting the forces and thus the flow directions of the background medium transforms it into a puller as depicted in panel (b). Background arrows indicate the flow field in a viscous fluid. Panels (c) and (d) show a larger section of the corresponding flow fields in panels (a) and (b), respectively, extended from the swimmer axes towards the top. Turning to vertical distances $\gtrsim L$ above the swimmer body, the flow lines bend away from the vertical symmetry axis between the two force centers. The depicted flow fields are mirror symmetric to the bottom half space below the swimmer (not shown). Here we fix $b = 0.4$ and $F = \mu L^2$.

follows. Expressing the traveled distance vector in a time interval $\tau = t - t'$ as $\mathbf{R}(t) - \mathbf{R}(t') = V\tau\hat{\boldsymbol{\Phi}}$, rescaling time by $(\eta/\mu)^{-1}$, and rescaling velocity by $(L\mu/\eta)^{-1}$, we obtain

$$V = \frac{F}{4\pi\mu L^2}\left[\frac{1-2b}{b(1-b)} - \int_0^\infty d\tau\, e^{-(1+\mathcal{V})\tau}\left\{\frac{1}{|V\tau \mp b|} - \frac{1}{|V\tau \pm (1-b)|}\right\}\right], \quad (21)$$

for pushers and for pullers, respectively. The first term on the right-hand side is the exact hydrodynamic limit for a purely viscous environment. Corresponding numerical evaluations can be performed using Mathematica [64]. Figure 5 shows the
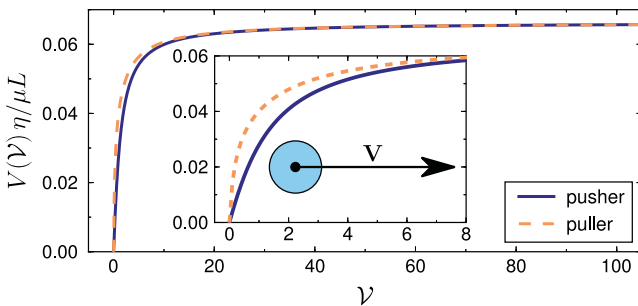

FIG. 5. Steady-state swimming speed $V(\mathcal{V})$ as a function of the rescaled "forgetfulness" parameter defined in Eq. (16). Single, isolated pusher and puller microswimmers are considered as introduced in Fig. 4. We observe the hydrodynamic value for $\mathcal{V} \gg 1$ and a continuous drop with decreasing $\mathcal{V}$ towards $V(\mathcal{V} \to 0) = 0$, the latter reflecting the completely reversible elastic case. The inset magnifies the behavior for small values of $\mathcal{V}$.

steady-state swimming speed $V(\mathcal{V})$ for pushers and for pullers obtained in this way.

As may have been expected, for $\mathcal{V} \to \infty$ the swimming speed tends towards the hydrodynamic value obtained for a microswimmer propelling through a purely viscous fluid. It is identical for pushers and for pullers. In contrast to that, in a completely reversibly deformable elastic environment, the active microswimmer ultimately must come to a rest when the forward drive is balanced by the elastic restoring forces. Thus, $V(\mathcal{V} \to 0) = 0$. In between, $V(\mathcal{V})$ continuously drops to zero with decreasing $\mathcal{V}$. That individual pushers in the intermediate regime tend to be slower than individual pullers seems reasonable from Fig. 4. The swimmer bodies propel into the trace that the heading concentrated force center has left in the viscoelastic medium. Due to the time lag, set by the swimming speed V, the memorized displacements that were induced on this trace by the heading force center are in the process of relaxation. While the medium around the heading force center of the pusher has been displaced into the swimming direction, it relaxes back into the opposite direction when the swimmer body arrives. Along these lines, a counteracting contribution results for pushers. The reverse follows for pullers.

In addition to that, we here address the mutual interactions mediated by the viscoelastic environment within a pair of microswimmers that propel alongside each other. Since the two microswimmers mutually attract or repel each other, see below, there is no steady-state finite distance between the two swimmers. Thus, as a measure for their mutual interaction, we evaluate the flow field alongside one microswimmer in a steady-state motion with velocity **V**; see Fig. 5. Another microswimmer exposed to this flow field will be affected
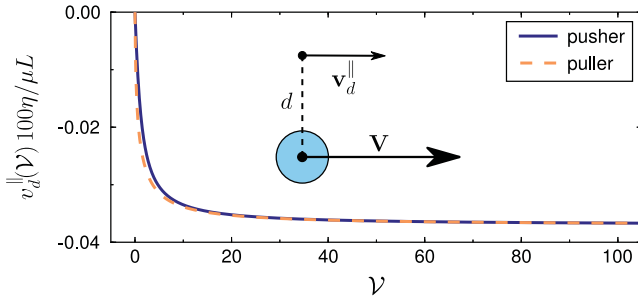
FIG. 6. Velocity field $\mathbf{v}_d$ alongside one isolated swimmer in steady-state motion (see Figs. 4 and 5) at a distance d and as a function of the rescaled "forgetfulness" parameter $\mathcal{V}$. $\mathbf{v}_d$ is a measure for the mutual interaction between two microswimmers propelling in parallel. Here, the value of the component $\mathbf{v}_d^{\parallel}$ pointing into the direction of the isolated swimming velocity $\mathbf{V}$ is plotted. $v_d^{\parallel} < 0$ indicates mutual slow-down when compared to the speed of an individual, isolated swimmer in Fig. 5. We here set $d = 2L$.
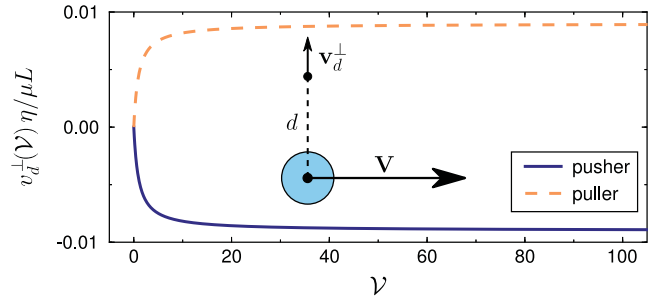

FIG. 7. Velocity field $\mathbf{v}_d$ alongside one isolated swimmer in steady-state motion (see Figs. 4 and 5) at a distance d and as a function of the rescaled "forgetfulness" parameter $\mathcal{V}$. In this case, the value of the component $\mathbf{v}_d^{\perp}$ pointing into a direction perpendicular to $\mathbf{V}$, away from the body of the steadily propelling swimmer, is plotted. $v_d^{\perp} < 0$ indicates mutual attraction between two swimmers propelling alongside, while $v_d^{\perp} > 0$ marks mutual repulsion. Again we set $d = 2L$.

accordingly. That is, the second swimmer will be sped up or slowed down along its swimming path, and it will be attracted towards or driven away from the first swimmer. Similar arguments apply to the displacements of nearby tracer particles.

Accordingly, we evaluate the velocity field $\mathbf{v}_d$ induced in the viscoelastic medium at a distance d alongside the swimmer. If the magnitude of the component $\mathbf{v}_d^{\parallel}$ pointing into the direction of $\mathbf{V}$ is positive, i.e., $v_d^{\parallel} > 0$, the nearby swimmer propelling in parallel will be sped up. The opposite applies for $v_d^{\parallel} < 0$. For $d = 2L$, corresponding results are depicted in Fig. 6. Obviously, since $v_d^{\parallel} < 0$, two swimmers propelling in parallel tend to weakly mutually slow each other down. Figure 6 indicates a slightly weaker magnitude of slow-down for pushers than for pullers.

The effect of mutual slow-down is in agreement with the flow fields outlined in Figs. 4(c) and 4(d), as the field lines bend away from the vertical center line when turning to vertical distances $\gtrsim L$ above (and below) the swimmer body. Thus, the flow fields there feature a component with direction opposite to the propulsion direction $\hat{\mathbf{\Phi}}(t)$. Swimmers propelling in parallel with their swimmer bodies in such positions will thus mutually slow each other down.

Similarly, if the magnitude of the component $\mathbf{v}_d^{\perp}$ pointing perpendicularly away from the first swimmer is positive, i.e., $v_d^{\perp} > 0$, a nearby swimmer propelling alongside will be pushed away, while it will be attracted for $v_d^{\perp} < 0$. The corresponding results are depicted in Fig. 7. As can be inferred already from the flow lines in Fig. 4, pushers attract while pullers repel each other [65]. The effect decreases in magnitude with decreasing $\mathcal{V}$.

In the future, this approach should be pursued along several different directions. First, the influence of a finite extension of the swimmer body should be investigated, using the formalism outlined in Sec. III. Second, the collective behavior of crowds of active microswimmers in viscoelastic media should be analyzed on the basis of our description, possibly combining it with statistical theories [29,63]. This might even allow to

extend related theories on mesoscale turbulence [66,67] to viscoelastic environments.

V. CONCLUSIONS

In summary, we have introduced and evaluated a formalism to describe the dynamic behavior of particulate inclusions in viscoelastic environments when driven by externally imposed, induced, or actively self-generated forces. Interactions of the particles mediated by the viscoelastic surroundings are covered explicitly. Both the limits of a reversibly elastic solidlike and a memoryless viscous fluidlike environment are comprised.

As examples, we characterized the drag of a sphere, the dynamic behavior and mutual interactions of spherical magnetizable particles, as well as dynamic properties of active microswimmers in viscoelastic media. We expect our results to be important, for instance, for the future characterization of the switching dynamics of soft actuation devices [8,52–54,68], to describe the collective dynamics in large ensembles of active microswimmers [16–19,37], to further improve evaluations of active microrheological measurements [3–5,69], or to extend previous studies on the interactions between living cells in soft environments [70,71]. In principle, the procedure can be carried over to other linear models of viscoelasticity as well, to adjust it to the specific properties of a given viscoelastic environment. In the present case, an explicit analytical expression was available in real space for the Green's function and facilitated our evaluation.

APPENDIX A: CONTINUUM DESCRIPTION FOR THE VISCOELASTIC BACKGROUND MEDIA DERIVED FROM A GENERALIZED HYDRODYNAMIC APPROACH

The continuum description in Eq. (3) for the dynamics of the viscoelastic environment was motivated by combining Stokes's equations for the viscous low-Reynolds-number hydrodynamics [Eq. (1)] with the Navier-Cauchy equations of linear elasticity [Eq. (2)]. Supplementing it by the simple relaxation relation in Eq. (4), we obtained the continuum characterization in Eq. (5) for the memory displacement field $\mathbf{u}(\mathbf{r}, t)$. Here we demonstrate that these relations can be obtained in a different way as well. For this purpose, we systematically linearize the continuum equations obtained by a previous generalized hydrodynamic theory on viscoelastic materials based on conservation laws and symmetry arguments [30].

In Ref. [30] the field $a(\mathbf{r}, t)$ describes the positions that the material elements currently located at positions $\mathbf{r}$ would tend to take, if all stresses were absent. Thus, $a(\mathbf{r}, t) = \mathbf{r} - \mathbf{u}(\mathbf{r}, t)$. Accordingly, the components of the elastic strain tensor are given by

$$U_{ik} = \tfrac{1}{2}[\delta_{ik} - (\nabla_i a_l)(\nabla_k a_l)], \qquad (A1)$$

with δ_{ik} the Kronecker delta. In the present case, we consider isotropic, homogeneous, infinitely extended viscoelastic environments and therefore do not keep track of reorientations of anisotropy directions of the viscoelastic medium, quantified in Ref. [30] by the rotation matrix $\mathbf{R}$. Moreover, since in our case the material displacements are assumed to vanish for $|\mathbf{r}| \to \infty$, we here identify $a(\mathbf{r}, t) \equiv \mathbf{r}$ for $|\mathbf{r}| \to \infty$ (and use Latin indices throughout).

Then our dynamic equation for the motion within the viscoelastic medium is obtained from the dynamic equation in Ref. [30] for the components of the momentum density $\mathbf{g}(\mathbf{r}, t) = \rho(\mathbf{r}, t)\mathbf{v}(\mathbf{r}, t)$,

$$\dot{g}_i + \nabla_j (\sigma_{ij} - \sigma_{ij}^{\mathrm{D}}) = f_{b,i}, \qquad (A2)$$

where we have added the bulk force density to the right-hand side for our purpose. Assuming incompressibility, the mass density ρ is constant.

In Eq. (A2), the components of the stress tensor σ_{ij} are given by $\sigma_{ij} = p\delta_{ij} + v_i g_j + \psi_{lj}\nabla_i a_l$ [30]. Here $\psi_{lj} = \Psi_{km}(\partial U_{km}/\partial \nabla_j a_l)$ and $\Psi_{km} = \mu U_{km}$. The latter follows via $d\epsilon = \Psi_{km} dU_{km}$ from the harmonic elastic energy density $\epsilon = K_{ijkm}U_{ij}U_{km}/2$ when expanding $K_{ijkm} = (K_L - K_T/3)\delta_{ij}\delta_{km} + K_T/2(\delta_{ik}\delta_{jm} + \delta_{im}\delta_{jk})$ for isotropic materials [30], assuming incompressibility, and identifying $\mu \equiv K_T/2$ in our notation.

To obtain the appropriate components of the dissipative stresses σ_{ij}^{D}, we involve the quantity $A_{ij} = (\nabla_i v_j + \nabla_j v_i)/2$ [30], leading to $\sigma_{ij}^{D} = \eta_{ijkl} A_{kl}$. Expanding the viscosity tensor η_{ijkl} similarly to K_{ijkl} above, only one viscosity η remains in the end for isotropic incompressible media.

Finally, we collect all these contributions and insert them into Eq. (A2). After strict linearization in $\mathbf{u}(\mathbf{r}, t)$ and $\mathbf{v}(\mathbf{r}, t)$, neglecting $\dot{g}_i$ in the overdamped situation and for low Reynolds numbers, we indeed obtain our Eq. (3) from the systematic hydrodynamic approach in Ref. [30] based on conservation laws and symmetry properties.

In view of our dynamic equation for $\mathbf{u}(\mathbf{r}, t)$, Eq. (4), we adopt the relation

$$\dot{U}_{ij} - A_{ij} = -\alpha_T \Psi_{ij}^0 - \frac{\delta_{ij}}{3}\alpha_L \Psi_{kk} \qquad (A3)$$

from Ref. [30], where we have already dropped obviously nonlinear contributions $\sim v_k \nabla_k U_{ij}$ and $\sim (\nabla_i v_k)U_{kj}$. The superscript zero indicates the trace-free part. α_T and α_L denote transport coefficients. Inserting the relations listed above, systematically linearizing in the fields $\mathbf{u}(\mathbf{r}, t)$ and $\mathbf{v}(\mathbf{r}, t)$, as well as exploiting incompressibility, we obtain

$$\nabla_i(\dot{u}_j - v_j + 2\mu\alpha_T u_j) + \nabla_j(\dot{u}_i - v_i + 2\mu\alpha_T u_i) = 0. \qquad (A4)$$

Identifying $\gamma \equiv 2\mu\alpha_T$, our Eq. (4) is in line with this relation, supported by $\mathbf{u}(\mathbf{r}, t) = \mathbf{0} = \mathbf{v}(\mathbf{r}, t)$ for $|\mathbf{r}| \to \infty$.

APPENDIX B: EXPLICIT DERIVATION OF THE GREEN'S FUNCTION

Here, we repeat the explicit derivation of the expression for the viscoelastic Green's function $\underline{\mathbf{G}}(\mathbf{r}, t)$ in Eq. (7) from the underlying linear partial differential equation in Eq. (5). For this purpose, the incompressibility relations stated in Eqs. (1) and (2) are used. The method works by Fourier transformation both in space and time, solution for the displacement field, and subsequent inverse Fourier transformation.

Starting from Eq. (5), the Green's function $\underline{\mathbf{G}}(\mathbf{r}, t)$ quantifies the displacement field $\mathbf{u}(\mathbf{r}, t)$ created by a point force impact $\mathbf{F}$ resulting from

$$\mathbf{f}_b(\mathbf{r}, t) = \mathbf{F}\delta(\mathbf{r} - \mathbf{R}_0)\delta(t - t_0), \qquad (B1)$$

where $\mathbf{R}_0$ and t_0 set the position and time of attack, respectively. That is, the resulting displacement field reads $\mathbf{u}(\mathbf{r}, t) = \underline{\mathbf{G}}(\mathbf{r} - \mathbf{R}_0, t - t_0) \cdot \mathbf{F}$. Without loss of generality, we choose $\mathbf{R}_0 = \mathbf{0}$ and $t_0 = 0$, for simplicity, so that this relation becomes

$$\mathbf{u}(\mathbf{r}, t) = \underline{\mathbf{G}}(\mathbf{r}, t) \cdot \mathbf{F}. \qquad (B2)$$

Integrating both sides of Eq. (5) over

$$\frac{1}{(2\pi)^2} \int_{\mathbb{R}^3} d^3 r \, e^{-i\mathbf{k}\cdot\mathbf{r}} \int_{\mathbb{R}} dt \, e^{-i\omega t}, \qquad (B3)$$

we obtain its space-and-time Fourier transform as

$$k^2(\mu + \gamma\eta + i\omega\eta)\tilde{\mathbf{u}}(\mathbf{k}, \omega) = -i\mathbf{k}\tilde{p}(\mathbf{k}, \omega) + \tilde{\mathbf{f}}_b(\mathbf{k}, \omega), \qquad (B4)$$

with Fourier-transformed quantities marked by the tilde. Equation (B1) implies

$$\tilde{\mathbf{f}}_b(\mathbf{k}, \omega) = \frac{1}{(2\pi)^2}\mathbf{F}. \qquad (B5)$$

Next, we involve the incompressibility relations stated in Eqs. (1) and (2). Together with Eq. (4), they read

$$\nabla \cdot \mathbf{u}(\mathbf{r}, t) = 0, \quad \nabla \cdot \dot{\mathbf{u}}(\mathbf{r}, t) = 0. \qquad (B6)$$

Their space-and-time Fourier transforms via Eq. (B3) follow as

$$\mathbf{k} \cdot \tilde{\mathbf{u}}(\mathbf{k}, \omega) = 0, \quad \mathbf{k} \cdot \tilde{\dot{\mathbf{u}}}(\mathbf{k}, \omega) = 0, \qquad (B7)$$

from which the relations $\mathbf{k} \perp \tilde{\mathbf{u}}(\mathbf{k}, \omega)$ and $\mathbf{k} \perp \tilde{\mathbf{u}}(\mathbf{k}, \omega)$ are obtained. Multiplication of Eq. (B4) by the projection operator $\hat{\mathbf{I}} - \hat{\mathbf{k}}\hat{\mathbf{k}}$, with $\hat{\mathbf{k}} = \mathbf{k}/|\mathbf{k}|$ and $\hat{\mathbf{I}}$ denoting the unity matrix, then solving for $\tilde{\mathbf{u}}$ yields

$$\tilde{\mathbf{u}}(\mathbf{k}, \omega) = \frac{1}{k^2(\mu^\star + i\omega\eta)}(\hat{\mathbf{I}} - \hat{\mathbf{k}}\hat{\mathbf{k}}) \cdot \frac{1}{(2\pi)^2}\mathbf{F}, \quad (B8)$$

where $\mu^\star := \mu + \gamma\eta$. We can rewrite Eq. (B8) as

$$\tilde{\mathbf{u}}(\mathbf{k}, \omega) = \underline{\tilde{\mathbf{G}}}(\mathbf{k}, \omega) \cdot \mathbf{F}, \quad (B9)$$

which corresponds to the Fourier transform of Eq. (B2). Therefore,

$$\underline{\tilde{\mathbf{G}}}(\mathbf{k}, \omega) = \frac{1}{(2\pi)^2 k^2(\mu^\star + i\omega\eta)}(\hat{\mathbf{I}} - \hat{\mathbf{k}}\hat{\mathbf{k}}) \quad (B10)$$

is the space-and-time Fourier transform of the Green's function. To obtain the Green's function in real space, we then need to calculate the inverse Fourier transformation,

$$\underline{\mathbf{G}}(\mathbf{r}, t) = \frac{1}{(2\pi)^2} \int_{\mathbb{R}^3} d^3k\, e^{i\mathbf{k}\cdot\mathbf{r}} \int_{\mathbb{R}} d\omega\, e^{i\omega t} \underline{\tilde{\mathbf{G}}}(\mathbf{k}, \omega). \quad (B11)$$

First, we evaluate the $\int d\omega$ integral,

$$\frac{1}{\sqrt{2\pi}\, i\eta} \int_{\mathbb{R}} d\omega \frac{e^{i\omega t}}{\omega - i\frac{\mu^\star}{\eta}}, \quad (B12)$$

with a singularity in the complex plane at $\omega = i\mu^\star/\eta$. For $t > 0$, the integration path is closed in the upper half plane. For $t < 0$, the integration path is closed in the lower half plane, where there is no singularity. Using the residue theorem, we thus find

$$\frac{1}{\sqrt{2\pi}\, i\eta} \int_{\mathbb{R}} d\omega \frac{e^{i\omega t}}{\omega - i\frac{\mu^\star}{\eta}} = \frac{\sqrt{2\pi}}{\eta}\Theta(t)e^{-\frac{\mu^\star}{\eta}t}, \quad (B13)$$

where $\Theta(\cdot)$ denotes the Heaviside step function.

Then the inverse transformation in space remains as

$$\underline{\mathbf{G}}(\mathbf{r}, t) = C \int_{\mathbb{R}^3} d^3k \frac{e^{i\mathbf{k}\cdot\mathbf{r}}}{k^2}(\hat{\mathbf{I}} - \hat{\mathbf{k}}\hat{\mathbf{k}}), \quad (B14)$$

with the abbreviation

$$C = \frac{\Theta(t)}{(2\pi)^3\eta}e^{-\frac{\mu^\star}{\eta}t}. \quad (B15)$$

As an ansatz for $\underline{\mathbf{G}}(\mathbf{r}, t)$, we choose [2]

$$\underline{\mathbf{G}}(\mathbf{r}, t) = A\hat{\mathbf{I}} + B\hat{\mathbf{r}}\hat{\mathbf{r}}, \quad (B16)$$

implying $A = A(r, t)$, $B = B(r, t)$, $r = |\mathbf{r}|$, and $\hat{\mathbf{r}} = \mathbf{r}/r$. First, from the trace $G_{jj}(\mathbf{r}, t)$, where summation over repeated indices is implied, we obtain the relation

$$\begin{aligned} 3A + B &= 2C \int_0^{2\pi} d\varphi \int_{-1}^1 d\cos\vartheta \int_0^\infty dk\, e^{ikr\cos\vartheta} \\ &= \frac{8\pi C}{r} \int_0^\infty dk \frac{\sin(kr)}{k} \\ &= \frac{8\pi C}{r} \int_0^\infty d\xi \frac{\sin\xi}{\xi} \\ &= \frac{4\pi^2 C}{r}. \end{aligned} \quad (B17)$$

Analogously, the contraction $G_{ij}(\mathbf{r}, t)\hat{r}_i\hat{r}_j$ yields the relation

$$\begin{aligned} A + B &= 2\pi C \int_{-1}^1 d\cos\vartheta \int_0^\infty dk\, (1 - \cos^2\vartheta)e^{ikr\cos\vartheta} \\ &= \frac{2\pi C}{r} \int_0^\infty d\xi \int_{-1}^1 d\cos\vartheta \left(1 + \frac{\partial^2}{\partial\xi^2}\right) e^{i\xi\cos\vartheta} \\ &= \frac{4\pi C}{r} \int_0^\infty d\xi \left(1 + \frac{\partial^2}{\partial\xi^2}\right) \frac{\sin\xi}{\xi} \\ &= \frac{2\pi^2 C}{r}. \end{aligned} \quad (B18)$$

In combination, we find from Eqs. (B17) and (B18) that

$$A = B = \frac{\Theta(t)}{8\pi\eta r}e^{-\frac{\mu^\star}{\eta}t}, \quad (B19)$$

resulting in Eq. (7) for the viscoelastic Green's function.

APPENDIX C: KRAMERS-KRONIG RELATIONS

Next, we briefly demonstrate that the Green's function derived in Eqs. (7) and (B10) indeed satisfies the famous Kramers-Kronig relations [57]. To this end, we solve Eq. (B4) for $\tilde{\mathbf{u}}(\mathbf{k}, \omega)$ and apply to both sides of the equation the projection operator $\hat{\mathbf{I}} - \hat{\mathbf{k}}\hat{\mathbf{k}}$; see above. Exploiting Eq. (B7), this projection leaves $\tilde{\mathbf{u}}(\mathbf{k}, \omega)$ unchanged. From the resulting equation of the form

$$\tilde{\mathbf{u}}(\mathbf{k}, \omega) = \chi(k, \omega)(\hat{\mathbf{I}} - \hat{\mathbf{k}}\hat{\mathbf{k}}) \cdot \tilde{\mathbf{f}}_b(\mathbf{k}, \omega), \quad (C1)$$

we thus obtain an effective susceptibility

$$\chi(k, \omega) = \frac{1}{k^2}\frac{\mu + \gamma\eta - i\omega\eta}{(\mu + \gamma\eta)^2 + \omega^2\eta^2}. \quad (C2)$$

It has a shape related to the Kelvin-Voigt model [although the additional parameter γ plays a decisive qualitative role in the present case and controls the long-term system behavior; this becomes clear from the rescaling at the beginning of Sec. IV A, which identifies $\mathcal{V} = \gamma\eta/\mu$ in Eq. (16) as the one remaining parameter to quantify the behavior of the viscoelastic environment]. We can rewrite $\chi(k, \omega)$ as

$$\chi(k, \omega) = \chi_1(k, \omega) + i\chi_2(k, \omega), \quad (C3)$$

with $\chi_1(k, \omega) = \Re\chi(k, \omega)$ an even and $\chi_2(k, \omega) = \Im\chi(k, \omega)$ an odd function of ω. A singularity is located in the upper complex half-plane at $\omega = i(\mu + \gamma\eta)/\eta$. Then the Kramers-Kronig relations for positive frequencies ω can be formulated as

$$\chi_1(k, \omega) = -\frac{2}{\pi}\mathcal{P}\int_0^\infty d\omega' \frac{\omega'\chi_2(k, \omega')}{\omega'^2 - \omega^2}, \quad (C4)$$

$$\chi_2(k, \omega) = \frac{2\omega}{\pi}\mathcal{P}\int_0^\infty d\omega' \frac{\chi_1(k, \omega')}{\omega'^2 - \omega^2}, \quad (C5)$$

linking the real and imaginary parts of $\chi(k, \omega)$ to each other. Since $\chi(k, \omega)$ vanishes as $\sim\omega^{-1}$ for $\omega \to \infty$ and $\eta \neq 0$, the requirements for the Kramers-Kronig relations Eqs. (C4) and (C5) to be satisfied are met.

APPENDIX D: BASIC EXAMPLE TRAJECTORY OF A MATERIAL ELEMENT SUBJECT TO AN INTERIM CONSTANT CONCENTRATED FORCE DENSITY

In this slightly academic example, we further illustrate via analytical formulas the background of our description introduced in Eqs. (3) and (4). For this purpose, we consider the force density,

$$\mathbf{f}_b(\mathbf{r}, t) = F\hat{\mathbf{x}}\,\delta(\mathbf{r})(\Theta(t) - \Theta(t - t_e)), \qquad (D1)$$

spatially concentrated at the origin, pointing with constant magnitude $F > 0$ into the x direction, switched on at time $t = 0$, and turned off at time $t = t_e$. Moreover, we here only consider positions $\mathbf{r}$ on the positive x axis, parameterized by $\mathbf{r} = r\hat{\mathbf{x}}$, with $r > 0$. Consequently, the spatial integral in Eq. (9) reduces to

$$\int_{\mathbb{R}^3} d^3 r'\, \underline{\mathbf{G}}(\mathbf{r} - \mathbf{r}') \cdot \mathbf{f}_b(\mathbf{r}', t') = \frac{F}{4\pi\eta r}\hat{\mathbf{x}}(\Theta(t') - \Theta(t' - t_e)). \qquad (D2)$$

Obviously, for $t < 0$, there is no motion and displacement of material elements.

For $0 < t < t_e$, via Eqs. (4) and (9), we calculate the velocity on the positive x axis as

$$\mathbf{v}(\mathbf{r}, t) = \frac{F}{4\pi\eta r}\hat{\mathbf{x}}\left[1 - \frac{1}{1+\mathcal{V}}\left(1 - e^{-\frac{\mu+\gamma\eta}{\eta}t}\right)\right], \qquad (D3)$$

where we have used the definition in Eq. (16). The trajectory $\mathbf{R}(t)$ of a material element initially located on the positive x axis at position $\mathbf{R}(t < 0) = R_0\hat{\mathbf{x}}$, with $R_0 > 0$, therefore remains confined to the x axis. From

$$\frac{d\mathbf{R}(t)}{dt} = \mathbf{v}(\mathbf{R}(t), t), \qquad (D4)$$

with $\mathbf{R}(t) = R(t)\hat{\mathbf{x}}$, we thus obtain

$$R(t)^2 = R_0^2 + \frac{F}{2\pi\eta}\frac{1}{1+\mathcal{V}}\left[\mathcal{V}t + \frac{\eta}{\mu+\gamma\eta}\left(1 - e^{-\frac{\mu+\gamma\eta}{\eta}t}\right)\right]. \qquad (D5)$$

Afterwards, for $t > t_e$, the velocity field on the positive x axis becomes

$$\mathbf{v}(\mathbf{r}, t) = -\frac{F}{4\pi\eta r}\hat{\mathbf{x}}\frac{1}{1+\mathcal{V}}\left(e^{\frac{\mu+\gamma\eta}{\eta}t_e} - 1\right)e^{-\frac{\mu+\gamma\eta}{\eta}t}. \qquad (D6)$$

Consequently, the trajectory is determined by

$$R(t)^2 = R_0^2 + \frac{F}{2\pi\eta}\frac{1}{1+\mathcal{V}}\left[\mathcal{V}t_e + \frac{\eta}{\mu+\gamma\eta}\left(e^{\frac{\mu+\gamma\eta}{\eta}t_e} - 1\right)\right. $$
$$\left. \times e^{-\frac{\mu+\gamma\eta}{\eta}t}\right], \qquad (D7)$$

which follows again via Eq. (D4) and upon inserting Eq. (D5) for $t = t_e$.

If we measure time in units of η/μ and again use the definition in Eq. (16), then Eq. (D7) becomes

$$R(t)^2 = R_0^2 + \frac{F}{2\pi\mu}\frac{1}{1+\mathcal{V}}\left[\mathcal{V}t_e + \frac{1}{1+\mathcal{V}}(e^{(1+\mathcal{V})t_e} - 1)\right.$$
$$\left. \times e^{-(1+\mathcal{V})t}\right]. \qquad (D8)$$

We can infer from this basic example the relevance of the parameter $\mathcal{V}$. In the fully reversible elastic situation, i.e., for $\mathcal{V} = 0$, the material element at long times $t \to \infty$ returns to its initial position $\mathbf{R}(t = 0) = R_0\hat{\mathbf{x}}$. This is not the case for $\mathcal{V} \neq 0$. Thus, the parameter $\mathcal{V}$ qualitatively determines the behavior of the system. One could perform another rescaling of time to remove the factor $1 + \mathcal{V}$ from the exponents, but this does not eliminate the influence of $\mathcal{V}$ on the first contribution of t_e in Eq. (D8).

APPENDIX E: ADDITIONAL NET TORQUES APPLIED TO THE SPHERICAL PARTICLES

The effect of net forces acting on the spherical particles has been addressed in Eq. (10). Since the underlying equations are linear in the displacement field [see Eq. (5)], the effects of additional torques can simply be superimposed.

We proceed in the same way as in the case of the applied forces. Applying a net torque $\mathbf{T}(t)$ to a spherical particle of radius a in analogy to the case of an applied force, we consider the displacement field

$$\mathbf{u}(\mathbf{r}, t) = \int_{\mathbb{R}} dt'\, G(t - t')\left\{-\frac{1}{2}\mathbf{T}(t') \cdot [\nabla \times \underline{\mathbf{G}}(\mathbf{s}(t'))]\right.$$
$$\times \Theta(|\mathbf{s}(t')| - a) + \frac{1}{8\pi\eta a^3}\mathbf{T}(t') \times \mathbf{s}(t')$$
$$\left. \times \Theta(a - |\mathbf{s}(t')|)\right\}, \qquad (E1)$$

with $\mathbf{s}(t') := \mathbf{r} - \mathbf{R}(t')$ and again a continuous integrand for each $|\mathbf{s}(t')| = a$. In analogy to Eq. (10), the expression in Eq. (E1) solves for $|\mathbf{s}(t)| > a$, i.e., inside the embedding medium, the linear Eq. (5) for $\mathbf{f}_b(\mathbf{r}, t) = \mathbf{0}$, together with $\nabla \cdot \mathbf{u}(\mathbf{r}, t) = 0$. Moreover, $\mathbf{u}(\mathbf{r}, t) \to \mathbf{0}$ for $|\mathbf{s}(t)| \to \infty$ [see Eq. (7)] if all $|\mathbf{R}(t')|$ remain finite. Additionally, at each instant in time t', the expression in square brackets now leads to a rigid rotation of all points on the surface of the sphere, i.e., for $|\mathbf{s}(t')| = a$. The latter can be shown by explicitly evaluating $\nabla \times \underline{\mathbf{G}}(\mathbf{r} - \mathbf{R}(t'))$. As for the case of applied forces in Eq. (10), the displacements and rotations of the sphere at time t resulting from the contributions generated in Eq. (E1) at earlier times $t' < t$ can then be calculated via Eqs. (12) and (13).

APPENDIX F: NUMERICAL DISCRETIZATION SCHEME

To trace the position $\mathbf{R}(t)$ and orientation of a displaced and rotated particle embedded in the viscoelastic environment over time, we numerically evaluate our equations. For this purpose, we use a discretization scheme as briefly summarized below. For brevity, we here only describe the positional updates. We proceed in a similar way concerning the rotational iteration, replacing velocities by angular velocities and displacements by rotations, respectively. Moreover, we here for illustration only consider displacements prescribed on the particle by the surrounding medium. If additional forces are exerted on a particle, their effect is superimposed. Finally, we here assume a point particle, the displacement of which coincides with the local displacement field of the viscoelastic medium at the particle position $\mathbf{R}(t)$. To evaluate

the displacements of the particles of finite size, the additional integrations according to the Faxén relations, Eqs. (12) and (13), are performed, or Eqs. (14) and (15) are evaluated, depending on the situation at hand.

Under the present assumptions, the position $\mathbf{R}(t)$ of our point particle is updated during the time step from time t to time $t + \Delta t$ via

$$\mathbf{R}(t + \Delta t) = \mathbf{R}(t) + \Delta \mathbf{R}(t). \tag{F1}$$

We calculate the particle displacement $\Delta \mathbf{R}(t)$ prescribed by the environment by integrating the velocity field at the particle position over time. This velocity field is obtained via Eq. (4) from the displacement field. During the numerical discretization one needs to be careful in distinguishing whether the positional coordinates refer to the undeformed or the deformed state of the material. In the linearized analytical theory, this difference is not resolved [30,38]. Yet, in our numerical treatment, involving finite time steps and displacements, this difference becomes relevant. Particularly, it must be treated with care to find a final static elastic state under constant applied forces. To solve this issue, we calculate in our numerical discretization the displacement field from the positions in the undeformed state. Accordingly, we shift back our particles as given by their present memorized displacements $\mathbf{U}(t)$, when we calculate during each time step the forces they exert on the environment and to determine the additional displacements they experience in the next time step.

Summarizing, the incremental new displacement of a particle $\Delta \mathbf{R}(t)$ at time t is calculated via

$$\Delta \mathbf{R}(t) = \int_t^{t+\Delta t} dt' \, \mathbf{v}(\mathbf{R}(t') - \mathbf{U}(t'), t') = \mathbf{u}(\mathbf{R}(t') - \mathbf{U}(t'), t')|_t^{t+\Delta t} + \gamma \Delta t \, \mathbf{u}(\mathbf{R}(t) - \mathbf{U}(t), t), \tag{F2}$$

where Eq. (4) has been used. Obviously, this computation of $\Delta \mathbf{R}(t)$ formally involves the value of the displacement field $\mathbf{u}(\mathbf{R}(t + \Delta t) - \mathbf{U}(t + \Delta t), t + \Delta t)$ at the next time step. Technically, we address this issue by an iterative procedure at each time step.

In the following, we evaluate for illustration over the first $N + 1$ time steps the translation of a pointlike particle, assuming an initially undistorted state at $t = 0$. The initial rest position of the particle is thus at $\mathbf{R}(0)$. Using Eqs. (F1) and (F2) together with $\mathbf{u}(\mathbf{R}(0), 0) = \mathbf{0}$, while defining for brevity $\bar{\mathbf{R}}(t) = \mathbf{R}(t) - \mathbf{U}(t)$, we obtain the positions at the $N + 1$ next time steps as

$$\mathbf{R}(\Delta t) \;=\; \mathbf{R}(0) + \Delta \mathbf{R}(0) = \mathbf{R}(0) + \mathbf{u}(\bar{\mathbf{R}}(\Delta t), \Delta t), \tag{F3}$$

$$\mathbf{R}(2\Delta t) = \mathbf{R}(\Delta t) + \Delta \mathbf{R}(\Delta t) = \mathbf{R}(0) + \mathbf{u}(\bar{\mathbf{R}}(2\Delta t), 2\Delta t) + \gamma \Delta t \, \mathbf{u}(\bar{\mathbf{R}}(\Delta t), \Delta t), \tag{F4}$$

$$\mathbf{R}(3\Delta t) = \mathbf{R}(2\Delta t) + \Delta \mathbf{R}(2\Delta t) = \mathbf{R}(0) + \mathbf{u}(\bar{\mathbf{R}}(3\Delta t), 3\Delta t) + \gamma \Delta t [\mathbf{u}(\bar{\mathbf{R}}(\Delta t), \Delta t) + \mathbf{u}(\bar{\mathbf{R}}(2\Delta t), 2\Delta t)], \tag{F5}$$

$$\vdots$$

$$\mathbf{R}((N+1)\Delta t) = \mathbf{R}(N\Delta t) + \Delta \mathbf{R}(N\Delta t) = \mathbf{R}(0) + \mathbf{u}(\bar{\mathbf{R}}((N+1)\Delta t), (N+1)\Delta t) + \gamma \Delta t \sum_{n=1}^{N} \mathbf{u}(\bar{\mathbf{R}}(n\Delta t), n\Delta t). \tag{F6}$$

In the completely reversible elastic limit of $\gamma \to 0$, the displacements at all time steps are thus calculated from the memorized initial position $\mathbf{R}(0)$, as then $\mathbf{U}(t) = \mathbf{R}(t) - \mathbf{R}(0)$ and thus $\bar{\mathbf{R}}(t) = \mathbf{R}(0)$. This guarantees that under a constant force field applied to the elastic environment the particle finally comes to a rest at the correct final position.

If a force is exerted on the particle, it transmits this force to the surrounding viscoelastic environment. The resulting displacement field in the environment is calculated from the Green's function; see Eq. (7). Then, likewise, in the argument of the Green's function, $\bar{\mathbf{R}}(t)$ appears to specify the position of the force center given by our point particle to determine the resulting distortion of the environment from its memorized undistorted state. That is, we use the Green's function in the form $\underline{\mathbf{G}}(\mathbf{r} - \bar{\mathbf{R}}(t))$, or, after discretization, as

$$\underline{\mathbf{G}}(\mathbf{r} - \bar{\mathbf{R}}((N+1)\Delta t), (N+1)\Delta t) = \underline{\mathbf{G}}\left(\mathbf{r} - \mathbf{R}(0) - \gamma \Delta t \sum_{n=1}^{N} \mathbf{u}(\bar{\mathbf{R}}(n\Delta t), n\Delta t)\right), \tag{F7}$$

after inserting Eq. (F6), with $\mathbf{u}(\bar{\mathbf{R}}((N+1)\Delta t), (N+1)\Delta t) = \mathbf{U}((N+1)\Delta t)$ for our point particle. Again, the correct reversible elastic limit is obtained for $\gamma \to 0$, in which the effect of the pointlike force center is always calculated from its position $\mathbf{R}(0)$ in the memorized undistorted state.

We stress that in Sec. III we considered particles of finite size. Addressing rotational degrees of freedom follows accordingly.

[1] P.-G. De Gennes, *Scaling Concepts in Polymer Physics* (Cornell University Press, Ithaca NY, 1979).

[2] M. Doi and S. F. Edwards, *The Theory of Polymer Dynamics* (Oxford University Press, Oxford, 1988).

[3] F. Ziemann, J. Rädler, and E. Sackmann, Biophys. J. **66**, 2210 (1994).

[4] T. A. Waigh, Rep. Prog. Phys. **68**, 685 (2005).

[5] C. Wilhelm, Phys. Rev. Lett. **101**, 028101 (2008).

[6] A. R. Bausch, W. Möller, and E. Sackmann, Biophys. J. **76**, 573 (1999).

[7] L. G. Wilson and W. C. K. Poon, Phys. Chem. Chem. Phys. **13**, 10617 (2011).

[8] G. Filipcsei, I. Csetneki, A. Szilágyi, and M. Zrínyi, Adv. Polym. Sci. **206**, 137 (2007).

[9] H.-N. An, J. Groenewold, S. J. Picken, and E. Mendes, Soft Matter **10**, 997 (2014).

[10] S. Huang, G. Pessot, P. Cremer, R. Weeber, C. Holm, J. Nowak, S. Odenbach, A. M. Menzel, and G. K. Auernhammer, Soft Matter **12**, 228 (2016).

[11] M. Puljiz, S. Huang, G. K. Auernhammer, and A. M. Menzel, Phys. Rev. Lett. **117**, 238003 (2016).

[12] J. Elgeti, R. G. Winkler, and G. Gompper, Rep. Prog. Phys. **78**, 056601 (2015).

[13] C. Bechinger, R. Di Leonardo, H. Löwen, C. Reichhardt, G. Volpe, and G. Volpe, Rev. Mod. Phys. **88**, 045006 (2016).

[14] A. Zöttl and H. Stark, J. Phys.: Condens. Matter **28**, 253001 (2016).

[15] A. M. Menzel, Phys. Rep. **554**, 1 (2015).

[16] E. A. Gaffney, H. Gadêlha, D. J. Smith, J. R. Blake, and J. C. Kirkman-Brown, Ann. Rev. Fluid Mech. **43**, 501 (2011).

[17] G. Li and A. M. Ardekani, Phys. Rev. Lett. **117**, 118001 (2016).

[18] J. R. Gomez-Solano, A. Blokhuis, and C. Bechinger, Phys. Rev. Lett. **116**, 138301 (2016).

[19] C. Lozano, J. R. Gomez-Solano, and C. Bechinger, New J. Phys. **20**, 015008 (2018).

[20] C. Datt, G. Natale, S. G. Hatzikiriakos, and G. J. Elfring, J. Fluid Mech. **823**, 675 (2017).

[21] A. Einstein, Ann. Phys. **324**, 289 (1906).

[22] A. Einstein, Ann. Phys. **339**, 591 (1911).

[23] H. M. Smallwood, J. Appl. Phys. **15**, 758 (1944).

[24] G. K. Batchelor and J. T. Green, J. Fluid Mech. **56**, 401 (1972).

[25] J. K. G. Dhont, An Introduction to Dynamics of Colloids (Elsevier, Amsterdam, 1996).

[26] J. F. Morris and J. F. Brady, J. Fluid Mech. **312**, 223 (1996).

[27] M. Rex and H. Löwen, Phys. Rev. Lett. **101**, 148302 (2008).

[28] P. Cremer, M. Heinen, A. M. Menzel, and H. Löwen, J. Phys.: Condens. Matter **29**, 275102 (2017).

[29] A. M. Menzel, A. Saha, C. Hoell, and H. Löwen, J. Chem. Phys. **144**, 024115 (2016).

[30] H. Temmen, H. Pleiner, M. Liu, and H. R. Brand, Phys. Rev. Lett. **84**, 3228 (2000).

[31] G. G. Stokes, Trans. Cambridge Philos. Soc. **8**, 287 (1845).

[32] A. L. Cauchy, Exercises de mathématiques **3**, 328 (1828).

[33] N. Narinder, C. Bechinger, and J. R. Gomez-Solano, Phys. Rev. Lett. **121**, 078003 (2018).

[34] M. Puljiz, S. Huang, K. A. Kalina, J. Nowak, S. Odenbach, M. Kästner, G. K. Auernhammer, and A. M. Menzel, Soft Matter **14**, 6809 (2018).

[35] A. J. Levine and T. C. Lubensky, Phys. Rev. Lett. **85**, 1774 (2000).

[36] A. J. Levine and T. C. Lubensky, Phys. Rev. E **63**, 041510 (2001).

[37] K. Yasuda, R. Okamoto, and S. Komura, Europhys. Lett. **123**, 34002 (2018).

[38] L. D. Landau and E. M. Lifshitz, Theory of Elasticity (Elsevier, Oxford, 1986).

[39] S. Kim and S. J. Karrila, Microhydrodynamics: Principles and Selected Applications (Butterworth-Heinemann, Boston, 1991).

[40] C. Teodosiu, The Elastic Field of Point Defects (Springer, Berlin, 1982).

[41] M. Puljiz and A. M. Menzel, Phys. Rev. E **95**, 053002 (2017).

[42] S. Kim and N. Phan-Thien, J. Elasticity **37**, 93 (1995).

[43] A. N. Norris, J. Acoust. Soc. Am. **123**, 99 (2008).

[44] C. H. L. Beentjes, Quadrature on a spherical surface, Working Note, University of Oxford, http://people.maths.ox.ac.uk/beentjes/Essays (2015).

[45] N. Phan-Thien, J. Elasticity **32**, 243 (1993).

[46] S. Odenbach, Arch. Appl. Mech. **86**, 269 (2016).

[47] R. Weeber, M. Hermes, A. M. Schmidt, and C. Holm, J. Phys.: Condens. Matter **30**, 063002 (2018).

[48] M. Schümann and S. Odenbach, J. Magn. Magn. Mater. **441**, 88 (2017).

[49] L. Roeder, P. Bender, M. Kundt, A. Tschöpe, and A. M. Schmidt, Phys. Chem. Chem. Phys. **17**, 1290 (2015).

[50] P. Ilg and A. E. A. S. Evangelopoulos, Phys. Rev. E **97**, 032610 (2018).

[51] S. Goh, A. M. Menzel, and H. Löwen, Phys. Chem. Chem. Phys. **20**, 15037 (2018).

[52] R. Fuhrer, E. K. Athanassiou, N. A. Luechinger, and W. J. Stark, Small **5**, 383 (2009).

[53] P. Ilg, Soft Matter **9**, 3465 (2013).

[54] J. Thévenot, H. Oliveira, O. Sandre, and S. Lecommandoux, Chem. Soc. Rev. **42**, 7099 (2013).

[55] J. Li, M. Zhang, L. Wang, W. Li, P. Sheng, and W. Wen, Microfluid. Nanofluid. **10**, 919 (2011).

[56] S. H. L. Klapp, J. Phys.: Condens. Matter **17**, R525 (2005).

[57] J. D. Jackson, Classical Electrodynamics (Wiley, New York, 1999).

[58] D. Saintillan and M. J. Shelley, Phys. Rev. Lett. **99**, 058102 (2007).

[59] F. Alarcón and I. Pagonabarraga, J. Mol. Liq. **185**, 56 (2013).

[60] N. Oyama, J. J. Molina, and R. Yamamoto, Phys. Rev. E **93**, 043114 (2016).

[61] A. Zöttl and J. M. Yeomans, arXiv:1710.03505 (2017).

[62] A. Daddi-Moussa-Ider and A. M. Menzel, Phys. Rev. Fluids **3**, 094102 (2018).

[63] C. Hoell, H. Löwen, and A. M. Menzel, New J. Phys. **19**, 125004 (2017).

[64] Wolfram Research Inc., Mathematica, Version 11.0.0 (Wolfram Research Inc., Champaign, IL, 2016).

[65] I. O. Götze and G. Gompper, Phys. Rev. E **82**, 041921 (2010).

[66] S. Heidenreich, J. Dunkel, S. H. L. Klapp, and M. Bär, Phys. Rev. E **94**, 020601 (2016).

[67] H. Reinken, S. H. L. Klapp, M. Bär, and S. Heidenreich, Phys. Rev. E **97**, 022613 (2018).

[68] J. Kim, S. E. Chung, S.-E. Choi, L. Howon, J. Kim, and S. Kwon, Nat. Mater. **10**, 747 (2011).

[69] A. S. Khair and T. M. Squires, Phys. Rev. Lett. **105**, 156001 (2010).

[70] U. S. Schwarz and S. A. Safran, Phys. Rev. Lett. **88**, 048102 (2002).

[71] O. Cohen and S. A. Safran, Soft Matter **12**, 6088 (2016).

Publication V

Displacement field around a rigid sphere in a compressible elastic environment, corresponding higher-order Faxén relations, as well as higher-order displaceability and rotateability matrices

M. Puljiz and A. M. Menzel,

Author's contributions

Both authors contributed to this work. I performed the analytical calculations. A. M. Menzel checked the analytical results independently. I found the modified derivation of the displacement field around a translated and rotated sphere. Moreover, I performed the exemplary studies in consultation with A. M. Menzel. I estimate my overall contribution to this work to approximately 85%.

Copyright and license notice

3 Concluding remarks

We have presented a particle-resolved theoretical description of interactions between rigid spherical inclusions mediated by linearly elastic environments, see Publication II and Publication V. The spheres can be displaced and rotated by external forces and torques, respectively, as well as by the deformation fields created by other spheres in the surrounding medium. These interactions were summarized in (mathematical) displaceability and rotateability matrices, which are formal analogs to the mobility matrices in low-Reynolds number hydrodynamics [69,73,74]. Our theory has successfully been used to describe rearrangements in experimental sample configurations of rigid paramagnetic particles embedded in soft polymeric gels, when exposed to external magnetic fields, see Publication I and Publication III. Especially for the linear particle displacements in Publication I, a very good agreement between experiment and theory was found using a refined method of calculating the magnetic dipole-dipole forces. Moreover, it was possible to extract the shear moduli from the experimental sample data, which in the present case were not accessible by direct measurements. In Publication III, our micromechanical estimation of the local sample modulus was confirmed by a very good agreement between the experimental data and high-resolution finite-element simulations that involved nonlinear and spatially resolved particle magnetization. A reversible magnetomechanical collapse of two paramagnetic particles into (virtual) contact was described. In total, a pronounced magnetomechanical hysteretic behavior for a magnetization-and-demagnetization cycle of the two-particle system was predicted both by theory and finite-element simulations.

The theory itself, as described particularly in Publication II and Publication V, is not restricted to magnetic gels but can serve as a tool for the analysis of other elastic composite materials as well, possibly, for example, materials that exhibit electrostrictive effects [78,79]. Often, particulate inclusions have geometrical shapes other than spherical so that in many cases closed-form expressions are unavailable in the corresponding description. It is, however, possible to approximate any shape by many-sphere compositions (raspberry model) [80,81]. This, for instance, shall enable

to model the behavior of elongated particles [9,72,82,83] for an analysis of their rotational characteristics and interactions between them under external magnetic torques in an elastic environment. From the computational point of view, three-dimensional systems with large particle numbers can quickly be analyzed numerically with our theory, depending on the degree of deformation either quantitatively or at least still qualitatively otherwise. These results could then be combined with finite-element simulations or related methods [34,39,42,43,84], to partly reduce the computational effort.

Finally, in Publication IV, we have introduced a dynamic theory to address particulate inclusions in incompressible linearly viscoelastic media that can be derived from a general macroscopic continuum approach [52]. Both extreme limits of a purely elastic solid and a viscous fluid are correctly reproduced. The key feature that distinguishes the viscoelastic regime from the two limits is the finite nonzero relaxation rate of the medium, which specifies the degree of preserved memory of the initial state during displacements. We have, inter alia, investigated the motion of magnetizable spheres when exposed to external magnetic fields and found for active self-propelled microswimmers that the hydrodynamic symmetry between model pushers and pullers concerning their steady-state velocity is broken in the viscoelastic regime. The relation to both low-Reynolds-number hydrodynamics and linear elasticity theory for incompressible media allows to transfer many concepts from either field to our viscoelastic description. As one example, it might be possible to describe the effect of a rigid wall on nearby particles by a viscoelastic Blake tensor in analogy to low-Reynolds-number hydrodynamics [85–87] and linear elasticity theory [88].

Summarizing, we consider our elastostatic theory and our dynamic viscoelastic theory to be of practical relevance for several future applications to characterize the behavior of soft (visco-)elastic composite materials. The strength of our approach when combined, e.g., with micromechanical measurements of the shear modulus in elastic composite materials has been demonstrated in Publication I and Publication III. Moreover, it can even be useful to analyze nonlinear situations in soft magnetic gels as well, see Publication III, if the nonlinearity mainly results from the magnetic interactions. The dynamic theory could possibly be utilized to improve the evaluation of microrheological measurements of complex fluids [89,90]. Other possible fields of application involve the examination of cytoskeletal properties [11,91], elastic interactions between biological cells [92–95], as well as further investigations of the dynamics of microswimmers [53,96–98]. Our results can be important when

describing in the future, starting from a particle scale, the applications of soft elastic composite materials as tunable dampers and vibration absorbers [99–102], actuators and sensors [19, 24, 25, 28, 103], as well as energy storage devices [79]. In conclusion, we expect our theories to help to deepen the general understanding of complex elastic and viscoelastic materials, also concerning scale-bridging efforts from the mesoscopic to the macroscopic picture [6, 50].

Bibliography

[1] M. Doi. Soft Matter Physics. Oxford University Press, Oxford, 2013.

[2] R. A. L. Jones. Soft Condensed Matter, volume 6. Oxford University Press, Oxford, 2002.

[3] G. Filipcsei, I. Csetneki, A. Szilágyi, and M. Zrínyi. Magnetic field-responsive smart polymer composites. Adv. Polym. Sci., 206:137, 2007.

[4] A. M. Menzel. Tuned, driven, and active soft matter. Phys. Rep., 554:1, 2015.

[5] S. Odenbach. Microstructure and rheology of magnetic hybrid materials. Arch. Appl. Mech., 86:269, 2016.

[6] A. M. Menzel. Mesoscopic characterization of magnetoelastic hybrid materials: magnetic gels and elastomers, their particle-scale description, and scale-bridging links. Arch. Appl. Mech., doi: 10.1007/s00419-018-1413-7, 2018.

[7] G. R. Strobl. The Physics of Polymers. Springer, Berlin, 2007.

[8] M. Zrínyi, L. Barsi, and A. Büki. Deformation of ferrogels induced by nonuniform magnetic fields. J. Chem. Phys., 104:8750, 1996.

[9] P. Bender, A. Günther, A. Tschöpe, and R. Birringer. Synthesis and characterization of uniaxial ferrogels with Ni nanorods as magnetic phase. J. Magn. Magn. Mater, 323:2055, 2011.

[10] L. Roeder, P. Bender, M. Kundt, A. Tschöpe, and A. M. Schmidt. Magnetic and geometric anisotropy in particle-crosslinked ferrohydrogels. Phys. Chem. Chem. Phys., 17:1290, 2015.

[11] F. Ziemann, J. Rädler, and E. Sackmann. Local measurements of viscoelastic moduli of entangled actin networks using an oscillating magnetic bead micro-rheometer. Biophys. J., 66:2210, 1994.

[12] A. R. Bausch, W. Möller, and E. Sackmann. Measurement of local viscoelasticity and forces in living cells by magnetic tweezers. Biophys. J., 76:573, 1999.

[13] C. Wilhelm. Out-of-equilibrium microrheology inside living cells. Phys. Rev. Lett., 101:028101, 2008.

[14] M. Babincová, D. Leszczynska, P. Sourivong, P. Čičmanec, and P. Babinec. Superparamagnetic gel as a novel material for electromagnetically induced hyperthermia. J. Magn. Magn. Mater., 225:109, 2001.

[15] Y. Li, G. Huang, X. Zhang, B. Li, Y. Chen, T. Lu, T. J. Lu, and F. Xu. Magnetic hydrogels and their potential biomedical applications. Adv. Func. Mater., 23:660, 2013.

[16] M. K. Lima-Tenorio, E. A. G. Pineda, N. M. Ahmad, H. Fessi, and A. Elaissari. Magnetic nanoparticles: in vivo cancer diagnosis and therapy. Int. J. Pharm., 493:313, 2015.

[17] M. Schümann and S. Odenbach. In-situ observation of the particle microstructure of magnetorheological elastomers in presence of mechanical strain and magnetic fields. J. Magn. Magn. Mater., 441:88, 2017.

[18] M. Schümann, D. Borin, S. Huang, G. K. Auernhammer, R. Müller, and S. Odenbach. A characterization of the magnetically induced movement of NdFeB-particles in magnetorheological elastomers. Smart Mater. Struct., 26:095018, 2017.

[19] M. M. Schmauch, S. R. Mishra, B. A. Evans, O. D. Velev, and J. B. Tracy. Chained iron microparticles for directionally controlled actuation of soft robots. ACS Appl. Mater. Interfaces, 9:11895, 2017.

[20] G. Diguet, E. Beaugnon, and J.-Y. Cavaillé. From dipolar interactions of a random distribution of ferromagnetic particles to magnetostriction. J. Magn. Magn. Mater., 321:396, 2009.

[21] O. V. Stolbov, Y. L. Raikher, and M. Balasoiu. Modelling of magnetodipolar striction in soft magnetic elastomers. Soft Matter, 7:8484, 2011.

[22] G. Pessot, P. Cremer, D. Y. Borin, S. Odenbach, H. Löwen, and A. M. Menzel. Structural control of elastic moduli in ferrogels and the importance of non-affine deformations. J. Chem. Phys., 141:124904, 2014.

[23] G. Schubert and P. Harrison. Large-strain behaviour of magneto-rheological elastomers tested under uniaxial compression and tension, and pure shear deformations. Polym. Test., 42:122, 2015.

[24] Y. An and M. T. Shaw. Actuating properties of soft gels with ordered iron particles: basis for a shear actuator. Smart Mater. Struct., 12:157, 2003.

[25] G. Ausanio, C. Hison, V. Iannotti, C. Luponio, and L. Lanotte. Elastomagnetic effect in novel elastic magnets. J. Magn. Magn. Mater., 272:2069, 2004.

[26] J. Baumgartl, M. Zvyagolskaya, and C. Bechinger. Tailoring of phononic band structures in colloidal crystals. Phys. Rev. Lett., 99:205503, 2007.

[27] R. Fuhrer, E. K. Athanassiou, N. A. Luechinger, and W. J. Stark. Crosslinking metal nanoparticles into the polymer backbone of hydrogels enables preparation of soft, magnetic field-driven actuators with muscle-like flexibility. Small, 5:383, 2009.

[28] H. Böse, R. Rabindranath, and J. Ehrlich. Soft magnetorheological elastomers as new actuators for valves. J. Intel. Mater. Syst. Struct., 23:989, 2012.

[29] P. Ilg. Stimuli-responsive hydrogels cross-linked by magnetic nanoparticles. Soft Matter, 9:3465, 2013.

[30] T. Potisk, D. Svenšek, H. R. Brand, H. Pleiner, D. Lisjak, N. Osterman, and A. Mertelj. Dynamic magneto-optic coupling in a ferromagnetic nematic liquid crystal. Phys. Rev. Lett., 119:097802, 2017.

[31] T. Potisk, A. Mertelj, N. Sebastián, N. Osterman, D. Lisjak, H. R. Brand, H. Pleiner, and D. Svenšek. Magneto-optic dynamics in a ferromagnetic nematic liquid crystal. Phys. Rev. E, 97:012701, 2018.

[32] S. Huang, G. Pessot, P. Cremer, R. Weeber, C. Holm, J. Nowak, S. Odenbach, A. M. Menzel, and G. K. Auernhammer. Buckling of paramagnetic chains in soft gels. Soft Matter, 12:228, 2016.

[33] P. Cremer, H. Löwen, and A. M. Menzel. Tailoring superelasticity of soft magnetic materials. Appl. Phys. Lett., 107:171903, 2015.

[34] P. Cremer, H. Löwen, and A. M. Menzel. Superelastic stress–strain behavior in ferrogels with different types of magneto-elastic coupling. Phys. Chem. Chem. Phys., 18:26670, 2016.

[35] M. A. Annunziata, A. M. Menzel, and H. Löwen. Hardening transition in a one-dimensional model for ferrogels. J. Chem. Phys., 138:204906, 2013.

[36] G. Pessot, R. Weeber, C. Holm, H. Löwen, and A. M. Menzel. Towards a scale-bridging description of ferrogels and magnetic elastomers. J. Phys.: Condens. Matter, 27:325105, 2015.

[37] G. Pessot, H. Löwen, and A. M. Menzel. Dynamic elastic moduli in magnetic gels: normal modes and linear response. J. Chem. Phys., 145:104904, 2016.

[38] S. Goh, A. M. Menzel, and H. Löwen. Dynamics in a one-dimensional ferrogel model: relaxation, pairing, shock-wave propagation. Phys. Chem. Chem. Phys., 20:15037, 2018.

[39] C. Spieler, M. Kästner, J. Goldmann, J. Brummund, and V. Ulbricht. XFEM modeling and homogenization of magnetoactive composites. Acta Mech., 224:2453, 2013.

[40] A. M. Biller, O. V. Stolbov, and Y. L. Raikher. Modeling of particle interactions in magnetorheological elastomers. J. Appl. Phys., 116:114904, 2014.

[41] A. M. Biller, O. V. Stolbov, and Y. L. Raikher. Mesoscopic magnetomechanical hysteresis in a magnetorheological elastomer. Phys. Rev. E, 92:023202, 2015.

[42] P. Metsch, K. A. Kalina, C. Spieler, and M. Kästner. A numerical study on magnetostrictive phenomena in magnetorheological elastomers. Comp. Mater. Sci., 124:364, 2016.

[43] A. Attaran, J. Brummund, and T. Wallmersperger. Modeling and finite element simulation of the magneto-mechanical behavior of ferrogels. J. Magn. Magn. Mater., 431:188, 2017.

[44] R. Weeber, S. Kantorovich, and C. Holm. Deformation mechanisms in 2d magnetic gels studied by computer simulations. Soft Matter, 8:9923, 2012.

[45] R. Weeber, S. Kantorovich, and C. Holm. Ferrogels cross-linked by magnetic nanoparticles – deformation mechanisms in two and three dimensions studied by means of computer simulations. J. Magn. Magn. Mater., 383:262, 2015.

[46] T. Gundermann, P. Cremer, H. Löwen, A. M. Menzel, and S. Odenbach. Statistical analysis of magnetically soft particles in magnetorheological elastomers. Smart Mater. Struct., 26:045012, 2017.

[47] P. Cremer, M. Heinen, A. M. Menzel, and H. Löwen. A density functional approach to ferrogels. J. Phys.: Condens. Matter, 29:275102, 2017.

[48] E. Jarkova, H. Pleiner, H.-W. Müller, and H. R. Brand. Hydrodynamics of isotropic ferrogels. Phys. Rev. E, 68:041706, 2003.

[49] S. Bohlius, H. R. Brand, and H. Pleiner. Macroscopic dynamics of uniaxial magnetic gels. Phys. Rev. E, 70:061411, 2004.

108

[50] A M. Menzel. Bridging from particle to macroscopic scales in uniaxial magnetic gels. J. Chem. Phys., 141:194907, 2014.

[51] L. D. Landau and E. M. Lifshitz. Theory of Elasticity. Elsevier, Oxford, 1986.

[52] H. Temmen, H. Pleiner, M. Liu, and H. R. Brand. Convective nonlinearity in non-Newtonian fluids. Phys. Rev. Lett., 84:3228, 2000.

[53] J. R. Gomez-Solano, A. Blokhuis, and C. Bechinger. Dynamics of self-propelled Janus particles in viscoelastic fluids. Phys. Rev. Lett., 116:138301, 2016.

[54] N. Narinder, C. Bechinger, and J. R. Gomez-Solano. Memory-induced transition from a persistent random walk to circular motion for achiral microswimmers. Phys. Rev. Lett., 121:078003, 2018.

[55] J. D. Eshelby. The determination of the elastic field of an ellipsoidal inclusion, and related problems. Proc. R. Soc. Lond. A, 241:376, 1957.

[56] J. D. Eshelby. The elastic field outside an ellipsoidal inclusion. Proc. R. Soc. Lond. A, 252:561, 1959.

[57] L. J. Walpole. A rotated rigid ellipsoidal inclusion in an elastic medium. Proc. R. Soc. Lond. A, 433:179, 1991.

[58] L. J. Walpole. A translated rigid ellipsoidal inclusion in an elastic medium. Proc. R. Soc. Lond. A, 434:571, 1991.

[59] N. Phan-Thien. Rigid spherical inclusion: the multipole expansion. J. Elasticity, 32:243, 1993.

[60] N. Phan-Thien and S. Kim. The load transfer between two rigid spherical inclusions in an elastic medium. ZAMP, 45:177, 1994.

[61] L. J. Walpole. The Green functions of an elastic medium surrounding a rigid spherical inclusion. Q. J. Mech. Appl. Math., 58:129, 2005.

[62] W. Voigt. Lehrbuch der Kristallphysik (mit Ausschluss der Kristalloptik). Teubner, Leipzig, 1910.

[63] A.-L. Cauchy. Exercices de Mathématiques, volume 3. Bure frères, Paris, 1828.

[64] Wolfram Research Inc. Mathematica 11.0.0. Wolfram Research Inc., Champaign, IL, 2016.

[65] T. Mura. Micromechanics of Defects in Solids. Martinus Nijhoff Publishers, Dordrecht, 1987.

[66] G. K. Batchelor and J. T. Green. The determination of the bulk stress in a suspension of spherical particles to order c^2. J. Fluid Mech., 56:401, 1972.

[67] S. Kim and S. J. Karrila. Microhydrodynamics: Principles and Selected Applications. Butterworth-Heinemann, Boston, 1991.

[68] S. Kim and N. Phan-Thien. Faxén relations and some rigid inclusion problems. J. Elasticity, 37:93, 1995.

[69] J. K. G. Dhont. An Introduction to Dynamics of Colloids. Elsevier, Amsterdam, 1996.

[70] J. D. Jackson. Classical Electrodynamics. Wiley, New York, 1999.

[71] E. C. Stoner and E. P. Wohlfarth. A mechanism of magnetic hysteresis in heterogeneous alloys. Philos. Trans. R. Soc. London A, 240:599, 1948.

[72] C. Schopphoven, K. Birster, R. Schweitzer, C. Lux, S. Huang, M. Kästner, G. K. Auernhammer, and A. Tschöpe. Elastic deformations in semi-dilute Ni nanorod/hydrogel composites. Arch. Appl. Mech., doi: 10.1007/s00419-018-1461-z, 2018.

[73] B. U. Felderhof. Hydrodynamic interaction between two spheres. Physica A, 89:373, 1977.

[74] P. Mazur and W. van Saarloos. Many-sphere hydrodynamic interactions and mobilities in a suspension. Physica A, 115:21, 1982.

[75] L. D. Landau and E. M. Lifshitz. Fluid Mechanics. Elsevier, Oxford, 1987.

[76] G. G. Stokes. On the theories of the internal friction of fluids in motion, and of the equilibrium and motion of elastic solids. Trans. Cambridge Philos. Soc., 8:287, 1845.

[77] A. M. Menzel, A. Saha, C. Hoell, and H. Löwen. Dynamical density functional theory for microswimmers. J. Chem. Phys., 144:024115, 2016.

[78] K. Wongtimnoi, B. Guiffard, A. Bogner-Van de Moortele, L. Seveyrat, C. Gauthier, and J.-Y. Cavaillé. Improvement of electrostrictive properties of a polyether-based polyurethane elastomer filled with conductive carbon black. Compos. Sci. Technol., 71:885, 2011.

[79] E. Allahyarov, H. Löwen, and L. Zhu. A simulation study of the electrostriction effects in dielectric elastomer composites containing polarizable inclusions with different spatial distributions. Phys. Chem. Chem. Phys., 17:32479, 2015.

[80] V. Lobaskin and B. Dünweg. A new model for simulating colloidal dynamics. New J. Phys., 6:54, 2004.

[81] C. Passow, B. ten Hagen, H. Löwen, and J. Wagner. Depolarized light scattering from prolate anisotropic particles: the influence of the particle shape on the field autocorrelation function. J. Chem. Phys., 143:044903, 2015.

[82] L. Roeder, P. Bender, A. Tschöpe, R. Birringer, and A. M. Schmidt. Shear modulus determination in model hydrogels by means of elongated magnetic nanoprobes. J. Polym. Sci. B: Polym. Phys., 50:1772, 2012.

[83] P. Bender, A. Tschöpe, and R. Birringer. Determination of the shear modulus of gelatine hydrogels by magnetization measurements using dispersed nickel nanorods as mechanical probes. J. Magn. Magn. Mater., 346:152, 2013.

[84] Y. Han, W. Hong, and L. E. Faidley. Field-stiffening effect of magneto-rheological elastomers. Int. J. Solids Struct., 50:2281, 2013.

[85] J. R. Blake. A note on the image system for a Stokeslet in a no-slip boundary. Proc. Camb. Phil. Soc., 70:303, 1971.

[86] T. M. Squires and M. P. Brenner. Like-charge attraction and hydrodynamic interaction. Phys. Rev. Lett., 85:4976, 2000.

[87] Y. W. Kim and R. R. Netz. Electro-osmosis at inhomogeneous charged surfaces: hydrodynamic versus electric friction. J. Chem. Phys., 124:114709, 2006.

[88] A. M. Menzel. Force-induced elastic matrix-mediated interactions in the presence of a rigid wall. Soft Matter, 13:3373, 2017.

[89] T. A. Waigh. Microrheology of complex fluids. Rep. Prog. Phys., 68:685, 2005.

[90] A. S. Khair and T. M. Squires. Active microrheology: a proposed technique to measure normal stress coefficients of complex fluids. Phys. Rev. Lett., 105:156001, 2010.

[91] D. Mizuno, C. Tardin, C. F. Schmidt, and F. C. MacKintosh. Nonequilibrium mechanics of active cytoskeletal networks. Science, 315:370, 2007.

[92] U. S. Schwarz and S. A. Safran. Elastic interactions of cells. Phys. Rev. Lett., 88:048102, 2002.

[93] I. B. Bischofs and U. S. Schwarz. Cell organization in soft media due to active mechanosensing. Proc. Natl. Acad. Sci. U.S.A., 100:9274, 2003.

[94] J. Yuval and S. A. Safran. Dynamics of elastic interactions in soft and biological matter. Phys. Rev. E, 87:042703, 2013.

[95] O. Cohen and S. A. Safran. Elastic interactions synchronize beating in cardiomy-ocytes. Soft Matter, 12:6088, 2016.

[96] E. A. Gaffney, H. Gadêlha, D. J. Smith, J. R. Blake, and J. C. Kirkman-Brown. Mammalian sperm motility: observation and theory. Ann. Rev. Fluid Mech., 43:501, 2011.

[97] G. Li and A. M. Ardekani. Collective motion of microorganisms in a viscoelastic fluid. Phys. Rev. Lett., 117:118001, 2016.

[98] K. Yasuda, R. Okamoto, and S. Komura. A three-sphere microswimmer in a struc-tured fluid. Europhys. Lett., 123:34002, 2018.

[99] H.-X. Deng, X.-L. Gong, and L.-H. Wang. Development of an adaptive tuned vibration absorber with magnetorheological elastomer. Smart Mater. Struct., 15:N111, 2006.

[100] T. L. Sun, X. L. Gong, W. Q. Jiang, J. F. Li, Z. B. Xu, and W. H. Li. Study on the damping properties of magnetorheological elastomers based on cis-polybutadiene rubber. Polym. Test., 27:520, 2008.

[101] G. J. Liao, X. L. Gong, S. H. Xuan, C. J. Kang, and L. H. Zong. Development of a real-time tunable stiffness and damping vibration isolator based on magnetorheological elastomer. J. Int. Mater. Syst. Struct., 23:25, 2012.

[102] V. S. Molchanov, G. V. Stepanov, V. G. Vasiliev, E. Y. Kramarenko, A. R. Khokhlov, Z.-D. Xu, and Y.-Q. Guo. Viscoelastic properties of magnetorheological elastomers for damping applications. Macromol. Mater. Eng., 299:1116, 2014.

[103] L. Lanotte, G. Ausanio, C. Hison, V. Iannotti, and C. Luponio. The potentiality of composite elastic magnets as novel materials for sensors and actuators. Sens. Actuators A, 106:56, 2003.